JULY 1961 VOLUME 12 (1961) No. 2

GREGG M. SINCLAIR LIBRARY
UNIVERSITY OF HAWAII
8-7-63

NUCLEAR INSTRUMENTS & METHODS

A JOURNAL ON ACCELERATORS, INSTRUMENTATION AND TECHNIQUES IN NUCLEAR PHYSICS

EDITOR: K. SIEGBAHN - UPPSALA

LAST NUMBER OF THIS VOLUME

CONTENTS

G. DEARNALEY and A. B. WHITEHEAD, The semiconductor surface barrier for nuclear particle detection 205

EKBAL BASHANDY, Methods for the measurement of sub-nanosecond lifetimes of low-energy nuclear levels 227

FRED S. GOULDING and WILLIAM L. HANSEN, Leakage current in semiconductor junction radiation detectors and its influence on energy-resolution characteristics 249

G. BOLOGNA, G. DIAMBRINI, R. TOSCHI, A. S. FIGUERA, U. PELLEGRINI, B. RISPOLI and A. SERRA, A pair spectrometer for energies up to 2 GeV 263

P. A. TOVE and K. FALK, Transit time of charge carriers in the semiconductor ionization chamber 278

ROLF NORDHAGEN, Proton resonances suitable to shape calibrate a scintillation γ-ray spectrometer 291

C. R. HILL, A method of alpha particle spectroscopy for materials of very low specific activity 299

R. GABRIEL and A. M. SEGAR, Some transistor circuits for nuclear physics research 307

N. A. BURGOV, A. V. DAVYDOV and G. R. KARTASHOV, An iron-free toroidal β-spectrometer with high transmission 316

H. W. K. HOPKINS, M. DAVISON, L. LYONS, J. M. BREARE, D. ROAF and D. F. SHAW, A 12 cm liquid deuterium bubble chamber 323

W. LOHMANN and W. H. PERKINS, Stabilization of the counting rate by irradiation of the liquid scintillation counting solutions with UV-light 329

L. CRANBERG, R. A. FERNALD, F. S. HAHN and E. F. SHRADER, Production of high intensity ion pulses of nanosecond duration 335

M. AGENO, Low jitter pulse discriminator and shaper 341

C. C. CHANG, Magnetohydrodynamic method of injecting charged particles into a magnetic field 345

MASATERU SONODA, AKIRA KATASE, MASAO SEKI and TSUNEKAZU AKIYOSHI, Magnetic field of alternately charged symmetric multipole magnet 349

D. J. ROWE, G. L. SALMON and A. B. CLEGG, Finite geometry corrections for angular correlation measurements 353

S. HOLMRYD, K. E. LARSSON and K. OTNES, A neutron time-of-flight spectrometer with a semi-monochromatizing chopper 355

Letters to the Editor

J. C. VANDERLEEDEN and M. K. RAMASWAMY, Total conversion coefficients with a sum-coincidence NaI spectrometer 362

A. A. ARZUMANOV, R. A. METSHCHEROV, E. S. MIRONOV, L. M. NEMENOV, S. N. RIBIN and J. A. KHOLMOVSKIJ, Extraction of a beam and energy regulation in the cyclotron with azimuthally varying magnetic field 363

R. E. SCHMUNK and R. M. BRUGGER, the scattering surface method of measuring dispersion relations with a phased chopper velocity selector 365

Book Reviews 367

Erratum 367

Author Index 368

Subject Index 370

NORTH-HOLLAND PUBLISHING COMPANY — AMSTERDAM

NUCLEAR INSTRUMENTS AND METHODS

A journal on accelerators, instrumentation and techniques in nuclear physics

EDITOR: K. SIEGBAHN, UPPSALA

EDITORIAL BOARD:

J. B. ADAMS (CERN)
F. A. ALSINA (Buenos Aires)
E. AMALDI (Rome)
H. L. ANDERSON (Chicago)
K. T. BAINBRIDGE (Cambridge Mass.)
P. R. BELL (Oak Ridge)
R. E. BELL (Montreal)
A. BERTHELOT (Saclay)
H. BRINKMAN (Groningen)
E. H. COOKE-YARBOROUGH (Harwell)
S. DE BENEDETTI (Pittsburgh)
M. DE HEMPTINNE (Louvain)
A. DE-SHALIT (Rehovoth)
M. DEUTSCH (Cambridge Mass.)
S. DU TOIT (Pretoria)
B. S. DŽELEPOV (Leningrad)
W. GENTNER (Heidelberg)
P. C. GUGELOT (Amsterdam)
H. HALBAN (Paris)
O. HAXEL (Heidelberg)
P. HUBER (Basel)
S. KIKUCHI (Tokyo)
J. KOCH (Copenhagen)
M. S. KOZODAEV (Moscow)
S. LIVINGSTON (Cambridge Mass.)
E. M. MCMILLAN (Berkeley)
M. G. MEŠČERJAKOW (Moscow)
P. B. MOON (Birmingham)
M. L. OLIPHANT (Canberra)
W. PAUL (Bonn)
A. S. RAO (Bombay)
G. SALVINI (Rome)
P. SAVIĆ (Belgrade)
P. SCHERRER (Zürich)
CH. SCHMELZER (CERN)
R. TANGEN (Oslo)
D. TAYLOR (Northampton)
V. I. VEKSLER (Moscow)
G. VON DARDEL (CERN)
O. WERNHOLM (Stockholm)
R. R. WILSON (Cornell)
S. D. WINTER (Saclay)

INSTRUCTIONS FOR CONTRIBUTORS

Contributions may be sent to the Editor, Professor K. Siegbahn, Institute of Physics, University of Uppsala, Sweden, either directly or through the intermediation of one of the members of the Editorial Board. Contributions may be written in English, French or German but should always, except for very short papers, be supplied with a brief abstract in English. Figures should be in inked original drawings or glossy prints and they should be sufficiently large. Contributors should make sure that important details in drawings and photographs will show up clearly in the diminished copy used by the publisher.

Books for review should be sent to Professor Siegbahn.

Objective and descriptive material on endeavours and product developments from the industry for the section "Spotlight on Industry" should be sent directly to the publishers, North-Holland Publishing Company, P.O. Box 103, Amsterdam.

Nuclear Instruments and Methods is published monthly. The subscription price of a volume of 360 pages is $ 17.00 (130 s), postage free.

Subscriptions should be sent to the publishers, North-Holland Publishing Company, P.O. Box 103, Amsterdam, or to any subscription-agent.

No part of this issue may be reproduced in any form, by print, photoprint, microfilm or any other means without written permission from the publisher.

Tracerlab nuclear instruments are often (not always) more expensive than competitive equipment.

Still they are always your best investment because they last longer and perform better.

They outlast others because Tracerlab uses the most advanced and finest components. They perform better because Tracerlab instruments represent the newest developments in the field of nuclear instrumentation.

(In 1960 alone, Tracerlab spent more than half a million dollars on research and development.)

Tracerlab

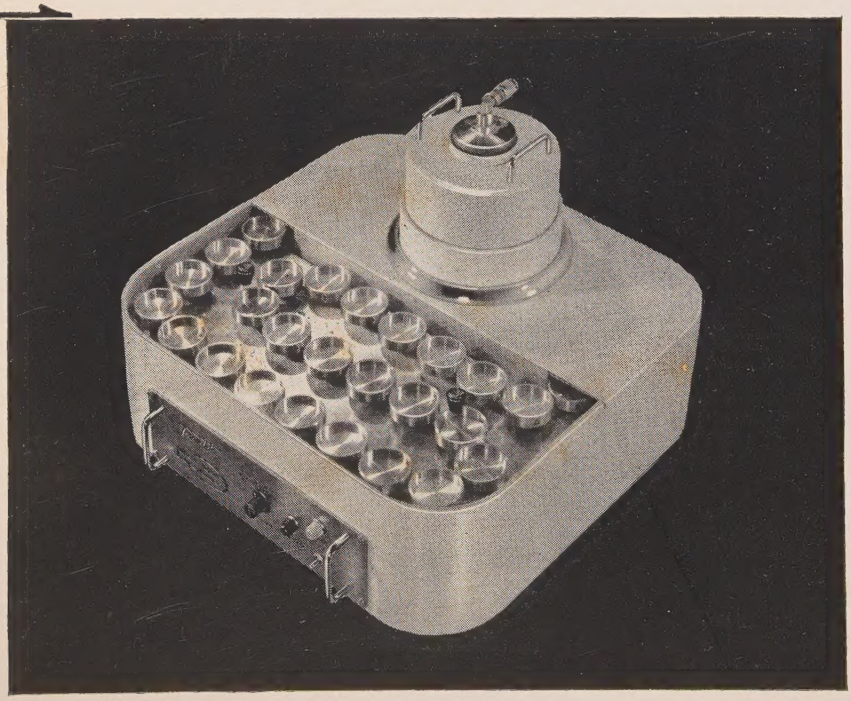

The new SC-100 Multi/Matic Sample Changer is one of Tracerlab's latest contributions to the field of nuclear instrumentation. It changes UP TO 50 one or two inch samples and can be used with standard Tracerlab Flow Counters, Geiger Tubes, Scintillation Detectors, as well as Tracerlab's new series of superthin window (less than 125 micrograms per CM^2) flow counters. ■ The new SC-100 Multi/Matic Sample Counter will replace a multitude of existing counting systems and soon will become an important part of a new automatic low background beta counting system which will provide guaranteed backgrounds of less than 0.5 counts per minute. ■ Ask the Tracerlab distributor in your country for more information or write to one of the addresses listed.

TRACERLAB, INC., 1601 Trapelo Rd., Waltham 54, Mass., U.S.A. ...or **TRACERLAB, S.A.**, Luchthaven Antwerpen, Antwerp, Belgium

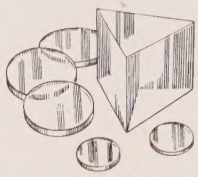

The Harshaw Chemical Company

is pleased to announce that

Effective July 1, 1961

the facilities of its affiliate company

HARSHAW-VAN DER HOORN N.V.
JUTFASEWEG 186
UTRECHT, NETHERLANDS

have been expanded to include a sales and technical service center for Harshaw scintillation and optical crystals. It is expected that actual production work will commence within the near future.

This new facility will offer "Harshaw Quality" crystals and provide the additional advantage of faster delivery, prompt personalized technical service, and freight economies.

Your inquiries are invited.

THE HARSHAW CHEMICAL CO.
CRYSTAL DIVISION
1945 EAST 97th ST. • CLEVELAND 6, OHIO

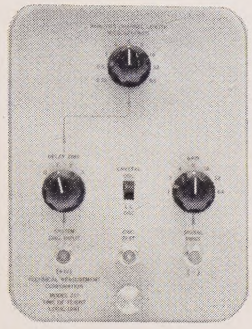

MODEL 211 TIME-OF-FLIGHT UNIT— Channel lengths from 0.25 to 64 μsec.

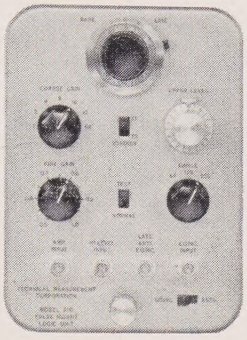

MODEL 210 PULSE HEIGHT UNIT—10+0.25 N μsec. dead time, built-in linear amplifier

NOW—

7 PLUG-IN LOGIC CIRCUITS

...for the TMC 256-channel Pulse Analyzer

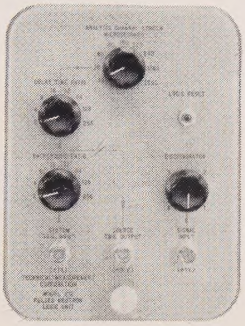

MODEL 212 PULSED NEUTRON UNIT—Used for exponential and critical experiments

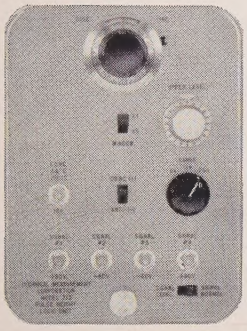

MODEL 213 PULSE HEIGHT UNIT—4 simultaneous inputs, 4 methods of storage, 10+0.25N μsec. dead time

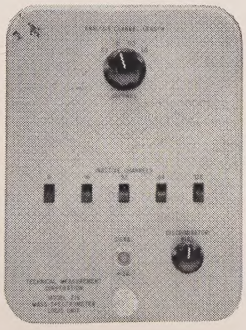

MODEL 215 MASS SPECTROMETER UNIT — Accepts ion counts in each channel for a preset time

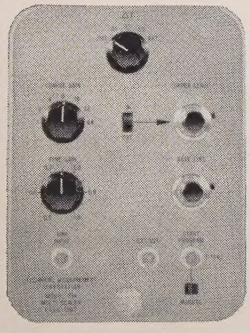

MODEL 214 MULTISCALER UNIT—Allows consecutive channel scaling for preset times

MODEL 216 COINCIDENCE PAIR UNIT—2-dimensional (16 x 16 channels) nuclear analyses

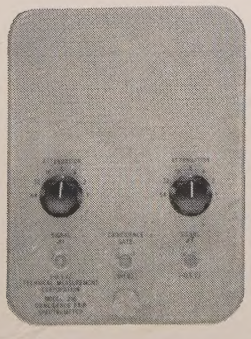

The 7 standard plug-in logic circuits now available make this 256-channel pulse analyzer the most useful system you can own.

By loosening one thumbscrew, you can remove one logic circuit — replace it with another — and have a completely different system in operation in a few seconds. The 7 units shown are standard but, TMC can build custom units to your exact requirements.

The basic transistorized 256-channel computer provides all memory circuits and data output selection circuits. Add the plug-in of your choice — have the exact system for your application.

Data handling is accomplished through an accessory, the Model 220 data handling unit. Strip chart and X-Y recorders, paper tape printers and punches may be used for readout.

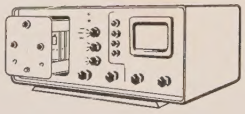

Complete literature on request.

TMC

TECHNICAL MEASUREMENT CORPORATION

441 WASHINGTON AVE., NORTH HAVEN, CONN., U.S.A.

AEI INSTRUMENTATION INFORMATION SERVICE

Transistorized....
4-5 litre ionization chamber
AEI GAMMA MONITORS

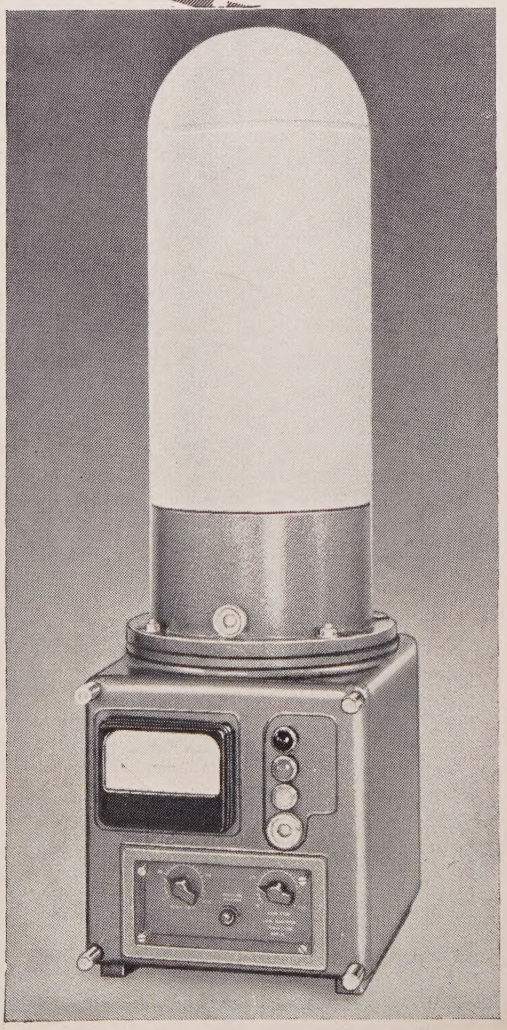

Designed for area radiation monitoring, the type GM2 logarithmic gamma monitor has a 5-decode scale with a maximum sensitivity of 100μ R/hr. The large and sensitive ionization chamber is filled with argon/air to ensure optimum flatness of gamma energy response. Circuitry is transistorized apart from the electrometer input stage which is used as a cathode follower feeding directly into a negative feedback amplifier to obtain maximum stability. An instrument failure alarm is incorporated and over-rides the trips to prevent spurious radiation alarms. Also available as a linear monitor type GM1.

Full details of types GM1 and GM2 monitors are given in Publication 2454-1 available from
AEI Instrumentation Division,
Process Control Department,
P.O. Box One, Harlow, Essex.

◀ GM2 logarithmic gamma monitor with ion chamber mounted on the splash proof case ; it can also be mounted remotely.

AEI | **Instrumentation Division**
Associated Electrical Industries Limited

sc/136

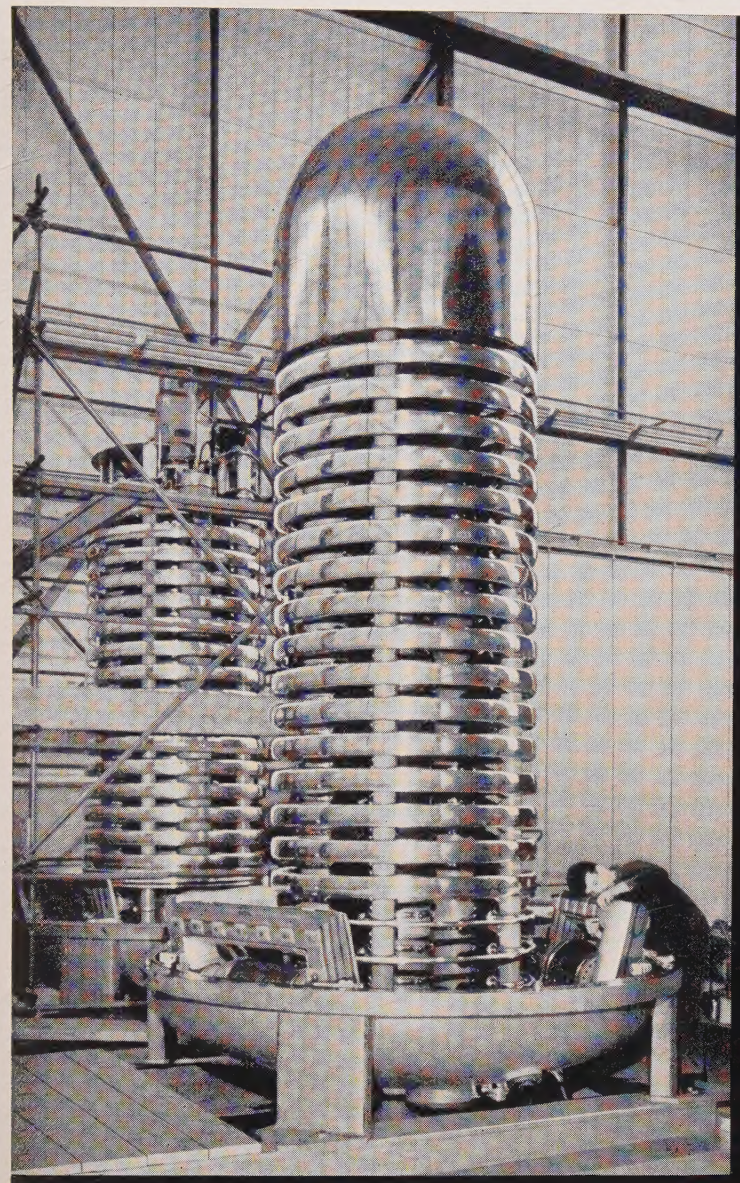

Assembly and testing of 4 MV Particle Accelerators

HAEFELY

Particle Accelerators
up to 4 MV
with high beam intensity

for basic nuclear research

for industrial radiation processing

Continuous irradiation of plastics

Sterilisation of drugs and preservation of foods

X-ray equipment for non-destructive product inspection

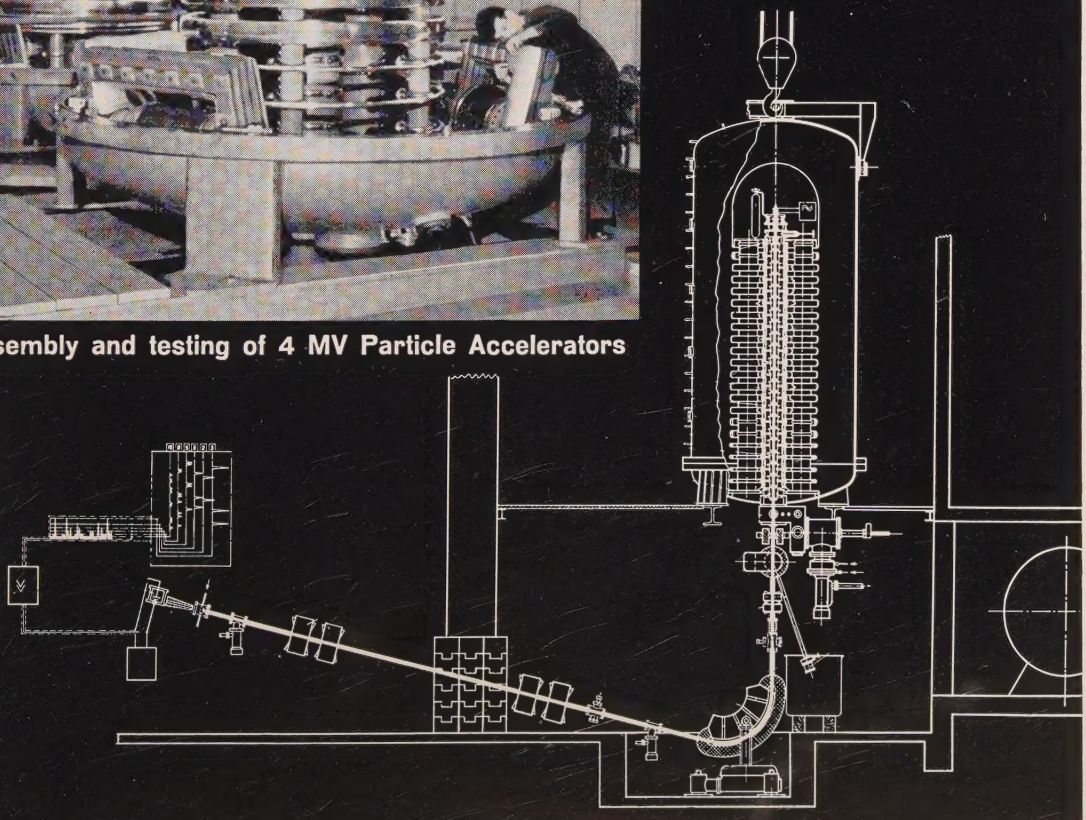

90 A

EMILE HAEFELY & CO LTD BASEL-SWITZERLAND

THE MOST VERSATILE ANALYZER

RIDL Model 34-8 200-Channel Analyzer
Model 34-12 400-Channel Analyzer

These two analyzers have earned their reputation as the most versatile analyzers in the field. As you read this the 150th RIDL *transistorized* Pulse Height Analyzer is being purchased. The 34-8 and 34-12 have been in production a long time. These are the best tested, most complete, most versatile transistorized analyzers of them all. For simple illustration of this consider the **choice of read-in and read-out** described below:

CHOICE OF READOUTS: Parallel or serial entry read-out devices, magnetic tape, punched paper tape, electric typewriter, point plotter, printers and strip-chart recorders . . . may all be linked with any of the RIDL line of transistorized pulse height analyzers.

CHOICE OF INPUTS: RIDL transistorized analyzers may be used with either transistorized or vacuum tube amplifiers such as the A61, A8, DD2, A1D, etc. Two input systems may be fed into an RIDL analyzer and used alternately at the flip of a switch. In addition, RIDL transistorized analyzers have new capability when used with the all solid state **Model 30-17 Four Channel Mixer Amplifier:**

Four Detector Input is easy, using the Model 30-17 Four Channel Mixer Amplifier for simultaneous operation with RIDL transistorized analyzers. The Model 30-17 provides the logic and electronics to operate 4 detectors simultaneously. Each detector stores into a separate quadrant of the analyzer memory.

Coincidence Sum Pulse Input is also easy, using the Model 30-17 alternate connectors. This is accomplished by storing the pulses from each separate detector into a quadrant of the analyzer memory. The sum of the coincidence pulses are stored in a third quadrant.

Many current designs for mutliple detector operation with a PHA make no provision for examination of coincidence between detectors. Also, amplitude information is distorted when pulses arrive simultaneously or when subsequent pulses change routing information during digitizing time in the analog-to-digital converter. With the RIDL Model 30-17 these can't happen. Cross talk is eliminated. **All** conditions for proper operation without cross talk are provided by this system.

RIDL Model 30-17
Four Channel Mixer Amplifier with Coincidence and Logic Circuits.

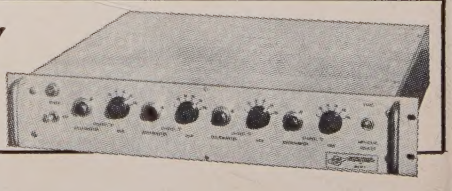

RIDL INC.

Radiation Instrument Development Laboratory, Inc.

61 EAST NORTH AVENUE • NORTHLAKE, ILLINOIS
PHONE: MUrray 1-2323 • Cable Address: RADILAB

SCANNED 24 of 66

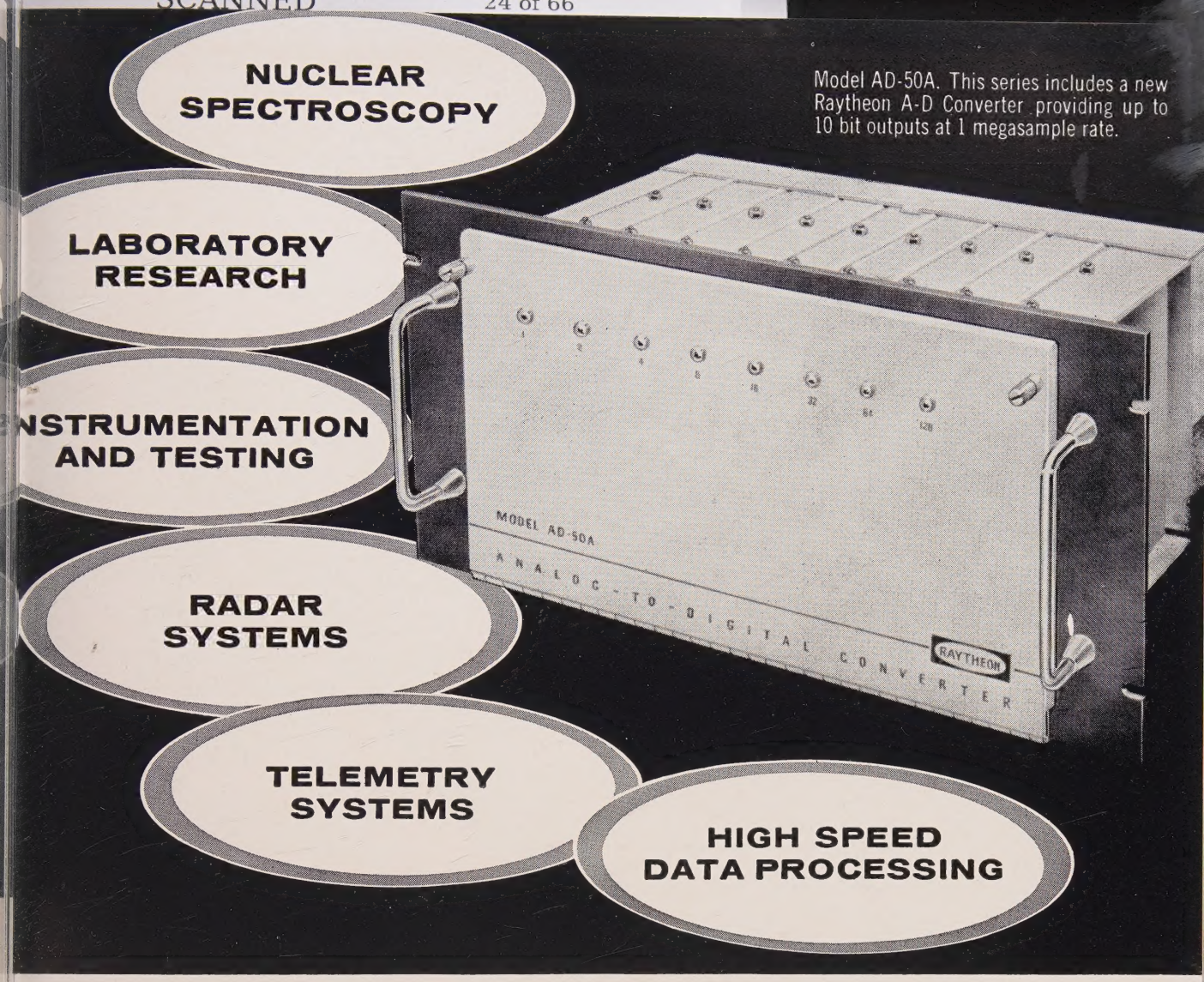
NUCLEAR SPECTROSCOPY
LABORATORY RESEARCH
NSTRUMENTATION AND TESTING
RADAR SYSTEMS
TELEMETRY SYSTEMS
HIGH SPEED DATA PROCESSING
Model AD-50A. This series includes a new Raytheon A-D Converter providing up to 10 bit outputs at 1 megasample rate.
MODEL AD-50A
ANALOG-TO-DIGITAL CONVERTER
RAYTHEON

RAYTHEON'S NEW A-D CONVERTER: UP TO 5.0 x 10^6 INDEPENDENT 8 BIT WORDS PER SECOND!

ster than any other available, Raytheon Analog-Digital nverter's 25-nanosecond aperture time allows digitizing pulses less than ½-microsecond in width. With multi-xed input, its applications encompass any product or ocess requiring digitized analog voltages in continuous intermittent form.

bout the size of an office typewriter, Model AD-50A is adily integrated with established systems: its flexible de-gn allows acceptance of variable input as well as wide riations in output format and logic. Its almost unlimited stems applications offer industry, government and the military a basic, solid state tool that revolutionizes t present state of the art.

All of its outputs are usable, every readout is valid, and can be operating in your system in less than 90 days.

RAYTHEON

RAYTHEON COMPANY

MAIL COUPON TODAY FOR BROCHURE

Raytheon Company, Dept. 31, Lexington 73, Massachusetts NI
Attention: M. B. Curran

Please mail me Specifications on:

☐ Model AD-50A 8 Bit Converter
☐ New 10 Bit, 1 megasample Converter

I'm interested in possible applications to the following type system(s):

_____

_____

_____

_____

Name & Title _____

Company _____

Address _____

City & State _____

SCINTILLATION

Scintillation Phosphors, Liquids & Crystals (Bulletins 9, 11, 12, 13, 23 and 25) The NaI(Tl) crystals, (illustrated above) form part of the extensive range of mounted crystals offered by Nuclear Enterprises. CsI(Tl) and LiI(Eu) crystals are also available in mounted form. All three are featured in the crystal-photomultiplier assemblies which afford improved resolution and offer special facilities for counting low level activities. Full details of NE 102 plastic phosphor scintillators, liquid scintillators, loaded liquid scintillators, neutron detectors, scintillation chemicals, crystals and crystal-photomultiplier assemblies will gladly be sent on request.

Complete Assemblies: Scanning Scintillation Spectrometer of high performance. Also Liquid Scintillation Spectrometer providing greatly simplified technique for measurement of C14, H3 and Fe55 (with efficiences of 90%, 30% and 20% respectively).

Probe Units: Compact probe units for study of gamma rays, low energy X-rays, slow neutrons, fast neutrons and alpha particles. Also special transistorised head units for pulse shape discrimination investigations.

Special Transistorised Units for Field Investigations: Four channel Scintillometer for geological and geophysical surveys; Moisture & Density Gauge; Beryllometer. etc.

Shielded Scintillation Head Units: To accommodate photomultipliers, phosphors, and samples. Special units for C14, & H3 analyses.

Precision Laboratory Instruments: Non-overloading linear amplifiers, pulse height selectors, EHT units, ratemeters, etc. Also a new range of transistorised instruments of unitised construction.

Low Level Counting Facilities: Wide range of human body radiation monitors. Also installations for measuring lean:fat ratios in carcases and live animals.

New:

NE 5550 and 5560 series probe units employing pulse shape discrimination techniques for detecting neutrons in a high gamma background.

For full details write for Technical Bulletins (Nos. 14, 15, 16, 18, 21, 22, 24) and Catalogue to the Sales Division.

Nuclear Enterprises (G.B.) Ltd

Sighthill, Edinburgh 11, Scotland. Tel: Craiglockhart 5262

Associate Company: Nuclear Enterprises Ltd., 550 Berry St., Winnipeg, 21, Canada.

(ndh) 7788

NUCLEONIC INSTRUMENTS

Nuclear Enterprises (G.B.) Ltd. offers a complete range of precision nucleonic instruments and a special design and development service to meet individual customer requirements.

COUNTING

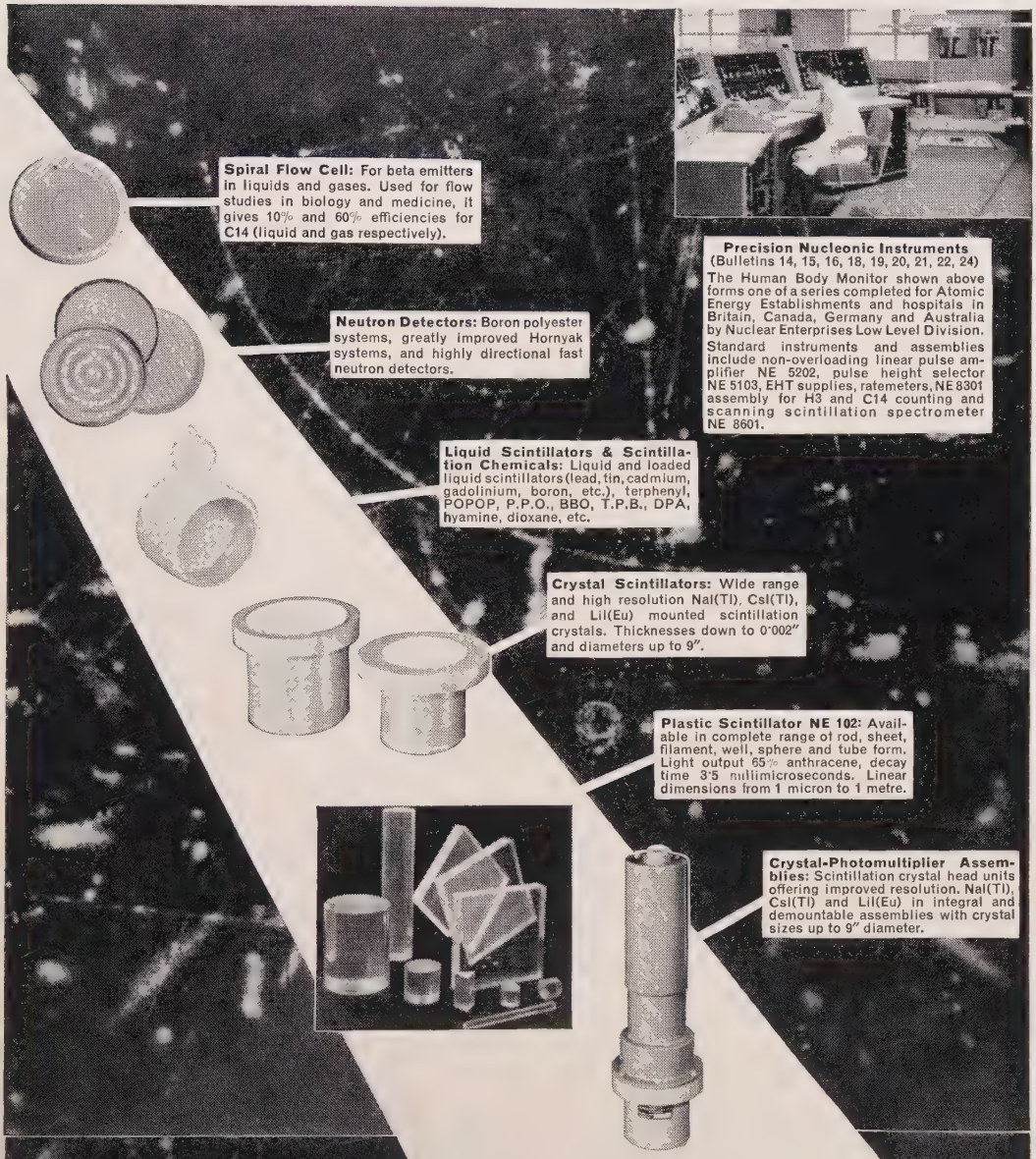

Spiral Flow Cell: For beta emitters in liquids and gases. Used for flow studies in biology and medicine, it gives 10% and 60% efficiencies for C14 (liquid and gas respectively).

Neutron Detectors: Boron polyester systems, greatly improved Hornyak systems, and highly directional fast neutron detectors.

Liquid Scintillators & Scintillation Chemicals: Liquid and loaded liquid scintillators (lead, tin, cadmium, gadolinium, boron, etc.), terphenyl, POPOP, P.P.O., BBO, T.P.B., DPA, hyamine, dioxane, etc.

Crystal Scintillators: Wide range and high resolution NaI(Tl), CsI(Tl), and LiI(Eu) mounted scintillation crystals. Thicknesses down to 0·002" and diameters up to 9".

Plastic Scintillator NE 102: Available in complete range of rod, sheet, filament, well, sphere and tube form. Light output 65% anthracene, decay time 3·5 millimicroseconds. Linear dimensions from 1 micron to 1 metre.

Crystal-Photomultiplier Assemblies: Scintillation crystal head units offering improved resolution. NaI(Tl), CsI(Tl) and LiI(Eu) in integral and demountable assemblies with crystal sizes up to 9" diameter.

Precision Nucleonic Instruments
(Bulletins 14, 15, 16, 18, 19, 20, 21, 22, 24)

The Human Body Monitor shown above forms one of a series completed for Atomic Energy Establishments and hospitals in Britain, Canada, Germany and Australia by Nuclear Enterprises Low Level Division.

Standard instruments and assemblies include non-overloading linear pulse amplifier NE 5202, pulse height selector NE 5103, EHT supplies, ratemeters, NE 8301 assembly for H3 and C14 counting and scanning scintillation spectrometer NE 8601.

SCINTILLATORS

The unique scintillation service afforded by Nuclear Enterprises (G.B.) Ltd. includes the highly efficient NE 102 plastic scintillator, liquid scintillators, neutron detectors, scintillation chemicals and an extensive range of crystals & crystal-photomultiplier assemblies.

New:

NE 150 plastic phosphor for pulse shape discrimination techniques and NE 160 a special high temperature plastic scintillator.

For full details write for Technical Bulletins (Nos. 9, 11, 12, 13, 23, and 25) and Catalogue to the Sales Division.

Nuclear Enterprises (G.B.) Ltd

Sighthill, Edinburgh 11, Scotland. Tel: Craiglockhart 5262

Associate Company: Nuclear Enterprises Ltd., 550 Berry St., Winnipeg, 21, Canada.

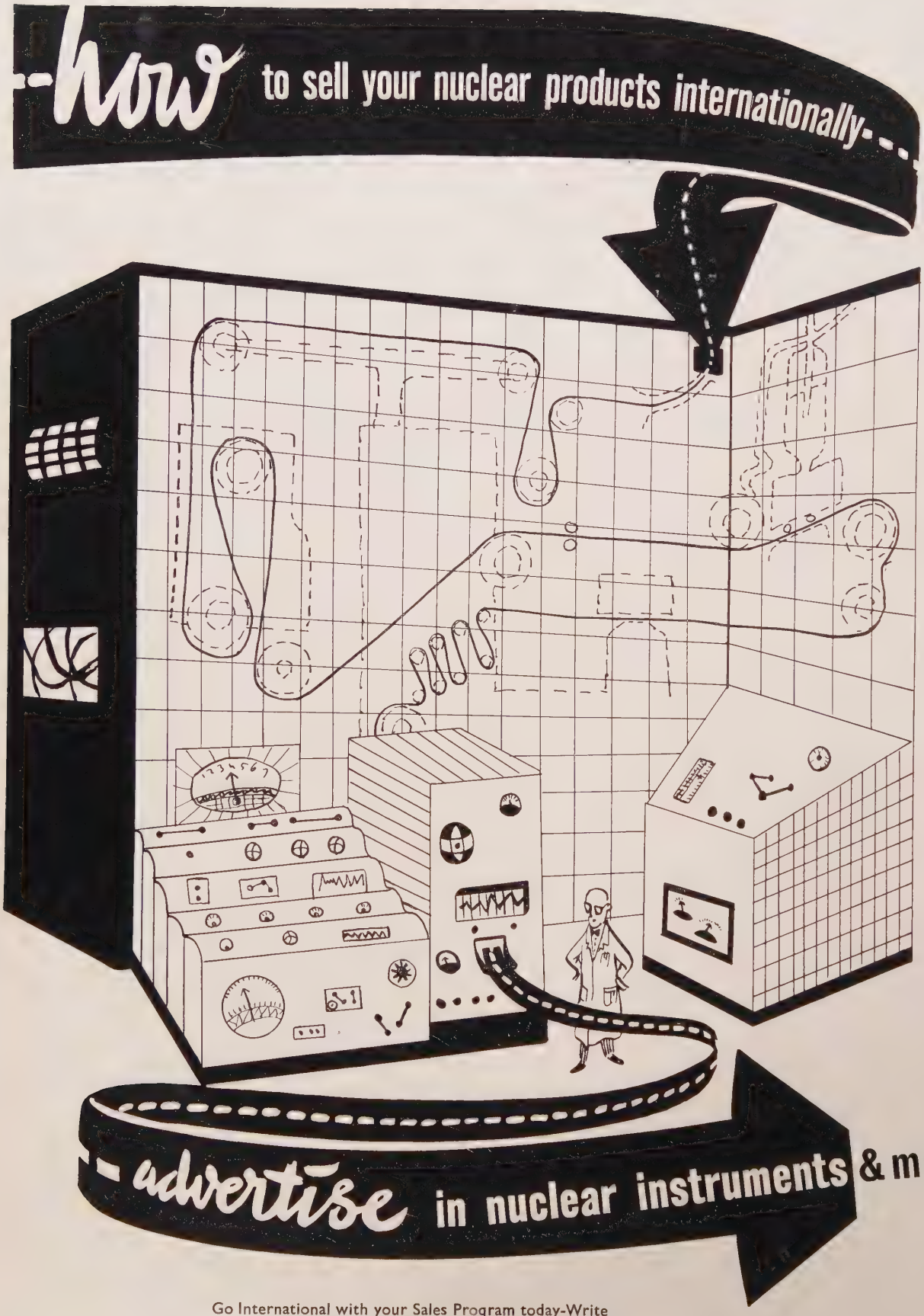

Go International with your Sales Program today-Write

William F. Baars-Advertising Manager, North-Holland Publishing Company

P.O. Box 103, Amsterdam, The Netherlands

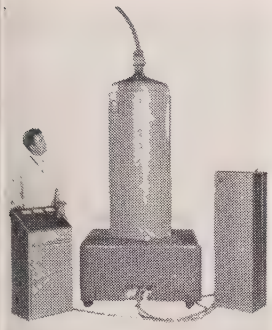

600 kV Generator

Research Centres and Industry alike find the modern, polished solution to the problem of continued high voltage in the

SAMES ELECTROSTATIC GENERATOR

Electrostatic Painting with the STATRON

HIGH VOLTAGE GENERATORS

* 50 kV to 600 kV
* 20W to 3 kW
* Positive or negative polarity
* Medium or high stability for
* Electrostatic precipitation
* Electrical testing
* Electronic optics
* X-rays
* Nuclear Physics, etc.

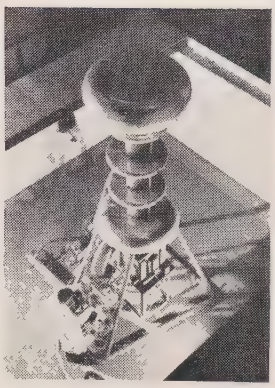

Vertical 600 kV
Accelerator at the Centre d'Etudes Nucléaires de Grenoble

ELECTROSTATIC PAINTING

The STATRON is a portable equipment for electrostatic painting, featuring

* 90 kV voltage
* Complete safety, owing to use of electrostatic generator.
* Paint output: 15 litres/hour
* Supply: 110 or 220 V, single phase.
* Consumption: 110 Watts

PARTICLE ACCELERATORS

Type	Acceleration Voltage	Particles Accelerated	Application
J	150 kV	ions	Neutron Generator by D/T or D/D reaction
L	300 kV	ions	
S	600 kV	ions or electrons	All applications

SAMES

SOCIETE ANONYME DE MACHINES ELECTROSTATIQUES

21, RUE JEAN MACÉ, P.O. BOX 150, TEL: 44.77.64 GRENOBLE, FRANCE

REPRESENTATIVES

GENERATORS AND ACCELERATORS

Austria: AUSTRONIK, Salzburg – Belgium: CENTRONICS, Brussels – Chinese People's Republic: Cie OLIVIER, Paris – Denmark: DANSK SCIENTA, Copenhagen – Great Britain: MILES HIVOLT LTD., Shoreham by Sea – Italy: SECI, Milan – Netherlands: PROJECTO, Amsterdam – Norway: LEHMKUHL, Oslo – Portugal: A.G.M.E., Lisbon – Spain: CRESA, Barcelona – Sweden: SCIENTA SCANDIA, Gothenburg – Switzerland: OMNIRAY, Zurich – Western Germany: DR. NAMUR, Darmstadt – Bulgaria, Czechoslovakia, Eastern Germany, Hungary, Poland, Rumania, U.S.S.R.: CIFAL, Paris.

ELECTROSTATIC PAINTING EQUIPMENT

Algeria: FAMPA, Algiers – Austria: PETER PETERSEN, Vienna – Belgium: DURMECO, Brussels – Chinese People's Republic: Cie OLIVIER, Paris – Denmark: DANSK SCIENTA, Copenhagen – Eire: HODGES & SONS, Dublin – Great Britain: AEROSTYLE LTD., London – Italy: TRASMETAL, Milan – Netherlands: STUURMAN, Wormerveer – Norway: LEHMKUHL, Oslo – Portugal, RAMADA, Ovar – Spain: INSTITUTO ELECTROQUIMICO, Barcelona – Sweden: SCIENTA SCANDIA, Gothenburg – Switzerland: REGSA, Lausanne – Western Germany: A. WIRTH, Reutlingen – Bulgaria, Czechoslovakia, Eastern Germany, Hungary, Poland, Rumania, U.S.S.R.: CIFAL, Paris.

High Voltage Engineering Corporation...

"Charged Particles"

Nuclear-Structure Research

Initial work with the 12-Mev Tandem Van de Graaff has confirmed beyond expectations our early conviction that this accelerator system would greatly extend areas of useful research. A previously "dark" area, in fact the whole upper half of the periodic table, can now be investigated with precision. The range now beginning to be explored with extremely stable monoenergetic particle beams includes many isotope-rich elements and the important domain of fissionable materials. Current research indicates *the Tandem has increased the number of resolvable energy levels by an order of magnitude.* In constructing a theory of the nucleus, the precision we speak of is every bit as important as the extension in energy. Tandem ion beams permit discrimination between closely associated energy levels and reveal new subtleties in the fine structure of heavier elements.

The Tandem Van de Graaff's external ion source at ground potential is a boon to experimenters. There are seventeen stable nuclei up to oxygen, and all of these may be used as bombarding particles. With multiple stripping and two-stage acceleration, oxygen ions have been accelerated to 60 Mev.

A characteristic of truly new research tools is evident in the way the Tandem is shaping the direction and objectives of physics research programs. As a result, four laboratories with machines installed and performing to specifications, and others awaiting Tandem delivery, are planning to undertake work that is new and challenging.

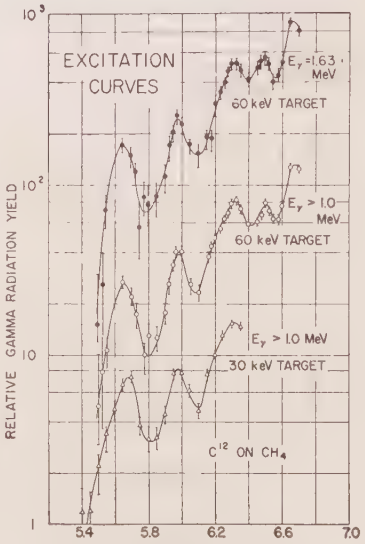

Data from current experimentation with the Tandem Accelerator at Chalk River Laboratories, Atomic Energy of Canada Limited.

At High Voltage, careful thought is already being given to feasible extension of the basic Tandem principle. A three-stage injector Tandem with guaranteed 17.5-Mev proton energy is on order for the University of Texas, and Tandem systems with 22-Mev proton energy are feasible today. This "second generation" of Tandems will employ higher terminal potentials, three stages of acceleration and developments to increase beam current. We are also investigating pulsing techniques for Tandems, and the possibility of polarized ion sources is being studied.

A paper at our recent Accelerator Conference, "Current Experimentation with the Tandem Accelerator at the Chalk River Laboratories[1]," describes an outstanding experimental physics program. Write us for a copy.

"Low-Energy" Physics

As we address ourselves to this subject, more elegantly called *nuclear-structure physics,* the reader may conclude we have an axe to grind, and we admit it. We believe a great deal of research remains to be done on light nuclei. There is, for example, time-consuming but rewarding precision nuclear spectroscopy to fill in gaps in existing energy level data, as well as new research related to the conservation of isotopic spin, excitation energies of low excited states and direct interaction mechanisms.

Because much nuclear-structure research can be accomplished with standard Van de Graaffs in the 1-5 Mev energy range, equipped with ion sources for hydrogen, helium or heavy elements, these machines represent ideal research instruments for the university physics laboratory of modest proportions. We are presently compiling information on exactly where machines of moderate cost and energy can make significant contributions in illuminating concepts of nuclear structure and would be happy to discuss this subject with you.

[1]*H. E. Gove, Proceedings of the Second Accelerator Conference, Amsterdam, Oct., 1960 (North Holland Publishing Company, 1961) p. 63.*

High Voltage Engineering Corporation
Burlington, Massachusetts, U.S.A.
•
Applied Radiation Corporation
•
High Voltage Engineering (Europa) N.V

NUCLEAR INSTRUMENTS AND METHODS 12 (1961) 205–226; NORTH-HOLLAND PUBLISHING CO.

THE SEMICONDUCTOR SURFACE BARRIER FOR NUCLEAR PARTICLE DETECTION

G. DEARNALEY and A. B. WHITEHEAD

A.E.R.E., Harwell, England

Received 24 February 1961

A simple and reliable technique for the preparation of surface barrier detectors in silicon and germanium is described. The performance and electronic requirements of these directors are discussed and compared with those of diffused junction counters.

Many properties of semiconductor detectors are of great value in nuclear physics and an outline is given of their advantages and limitations. Some special configurations for fission studies, dE/dx counters and neutron detection are described.

CONTENTS

1. Introduction 206
2. Construction Techniques 207
3. Pulse Amplification 209
4. Characteristics of Gold-Silicon Detectors 210
   4.1. Reverse current 210
   4.2. Capacitance 212
   4.3. Barrier depth 212
   4.4. Energy resolution 213
   4.5. Pulse rise-time 215
   4.6. Window thickness 216
   4.7. Sensitivity to gamma-rays 216
   4.8. Sensitivity to neutrons 216
   4.9. Radiation damage 217
   4.10. Useful life of detectors 218
   4.11. Photosensitivity 219
   4.12. Effect of a magnetic field 219
5. Characteristics of Gold-Germanium Detectors 219
   5.1. Reverse current 219
   5.2. Barrier depth 219
   5.3. Energy resolution 219
   5.4. Pulse rise-time 220
   5.5. Sensitivity to neutrons 220
6. Comparison of Surface Barrier and Diffused Junction Counters 220
7. Applications to Nuclear Physics 221
8. Special Configurations 223
   8.1. Fission detector 223
   8.2. Fast neutron detectors 223
   8.3. Thin dE/dx detectors 225
   8.4. Multiple detector 225

1. Introduction

There has arisen recently a widespread interest in the detection of nuclear particles by means of semiconductor devices. Such detectors have shown very good energy resolution and linearity, coupled with a fast rise time, compact size, and a relatively low sensitivity to background gamma-rays and neutrons. Other advantages are their low cost, simple power supply requirements, and adaptability to special applications. In fact, experience gained so far suggests that semiconductors in one form or another may ultimately replace most other types of particle detector.

Basically the principle of operation is similar to the gaseous ion chamber. An electric field is established across a medium of low conductivity. When a charged nuclear particle penetrates the medium, collisions occur, producing ion pairs in the case of the gaseous chamber or electron-hole pairs in the solid lattice. Ideally the charges are separated by the field and collected at the boundaries, producing an electrical pulse which can be amplified and recorded. Recombination of the charges before collection must be avoided, so the medium must have a high carrier mobility, must be free of defects, and capable of withstanding a high collecting field without breakdown. The earlier crystal counters of materials such as diamond, ZnS, and CdS, were not satisfactory in this respect. On the other hand germanium and silicon can be made to satisfy these requirements, and several other materials such as gallium arsenide show promise of being suitable in the near future.

The simplest arrangement would be to have a block of semiconductor between parallel electrodes so that a uniform electric field could be set up throughout the whole volume. This has been termed a bulk conductivity counter and charge produced anywhere throughout the volume of the block is collected. In practice the conductivity of the most suitable materials is too great, due to impurity and thermally generated carriers, but by using extremely pure material at a very low temperature the conductivity has been reduced[1,2]) sufficiently to allow an adequate collecting field to be established. Alternatively the impurity conductivity in some cases has been reduced by counter-doping, as in gold-doped silicon[3]) and oxygen-doped gallium arsenide[4]), but at the expense of shortened carrier lifetime and corresponding loss of collection efficiency.

So far the bulk conductivity counter has not been as practicable as those employing the depletion layer effect which occurs in a semiconductor diode. This exists between an n-type or donor-rich region and a p-type or acceptor-rich region of a semiconductor. A shallow volume of the interface is depleted of carriers, leaving the impurity atoms ionized, positive in the n-region and negative in the p-region. The strong dipole field which results will rapidly collect any electron-hole pairs created in the interface by a charged nuclear particle. A voltage applied in the reverse-biased direction will extend the depletion layer thus increasing the volume which is effective for particle detection. In materials having a small gap between valence and conduction bands, cooling reduces the number of thermally generated carriers.

If the whole of the sensitive volume is to be accessible to nuclear particles, the n-p interface must be formed close to the surface of the crystal. One way in which this may be accomplished is by the shallow diffusion of a doping impurity of one type into a crystal having a weak impurity concentration of the other type. Diffused junctions have been employed as detectors by a number of laboratories[5–8]) with results which are a considerable improvement over more conventional methods. A second approach is to employ the surface barrier which forms spontaneously on clean silicon and germanium. The surface readily oxidizes and surface states are formed which behave predomi-

[1]) P. E. Gibbons and D. C. Northrop, Nature **188** (1960) 803.

[2]) F. J. Walter, J. W. T. Dabbs and L. D. Roberts, Rev. Scient. Instr. **31** (1960) 756.

[3]) J. D. Van Putten and J. C. Van der Velde, I.R.E. Trans. NS-8 (1960) 124.

[4]) Harding, Hilsum, Moncaster, Northrop and Simpson, Nature **187** (1960) 405.

[5]) G. L. Miller, W. L. Brown, P. F. Donovan and I. M. Mackintosh, B.N.L. Report 4662 (1960).

[6]) S. S. Friedland, J. W. Mayer, J. M. Denney and F. Keywell Rev. Scient. Instr. **31** (1960)74.

[7]) J. M. McKenzie and J. B. S. Waugh, I.R.E. Trans. TS-7 (1960) 195.

[8]) G. Amsel, P. Baruch and O. Smulkowski, Nucl. Instr. and Meth. **8** (1960) 92.

nantly as electron acceptors. Electrical connection to the surface layer is made by evaporating a thin layer of metal, usually gold, over a certain area. A reverse bias applied to this electrode extends the depletion layer, or barrier, into the semiconductor to a depth of as much as a millimetre.

Several methods of preparing surface barrier detectors have been reported[9,10,11]) but we feel that there is still need for a detailed account of a reliable technique which can be readily adapted to the requirements of most experiments. At Harwell, we have concentrated attention on the surface barrier detector[12]), because it has a simpler construction and potentially better performance than a junction prepared by diffusion. A comparison of the two types of detector will be attempted in section 6.

2. Construction Techniques

The technique is quite straightforward but requires a vacuum evaporation system and a fume cupboard. Extreme cleanliness is essential at all stages because impurities present in high resistivity silicon and germanium represent only a few parts in 10^{10}. The crystals should not be touched with bare hands, for instance.

Zone-refined crystals of silicon have been obtained from several firms, cut to the required size and lapped to a fine matt finish with aluminium oxide of about 7 microns grain size. Our procedure is then as follows.

(1) While not essential, it is good practice to clean the crystals prior to etching by boiling for a few minutes in concentrated nitric acid.

(2) The crystal is then put in a polyethylene beaker, and about 20 cc of CP-4A is added, the mixture being kept ice-cold. Etch-pit formation has been observed if the temperature is allowed to rise. CP-4A is a standard solution used in semiconductor processing, and consists of:

concentrated nitric acid	2 volumes
glacial acetic acid	1 volume
40% hydrofluoric acid	1 volume.

Chemicals should be of analytical reagent purity, mixed in clean polyethylene apparatus, and allowed to stand for 30 minutes before use. Fresh etch must be made up for each day's requirements. This step must be carried out with due care in a fume cupboard as HF produces serious burns on the skin and is highly toxic if inhaled. Five to ten minutes in the etch bath should be sufficient to produce a mirror-like finish on the silicon surface. In some cases uneven etching has been observed and is attributed to the presence of strain dislocations. Such crystals

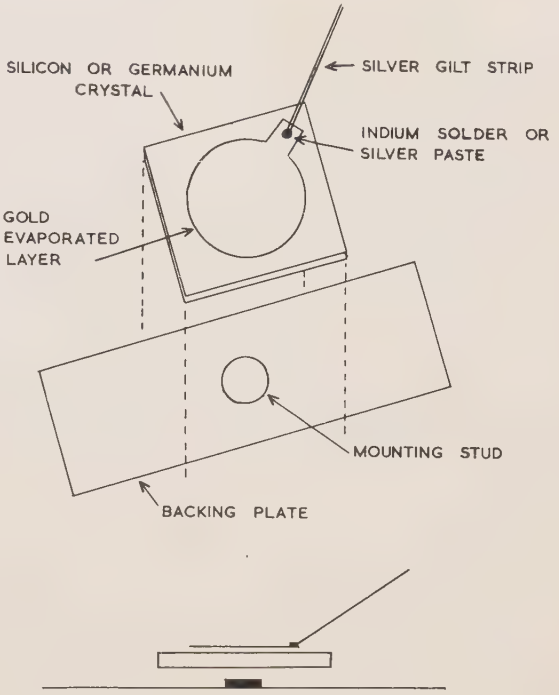

Fig. 1. Construction of surface barrier detector.

do not make good detectors. Bubbles which occur on the surface during etching should be removed by occasional agitation, and we have recently found supersonic agitation very effective at this stage for removing bubbles.

(3) Demineralised water is run into the etch and the crystal is washed by alternate dilution and decanting, avoiding exposure of the silicon during the early stages of the procedure. A dark stain results if this precaution is not taken. The crystal is transferred to a clean polyethylene beaker and

[9]) J. L. Blankenship and C. J. Borkowski, I.R.E. Trans. NS-7 (1960) 190.

[10]) J. L. Blankenship and C. J. Borkowski, I.R.E. Trans. NS-8 (1961) 17.

[11]) F. J. Walter, J. W. T. Dabbs, L. D. Roberts and H. W. Wright, O.R.N.L. report CF-58-11-99 (1958).

[12]) G. Dearnaley and A. B. Whitehead, A.E.R.E. report R-3278; and R-3437 (1960).

washed several more times with demineralised water. This beaker must be used for no other purpose. A water conductivity cell can be employed at this stage to verify that the washing is complete. The crystal is then dried on pure tissue, and allowed to stand for 3–6 hours to undergo the initial oxidation process. The work of Green and Maxwell[13]) shows that the oxidation is initially rapid, followed by a slow adsorption.

(4) A mica mask is prepared for the evaporation. A convenient shape is the keyhole as shown in fig. 1 which provides a small gold area for the front contact leaving a circular area free. The purpose of the mask during evaporation is to define the area of the counter and avoid deposition of gold on or near the crystal edges. The mask is then cleaved to ensure that the faces which are in contact with the crystal are perfectly clean, and the crystal is lightly clipped between them.

(5) The masked crystal is then mounted in the vacuum evaporator so as to deposit gold on the face which has the best finish. The gold is evaporated at a pressure of less than 10^{-4} mm of Hg. For most purposes a film of about 75% light transmission, corresponding to 20–40 micrograms per square centimetre, is satisfactory. If the gold layer is to be of minimum thickness, for example for a fission detector, it is convenient to mount a small quartz strip with electrodes beside the crystal. The surface resistivity of the film deposited on the quartz can then be monitored. We are indebted to Mr. M. Nobes (A.E.R.E.) for suggesting and constructing this arrangement.

(6) The crystal is then removed and placed on pure tissue in a covered box. We have found, as has Blankenship[9]), that it is better to age the dectectors for a few days after deposition of the gold before making the connections. This is presumably to allow the full development of the surface oxide which appears to take place through the thin gold.

(7) A second gold evaporation is made, this time with the circular counting area shielded, forming a thicker deposit on the small tab to which electrical connection is to be made. This avoids the possibility of the organic binder in the silver paste penetrating and damaging the surface layer. It is known from studies by Buck[14]) that organic contaminants cause deterioration in shallow junctions on N-type silicon, while water vapour improves them, in respect of leakage current. Conversely, water vapour is deleterious to junctions on P-type silicon. We have sometimes found an increase of leakage current over a period of months, and restored the behaviour by scraping away the contact and making a new one elsewhere. The double evaporation of gold should avoid this trouble.

(8) The crystal is then cemented on to the required mount which may simply be a small plate of metal with fixing holes. Kovar is recommended as it has a coefficient of thermal expansion similar to that of silicon. Johnson, Matthey FSP 43 flake silver paste† has proved satisfactory. In order to give a long surface leakage path and avoid the possibility of cement on the edges of the crystal a dimple can be pressed into the plate or a small spacing disc inserted as shown in fig. 1. The silver paste contact is only slightly rectifying, presumably due to the effect of its organic constituents on the surface inversion layer, thus despite the symmetrical preparation of the etched crystal the finished unit is a diode. A more nearly ohmic contact can be obtained by nickel plating but the present method proves simpler and is satisfactory for most purposes.

(9) Front contact to the gold is made by a short length of silvergold alloy galvanometer suspension strip, cemented to the gold tab with a small drop of FSP 43. The paste should be sufficiently fluid to wet the gold but on no account should it be allowed to flow on to the uncoated silicon.

(10) The whole assembly is maintained at approximately 80°C for a few hours to set the conducting cement.

The device is then complete and ready for testing. The success rate of this method is very high and most of the differences in performance of detectors are believed to be due to characteristics of the semiconductor starting material. Thus a good detector

† This is a new resin-based two-component paste which gives a stronger bond than the FSP 36 used hitherto.

[13]) M. Green and K. H. Maxwell, J. Phys. and Chem. of. Solids **13** (1960) 145.

[14]) T. Buck, Proc. of N.A.S. Conference, Asheville (Sept. 1960) to be published.

can be reground and remade satisfactorily, while inferior detectors remain poor after reprocessing. Fig. 2 shows a photograph of a pair of detectors.

The procedure for gemanium is identical to that described above for silicon except that (i) the etch

Fig. 2. Two completed detectors. The unit on the left is slitshaped for use with a magnet spectrometer.

may be used at room temperature, and (ii) the method of making electrical connections is altered. Silver paste tends to fracture when cooled, so that it is better to make a solder connection, both to the base and to the gold layer, with indium (m.p. 155°C) as a solder.

3. Pulse Amplification

The energy loss per electron-hole pair in silicon is 3.6 eV so that the charge liberated by a nuclear particle is 4.4×10^{-14} coulomb per MeV lost in the barrier. A typical counter capacitance is of the order of 20 pF yielding voltage pulses of about 2 mV per MeV. Counters with large sensitive areas have much higher capacitance and correspondingly lower voltage signal. Both of these types require amplifiers with high gain and very low noise. On the other hand, small, high resistivity counters with very deep barriers can have a capacitance of as little as 1 pF and would give best performance with a very low input capacity amplifier.

The circuit resembles that for an ion chamber (fig. 3). For minimum noise the load resistor should be as high as possible without causing undue pile-up of pulses under operating conditions. With a high impedance amplifier the decay time of the pulse is governed by the counter and stray capacitance together with the load resistance. If the amplifier has a low input impedance, this will govern the pulse decay.

The amplifier used at Harwell for most applications has been the A.E.R.E. type 1430, which is a conventional 2 Mc/s voltage amplifier, with a 6AK5 first stage. The signal to noise ratio with such an instrument is usually adequate, but the pulse height stability is limited by variations in the effective

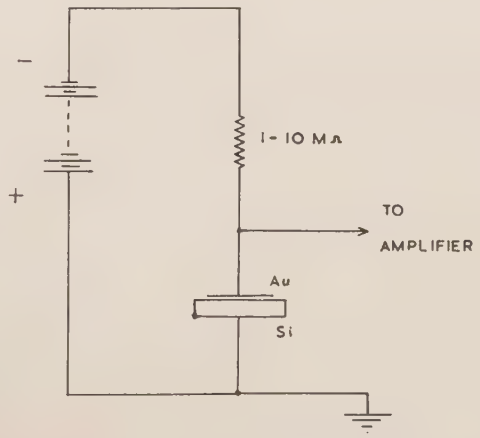

Fig. 3. Circuit diagram of counter.

capacitance of detector and input circuit. Any change in current through the detector alters the detector bias, and thus its capacitance, while

McKenzie[15]) has found that heater voltage variations alter the effective input capacitance of the amplifier, due to variations of space charge. To overcome this, charge sensitive amplifiers employing feedback through a small capacitance to the input grid have been designed by Gatti[16]), Blankenship[10]) and Chase[17]).

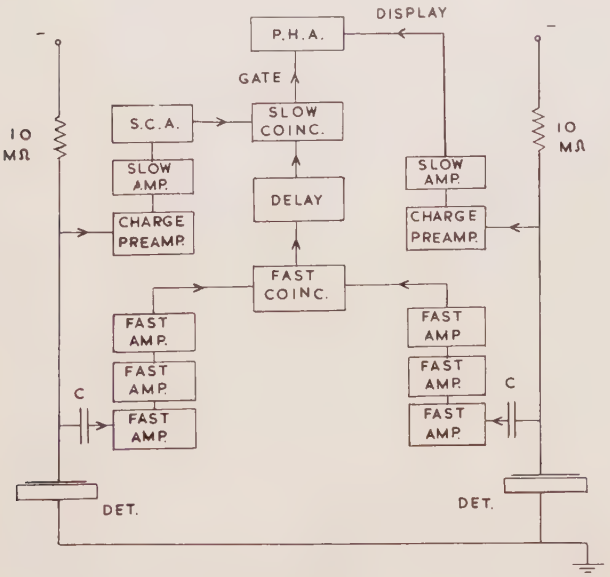

Fig. 4. Block diagram of coincidence counting system.
Amp. = amplifier
S.C.A. = single channel analyser
Det. = detector
Coinc. = coincidence unit
P.H.A. = pulse height analyser
C = coupling condenser, about 500 pF.

In order to utilise the fast rise-time of the detectors, an amplifier of higher bandwidth is required, but the signal to noise ratio, and the stability of gain are then inferior. Thus with the A.E.R.E. type 2002A 200 Mc/s amplifier the noise level is around 0.5 mV. In many cases it is possible to use a combination of fast and slow amplification, so that fast coincidence measurements can be made simultaneously with high resolution pulse-height analysis. An example of such an arrangement is shown in fig. 4.

The time for collection of charges in the detector itself is generally of the order 10^{-9}–10^{-8} sec in silicon detectors, and less than 10^{-9} sec in germanium detectors. However, there is a time-constant associated with the transfer of charge into the amplifier due to the resistance of the undepleted silicon in series with the detector capacitance. The existence of this effect was brought out in a discussion with J. W. Mayer, who has since verified it experimentally[18]). It is necessary to minimise this effect in fast applications by choosing a silicon wafer thickness no more than the depletion layer depth required. There is some advantage in detectors of N-type material, in that the carriers of higher mobility electrons make the transit through the weaker field region near the base electrode, and hence the charge collection time can be shorter by a factor of 3, the ratio of carrier mobilities.

Frequently there may be present a high background of small unwanted pulses, e.g. from electrons or elastically scattered particles, and the pile-up of such pulses may interfere with the observations. Then it is necessary to use a small load resistor, and short amplifier time-constants. The size of electron pulses is minimised by working with a depletion layer no deeper than is necessary to stop the particles under investigation.

4. Characteristics of Gold-Silicon Detectors

4.1. REVERSE CURRENTS

This is a somewhat variable quantity, sensitive to the amount of surface contamination. The work of Buck[14]) has shown that organic vapours cause higher leakage in the case of P-type surface layers. We have therefore tested counters under good vacuum conditions with adequate vapour trapping by liquid nitrogen. However, it is quite possible to operate counters satisfactorily in the presence of air or, presumably, many other gases. Measurements by Buck (private communication) on one of our detectors show a relatively smaller amount of variation in reverse leakage under various ambient conditions than for diffused counters on P-type base material.

A good detector should have a reverse current less than 0.3 μA/cm^2 at 50 volts bias. This corresponds with the space-charge generated current

[15]) J. M. McKenzie and G. T. Ewan, I.R.E. Trans. NS-8 (1961) 50.
[16]) C. Cottini, E. Gatti, G. Giannelli and G. Rossi, Il Nuovo Cimento 3 (1956) 473.
[17]) R. L. Chase, W. A. Higinbotham and G. L. Miller, I.R.E. Trans. NS-8 (1961) 147.
[18]) J. W. Mayer and C. T. Raymo, I.R.E. Trans. NS-8 (1961) 157.

in the volume of the barrier, which is proportional to $\sqrt{V}$, where V is the bias voltage. Fig. 5 shows some typical results in agreement with this, and we infer that the surface leakage current is relatively small. At a fairly critical reverse bias break-down occurs, manifested by a marked fluctuating increase in current accompanied by severe electronic noise. With some detectors over 500 volts bias has been applied before any sign of this, but 200 volts is a more typical limit. Cooling the units reduces the leakage and increases the breakdown potential, and by such means Blankenship[10]) has applied 2100 volts bias to surface barrier detectors.

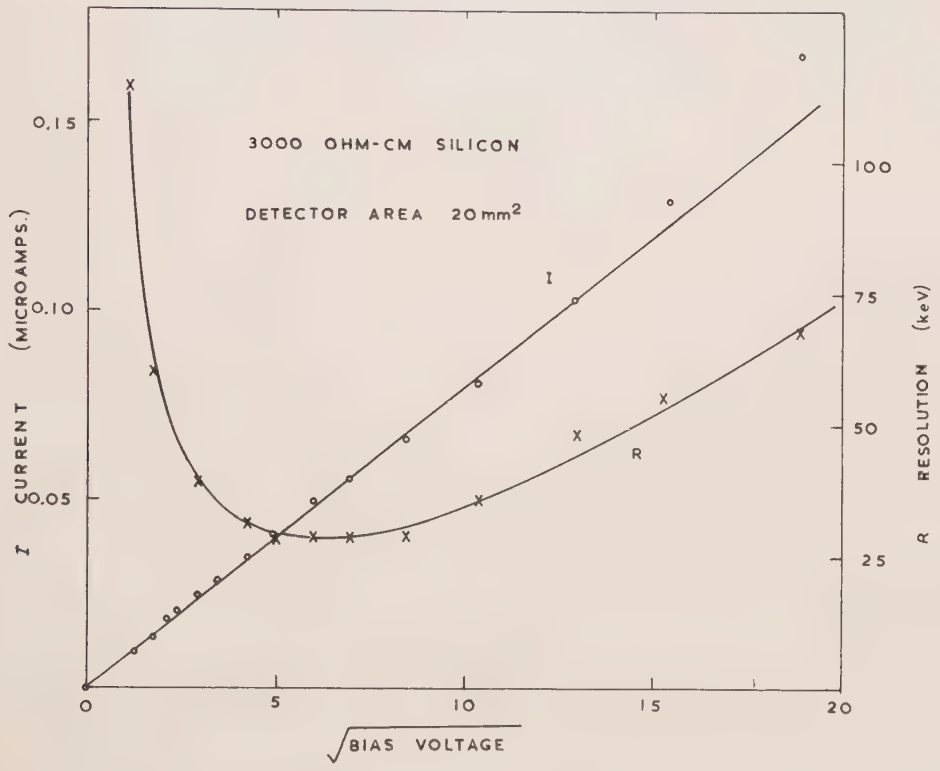

Fig. 5. Reverse current and resolution as a function of (bias voltage)$^{\frac{1}{2}}$.

Due to effects such as dislocation density and uniformity of impurity concentration (which controls the uniformity of barrier depth), different crystals behave in different ways. We find there is often little connection between the magnitude of the leakage current at low bias, and the breakdown potential. Possibly a non-uniform barrier depth leads to early breakdown without causing large current at lower bias.

We have studied some alternative methods of making the base contact to the detector, and find that it may have a marked influence on the reverse current. A method[10]) in which the back of the silicon wafer is protected during the etching process so as to retain a lapped surface results in a good ohmic contact to the silicon either by subsequent evaporation of a gold layer, or by a silver pasted connection. However, the leakage current is greater than that observed following our normal procedure, and if the detector is lapped again and remade by the method described in section 2, the current is reduced. Similar effects have been observed by R.B. Owen at A.E.R.E. when the back crystal surface is roughened by an air-blown abrasive before making the base contact.

It seems likely that carriers are being injected at the base contact and owing to their long lifetime in the bulk silicon some of them are able to diffuse across the crystal to the depletion layer. The damaged surface will contain a large number of sites at which electron-hole production can occur.

The effect of this process is found to be much more pronounced in thin slices of silicon, as would be expected. Therefore the lifetime should be made high at both surfaces by symmetrical etching, and the area of the base contact should be kept small, as in the procedure we advise.

ments on a fairly large area (2 cm²) detector up to 200 volts bias show a $V^{-(0,49+0,01)}$ power law in agreement with expectation (fig. 6). The stray capacitance was here determined by extrapolation of the straight line obtained by plotting capacitance against $V^{-\frac{1}{2}}$.

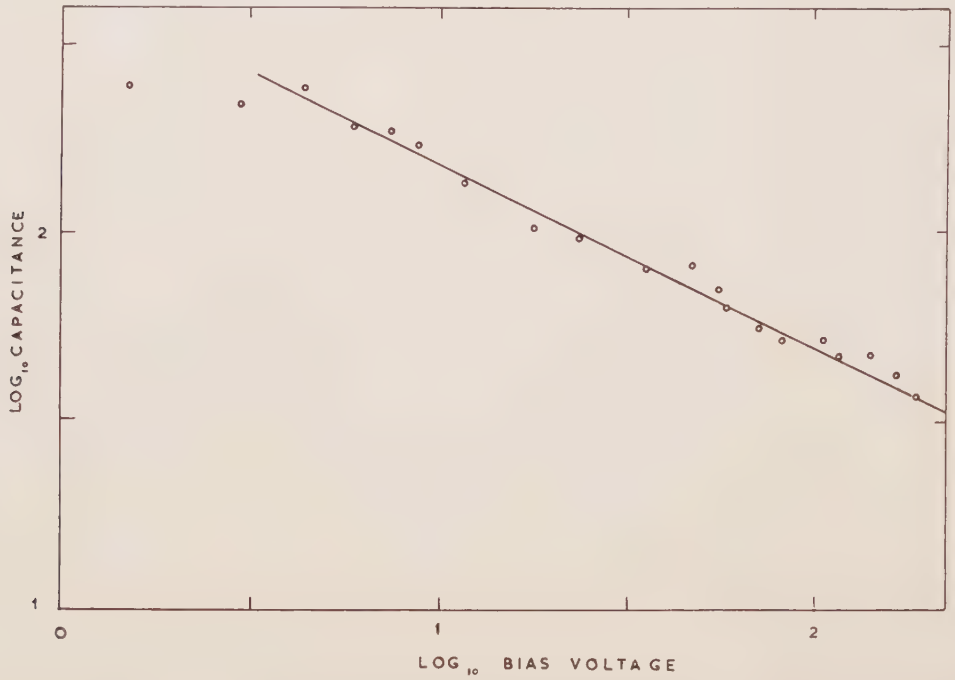

Fig. 6. Detector capacitance as a function of bias voltage (logarithmic scale). The points are fitted with a straight line of slope 0.49 ± 0.01 in the region above 4 volts bias.

4.2. CAPACITANCE

The surface barrier acts as a shallow insulating region between conductors, in a medium of high dielectric constant, and the capacitance is inversely proportional to the barrier depth. The capacitance can be measured by the change in pulse height produced by connecting a standard comparable capacitance in parallel with the detector, while it is exposed to monoenergetic alpha particles.

In an abrupt junction, such as we expect for a surface barrier, the capacitance should be proportional to (bias voltage)$^{\frac{1}{2}}$, and in N-type silicon integration of Poisson's equation leads to the formula $C \approx 1.8 \times 10^4/\sqrt{\rho(V + V_0)}$ pF/cm² after insertion of constants and boundary conditions. Here ρ is the resistivity in ohm cm, V is the applied bias voltage, and V_0 is the intrinsic potential between surface and interior of about 0.6 volts. Measure-

4.3. BARRIER DEPTH

For practical purposes this is the distance from the front electrode over which efficient carrier collection can be achieved, and it is most directly measured by the linearity of pulse height with particle energy. When the particle penetrates beyond the region of the barrier field, carriers are lost by recombination, and linearity ceases. Different types of particle of the same energy give the same pulse height up to an energy at which they penetrate the barrier. This method gives more information than capacitance measurements, since non-uniformity of impurities across the crystal can lead to a non-uniform barrier depth, which becomes apparent from measurements with accelerated particles.

Figs. 7 to 9 show results of scattering protons of different energies, from the Harwell Van de Graaff

and Tandem Generators, into detectors at various bias voltages. The turnover is not abrupt, showing that there is not a sharp boundary to the barrier. Some charge diffuses to the barrier, and is collected, so that the value of barrier depth obtained will be

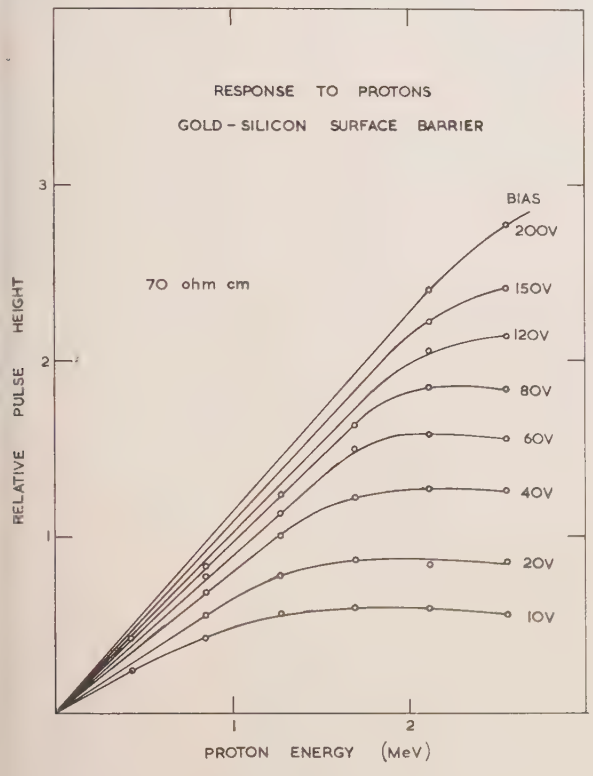

Fig. 7. Response of 70 ohm cm silicon detector to protons of various energies as a function of bias voltage.

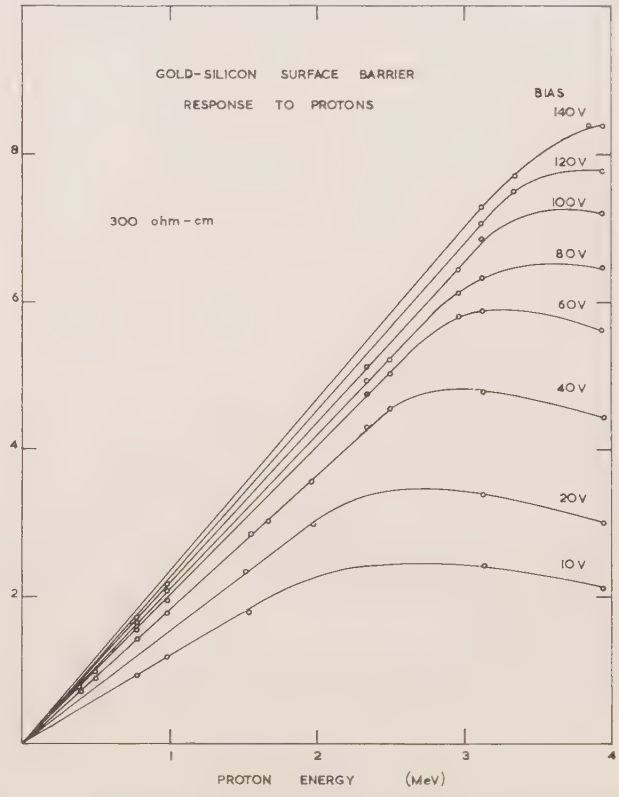

Fig. 8. Response of 300 ohm cm silicon detector to protons of various energies as a function of bias voltage.

dependent on the amplifier bandwidth. Equal integration and differentiation time constants of 0.8 μsec were used in these measurements.

Some earlier measurements[19]) with material which had a resistivity at the surface of 1900 ohm cm are invalidated by the fact that the resistivity changed by a factor of 5 through the 1 mm specimen. Resistivity measurements on both faces of the crystal are now made.

In N-type silicon, the barrier depth d is given by $d\ \Omega\sqrt{\rho(V + V_0)}/1.8$ microns, where the symbols are as in § 4.2. If $V \gg V_0$ the barrier depth is proportional to $\sqrt{V}$, as is the electric field at any given depth. Blankenship[20]) has given a useful nomogram relating barrier depth, bias and resistivity.

4.4. ENERGY RESOLUTION

Several factors influence the resolution of a counter.

(i) *The statistics of the electron-hole pair formation.* If the number of pairs is related to the incident particle energy by a constant $W \approx 3.6$ eV independent of particle energy, as all evidence suggests, then this is unlikely to limit detector performance. The advantage over gas counters is here apparent, the number of events being 8–10 times greater in the solid detector.

(ii) *Recombination effects.* Some small fraction of the carriers will inevitably encounter recombination sites before being collected, and if this fraction varies over the crystal the pulse height will be a function of the position of the ionized track. Initially as the carriers begin to be separated there will be a strong mutual field between the electrons

[19]) G. Dearnaley, I.R.E. Trans. NS-8 (1961) 11.
[20]) Contribution to Nucleonics **18** (1960) 98.

and holes, diminishing as they diffuse away from the track. At a certain stage the externally applied field will become predominant, and collection will take place governed by the normal carrier mobility. An increased field reduces the time for both these processes, and so shortens the time in which recombination is possible. The minority carrier lifetime in high-quality silicon is around 1 msec, but if the impurity concentration is non-uniform, and there are local dislocations around which impurities tend to cluster, there will be regions of much lower lifetime, and carriers may be lost during transit times as short as 10^{-8} sec. However, in diffused junction counters a marked reduction in lifetime follows the heating process necessary for diffusion. Multiple peaks from monoenergetic alphas have been observed in such counters much more commonly than in surface barrier counters[21]), with consequently often poorer resolution. Further evidence that such effects are linked to poor carrier lifetime is provided by radiation damage observations (see also § 4.8), in which multiple peaking becomes apparent after bombardment with charged particles.

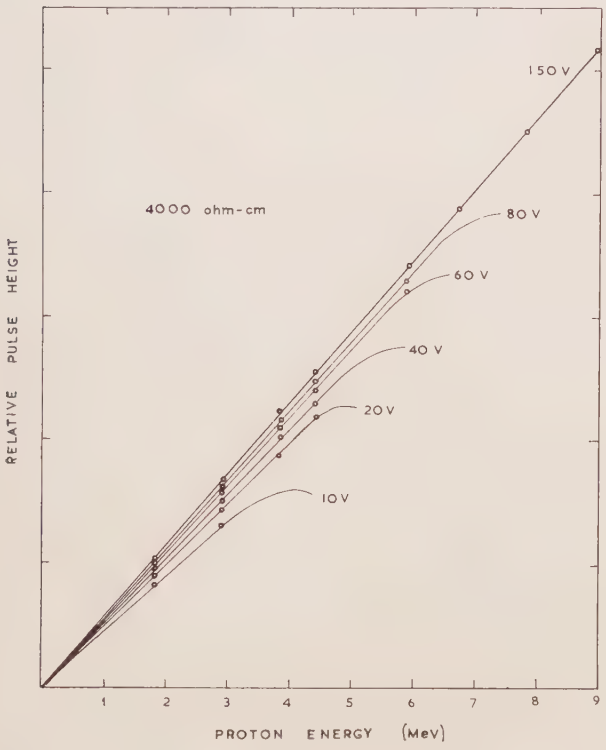

Fig. 9. Response of 4000 ohm cm silicon detector to protons of various energies as a function of bias voltage.

(iii) *Detector noise.* This arises from fluctuations in the detector leakage current, which is a function of the applied bias. The detector acts simply as a reverse-biased diode, which has been studied before in this respect[22]). The noise consist of shot noise due to fluctuations in the bulk leakage current, and two types of flicker noise characterized by a $1/f$ frequency dependence. One is due to surface noise arising from fluctuations in the density of recombination centres at the diode surface, and the other is leakage noise due to a conducting film by-passing the junction at its perimeter. Flicker noise is very dependent on the ambient atmosphere. The contributions of these noise sources vary with detector current.

At low bias voltages the detector noise is usually less than the amplifier noise, which then limits performance, and for which the amplifier time constants must be optimised. At high bias the detector noise becomes dominant and we find that the signal to noise ratio is improved by shorter (equal) time constants.

(iv) *Amplifier noise.* This arises principally from shot noise and grid current noise at the input stage. There is a certain time constant, dependent upon tube characteristics and input capacitance, for which the sum of these noise contributions is minimised, and this determines the optimum conditions at low detector bias. A detailed study of amplifier noise in these applications has been given by Fairstein[23]) and Goulding[24]).

At A.E.R.E. we have used the conventional 1430 amplifier, and so far this has limited the resolution attained to about 16–18 keV (i.e. 0.35% for a 5.4 MeV alpha). Fig. 10 shows the response of a 30 mm^2 detector to Am^{241} alphas. The vertical lines indicate the expected positions and intensities of the lines, normalised to the main peak.

Such voltage-sensitive amplifiers are, however,

[21]) Discussion at N.A.S. Conference, Asheville (Sept. 1960) (to be published).

[22]) See for example Van der Ziel, Fluctuation Phenomena in Semiconductors (Butterworths, 1959).

[23]) E. Fairstein, I.R.E. Trans. NS-8 (1961) 129.

[24]) F. S. Goulding and W. L. Hansen, U.C.R.L. Report 9436 (1960).

inferior to charge-sensitive configurations as mentioned in § 4.3. With a cascode charge-amplifier, Blankenship[9]) has reported a resolution of 14 keV for 5 MeV alphas.

Not all counters give such high resolution, however, probably for a variety of reasons. Inferior

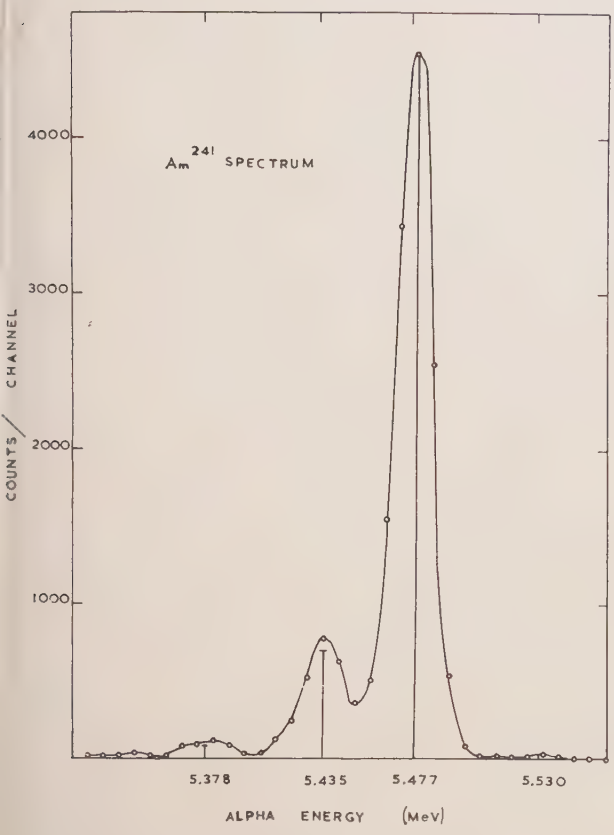

Fig. 10. Resolution of Am^{241} alpha spectrum in a silicon detector of 30 mm^2 area (3000 ohm cm resistivity, bias 60 volts). The vertical lines show the expected positions and intensities of the lines normalised to the main peak. The resolution is 17 keV or 0.3 % in energy.

silicon can be the cause of a high detector current, producing noise which is apparent in the absence of any charged particles, while nonuniform trapping causes a spread in pulse height. Surface contamination of the detector can cause surface leakage noise. Such surface effects cause a variation in performance with time, whereas the bulk effects remain constant, provided radiation damage or overheating does not occur.

(v) *Practical considerations.* When detectors are used in conjunction with an accelerator to detect particles from a nuclear reaction, there is some spread in particle energies at the detector due to its angular acceptance. Target thickness may also limit the resolution.

There is an optimum detector bias for best resolution (fig. 5), since the voltage signal increases as the capacitance is reduced by increasing bias, but the leakage current increases. However, other considerations will generally determine the bias voltage used to obtain a barrier depth to suit the relevant particle energy. Bias of 200 volts often gives us a resolution still better than 50 keV, and in the highest resistivity N-type material available (around 10000 ohm cm) this produces barriers almost 1 mm deep, sufficient to stop 11 MeV protons, or 40 MeV alphas.

4.5. PULSE RISE-TIME

The mobility of electrons in silicon at room temperature is about 1300 cm^2/volt sec while that of holes is approximately one-third that value. For a given barrier depth and bias the charge collection time can thus be calculated, and typical values lie between 10^{-9} and 10^{-8} seconds. As the range of the ionising particle will in general be less than the barrier depth, the electrons make the longer transit. Here incidentally is a slight advantage of surface barrier detectors over P-type diffused junction counters, in which the slower carriers make the longer transit. The simple approach neglects the separation time of the electrons and holes, during which they must diffuse until the collecting field can overcome their mutual attraction. This time can be appreciable in the densely ionised tracks of fission fragments[5]).

Measurements were made at A.E.R.E. on the rise-time of pulses from 5 MeV alphas in a barrier $\approx 120\ \mu$ deep formed by 72 volts bias in 1000 ohm cm silicon. After amplification by two type 2002A distributed amplifiers in series pulses of 0.4 volts amplitude were observed with a rise-time of 6×10^{-9} sec on a Tektronix type 517A oscilloscope. The rise time of the system was not appreciably less than this, so that the result is in accordance with the calculated rise time of 3×10^{-9} sec.

4.6. WINDOW THICKNESS

By this is meant the effect of any insensitive layer at the surface of the detector.

Extrapolation of pulse height against energy calibrations for alpha particles of energies down to 300 keV show no appreciable intercept. Measurements by R. Segel (priv. comm.) on one of our detectors, in which 1.8 MeV alphas were injected at 0° and 45° showed that the dead layer was $< 0.05\ \mu$ of silicon, or equivalent.

Low energy C^{12} ions, of 200 keV, have been detected with good agreement with the proton energy calibration. This was carried out by bombarding a thin foil of carbon with alphas, and detecting the scattered alphas and recoiling carbon ions. This again shows that the dead layer must be $< 0.03\ \mu$ of silicon.

Such figures are consistent with the thickness of the gold film, and the expected thickness of the oxide layer, of the order 10 Å. The results are significantly better than those for most diffused junction counters.

4.7. SENSITIVITY TO GAMMA-RAYS

Gamma-rays produce photoelectrons, Compton electrons, and pairs in the silicon itself and in surrounding material. Because of the low atomic number of silicon the photoelectric process and pair formation are unfavoured.

In the case of a shallow barrier the sensitive volume is so thin that electrons lose negligible energy before escaping from it, and thus gamma-rays produce only small pulses with low efficiency. Barriers as deep as 1 mm however have shown much greater efficiency and pulse height for electrons and gamma-rays. Donovan[25]) and McKenzie[15]) have reported good resolution for these radiations up to a few hundred keV. Pile-up of unwanted small pulses can be minimised by the precautions mentioned in section 3.

4.8. SENSITIVITY TO NEUTRONS

Neutrons can produce pulses in a surface barrier detector by three possible means:

(i) (n,p) and (n,α) reactions in silicon. Known reactions occurring[26]) are:

Si^{28}(n,p) $Q = -3.86$ MeV. Percentage abundance = 92%. The cross-section[27]) rises from 0.02 barns at 5 MeV to 0.40 barns at 8 MeV falling to 0.22 barns at 14 MeV.

Si^{28}(n,α) $Q = -2.66$ MeV.

Si^{29}(n,p) $Q = -3.20$ MeV. Percentage abundance = 4.7%. The cross-section is 0.10 barns at 14 MeV.

Si^{30}(n,α) $Q = -4.19$ MeV. Percentage abundance = 3.1%. The cross-section is 0.05 barns at 14 MeV.

The reactions induced in Si^{28} are clearly the most important, due to the large cross-section and isotopic abundance.

(ii) Reactions in the gold layer. Charged particle emission is inhibited by the high atomic number. Capture followed by emission of a 412 keV gamma-ray is the only effect which might be observed, but the yield is very low for film thicknesses of 50 μ g/cm^2 or less.

(iii) Recoil protons ejected from adsorbed hydrogen and water vapour in the surface, and neighbouring surfaces. Gold has a very low adsorption and is particularly suitable in this respect.

Measurements have been made, with A. T. G. Ferguson, on the response of a detector mounted in a gold-lined evacuated chamber and exposed to a flux of $\approx 10^5$ neutrons/cm^2 sec at different energies. At 2 MeV neutron energy the spectrum observed in the detector corresponds to a low yield of protons recoiling out of a thick layer, and this is attributed to residual hydrogen and water in the chamber walls. A lower background level could be obtained by vacuum-baking all the components, then introducing the detector in a dry-box. The response of semiconductor counters to low energy neutrons is made low by their high purity, which ensures the absence of any bulk contamination by hydrogenous materials.

At 6.3 MeV neutron energy the spectrum is very different, and is shown in fig. 11. The Si^{28}(n,p) cross-section is known[27]) to be large at this energy, ≈ 0.2 barns, and the Si^{28}(n,α) reaction, not previously observed, appears to have a cross-section

[25]) P. F. Donovan, G. L. Miller and B. M. Foreman, Bull. Amer. Phys. Soc. **5** (1960) 355.

[26]) P. M. Endt and J. C. Kluyver, Rev. Mod. Phys. **26** (1954) 95.

[27]) R. J. Howerton, U.C.R.L. Report 5226 (1958).

almost as great. In fig. 11 the arrows indicate the expected positions of proton and alpha groups to known levels in Al^{28} and Mg^{25} respectively, and there is obvious correspondence with the spectrum observed. The resolution is inevitably poor since

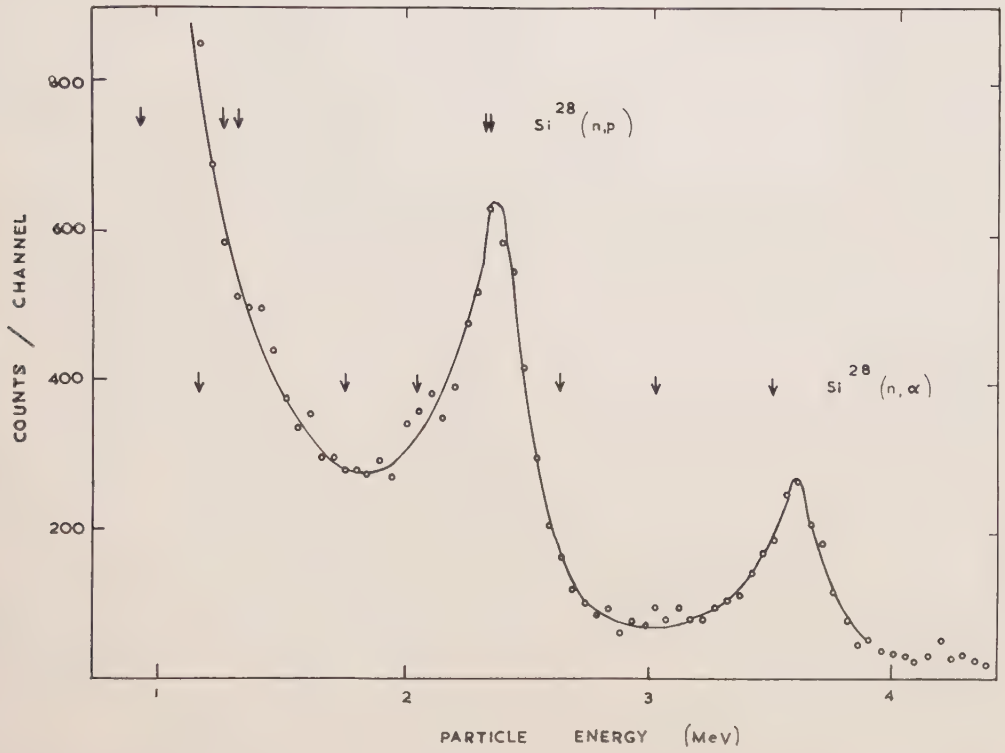

Fig. 11. Spectrum observed in a silicon detector under a high flux of 6.2 MeV neutrons. The arrows indicate possible charged-particle transitions to known energy levels.

particles from reactions induced near the barrier boundaries may escape.

These reactions impose a limitation on the usefulness of silicon detectors, of any type, in a flux of fast neutrons, especially in the region of 8 MeV, where the Si^{28}(n,p) cross-section peaks. The response to neutrons can, however, always be minimised as for gamma-rays by simply adjusting the barrier depth to be no greater than is necessary. As we shall see in § 5.5., there are advantages here in the use of germanium detectors.

4.9. RADIATION DAMAGE

Lattice defects are known to be produced in semiconductors by bombardment with alphas, deuterons, neutrons and electrons. In silicon this results in an increase in resistivity due to the trapping of carriers in levels formed near the middle of the band gap. The presence of these trapping centres lowers the lifetime of minority carriers and leads to a greater reverse diode current, due to the possibility of transitions via the intermediate defect states. The possibility that the useful life of a detector may be limited by radiation damage must therefore be considered.

Measurements by Klingensmith[28]) on several surface barrier detectors exposed to fission neutrons indicate that deterioration is not appreciable up to about 5×10^{11} fast neutrons/cm^2. Above this dose the resolution worsens and multiple peaking appears in the spectrum for monoenergetic alphas, while after 10^{13} neutrons/cm^2 the pulse height is much reduced. These measurements were made for a low bias of 6 volts in 3000 ohm cm silicon, and so correspond to a low collecting field. We would expect that recombination effects would be reduced

[28]) R. W. Klingensmith, I.R.E. Trans. NS-8 (1961) 112.

by using higher fields, and the life of detectors might then be appreciably greater.

Little information seems to be available on damage by charged particles, so an empirical measurement was made to assess this. Several detectors of around 1000 ohm cm silicon were exposed

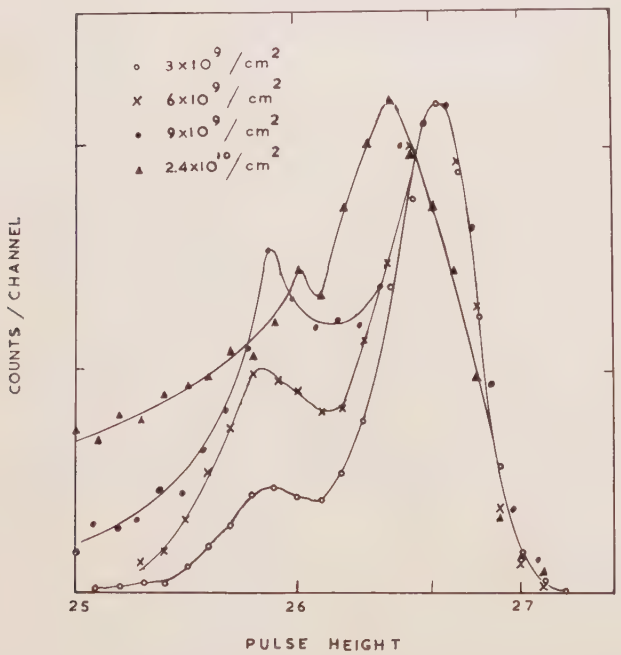

Fig. 12. Alpha-particle spectrum in a silicon detector after various amounts of irradiation by 5 MeV alphas.

to a high flux of 5.5 MeV alphas from a source of Am^{241}. Since the region of damage will be limited by the alpha range to about 0.003 cm it is to be expected that damage effects will be most apparent for a barrier depth only slightly greater than this, produced by only 2 volts bias. The resolution was measured by replacing the strong source by a weak one of good resolution. At this low bias the initial resolution of the detectors was about 1.5%.

After 10^8 alphas/cm² a slight increase of reverse current could be observed, and after 10^{11} alphas/cm² the current had increased by 3 μ A/cm² at 2 volts bias, from a very small initial value. This corresponds to a reduction in mean carrier lifetime to ≈ 1 μsec. There was a significant variation around these figures for different detectors. The resolution began to deteriorate after 2×10^9 alphas/cm² and soon a secondary peak of lower pulse height began to appear, increasing in size with further damage, as shown in fig. 12. In one detector, three peaks became visible, merging together as the resolution progressively worsened. These effects were strikingly similar to those observed by Klingensmith for neutron damage. After 10^{11} alphas/cm² the resolution in different counters had deteriorated to between 6% and 15% at 2 volts bias. At a higher bias of 20 volts the resolution was only increased to 3–4%, and multiple peaking was never apparent.

The most serious damage is expected to be near the end of the alpha particle range, owing to the heavy ionisation and likelihood of nuclear collisions. It is just in this region that the carriers are produced in a relatively weak field, which must overcome the forces between the electron and hole plasmas as they begin to separate. Recombination may under these conditions become possible before the charges can be collected, and local regions of low carrier lifetime may be the cause of multiple peaking. The effects are not seen at higher bias voltages because the carriers are produced in a much stronger field, and recombination is less likely. Variations between detectors are then due to differences in the initial carrier lifetime and in the uniformity of distribution of recombination centres.

There was some evidence that the peaks tended to merge on allowing the detector to stand at room temperature, without further damage. A period of 24 hours at 120°C produced no improvement un resolution.

The assistance of Dr. Jan Kuperus, (on attachment from Rijks Universiteit, Utrecht) is gratefully acknowledged in these measurements.

4.10. USEFUL LIFE OF DETECTORS

At A.E.R.E. detectors have been used over periods of 15 months without deterioration, and without more protection than a covered box when not in use. Measurements on one such counter, by R. Segel, have shown that its characteristics remain essentially unchanged over this time. Some detectors have shown increased noise and leakage current after a time, and in some cases this has been found to be associated with the front contact, since the counters were restored by making a new contact elsewhere. Other cases of deterioration have been

due to surface contamination caused by a visible film of grease or amalgamation of the gold with mercury. The use of nickel instead of gold for the evaporated film overcomes this if it is for some reason impossible to trap the mercury vapour. A period of surface breakdown caused by contamination while the bias voltage is applied can produce permanent damage.

We have not observed the deterioration under vacuum which some groups have experienced, especially with high resistivity counters. Some counters of 1000 ohm cm silicon have been operated for two months under vacuum with no apparent ill effects.

Radiation damage may under some circumstances limit the useful life, for instance in applications to neutron spectrometry inside a reactor. A difficulty is caused by the low efficiency of some such devices[29]) for fast neutrons, ($\approx 10^{-6}$) since $\approx 10^{12}$ fast neutrons/cm^2 can produce appreciable damage.

4.11. PHOTOSENSITIVITY

All detectors exhibit photoconductivity, and they should therefore be tested and used in reasonably dark conditions.

4.12. EFFECT OF A MAGNETIC FIELD

A transverse magnetic field will deflect the electron paths in a surface barrier, but no effect on the detection of 5 MeV alphas was observed in a field of 3000 gauss parallel to the surface. From formulae given by Shockley[30]) an appreciable effect would not be expected below about 50000 gauss, in silicon. This characteristic is valuable when the detectors are used in conjunction with a magnetic spectrometer.

5. Characteristics of Gold-Germanium Detectors

5.1. REVERSE CURRENT

Owing to the lower band gap of germanium, it is necessary to cool detectors made with it to the region of liquid air temperatures in order to reduce the intrinsic conduction by thermal carriers. All the measurements described here were made at 77° K.

The reverse current is somewhat more variable with germanium than with silicon detectors, possibly because the cooling required may cause condensation of contaminants on the surface. Another factor is the apparently greater surface conductance of the surface layer on germanium compared with silicon. This was already known from the work of Brown[31]) and is confirmed by two effects we have observed. First, if the whole crystal face is exposed to alpha particles, then as well as the fast-rising pulses of good resolution there are also pulses of lower amplitude which rise in several microseconds. These pulses disappear if the uncoated germanium is masked by a collimator, and they are attributed to collection by the unbiased surface barrier which exists on the germanium, followed by diffusion through the surface layer to the gold electrode. Secondly, measurements with a guard-ring type of structure show that there is usually an appreciable surface conductance between separate gold electrodes. This surface conductivity influences the design of a multiple detector of germanium (§ 8.4).

It has been possible to apply 200 volts reverse bias to a gold-germanium detector without breakdown, but this is not easily reproducible and more often 50 volts is the limit.

5.2. BARRIER DEPTH

Owing to the greater stopping power of germanium compared with silicon, the same barrier depth will stop particles of about twice the energy. Also, due to its lower melting point, it is rather more easily zonerefined and lower uncompensated donor densities can be obtained. For these reasons it has been possible to achieve linearity of pulse height with proton energy to over 6 MeV for only 40 volts bias (fig. 13). For comparison, it would require a resisitivity of 10000 ohm cm in silicon to give the same performance.

5.3. ENERGY RESOLUTION

The best resolution obtained at A.E.R.E. has been 20 keV for 5.4 MeV alphas. The resolution seems to be rather more consistently good with germanium detectors than with silicon, probably owing

[29]) T. A. Love and R. B. Murray, O.R.N.L. report CF 60-5-121 (1960).

[30]) W. Shockley, Electrons and Holes in Semiconductors (Van Nostrand, 1950) p. 214.

[31]) W. L. Brown, contribution to "Semiconductor Surface Physics" ed. R. H. Kingston (Penn. Univ. Press, 1957).

to the greater carrier mobility and lower likelihood of recombination effects.

5.4. PULSE RISE-TIME

The mobility of electrons and holes is much greater in germanium at 77°K than in silicon at

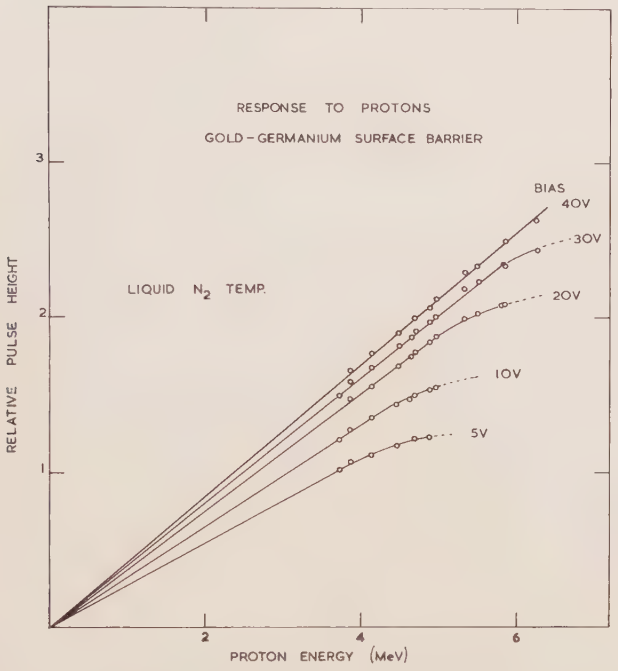

Fig. 13. Response of germanium detector at 77° K to protons of various energies as a function of bias voltage.

room temperature, and is of the order 1.5×10^4 cm²/volt sec, so that the anticipated pulse rise time is around 5×10^{-10} sec. It is again important to minimise the time constant due to the detector capacitance and its base resistance. It has been verified by P. Orman, at A.E.R.E., by means of a sampling oscilloscope, that the rise time of 5 MeV alpha pulses in a gold-germanium detector is less than 3×10^{-9} sec.

5.5. SENSITIVITY TO NEUTRONS

Known (n,p) reactions induced in germanium isotopes are[27]:

$Ge^{70}(n,p)$ $Q = -0.82$ MeV.
Isotopic bundance = 20.5%,
cross-section $\sigma = 0.014$ b at 1.8 MeV, 0.09 b at 14 MeV.

$Ge^{72}(n,p)$ $Q = -3.2$ MeV.
Isotopic abundance = 27.4%,
cross-section $\sigma = 0.06$ b. at 14 MeV.

$Ge^{73}(n,p)$ $Q = -0.71$ MeV.
Isotopic abundance = 7.6%,
cross-section $\sigma = 0.13$ b at 14 MeV.

Other isotopes present in the natural element are Ge^{74} (36.7%) and Ge^{76} (7.7%), but the (n,p) thresholds for these neutron-rich isotopes will be well over 5 MeV. In spite of the rather low thresholds for some of these reactions, it can be seen that the higher atomic number of germanium, 32 compared with 14 for silicon, is effective in inhibiting charged particle emission. Alpha particles will be even less favoured.

The result is that, as we have found qualitatively, germanium counters produce a lower background from a flux of fast neutrons compared with silicon counters of the same barrier depth, a fact which may sometimes be a considerable advantage. Another factor of three is gained because the depletion layer thickness required to stop protons of a given energy contains three times fewer nuclei in the case of germanium.

6. Comparison of Surface Barrier and Diffused Junction Counters

There have been some unjustified criticisms of the performance of surface barrier counters compared with diffused junction counters, and these should be dispelled.

Earlier techniques[7]) in which synthetic resin was employed to encapsulate the crystal before etching give unreliable results because of the difficulty of washing the etch away from small crevices at the silicon-resin boundary. Also, impurities from the resin may enter and contaminate the silicon at the edge of the barrier, leading to deterioration with time. We find that the present technique gives detectors with a very stable characteristic and long life.

A second criticism has been that the N-type silicon used for surface barriers is not available to the degree of purity possible for P-type silicon. This is true, as a rule, since the boron impurity which is the most difficult to remove is an acceptor. However, a small degree of compensation provides

N-type material of high resistivity which still retains a lifetime in the millisecond region. The supply of 3500 ohm cm N-type silicon seems as plentiful as 10000 ohm cm P-type, which, because of the ratio of 3 in carrier mobilities, is the equivalent in uncompensated carrier density and hence in barrier depth.

We must rule out the objection that less is known about conditions at the crystal surface compared with the interior, and hence that we should not make use of its properties. The detectors have shown themselves to perform extremely well, and the study of them is itself already providing information regarding the surface states of semiconductors.

Perhaps a valid criticism is that surface barrier units are less easily protected in a metal can than the diffused counters. The surface film is more easily damaged in handling, and the present construction methods are less suited to industrial production than to laboratory preparation. This, however, is probably not an insuperable obstacle if there are merits elsewhere.

Turning to the advantages of the surface barrier counter, we have at once a much simpler construction, easily carried out in most laboratories. There is no heating process and hence the lifetime is not degraded. The thickness of the gold film is not critical, and is easily made uniform, whereas the shallow diffusion must be carefully controlled to give a counter that is to be essentially windowless. The window of a surface barrier counter is always extremely thin. Because of the higher carrier lifetime the bulk leakage current is lower in surface barrier counters, especially for large area units. Surface barrier counters have been operated successfully with an area of 6 cm² on germanium and 3 cm² on silicon.

The simplicity of the evaporation method allows a variety of structures to be made with ease, and some of these are outlined in section 8.

Finally, we must not overlook possible combinations of both techniques. D. A. Bromley[32]) has pointed out that a surface barrier could be formed on a deep-diffused N-type layer on high-resistivity P-type silicon. This would produce a thin dE/dx counter integral with an energy counter. Such a unit would seem to have valuable possibilities.

7. Applications to Nuclear Physics

In the light of the performance of surface barrier detectors in a variety of experiments at Harwell, we may summarise the advantages and disadvantages which have become apparent.

The excellent energy resolution, down to 20 keV

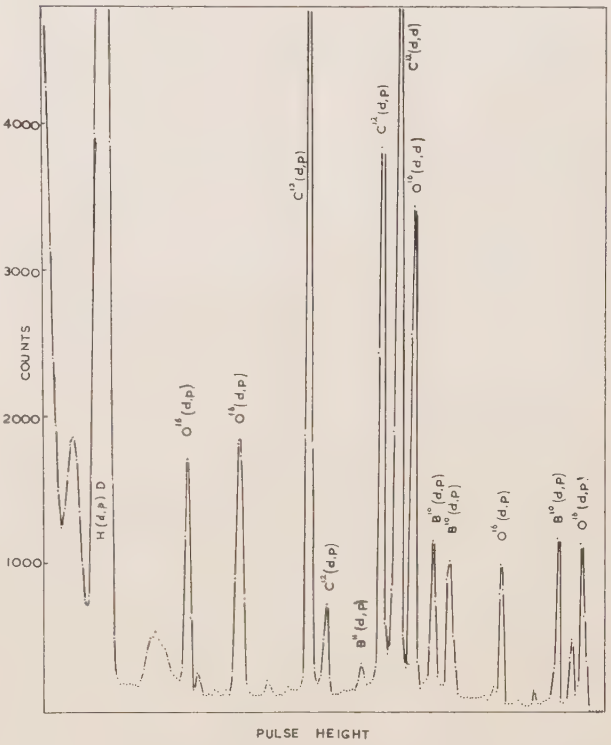

Fig. 14. Spectrum resulting from the bombardment of a thin target containing carbon, boron and oxygen with deuterons of 5.0 MeV.

even with conventional types of amplifier, enables them to be used in place of magnet spectrometers for the investigation of charged particle reactions and scattering processes in many cases, (fig. 14). The whole spectrum is displayed by pulse height analysis, instead of by slow scanning by variation of the magnetic field, so that effects due to changes in the target under bombardment are less serious. The linearity of response makes calibration simple.

The low cost of the detectors, if prepared by a laboratory technique such as that described, and the simple requirements for voltage supplies enable

[32]) D. A. Bromley, Proc. of N.A.S. Conference, Asheville (Sept. 1960) (to be published).

numbers of them to be used in laboratories without extensive facilities.

Compactness of size of the counters enables them to be mounted easily so as to rotate about a target, and although they may be relatively small, they can be brought close to a target in order to subtend an appreciable solid angle. The detector can be made in a slit shape to minimise the energy spread due to the spread in azimuthal angle. Detectors can be mounted at angles very close to 180°, a region which has not been accessible for magnetic analysis, so that high resolution data is usually lacking. Often stripping reactions show interesting behaviour at these large angles. Bromley[32]) has described an annular detector designed so that the particle beam can be directed through it, to give symmetrical detection at 180°. Such an arrangement brings great simplification to the analysis of angular correlation experiments.

A number of detectors can be used simultaneously for the measurements of an angular distribution of charged particles, under identical beam and target conditions. The problem of handling the amount and precision of data which can then be obtained is considerable, but multi-track magnetic tape equipment enables simultaneous storage of information to give counter angle and pulse height.

Detectors can be employed singly or as a multiple system in conjunction with a magnetic spectrometer, so that simultaneous high resolution in momentum and energy is then possible. Their low sensitivity to magnetic fields is a significant advantage over scintillation counters.

The excellent signal to noise ratio obtainable allows the detection of particles of very low energy. The detectors are essentially windowless.

It is possible to control the thickness of the sensitive region, by means of the applied bias, and thus discriminate between particles of different range. This is easily performed by remote control, and does not affect the energy resolution as does the use of stopping foils. The fact that the sensitive thickness can be suited to the particles investigated enables the response to background gammas and electrons to be minimised.

The low response to neutrons (below about 5 MeV) due to the absence of hydrogenous material is very valuable, for instance in polarisation experiments. Fast neutrons can cause a considerable background, however, though again this can be minimised by suitable choice of barrier depth. Germanium detectors have some advantages here.

The fast rise time is important in coincidence measurements, but it is then difficult to make use of the good detector resolution owing to the small size of the detector output. Fast amplifiers have too poor a signal to noise ratio, but it is possible to employ simultaneous slow amplification as suggested in section 3.

Most use of the counters has been made for the detection of low energy particles, of range less than the depletion layer thickness, but the detectors may not be without applications to high energy physics. Here they behave as dE/dx counters, in which the energy loss for all minimum ionising particles is about 400 keV/mm (in silicon). The pulses are therefore of small size, and require considerable amplification, which leads to difficulties due to electrical pick-up and radiation background near large accelerators. There is a spread in pulse height amounting to 20–30%[33]) owing to the statistical fluctuations in energy loss, the Landau effect. It would seem that bulk conductivity counters hold more promise for this field, in the future.

Similar considerations apply to the detection of fast electrons for which the resolution is good up to a few hundred kilovolts[15]). At higher energies the output becomes essentially independent of energy, due to the broad minimum in the rate of energy loss. In tracer experiments and activity measurements some features of semiconductor counters, such as their small size, will probably be advantageous.

Further applications are made possible by elaborations of the detector design, and some of these will be described in the next section. It is already clear that in the design of any experiment in nuclear physics the possible advantages of semiconductor detectors, of the various types, must be considered.

[33]) G. L. Miller, B. M. Foreman, L. C. L. Yuan and P. F. Donovan, I.R.E. Trans. NS-8 (1961) 73.

8. Special Configurations

The design of the surface barrier detector is easily modified to meet special requirements, and its versatility is illustrated by some variations which have been studied at A.E.R.E.

8.1. FISSION DETECTOR

If a thin film of fissile material, such as uranium oxide, is evaporated on to the gold layer, fission fragments emitted from it can be detected. Such a structure was first described by McKenzie and Bromley[34]). If two such counters are spaced a short distance apart, the coincidences corresponding to collection of both fragments can be recorded and the pulse heights added in such a way as to yield the mass spectrum. The use of solid counters eliminates the need for the self-supporting thin film of fissile material required for ionization chambers. Experiments with such an arrangement of surface barrier detectors have been carried out at A.E.R.E. by Melkonian[35]) and Gooding[36]). The performance was as good as the best published results by other means, and it was possible to study the influence of neutron energy on the mass spectrum. Some preliminary measurements on ternary fission were made with array of three detectors, and the fission cross-section of uranium was studied with a square array of counters. Their compactness and the small amount of scattering material present is of particular advantage, while the high speed allows shorter resolving times and less pile-up from alpha-activity.

During this work it was found that the ratio of pulse heights corresponding to the peaks of the fission energy spectrum was lower by a few percent than the value obtained by time-of-flight measurements. It has been shown that this is not due to a detector "window", by measurements with a detector at 90° and then 45° to the source. It seems most likely to be due to recombination effects enhanced by the very high density of ionization caused by fission fragments. The work of Miller, Brown and Donovan[5]) has shown the existence of "ambipolar" effects by which the rise-time of pulses from fission fragments is extended to about 4×10^{-8} sec. Similar nonlinear behaviour has since been reported by Joyner *et al.*[37]).

8.2. FAST NEUTRON DETECTORS

Several types of fast neutron detector are under investigation at A.E.R.E., with special regard to their use for neutron spectrum measurements inside low powers reactors or other integral systems.

One type has been described by Love and Murray at O.R.N.L.[29,38]) and makes use of the $Li^6(n,\alpha)H^3$ reaction. Two close and parallel surface barrier counters are exposed to a thin film of Li^6F in an evacuated chamber: In the units constructed at A.E.R.E. it has proved simple to evaporate Li^6F on to the gold surface of one of the detectors, taking care to mask the counter during the process so that the fluoride does not extend beyond the area of the gold. The alpha particle and triton from the neutron-induced reaction are counted in coincidence, and addition of the pulses gives an output proportional to the neutron energy added to the reaction Q, which is 4.7 MeV. Resolution of 70 keV has been obtained for this summed pulse for thermal neutrons. At higher energies this resolution improves, but the reaction cross-section becomes low, and the efficiency of the detector falls to $\approx 10^{-6}$ at 3 MeV. With such a low efficiency there is danger of radiation damage occurring before the experiment is complete. At neutron energies above about 8 MeV the background due to $Si^{28}(n,p)$ and (n,α) reactions becomes serious, despite the coincidence condition, for it is possible for a charged particle produced in one crystal to cross to the other.

In collaboration with Dr. S. B. Wright at A.E.R.E., studies are now being made of a similar unit in which the Li^6F is replaced by He^3 gas. The reaction then involved is $He^3(n,p)H^3$ which has a Q of only 770 keV and the added advantage of a larger cross-section in the region of a few MeV neutron energy. The pressure of He^3 can be adjusted to suit different conditions, a higher pressure being allowed at higher energies to give increased efficiency without too much energy loss taking

[34]) J. M. McKenzie and D. A. Bromley, Phys. Rev. Letters 2 (1959) 303.

[35]) E. Melkonian, A.E.R.E. Report R-3524 (1960).

[36]) T. J. Gooding, Proc. Phys. Soc. London (to be published).

[37]) W. T. Joyner, H. W. Schmitt, J. H. Neiler and R. J. Silva, I.R.E. Trans. NS-8 (1961) 54.

[38]) T. A. Love and R. B. Murray, I.R.E. Trans NS-8 (1961) 91.

place in the gas. A pressure of 1–5 atm of He^3 is to be used, but the volume of the detector can be quite small. Owing to the fast pulses, pile-up from possible tritium contamination of the He^3 is less important than in an ion chamber. There is, of course, the possibility of background due to rand-

Measurements have been made with both types of recoil counter exposed to monoenergetic neutrons produced from the 5 MeV Harwell Van de Graaff generator by protons on a thin tritium target. A radiator of 250 $\mu g/cm^2$ glyceryl tristearate was evaporated on to a gold disc in front of a

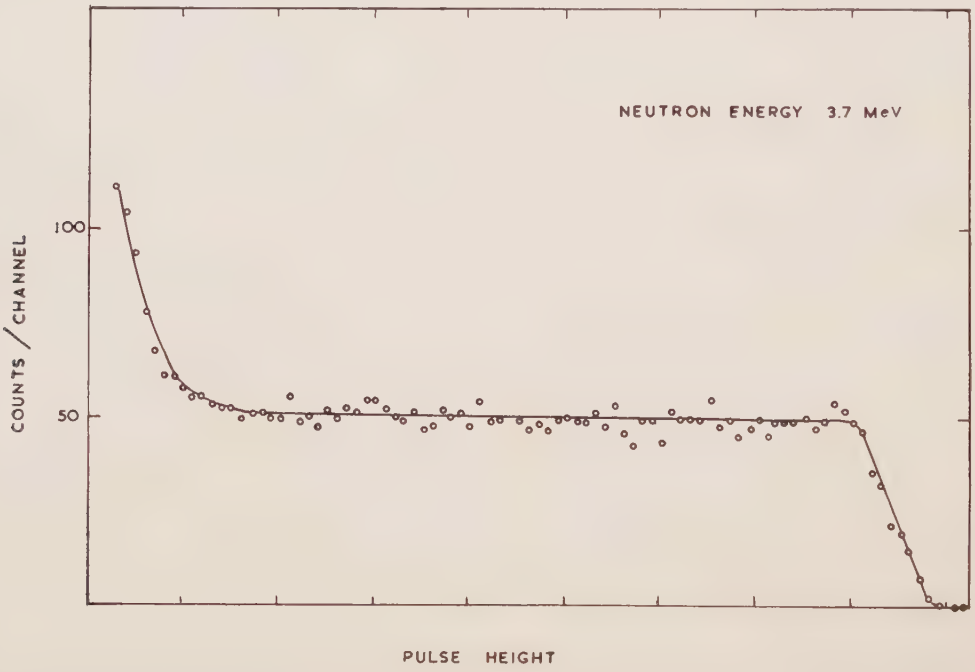

Fig. 15. Spectrum observed in a proton-recoil detector with a radiator of 800 $\mu g/cm^2$ glyceryl tristearate exposed to monoenergetic neutrons of 3.7 MeV.

om coincidences fron recoiling He^3 ions following elastic collisions, but this is minimised by a short coincidence resolving time.

The third type of neutron detector being investigated makes use of recoil protons from a thin hydrogenous radiator. The cross-section for this process remains high in the MeV region and the counter does not suffer from over-sensitivity to thermal neutrons, which is a disadvantage of the other types. At energies above 5 MeV, however, difficulties arise from the $Si^{28}(n,p)$ and (n,α) background. There are two forms of recoil detector: in one, recoils at all angles to the incident neutron direction are detected, giving a uniform spectrum up to the neutron energy, while in the second the protons are collimated with respect to a neutron beam, giving a single peak. In the isotropic flux of a reactor only the first method is possible.

silicon surface barrier, and a collimator consisting of four spaced gold discs drilled with many holes could be interposed. The whole unit was in an evacuated tube. With the collimator in place the yield of protons from the radiator was reduced with respect to a background of protons due to adsorbed hydrogen and water on the surfaces exposed to the detector. It would be difficult to detect neutrons below 1 MeV in the presence of a flux at higher energies, due to this background. With the collimator removed good spectra for recoil protons were obtained (see fig. 15) over a range of energies down to 400 keV neutron energy, but below this energy the thickness of radiator which can be tolerated must be reduced. In both cases the pile-up of electron pulses due to the gamma-ray flux contributed to the spectrum in the region corresponding to protons below 200 keV. The background was

measured by reversing the radiator disc and recording the spectrum for the same neutron flux.

A simpler and more accurate arrangement is shown in fig. 16. Here two semicircular detectors are prepared by evaporation through a mask on to a single disc of silicon, and contacts are attached in the

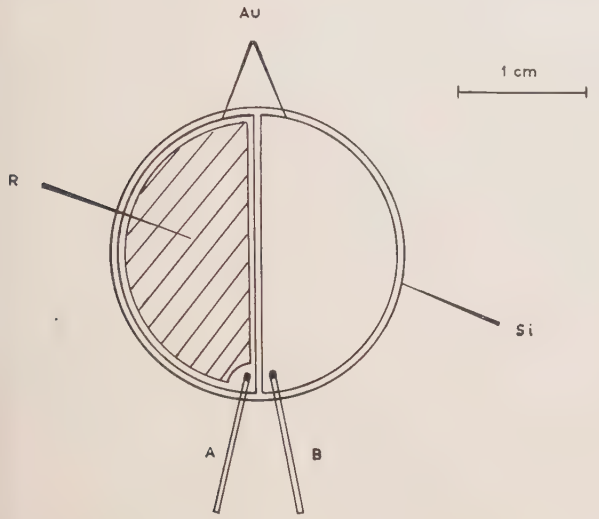

Fig. 16. Suggested form of proton-recoil detector for simultaneous measurement of neutron flux and background.

Si = silicon disc
Au = two semicircular gold-coated areas
R = hydrogenous radiator evaporated on gold layer.
A, B = leads to contacts.

usual way. It can be verified at this stage that both counters yield the same spectrum due to electron pulse pile-up and recoil protons from adjacent surfaces under a combined neutron and gamma-ray flux. Then the radiator of glyceryl tristearate is evaporated on to the gold layer of one semicircular counter. The difference in the spectra then obtained is due to recoil protons from the radiator.

The neutron spectrum is obtained from the proton recoil distribution by differentiation, and this places much greater demands upon the accuracy of the initial spectrum. Making allowances for this for typical spectra, Dr. Ferguson finds that the equivalent efficiency is still greater for the proton recoil detector than for those making use of the He^3 or Li^6 reactions. Further work is in progress, and it is hoped to publish the results of this study at a later date.

8.3. THIN dE/dx DETECTOR

It is possible to make a very thin transmission detector in which a particle loses in general only a small fraction of its energy. The most important application of this is in the discrimination between different types of particle of the same energy. This is performed with a thin counter followed by a deep barrier counter so giving simultaneous measurement of dE/dx and energy. Another possibility with thicker wafers is to build up a stack of counters in series so that linear response can be obtained up to energies no longer limited by the depth of a single depletion layer.

At A.E.R.E. slices 0.012 cm thick of 300 ohm cm silicon were etched and coated with gold on both faces. Contact to the gold was made by gold-silver strip cemented in the usual way with silver paste. Application of a sufficiently high bias voltage then produces a field extending throughout the whole volume. This condition was tested by irradiating with 5.5 MeV alphas first one side of the detector and then the other. The particle range in silicon is only 20% of the wafer thickness so that complete collection of the carriers produced proves the full penetration of the field. This was achieved at 30 volts bias. More recently thinner slices of 0.005 cm thickness were obtained of 2000 ohm cm resistivity, and in these complete collection is achieved at under 3 volts bias. These detectors all showed excessive leakage current and noise, however, and this may be due to the proximity of the back contact which is able to inject carriers into the field region. Studies are being made of a variety of contact methods in order to overcome this effect.

Mention must be made of the excellent results obtained with thin diffused junction counters by H. Wegner[39]) at Los Alamos and which have fully demonstrated the value of such detectors.

8.4. MULTIPLE DETECTOR

If gold is evaporated on to an etched silicon crystal through a comb of fine wires, it is possible to produce a multiple detector in a single process. Separate contacts are made at the ends of the strips in the usual way. Such detectors made at A.E.R.E. with a separation of only 0.1 mm have

[39]) H. E. Wegner, I.R.E. Trans. NS-8 (1961) 103.

been operated without interaction when used in the normal counting circuit. However, this is not usually possible with germanium, probably owing to surface conductance (see section 5) and it is preferable to construct the device from separate insulated bars[40,41]).

The problem arises of how to handle the output from such an arrangement. Parkinson[40]) has used separate transistor amplifiers for each detector, while Bilaniuk[41]) has successfully applied a method in which a delay line is formed by the capacitance of the detectors linked by inductances. The difference in time of the pulses arriving at the two ends of the line gives the location of the counter in which they originated.

Such a unit extended to at least 100 counters would supplement the use of nuclear emulsions in a broad-range magnetic spectrometer. The multi-track magnetic tape storage under development at A.E.R.E. could be adapted to record the counter location together with a digital pulse height indication.

[40]) W. C. Parkinson and M. O. Bilaniuk (to be published).

[41]) O. M. Bilaniuk, A. K. Hamann and B. B. Marsh, Univ. of Rochester Report No. AT (30-1)-875 (May, 1960).

Acknowledgements

The authors are indebted to Dr. L. D. Roberts of O.R.N.L. for helpful information in the initial stages, to Dr. A. A. Shepherd, Mr. R. Walker and Mr. W. Thorp of Ferranti Ltd., Mr. M. Possener of Semiconductors Ltd,. Drs. O. Simpson and D. C. Northrop of S.E.R.L., Baldock, and Mr. R. B. Owen, Dr. A. T. G. Ferguson, Dr. E. Melkonian, and Dr. T. E. Gooding of A.E.R.E. for their assistance and fruitful discussions during the course of the work. We are especially grateful to Mr. M. Nobes and Mr. M. F. Wilkins for their assistance in preparation and testing of detectors. This work was performed under tenure of U.K.A.E.A. Senior Research Fellowships.

NUCLEAR INSTRUMENTS AND METHODS 12 (1961) 227–248; NORTH-HOLLAND PUBLISHING CO.

METHODS FOR THE MEASUREMENT OF SUB-NANOSECOND LIFETIMES OF LOW-ENERGY NUCLEAR LEVELS

EKBAL BASHANDY†

Institute of Physics, University of Uppsala, Uppsala, Sweden

Received 24 April 1961

A review is given of the various methods available for the measurement of lifetimes of low-energy excited nuclear states. The review is limited to the nano- and sub-nanosecond region. Direct measurements by means of delayed coincidence technique, high frequency acceleration or deflection, direct timing, distance of flight, and recoil methods are discussed. In addition, certain related, indirect methods are considered. These are nuclear resonance scattering and absorption and Coulomb excitation. Finally, an evaluation of and comparison between the different methods is presented.

1. Introduction

During the last few years there has been a great deal of progress in the techniques and methods available for the measurement of nano†† - and sub-nanosecond lifetimes of excited nuclear energy levels. A direct measurement implies the determination of the half-life ($t_{\frac{1}{2}}$) or the mean lifetime (τ) of the nuclear state. From either of these, the partial transition rates, P_{EL} and P_{ML} for the electric transition of multipole order L (EL) and the magnetic transition of multipole order L (ML), respectively, are easily calculated. The appropriate relationships are

$$P_{EL} = \left[t_{\frac{1}{2}} \times 1.44\,(1 + \alpha_{tot})\left(1 + \frac{1}{\delta^2}\right) R\right]^{-1} \qquad (1)$$

$$P_{ML} = [t_{\frac{1}{2}} \times 1.44\,(1 + \alpha_{tot})\,(1 + \delta^2)\,R]^{-1}\,. \qquad (2)$$

In (1) and (2) $t_{\frac{1}{2}} = \ln 2\tau$ is the half-life of the nuclear state, R is related to the branching ratio and is here defined as the fraction of all transitions from the level with half-life $t_{\frac{1}{2}}$ which proceed through the transition under consideration. δ^2 is the mixing ratio defined as

$$\delta^2 = \frac{P_{EL}}{P_{ML}} \qquad (3)$$

and α_{tot} is the total internal conversion coefficient.

The partial transition rates, P_{EL} and P_{ML}, are the relevant nuclear parameters of interest for a comparison with theoretical predictions based in various nuclear models. It is obvious that the lifetime (or half-life) measurement may be completed only if the remaining factors in (1) and (2) are known. The R factor may be found from a careful study of the nuclear decay scheme. In the case of a transition from the first excited state to the ground state, R becomes, of course, equal to 1. It is generally sufficient to determine one of the two quantities, δ^2 or α_{tot}. Since α_{tot} may be calculated from δ^2 and vice-versa, by making use of the theoretical tables of internal conversion coefficients[1,2]). The theoretical calculations have been made only for the K, L and, with less accuracy, M shells. Empirical K/L and K/L + M + N relations may be used. The expression for α_{tot} becomes,

$$\alpha_{tot} = \frac{\delta^2\,\alpha_{tot}\,(EL) + \alpha_{tot}\,(ML)}{1 + \delta^2}\,. \qquad (4)$$

Since for the transitions of interest, in this connection, α_{tot} is generally a fairly small correction. The uncertainty in the calculated value for α_{tot} provides only a minor contribution to the errors. This is not necessarily the case, however. In very low energy transitions α_{tot} becomes large, which, of

† On leave from the Egyptian Atomic Energy Commission, Cairo-UAR.

†† nanosecond = millimicrosecond = 10^{-9} sec.

[1]) M. E. Rose, Internal conversion coefficients (North-Holland Publishing Company, 1958).

[2]) L. A. Sliv and I. M. Band, Coefficients of the Internal conversion of Gamma Radiation, Part I and II C (Academy of Sciences of the USSR, Moscow, Leningrad, 1956).

course, means that the conversion process is the dominating mode of de-excitation. In this case, large errors are introduced, unless α_{tot} is directly measured in a separate experiment.

It should also be observed that for certain much retarded M1 and E1 transitions, anomalies appear in the internal conversion process. These are due to the finite nuclear size and depend on the structure of the nucleus. Consequently, no reliable theoretical prediction of internal conversion coefficients can be made. The presence of these anomalies can, however, be unambiguously determined from a combination of conversion coefficient measurements and studies of gamma-gamma and electron-gamma directional correlations[3,4,5]).

The mixing ratio, δ^2, can be measured by directional or polarization measurements or from the conversion coefficient, K/L ratio, or L subshell ratios. Anomalies in the conversion process, if present, will hamper the determination of δ^2 by the methods involving internal conversion electrons.

The partial transition rate can also be obtained from indirect measurements of the nuclear lifetime. The nuclear resonance method provides an experimental determination of the cross-section for an electromagnetic excitation from the ground state to the level under consideration. This cross-section is closely related to the gamma transition rate.

$$\sigma = g \frac{\lambda^2}{8\pi} \frac{\Gamma^2}{(E - E_\gamma)^2 + \frac{1}{4}\Gamma^2} \tag{5}$$

and $\Gamma\tau = \hbar$,

where Γ is the width of the nuclear energy level, τ is the mean life time, E_γ is the energy of the level, E is the energy supplied by the incident gamma-ray, λ is the wavelength of the incident gamma-ray, and g is a statistical factor.

Finally, in Coulomb excitation, the interaction between the target nucleus and the projectile particles gives an excitation from the ground state to one of the excited energy levels. Further excitation, cascading upward to higher levels, is possible (multiple Coulomb-excitation) but requires heavy ions of higher energies[6]).

With only a very few exceptions, the Coulomb-excitations may be considered as a pure electric quadrupole (E2) excitation. From the measured cross-section, the reduced transition probability $B(\mathrm{E2})$ is calculated and from this the partial transition rate for the corresponding de-excitation process is easily derived.

$$\lambda_{\mathrm{E2}} = 1.16 \times 10^{13} (\Delta E_{\mathrm{MeV}})^5 \times (B\ \mathrm{E2}) \tag{6}$$

$B(\mathrm{E2})$ is expressed in units of 10^{-48} cm^4 e^2. Once P_{EL} and P_{ML} have been determined, a comparison with theory is possible. Theoretical expressions for electromagnetic transition rates have been published by Weisskopf[7]), Blatt and Weisskopf[8]), Moszkowski[9]), Bohr and Mottelson[10]) and others. A convenient expression is given by Mayer and Jensen[11])

$$P_{EL} = \frac{e^2}{\hbar} \frac{L+1}{L\,[(2L+1)!!]^2} \left(\frac{E}{\hbar c}\right)^{2L+1} R^{2L} (2J_f + 1) S \mid M_{EL} \mid^2 \tag{7}$$

$$P_{ML} = \frac{1}{\hbar} \frac{L+1}{L\,[(2L+1)!!]^2} \left(\frac{E}{\hbar c}\right)^{2L+1} \left(\frac{e\hbar}{Mc}\right)^2 R^{2L-2} (2J_f + 1) S \mid M_{ML} \mid^2 \tag{8}$$

In these formulae E is the transition energy, A is the nuclear mass-number, and $|M_{EL}|$ and $|M_{ML}|$ are the transition matrix elements. All nuclear structure dependent parameters are represented in these matrix elements which therefore can be predicted only from the basis of a specified model. Moszkowski considered the Mayer particle shell model and used a harmonic oscillator potential. From the wavefunctions determined we obtain:

[3]) T. R. Gerholm, B.-G. Pettersson, B. van Nooijen and Z. Grabowski, Nucl. Phys. **24** (1961) 177.

[4]) B.-G. Pettersson, T. R. Gerholm, Z. Grabowski and B. van Nooijen, Nucl. Phys. **24** (1961) 196.

[5]) Z. Grabowski, B.-G. Pettersson, T. R. Gerholm and J. E. Thun, Nucl. Phys. **24** (1961) 251.

[6]) F. K. McGowan and P. H. Stelson, Phys. Rev. **120** (1960) 1803.

[7]) V. F. Weisskopf, Phys. Rev. **83** (1951) 1073.

[8]) J. M. Blatt and V. F. Weisskopf Theoretical Nuclear Physics (Wiley, 1952) Ch. XII, sec. 6.

[9]) S. A. Moszkowski, in Beta and Gamma Ray spectroscopy, Editor Kai Siegbahn (North-Holland Publishing Company, 1955).

[10]) A. Bohr and B. R. Mottelson, Mat. Fys. Medd. Dan. Vid. Selsk. **27**, No. 16 (1953).

[11]) Maria Goeppert Mayer and J. Hans D. Jensen, Elementary Theory of Nuclear Shell Structure (1957) Ch. XII, sec.4.

$$P_{EL} = \frac{2(L+1)}{L\,[(2L+1)!!]^2}\frac{e^2}{\hbar}\left(\frac{w}{c}\right)^{2L+1} R^{2L}\, S(J_i, L, J)\,|\,M_{EL}\,|^2 \tag{9}$$

$$P_{ML} = \frac{2(L+1)}{L\,[(2L+1)!!]^2}\frac{e^2}{\hbar}\left(\frac{w}{c}\right)^{2L+1} R^{2L-2}\left(\frac{e\hbar}{Mc}\right)^2 S(J_i, L, J)\,|\,M_{ML}\,|^2 . \tag{10}$$

These expressions, though valid only in the extreme single particle model, have been accepted as "units" for experimentally measured transition rates. If P_{EL} (exp) and P_{ML} (exp) are found to be larger than the theoretical estimate, the transition is said to be enhanced. The enhancement factor is defined as:

$$F = \frac{P_{(exp)}}{P_{(theor)}} . \tag{11}$$

Likewise, if P_{EL} (exp) and P_{ML} (exp) are smaller than the theoretical values, the transitions are said to be retarded (or unfavoured). The retardation factor is given by:

$$R = \frac{P_{(theor)}}{P_{(exp)}} . \tag{12}$$

According to the systematics of short-lived, low energy levels, E1 transitions are frequently found, to be very much retarded; E2 transitions, on the contrary, are generally enhanced by one or two orders of magnitude. M1 transitions are very frequently retarded. The reason for these trends can, at least qualitatively, be understood in terms of the current nuclear models, but detailed explanations call for further refinement of the theories.

Determinations of short-lived nuclear lifetimes, therefore, contribute an important approach to the problem of nuclear structure; in many cases it is the most direct and unambiguous way to test the validity of the nuclear models.

It is evident from the experiments[12,13]) and from what is known about the systematics of transition rates that most low-energy levels are to be expected to have lifetimes in the nano and sub-nanosecond region except for the fairly infrequent transitions of higher multipolarity, M2, E3, M3, E4, M4, E5, etc, which de-excite longer-lived levels.

A survey of the present experimental methods, for these partial transition rates seems justified, especially since a great deal of progress has been made in the past few years.

2. Direct Measurements of Sub-Nanosecond Lifetimes

2.1. THE DELAYED COINCIDENCE METHOD

Experimental techniques

The delayed coincidence method can be used to measure half-lives between 10^{-4} and 10^{-10} sec. The ultimate limitation in the time resolution is due to the response time of the scintillation detector. Photomultiplier tubes have been introduced with

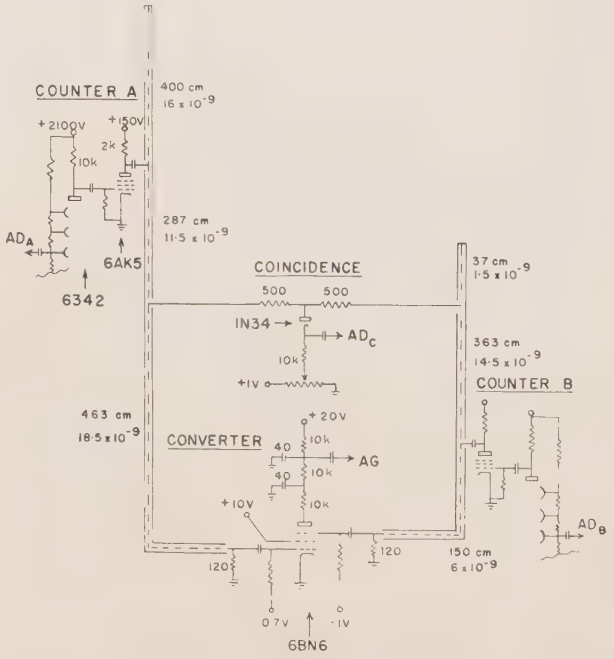

Fig. 1. Diagram of the part of the circuit handling the fast pulses. The two photomultipliers are shown only in part. The fast coincidence circuit appears at the center of the diagram, and the 6BN6 converter at the bottom. [From R. E. Green and R. E. Bell, Nucl. Instr. and Meth. **3** (1958) 127.]

excellent light collection properties, high gain, and reduced transit time spread. These tubes permit the use of shorter resolving times. With present day techniques the best resolving time is about 10^{-9} sec. A simple coincidence circuit has been designed by Bell, Graham and Petch[14]).

Very recently a new technique has been developed

[12]) J. Lindskog, E. Bashandy and T. R. Gerholm, Nucl. Phys. **16** (1960) 175.

[13]) D. G. Alkhazor, Esptl. i Theoret. Fiz. **35** (1958) 1058.

[14]) R. E. Bell, R. L. Graham and H. E. Petch, Can. J. Phys. **30** (1952) 35.

by Sunyar[15]), which appears to be a significant advance in the determination of very short half-lives. In this method a time-to-pulse height converter is connected to a multichannel analyzer. The time-to-pulse height converter consists of a coincidence circuit which gives an output pulses with an amplitude, which is a function of the time difference between the two input pulses within the operating range. Fig. 1 shows an arrangement for the time-to-pulse height converter built by Green and Bell[16]). The supervisory coincidence circuit is a simple diode arrangement like that of Bell,

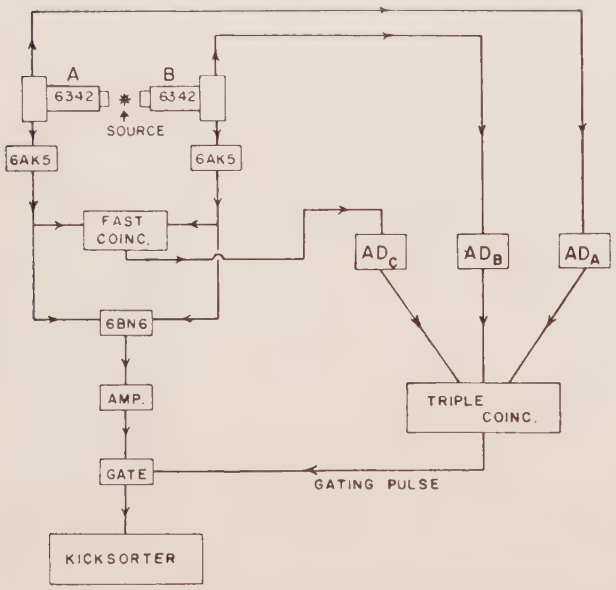

Fig. 2.
Simplified block diagram of the whole time-to-amplitude assembly. It consists of a conventional fast-slow coincidence apparatus plus the units 6BN6, Amp, Gate, kicksorter. [From R. E. Green and R. E. Bell, Nucl. Instr. and Meth. 3 (1958) 127.]

Graham and Petch[14]), with the addition of 500 ohm isolating resistors to reduce reflections on the two transmission lines and cross coupling between them. The output of the coincidence diode is taken to an amplifier and discriminator ADC. The two photomultipliers, A and B, also have slow outputs from their eighth dynodes to amplifiers and discriminators AD_A and AD_B. The outputs from these units are used for pulse height selection by the fast-slow system. At the 6BN6 time-to-amplitude converter the overlapping input pulses are integrated in the anode circuit. The output of the converter circuit is taken to an amplifier and gate circuit AG which feed to a multichannel analyzer or kicksorter. The channel width, in this case, determines the resolving time. Fig. 2 is a block diagram of the whole apparatus showing the connection between the various units used for lifetime measurements by Green and Bell[16]). The time scale of the kicksorter can be calibrated in several ways. One may place a source of prompt coincidences between the counters, and observe the displacement of the prompt coincidence peak along the scale as the cable between the common terminal and the coincidence unit is varied by known amounts. Another scheme is to measure the pulse height distribution for a prompt source, (gamma-gamma coincidences) after moving one of the detectors to different distances from the source. The shift in pulse height will then be governed by the change in distance between the source and the detector and by the velocity of light. By Sunyar's method the limit of the half-life is reduced by a factor ≈ 5 below the capability of the ordinary delayed coincidence technique. This improvement is due partly to the increase in the stability. The circuit can be left undisturbed and only the sources need to be interchanged. It should also be observed that with the use of the multichannel analyzer all of the delayed coincidence events are recorded during a given counting period. This greatly reduces the time necessary to find the true distribution of the delayed coincidences as compared to ordinary delayed coincidence technique, where one delay point is measured at a time. Consequently, one may obtain a substantially improved statistical accuracy. The time-to-pulse height converter has also been used[17]) with an electron-electron spectrometers (see fig. 3) for measuring short lifetimes of the excited nuclear states.

It should be noted that the delayed coincidence technique can also be applied to very low transition energies if the conversion electrons are accelerated so that their kinetic energy is increased. Such method has been used for measuring the lifetime of

[15]) Private communication from A. W. Sunyar quoted by D. E. Alburger: D. E. Alburger, Handbuch der Physik, Band 42 (Springer, 1957) p. 31.

[16]) R. E. Green and R. E. Bell. Nucl. Instr. 3 (1958) 127.

[17]) T. R. Gerholm *et al.*, to be published.

8.42 keV level in Tm^{169} (ref.[18])). A large negative voltage was applied to the source while the detectors were kept at ground potential, fig. 4. The space between the source and the electron detector was evacuated, and the gap between the gamma detecting crystal and the source was filled with oil in order to prevent sparking at the small distance

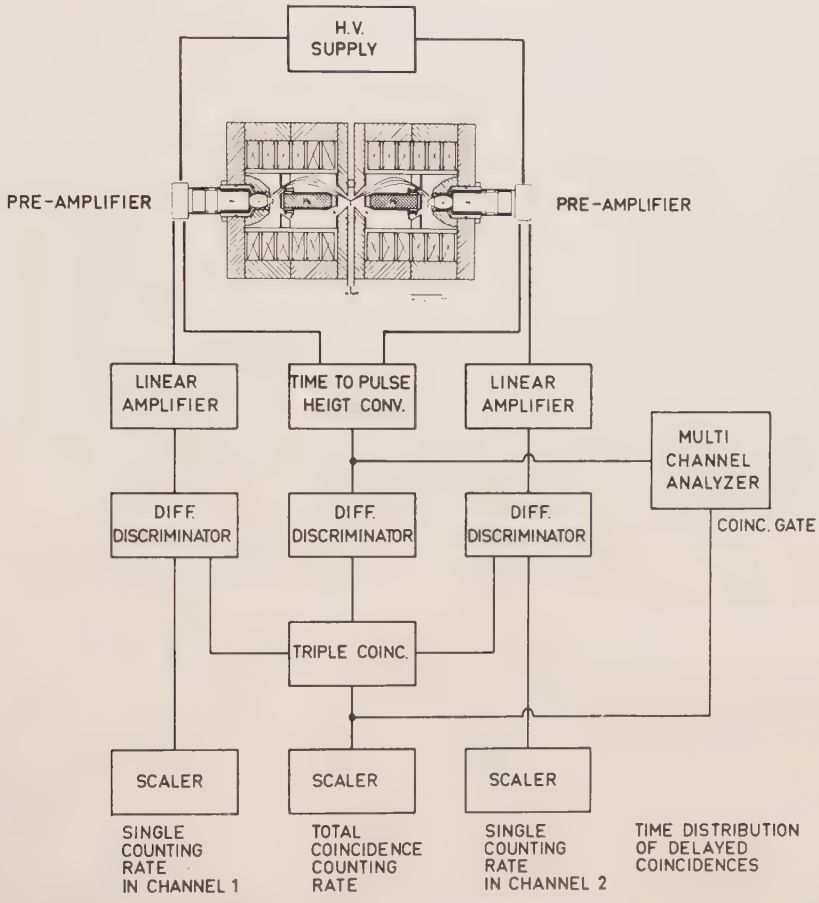

Fig. 3. Block diagram of apparatus for measuring short lifetime using an electron-electron coincidence spectrometer with time-to-pulse-height-converter. [From T. R. Gerholm *et al.*, to be published.]

used. The half-life of 8.42 keV state was determined from the slope of the delayed coincidence curves taking between 308 keV gamma rays and the accelerated M and N conversion electrons of the 8.42 keV level. The accelerating voltage was about 30 keV.

Evaluation of data

Short lifetime measurements using the coincidence technique consist of measuring the time distribution between the pulse signals corresponding to the pair of successive radiations x, y. The coincidence circuit responds whenever the two pulses are separated in time by less than a fixed interval T, the resolving time. The pulse in either detector may be artificially delayed (for example by passage through a specified length of cable with known transmission properties) and the coincidence rate n_c studied as a function of z, the delay introduced. Even if x and y are simultaneous, the coincidence rate will not vanish when $z > T$ on account of the random fluctuations in time between the radiations and the pulses they produce. The curve showing the variation of coincidence rate n_c with z, which is referred to as the "prompt" coincidence curve, has a general shape as in fig. 5. When there is a finite

[18]) H. Beckhuis and H. de Waard, Physica **24** (1958) 767.

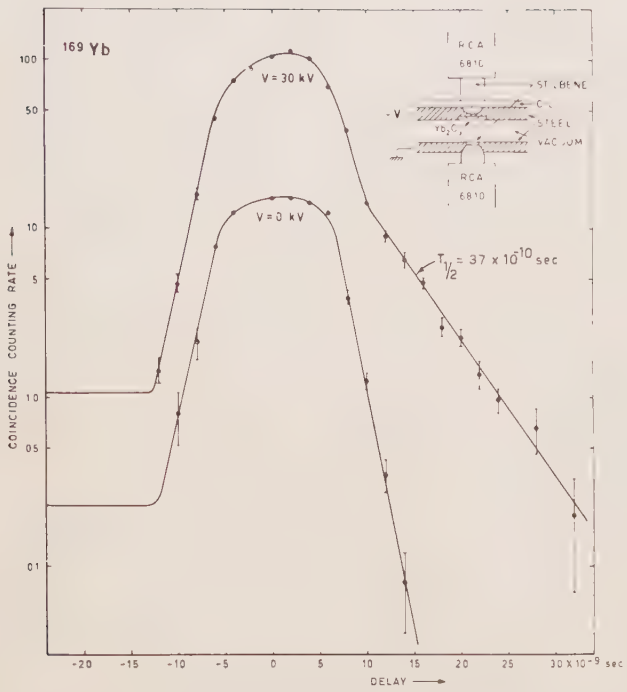

Fig. 4. A delayed coincidence curve from the first excited state in Tm^{169}, and an arrangement used for accelerating the M and N conversion electrons of the 8.42 keV level. [From H. Beekhuis and H. de Waard, Physica **24** (1958) 767.]

average delay in the emission of radiation y after x, characterized by the nuclear decay constant λ, the coincidence curve will show an assymmetry with more coincidence for $z > 0$ [pulse from x delayed] than for $z < 0$. $z = 0$ is identified with the centre of the "prompt" coincidence curve as indicated in fig. 5. There are several ways in which the value of λ can be deduced from two such curves[19]); but the two generally used are:

(a) From the slope of $\log c(t_0)$ versus t_0, where $c(t_0)$ is the coincidence counting rate; t_0 is the time delay

(b) From the displacement of the centroid of the delayed curve from that of the prompt curve.

For lifetimes much larger than the width of the prompt coincidence curve, this first relationship is normally used, as illustrated in fig. 5. Lifetimes shorter than the resolving time can be determined from a careful measurement of the distance between the centroid positions of the delayed coincidence curve for the cascade under investigation and the centroid of the comparison delayed coincidence curve. This comparison curve should be obtained under identical conditions, and the lifetimes should be known or known to be negligibly short (prompt curve). It may be shown[20]) that the difference between the time co-ordinate of the centroid positions correspond to the difference in mean lifetime of the two nuclear levels involved, i.e.

$$C - C_0 = \tau - \tau_0 \qquad (13)$$

where C is the time co-ordinate of the delayed coincidence resolving curve under investigation, and C_0 is that of the comparison curve; τ is the mean lifetime of the intermediate level and τ_0 is the known (or negligibly short) comparison lifetime. In practice, however, it is difficult to find a suitable comparison curve corresponding to the same transition energies. The so-called "self-comparison method"[14]) presents a possibility of circumventing these difficulties. The self-comparison method implies that the delayed coincidence curve is compared with its

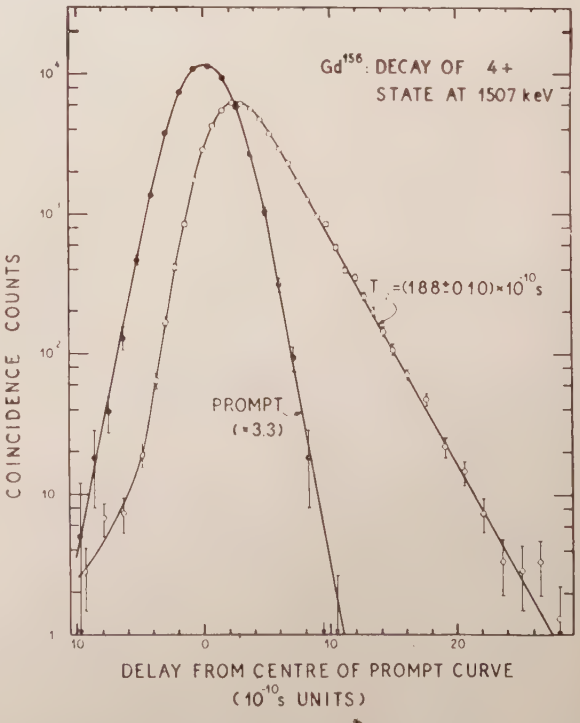

Fig. 5. A delayed resolution curve with an approximate prompt curve for comparison. [From R. E. Bell and M. H. Jørgensen, Nucl. Phys. **12** (1959) 413.]

[19]) T. D. Newton, Phys. Rev. **78** (1950) 490.
[20]) Z. Bay, Phys. Rev. **77** (1950) 419.

own "inverse". The latter is obtained by interchanging the order of the two detectors, such that if in the first measurement detector 1 responds to transition A and detector 2 responds to transition B, the inverse curve will correspond to transition B recorded in detector 1 and transition A in detector

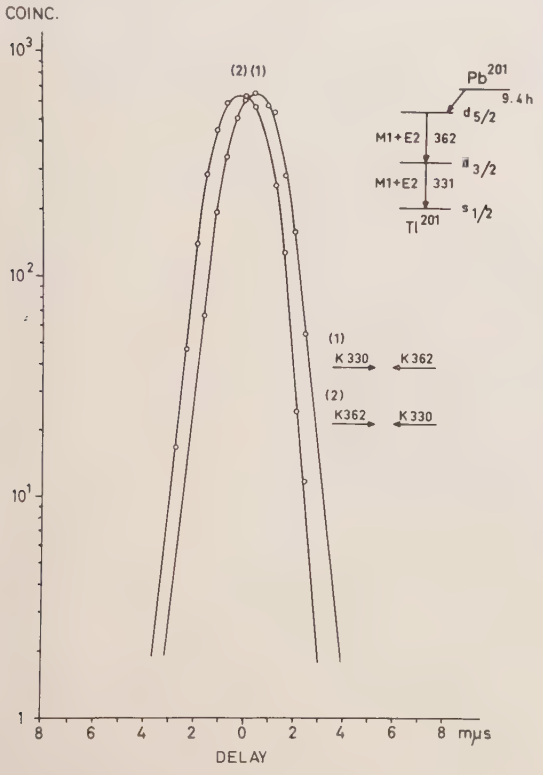

Fig. 6. Self-comparison plot for the 330 keV and the 362 keV transitions in Tl^{201}. [From J. Lindskog, E. Bashandy and T. R. Gerholm, Nucl. Phys. **16** (1960) 175.]

2. The curves in fig. 6, which are typical of measurements of the fast transitions, show that the coincidence resolving time achieved is of the order of a few millimicroseconds, and that lifetimes one or two orders of magnitude shorter can nevertheless be measured. In the general case, the position of the centroid is influenced by factors other than the lifetime of the intermediate level. Unless these contributions to the centroid shift are not properly taken into account, systematical errors will appear. These may easily be of the same order of magnitude as the nuclear lifetime to be measured[21]). The successive physical processes contributing to the centroid positions are:

1. The transit time for the passage of radiation from the source to the surface of the detector. This time interval may be quite large in some geometrical arrangements. For gamma-rays this transit time is of course a constant, built in delay which has not to be considered as long as the source to detector distance is kept constant. But for conversion electrons and beta-rays the time of flight varies with the energy of the electron. The transit time of the electron through a distance L, e.g. the length of the trajecting in a magnetic spectrometer can be written as[21]).

$$t_L(E) = \frac{L}{v} = \frac{L}{c}\frac{E_0 + E}{\sqrt{E^2 + 2E_0E}} \quad . \tag{14}$$

v and E are the velocity and energy of the electron, respectively, and c is the velocity of light. Thus the difference in transit time associated with a small energy change ΔE becomes

$$t_L(E + \Delta E) - t_L(E) = -\Delta E\frac{L}{c}\frac{E_0^2}{(E^2 + 2E_0E)^{\frac{3}{2}}} + \\ + \frac{\Delta E^2}{2}\frac{3E_0^2}{(E^2 + 2EE_0)^2}t_L(E) \, . \tag{15}$$

The first term in the right-hand side of the equation can be eliminated by means of an interpolation or extrapolation procedure. However, it is sometimes necessary to take even the second order term into consideration in the case of short lifetimes. The second order requires knowledge of the electron trajectory length which can be measured directly by the time of flight method.

2. The influence of the magnetic field on the transit time of the photoelectrons through the photomultiplier tube should be considered if it exists. Careful shielding of the photomultipliers eliminates these effects.

3. The time lag between the absorption of the radiation or conversion electrons in the crystal and the appearance of the first photoelectron.

Post and Schiff[22]) have derived an expression for the time elapsed between the excitation of the scintillator and the appearance of the first photoelectron. Their calculation is based on the assumption that the scintillation light flash can be expressed by a simple exponential decay.

[21]) E. Bashandy, Nucl. Instr. and Meth. **6** (1960) 289.
[22]) R. F. Post and L. I. Schiff, Phys. Rev. **80** (1950) 1113.

$$R_t = R(1 - e^{-\lambda t}) , \qquad (16)$$

where R is the total number of photoelectrons produced during the pulse, and λ is the decay constant of the scintillator. The difference in response time for the energies $E + \Delta E$ and E is given by[21,12]),

$$t'(E + \Delta E) - t'(E) = \frac{\Delta E}{E}\frac{k}{E} + \left(\frac{\Delta E}{E}\right)^2 \frac{k}{E} \qquad (17)$$

k is constant and equal to

$$k = \frac{EQ}{R\lambda} , \qquad (18)$$

where Q is the number of photoelectrons necessary to trigger the coincidence circuit. This can be calculated or determined experimentally[21]). If the time-to-pulse height converter method is used, the simple derivation given here is no longer correct since in this case the total (or a fractional) amount of the photoelectrons produced during the light flash all contribute to the determination of the time. Gatti and Svelto[23]) have given a careful analysis of this problem and derive expressions for the most suitable choice of instrumental parameters.

It is evident, however, that the factors discussed above will introduce energy dependent instrumental time delays, which will lead to systematic errors if not properly taken into account. One can also eliminate these effects by either of two methods which have been developed:

(a) Interpolation or extrapolation method

This method can be applied when the experiments are performed with an electron-electron coincidence spectrometers. In this case, the K and L conversion lines of the same transition may be used to determine the influence of a minor energy difference between the two cascading transitions. Consider for instance a beta-conversion electron experiment The unknown lifetime is measured against a known lifetime (or a lifetime known to be negligibly short). The comparison experiment involves the energies E_c and E. The unknown value is measured with a fraction of the beta-spectrum focused corresponding to the same energy E_c. The energy of the conversion line in the opposite channel, however, is not exactly equal to E, but E_1 for the K conversion line and E_2 for the L conversion line. If the expressions above are applied, it may easily be seen that[21,12])

$$\tau_1 - \tau_2 = \frac{(C_1' - C_2)\,\Delta E_2 - (C_1'' - C_2)\,\Delta E_1}{\Delta E_2 - \Delta E_1} +$$

$$+ 2\Delta E_1 \cdot E_2 \left[\frac{3E_0}{2(E^2 + 2E_0E)^2} t_c + \frac{K}{E^3}\right] , \qquad (19)$$

where

Same source $\begin{cases} E_{const} - E_1 & \text{centroid position } C'_1 \\ E_{const} - E_2 & \text{centroid position } C'_1. \end{cases}$

Comparison source $E_{const} - E$ centroid position C_2.

In the case of the self-comparison measurements, $\tau_2 = \tau_1$.

It is generally assumed that the position of the centroid of a curve can be determined to within $\frac{1}{10}$ of the full width at half maximum. The self comparison method has the obvious advantage of doubling the shift and therefore increasing the accuracy and reducing the ultimate limitations. Thus it allows the determination of lifetimes down to about $\frac{1}{20}$ of the half width[12]).

(b) The third moment method

Weaver and Bell[24]) have proposed a method to calculate the lifetime of the nuclear excited levels from the shape of the delayed curve with only rough knowledge of the shape of the prompt curve. The relative positions of the centroids of the two curves do not enter the analysis. It was found that

$$\tau = \left[\frac{N_3(F) - \varepsilon}{2}\right]^{\frac{1}{3}} , \qquad (20)$$

where $N_3(F)$ is the third moment of the delayed curve about its center. ε is the third moment of the prompt curve about its center.

ε is usually small and frequently negligible, so that for many cases it is sufficient to write

$$\tau = \left[\frac{N_3(F)}{2}\right]^{\frac{1}{3}} . \qquad (21)$$

Even if ε is as large as $\frac{1}{3}$ of $N_3(F)$, the error in τ caused by ignoring it altogether is only about 10%[24]).

[23]) E. Gatti and V. Svelto, Nucl. Instr. and Meth. **4** (1959) 189.

[24]) R. S. Weaver and R. E. Bell, Nucl. Instr. and Meth. **9** (1960) 149.

The chief advantage of this method is that the above-mentioned instrumental errors are avoided. From the point of view of statistical accuracy, however, the third moment method is inferior to the centroid shift method since a relatively heavier weight is given to the flanges of the curve, where the third moments are large but the statistical accuracy reduced.

Very recently[25]) a new technique to reduce the systematic errors was introduced for which the prompt comparison method is used. This technique requires the radioactive source to exhibit the delay coincidence event to be measured and a prompt coincidence event to be used for comparison. Two isotopes can also be mixed to form a single source if the above condition is not available in the isotope of interest. The prompt and delayed coincidence events are observed simultaneously by two fast scintillation detectors connected to a time to amplitude converter. In order to distinguish between the delayed and the prompt event, a third radiation must be emitted in coincidence with the two radiations which are observed by the fast scintillation detectors. Hence a third detector is used, operating in coincidence with one of the two fast detectors to recognize the events. A complete distinction can be made when both the prompt and delayed events exhibit a triple coincidence. By this technique the systematical errors are greatly reduced since the prompt and delayed time distribution can be recorded at the same time by a multichannel analyzer.

To summarize: The delayed coincidence technique is the most general and accurate method at present available for the measurement of short nuclear lifetimes. It has a wide range of application which covers most of the region of interest in this connection. It can be applied to stable as well as unstable isotopes and be extended towards very low transition energies. If magnetic momentum resolution is used, the lifetimes of specified higher excited states can be measured in the presence of intense transitions to other levels in the decay. Systematical errors can be reduced or eliminated.

The main limitations are due to the necessity of having a coincidence cascade of sufficient intensity passing through the level of interest. The coincidence measurements are also fairly time consuming which means that the lifetime of the mother isotopes must not be too short. The time-to-pulse height converter and multichannel analyzer method has substantially increased the range of application in this respect.

A disadvantage is that the timing action takes place after the detection process. This imposes as discussed above certain ultimate limitations. It seems unlikely, therefore, that lifetimes below 10^{-11} sec can be measured by delayed coincidence technique with present scintillations and photomultiplier tubes.

2.2. DIRECT TIMING METHODS

The principle of direct timing can be applied to coincidence measurements[26,27]), in which case each of two successive radiations, both detected as conversion electrons, are subject to energy modulation in the same field, or in separate fields which are phase locked. Coincidences between the two energy-modulated radiations, after spectrometric analysis, will clearly depend on the energy settings of the spectrometers. This energy dependence of the coincidence rate is in turn related to the distribution of the time intervals between the emission of the radiations. The most suitable application is clearly for low-energy transitions with high internal conversion coefficients. The ultimate time resolution depends on such factors as available intensity and other source characteristics, the frequency and amplitude of applied field, and spectrometer transmission and resolution.

(*a*) *Acceleration method*

The microwave method for measuring short lifetimes of nuclear levels was developed recently by Blaugrund[28,29,30]). In this method a time scale is

[25]) P. C. Simms, N. Benczer Koller and C. S. Wu, Phys. Rev. **121** (1961) 1169.

[26]) S. Devons, (Private Communication quoted by A. E. Blaugrund, ref.[30]).).

[27]) T. R. Gerholm, Arkiv för Fysik **11** (1956) 255.

[28]) A. E. Blaugrund, Proc. Rehovoth Conference on Nuclear Structure, ed. H. J. Lipkin (North-Holland Publ. Co., 1958) p. 542.

[29]) A. E. Blaugrund, Phys. Rev. Letters **3** (1959) 226.

[30]) A. E. Blaugrund, Thesis (1960) (Nuclear Physics Department of the Weizmann Institute of Science, Rehovoth, Israel).

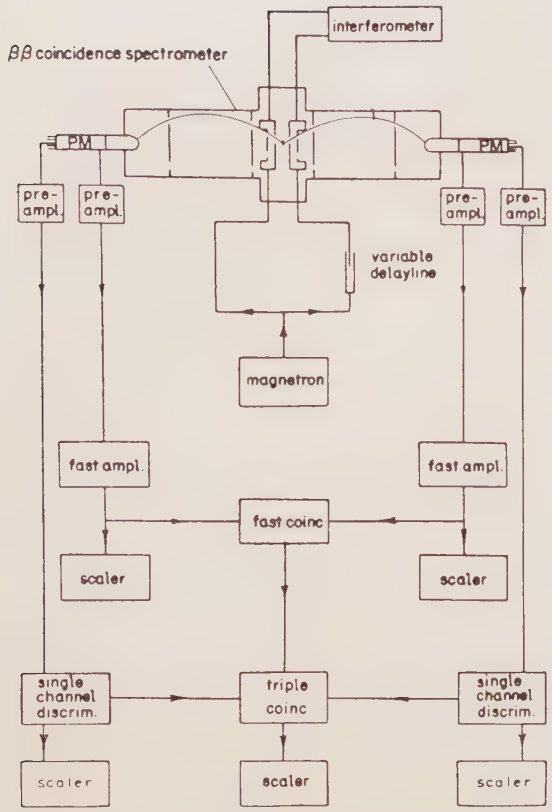

Fig. 7. Schematic diagram of the apparatus used for measuring short lifetime by the microwave method. [From A. E. Blaugrund, Phys. Rev. Lett. 3, No. 5 (1959) 226.]

established by interaction of charged particles with high frequency electric field. In the experiments a thin source is placed between two beta-ray spectrometers, fig. 7. Two conversion lines emitted in cascade are focused by the two spectrometers. An electronic coincidence circuit selects pairs of conversion electrons emitted in a cascade transition. Before entering the spectrometer proper, the electrons undergo an energy modulation. This modulation is brought about by electric fields present in two microwave resonant cavities fed from one oscillator. For both conversion lines the modulation amplitudes are larger than the line width. Thus, each combination of modulator and spectrometer works as a shutter transmitting electrons only during short time intervals when the electric field in the cavity is close to zero. The opening times of the two "shutters" can be shifted with respect to each other by changing the phase difference between the two cavities. By recording the number of coincidences as a function of the phase shift between the two modulating fields, the lifetime of the level involved in the cascade transitions can be determined according to,

$$C_{\tau T}(\phi) = \frac{c}{p}\int_0^{\infty} F(\phi - x)\exp\left(-\frac{x}{p}\right)\mathrm{d}x \qquad (22)$$

where,

C is the number of the true coincidences counted per unit time;

$P = 2\pi\tau/T$;

T is the modulation period;

τ is the mean lifetime of the intermediate level;

ϕ is the phase shift.

It can also be seen that,

$$\mathrm{Lim}_{p\to 0}\, C_{\tau T}(\phi) = C_{0T}(\phi) = C_{\tau\infty}(\phi) = CF(\phi)\,, \qquad (23)$$

i.e. for τ approaching zero, the delayed curve should indeed assume the form of the prompt curve. The prompt curve can be determined by choosing the modulating frequency such that $\tau \ll T$. Once the prompt curve is known, exponential decay function with different values of the lifetime τ are folded

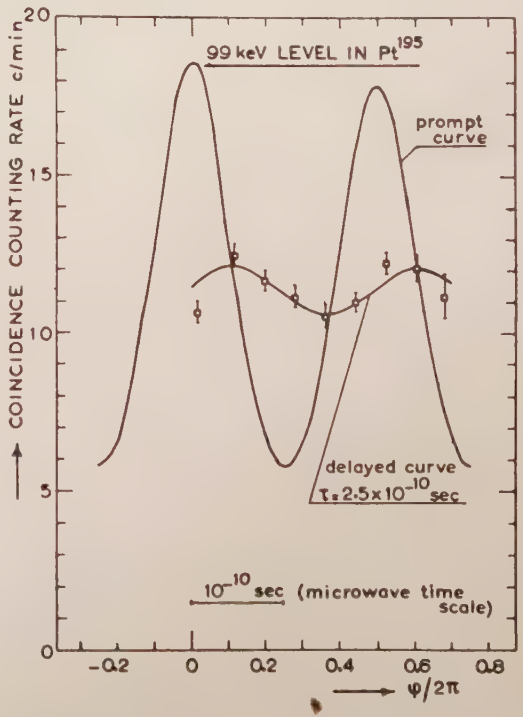

Fig. 8. Prompt and delayed curve for the 99 keV level in Pt^{195}. [From A. E. Blaugrund, Thesis, 1960.]

into it. Using equation (22) for each value of the parameter τ, a possible delay curve is obtained. The computed delayed curve is compared with experimental points, and the most probable value of the lifetime can be determined by means of the least squares method. A prompt and delayed curve for the case of 99 keV level in Pt^{195} measured by Blaugrund[31]) is shown in fig. 8. The microwave method is suited to lifetime measurements in the region of 10^{-11}–10^{-9} sec. It was found[31]) that the frequency of modulation should be chosen so that $T \approx 5\tau$ or, for the region 10^{-11}–10^{-9} sec, $T \approx 5 \times 10^{-10}$ sec (2000 Mc/sec). Since this method required a considerable time to measure the lifetime, the half-life of the source ought to be sufficiently long. A source half-life of one day can be regarded as a lower limit[31]). Moreover the two transitions in cascade must both be of low energy. These requirements limit the number of levels the lifetime of which can be measured. To overcome these limitations, the microwave method is widened by exciting nuclear levels by means of accelerated charged particles[31]).

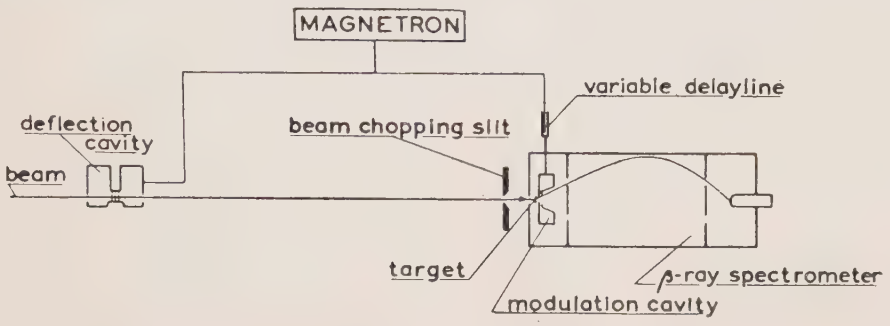

Fig. 9. Schematic diagram of the experimental arrangement employing a beam of accelerated charged particles. [From A. E. Blaugrund, Thesis, 1960, Nuclear Physics Department of the Weizmann Institute of Science in Rehovoth, Israel.]

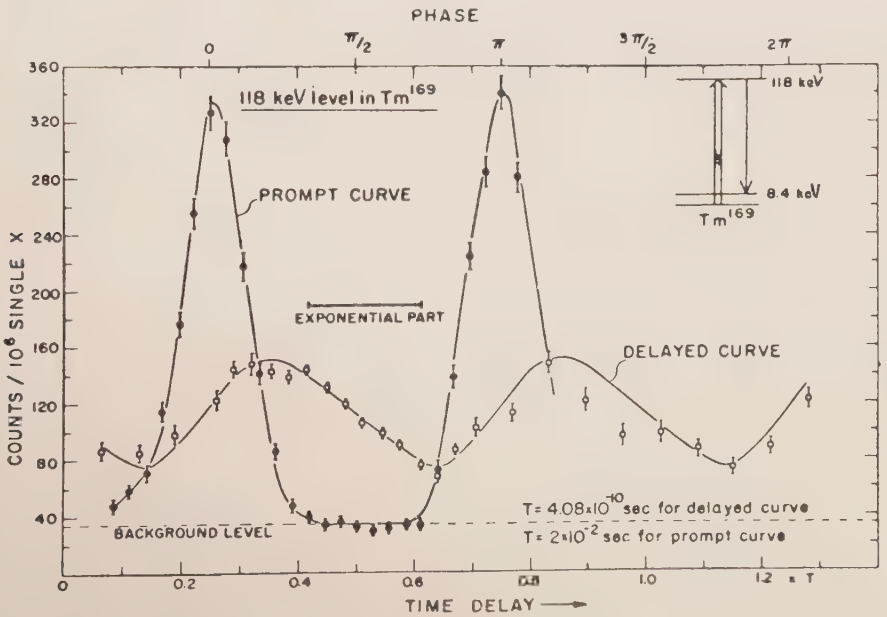

Fig. 10. Prompt and delayed curve for the 118 keV level in Tm^{169} [From, A. E. Blaugrund, Phys. Rev. Lett. 3, No. 5 (1954) 226.]

In the experiment, fig. 9, a beam of charged particles from the accelerator is swept over a chopping slit by a transverse electric field excited in a microwave cavity. Thus, the target nuclei are excited by short bursts of particles and decay by

[31]) G. Goldring, Nucl. Instr. and Meth. 11 (1961) 29.

emission of conversion electrons. These electrons are time analysed by a combination of an energy modulating microwave cavity and a beta-ray spectrometer. The energy modulating cavity and the deflection cavity are fed from one oscillator. The lifetime of the excited state can be determined from a measurement of the number of conversion electrons as a function of phase shift between the two microwave cavities:

$$S_{\tau T}(\phi) = \frac{1}{p}\int_{-\infty}^{\phi} S_{0T}(\phi')\exp\left(-\frac{\phi - \phi'}{p}\right)\mathrm{d}\phi' \qquad (24)$$

where

$S_{\tau T}(\phi)$ is the delayed curve with both cavities energized.

$$p = 2\pi\tau/T\,.$$

(b) The deflection method

This method differs from the acceleration method discussed in the preceding paragraph only in so far as the high frequency modulating field is applied perpendicularly to a beam of conversion electrons. Thus, instead of obtaining an energy shift relative to the time delay between the two coincidence conversion electrons, one will observe a displacement. Energy selection takes place by means of magnetic spectrometers. Two arrangements are possible: deflection before energy analysis or after.

Recently, Johansson *et al.*[32]) used the high frequency deflection method to measure short half-lives of the order of 10^{-10} sec. In the measurement the source (S) is placed between two magnet spectrometers, fig. 11A. The source emits two conver-

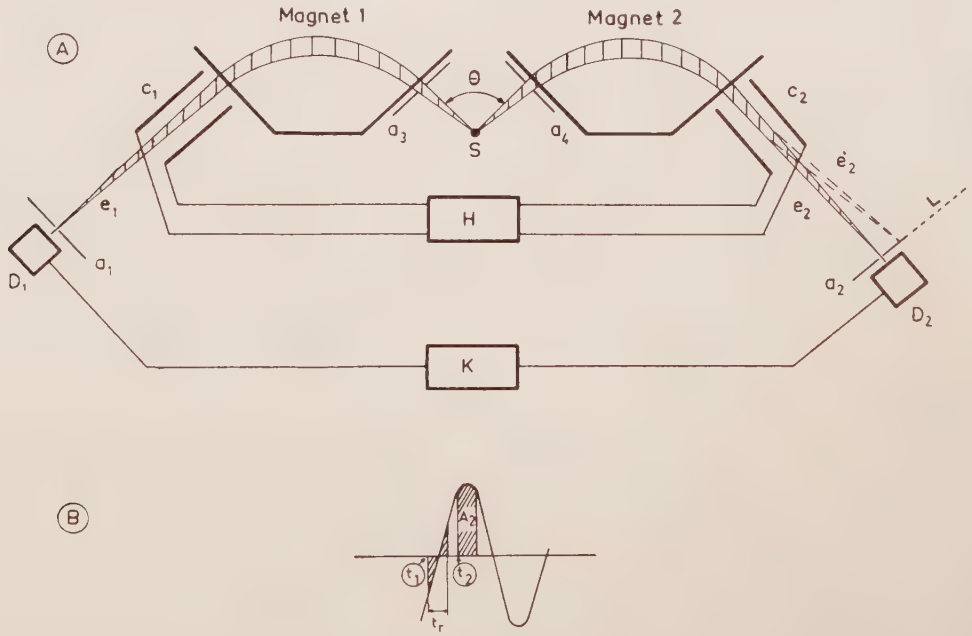

Fig. 11.

A. Simplified diagram of the principle of the high-frequency deflection method for measuring short half-lives. The symbols used have the following meanings:

$a_{1,2,3,4}$ = Apertures
$c_{1,2}$ = Deflection condensers
$D_{1,2}$ = Detectors
$e_{1,2}$ = Electron trajectories
H = high frequency source
k = coincidence unit
s = Radioactive source

B. Time-positions for the electrons in the deflection moment. t_r = Transit time for the electrons through the deflection condensers. [From B. Johansson and T. Alväger, Arkiv för Fysik **17**, No. 10 (1960) 164.]

Fig. 10 shows the delayed curve $S_{\tau T}(\phi)$ obtained with microwave modulation and the prompt curve $S_{\tau\infty}(\phi)$ measured with a modulation frequency of 50 c/sec. The half-life is determined from the exponential part shown in the figure.

sion electrons in cascade. Magnet I is set to focus the first conversion electrons while magnet II is adjusted to accept the second one. D_1 and D_2 are

[32]) B. Johansson and T. Alväger, Arkiv för Fys. **17**, no. 16 (1960) 163.

the two detectors. The coincidence unit, k, registers coincident electron pairs when the plane parallel condensers, C_1 and C_2 are connected to a high frequency source, the spectrometer lines are swept backwards and forwards over the apertures a_1 and a_2, respectively. If the electron e_1 passes through the condenser c_1 at the time b_1 (fig. 11B), it will undergo no deflection. If e_2 is an electron in prompt coincidence with e_1, it will also pass through without deflection, provided that the phase-differences in transit times for the two electrons through the magnets. If $e_2(e_2')$ had been emitted at a short time after e_1, then it would have received a deflection proportional to the shaded area A_2 indicated in fig. 11B. Thus, for emission time difference exceeding a certain value, the electron e_2 will fall outside the aperture a_2. By measuring the number of coincidences as a function of position of the aperture a_2 along the line L, a time resolution curve will be obtained. Fig. 12A shows a typical experimental time-resolution curve measured with Bi^{206} source[32]). The time-resolution curve has two peaks, the distance between which depends on the phase difference between the high frequency voltages on the deflection condensers. The two peaks are due to the fact that the electrons can be deflected in two directions depending on the polarity of the high frequency voltage in the deflection moment. Fig. 12B shows the two possibilities indicated by $a_1 - a_2$ and $b_1 - b_2$. The two peaks are completely separated, and two asymmetric curves are obtained. The slope of one side of these curves will then be a measure of the half-life of the level in question, provided that a clear asymmetry appears. In this method, the variation of the position of the aperture can be compared with variation of the time delay in the conventional delayed coincidence technique. Thus the curves obtained can be treated in a similar fashion.

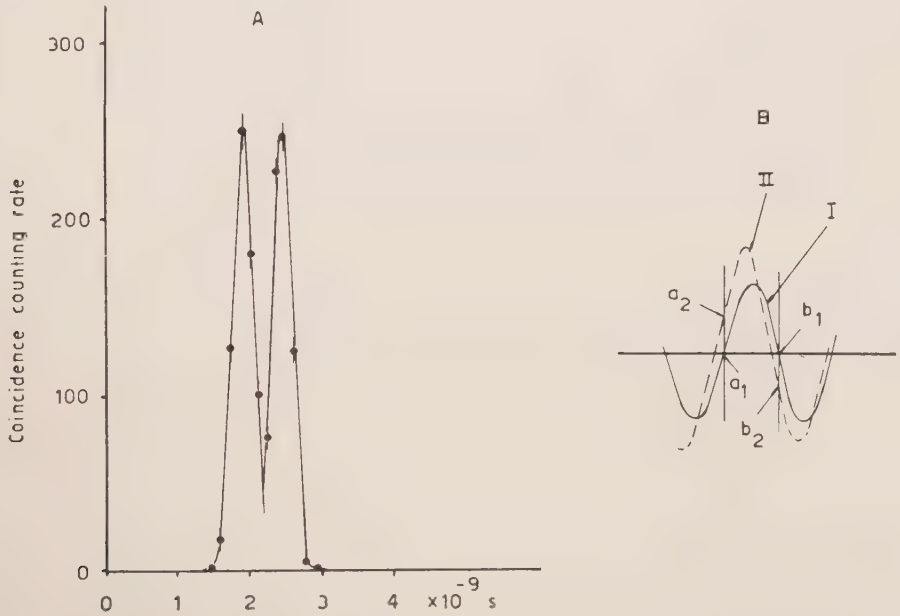

Fig. 12.
A. Time resolution curve for a Bi^{206} source, obtained by varying the D.C. voltage on one of the deflection condensers. The K-conversion electrons from the cascade 398 keV–184 keV were focused by the magnets.
B. The phase-positions of the voltages on the two deflection condensers. The two possibilities for the positions of the two coincidence curves are indicated by $a_1 - a_2$ and $b_1 - b_2$, respectively. [From B. Johansson and T. Alväger, Arkiv för Fysik **17**, No. 10 (1960) 165.]

To summarize The direct timing methods have only recently been introduced and so far only fairly few experimental results, have been reported. The technique is still in the development stage, and it is yet too early to say how these methods, when fully developed, will compare with each other and with the delayed coincidence method. For the accelerator and deflection methods certain inherent

limitations appear to be unavoidable. The coincidence counting efficiency is low, and the measurements are time consuming. Under favourable circumstances it seems likely that lifetimes below 10^{-11} sec should eventually become measurable but above this limit the methods offer no advantages when compared to the delayed coincidence technique.

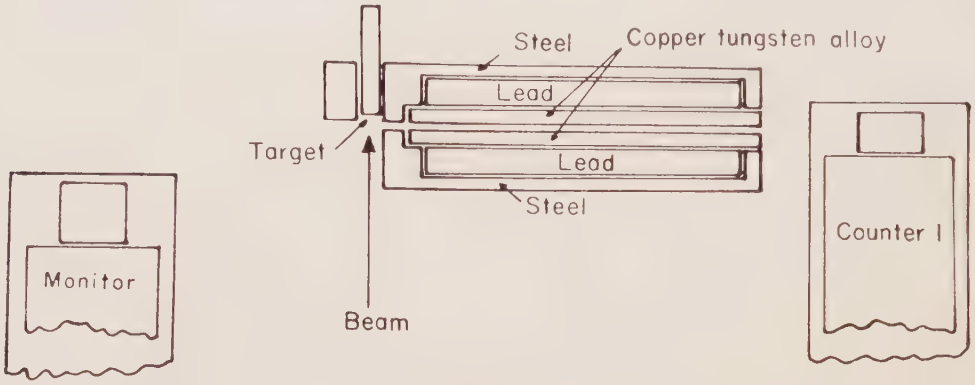

Fig. 13. Geometrical arrangements in recoil-distance measurement. [From S. Devons, G. Manning and D. St. P. Bunbury, Proc. Phys. Soc. (London). A **68**, 18 (1955).]

2.3. RECOIL METHODS

(*a*) *Direct distance measurements*

The half-lives of states excited in nuclear reactions may sometimes be determined by the nuclear recoil method as used by Thirion and Telegdi[33]). This consists of measuring the distance that an excited recoil nucleus moves before it emits a gamma-ray. In the experiment of Thirion and Telegdi, an accelerated beam produces a reaction in a very thin target such that excited nuclei can detach from the target and recoil forward, in vacuo, with reasonably well defined velocity. If the lifetime is long enough, the excited nuclei will decay at a measureable distance from the target depending on the recoil velocity and on the half-life of the state. A gamma-ray collimator and detector are arranged so as to examine at 90° to the beam in a limited region, dx, in front of the target. A typical arrangement is shown in fig. 13. The measurement consists of moving either the target or the collimator and the counter together along a line parallel to the beam and noting the variation of the counting rate. From the shape of the observed distribution and other parameters of the experiment, the half-life for gamma-ray emission can be deduced. The method is useful for measuring half-lives of $\geqslant 10^{-10}$ sec, depending on, the mass of the target nucleus, the incident particle mass and the incident particle velocity. When excited nuclei are produced in typical nuclear reactions involving heavy particles, they recoil with velocities of the order 10^8–10^9 cm/sec. For transition lifetimes $\geqslant 10^{-12}$ sec, the distance covered by the recoiling excited nucleus before de-excitation is often sufficient ($\geqslant 10^{-3}$ cm) to permit direct measurement. The shortest lifetimes that can be measured by these techniques appear at present, to be about 10^{-12} sec[34]). It may be possible to extend such measurements to rather short times, by using bombarding particles which are heavier and have higher energies than the conventional ones, thereby producing excited nuclei with rather high recoil velocities ($\geqslant 10^9$ cm/sec). A higher bombarding energy would evidently increase the dispersion, and hence would allow shorter half-lives to be measured.

(*b*) *Doppler shift and Doppler broadening*

In the direct distance experiment, it is assumed that all the product nuclei are recoiled in the forward direction. Accurate measurement of the energies of the gamma-rays were made by observing them in the forward direction and then at 90° to the beam. The Doppler effect would cause

[33]) J. Thirion and V. L. Telegdi, Phys. Rev. **92** (1953) 1253.
[34]) S. Devons, G. Manning and D. St. P. Bunbury, Proc. Phys. Soc. A **68** (1955) 18.

the gamma-rays at 0° to appear somewhat higher in energy than at 90°. If a thick target is used and the lifetime is longer than the slowing down time of the recoil nuclei, the gamma-ray energy observed in any direction would be the same. From the slowing-down time, which can be estimated, one can place a lower limit on the half-life of a state for if there were no shift in energy between 0° and 90°.

determination of the lifetime of the nuclear excited states in heavy radiative nuclei recoiling after natural alpha-particle emission[35]). The experimental Doppler shift of the internal conversion line was measured with a magnetic spectrometer for different distances between the source and the stopping foil, fig. 14. At one end of the magnetic lens spectrometer an α-detector is mounted at a short distance

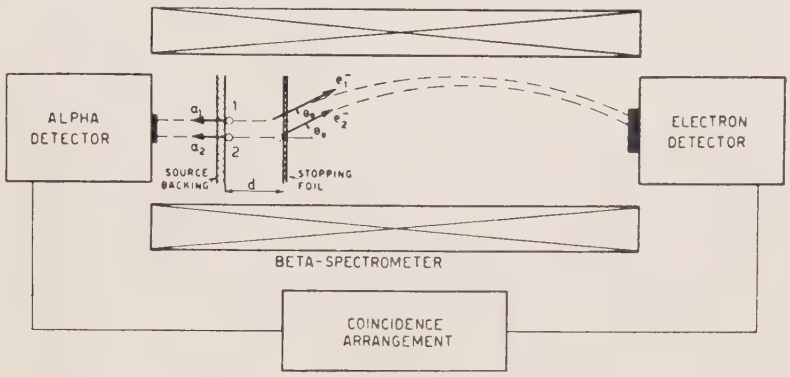

Fig. 14. Diagram of the experiment used for recoil after natural alpha-particle emission. [From J. G. Siekman, thesis 1959 Groningen, Netherlands, State University.]

On the other hand, if a shift in energy is observed which is just the amount expected for a nucleus having its initial recoil velocity, then the lifetime would be shorter than the slowing-down time, thus leading to an upper limit for the half-life. For an intermediate energy shift it would be possible to estimate the actual value of a lifetime. The general problems involved in measuring such energy shifts and their utilization for lifetime determination have been discussed in detail by Devons *et al.*[34]). Experimentally, the recoil nuclei move freely in vacuo for a short, measureable distance, and then are stopped by impact with a dense material. The variation of the observed Doppler shift with distance of free recoil would then give the lifetime of the excited state directly since[34]),

$$E_0 = 1 + \frac{v}{c}\cos\theta\frac{\lambda\alpha}{\lambda\alpha + 1}, \quad \lambda = T^{-1}\ln 2 \qquad (25)$$

where E_0 is the radiation energy for the nuclei at rest, v is the initial recoil velocity, T is the half-life for the radiation transition, and $\alpha = R/v$, R being the range of recoil nuclei of velocity v in the stopping material. This method has also been used for the

behind the source. Coincidences are recorded between α-particles and conversion electrons. The conversion electrons selected in this way are emitted by recoiling nuclei shot out of the very thin sources within a certain solid angle. Their velocities are increased on the average (i.e. the conversion line is shifted) by an amount,

$$V = f_1 f_2 (M_\alpha / M_{\mathrm{nucl}})\, V_\alpha = f_1 f_2 V_{\mathrm{nucl}} \qquad (26)$$

where f_1 and f_2 are reduction factors; M_α and V_α are the mass and the velocity of the alpha-particle; M_{nucl} and V_{nucl} are the mass and the velocity of the daughter nucleus.

Result of the line shift measured of the 40 keV level of Tl^{208} is shown in fig. 15. In this way a value of 3.8×10^{-12} sec has been obtained for the mean lifetime.

The Doppler shift or broadening methods depend on several factors. The most serious limitation is due to the uncertainty in the range-velocity

[35]) J. G. Siekman and H. de Waard, Nucl. Phys. 8 (1958) 402; J. G. Siekman, Thesis (1959) (Groningen, Netherlands State University).

relationship for the medium and the small effects to be measured.

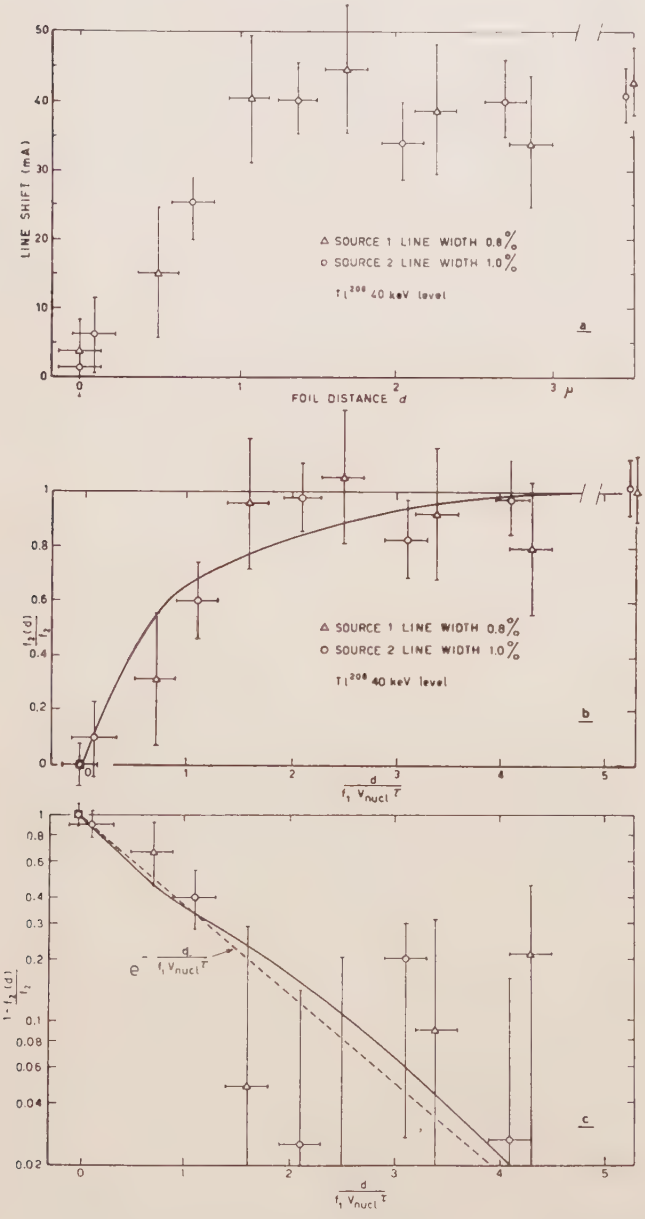

Fig. 15. Result of the line shift measurement of the 40 keV level of Tl^{208}

(a) Observed line shift plotted as a function of source-to-foil distance d. (b) $f_2(d)/f_2$ plotted as a function of $d/(f_1 V_{\mathrm{nucl}}\,\tau)$ (c) $1 - f_2(d)/f_2$ plotted on a logarithmic scale as a function of the source to foil distance expressed in units $d/(f_1 V_{\mathrm{nucl}}\,\tau)$.

The solid lines give the theoretical dependence of $f_2(d)/f_2$ fig. (b) and $1 - f_2(d)/f_2$ fig. (c) for the value $\tau = 3.8 \times 10^{-12}$ sec. [From J. G. Siekman, thesis 1959 Groningen, Netherlands State University.]

Moreover, for the fastest transitions $< 10^{-12}$ sec, and typical recoil velocities, only very short distances of the recoil can be used ($\lesssim 10^{-4}$ cm). Instead, the slowing down of the recoil nuclei in a continuous solid material or a medium composed of layers of light and denser materials may be measured[34]). A thin layer of the target material deposited in several backing materials of widely different densities, to provide a range of stopping media for the recoil motion. In cases where there is substantial difference in the recoil motion, and, therefore, in the Doppler shift, for two different backing materials, a measurement which is much less dependent on the range-velocity relationship can be made by interposing a layer of known thickness of the less dense material between the target layer and a backing of the dense material. The mean Doppler shift is then given by [34]),

$$\Delta E = E_0 \frac{v}{c} \cos\theta \left[1 - \exp\left(-\frac{\lambda x}{v}\right)\right]. \qquad (27)$$

This technique has been used by Bunbury *et al.*[36]), fig. 16. However, the precision of such methods depend on the accuracy of measurement of the small gamma-energy changes involved (which may be from a few percent down to one part in ten thousand) and on the estimate of the slowing down of the recoil nucleus.

In the limiting case, where the directional distribution of recoil nuclei is isotropic, the mean energy of gamma-rays observed in all directions is the same and is equal to the transition energy. However, the recoil effect gives rise to a continuous spectrum, or Doppler broadening, about the mean energy given by eq. (25), as well as a term dependent upon the angular distribution of the recoil and the correlation between recoil direction and gamma-emission. Such a case is that of the B^{10} (n, α)Li^7 reaction studied by Elliott and Bell[37]). They showed that the amount of broadening, fig. 17, varied according to the target material, and they were able to derive a lifetime of 7.4×10^{-14} sec.

In most reactions the broadening is less than 1%.

[36]) D. St. P. Bunbury, S. Devons, G. Manning and J. H. Towle, Proc. Phys. Soc. **69** (1956) 165.

[37]) L. G. Elliott and R. E. Bell, in Beta and gamma-ray spectroscopy edited by K. Siegbahn (North-Holland Publishing Company, Amsterdam, 1955) 518.

Therefore, very high spectral resolutions would be required in the gamma measurements. To overcome this difficulty attempts have been made[34]) to convert the broadening into energy shift.

Firstly, the gamma-transitions corresponding to particular direction of recoil motion are determined from the gamma-rays which are in coincidence with the preceding heavy particles moving in a fixed direction. For example, if the gamma-spectrum is measured with the particle and gamma-detector first on opposite side of the target and then in the same side, the mean gamma-energy in the former case exceeds that in the latter by

$$2E_0 \frac{v}{c} \frac{\lambda\alpha}{1 + \lambda\alpha} \tag{28}$$

where the assumptions are as in eq. (25).

Secondly, the introduction of an anisotropy in the target arrangements may cause an energy shift. In the simplest form, the target should be thin and deposited onto a solid backing, where by the recoil motion in the direction of the backing will be slowed down and stopped. Then if the target and backing are rotated by 180°, the mean energy of the radiation will shift. The observed shift will then be,

$$\Delta E = E_0 \frac{v}{c} \left[1 - \frac{\lambda\alpha}{\lambda\alpha + 1}\right] g \tag{29}$$

where g is a factor of the order $\frac{1}{2}$ [34]), depending on the angular distribution and correlation (exactly $\frac{1}{2}$ if these are isotropic).

A Doppler shift in two retarding media can be compared directly. This can be done by rotating the target which is covered in one side with one medium and the other side with another. In this case, the shift will be

$$\pm E_0 \frac{v}{c} \left[\frac{\lambda\alpha'}{\lambda\alpha' + 1} - \frac{\lambda\alpha''}{\lambda\alpha'' + 1}\right] g \,. \tag{30}$$

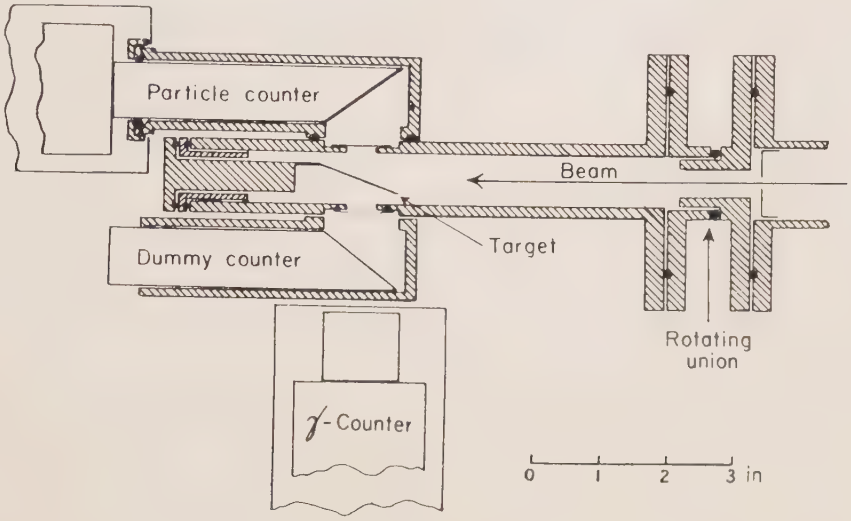

Fig. 16. Geometrical arrangements of Doppler-shift measurement. [From D. St. P. Bunbury, S. Devons, G. Manning, and J. H. Towle, Proc. Phys. Soc. (London) **69** (1956) 165.]

This method is useful when $\lambda\alpha \leqslant 1$ in all suitable media. The coincidence method has two advantages as compared with the target rotation method. Firstly, the shifts are on the average about four times larger. Secondly, no knowledge of the angular distribution is required. As against this, the more elaborated coincidence arrangement provides much slower counting rate in the measurement of the gamma-radiation. The shortest lifetimes that have been measured with these methods are of the order 10^{-14} sec. These methods are useful for radiation lifetimes which are typical for gamma-transitions in light nuclei where other methods are not convenient.

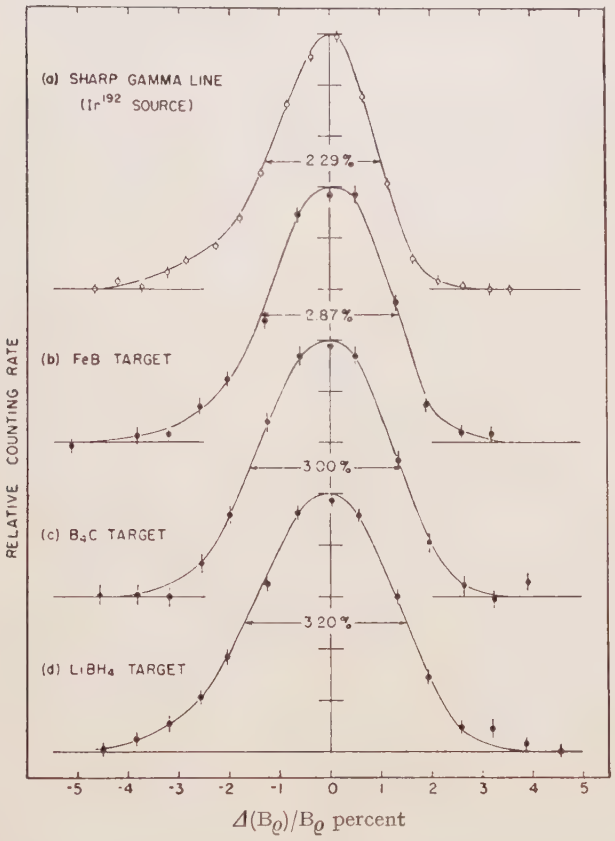

Fig. 17. Diagram showing Doppler broadening of the 279 keV gamma-ray of Li^7, (a) comparison gamma-ray. (b), (c), (d) Li^7 gamma rays from three targets of progressively decreasing density. [From L. G. Elliott and R. E. Bell, in Beta and gamma-ray spectroscopy, edited by K. Siegbahn (North-Holland Publishing Co., Amsterdam, 1955) p. 518.]

3. Indirect Measurements of Sub-Nano Second Lifetimes

3.1. NUCLEAR RESONANCE SCATTERING AND ABSORPTION

The natural energy spread or width Γ of a nuclear energy level is related to the mean life τ for the emission of radiation by the uncertainty relation.

$$\Gamma\tau \sim \hbar \ . \tag{31}$$

Thus, an experimental determination of Γ can lead directly to a value of the mean life of the state. If gamma radiation is incident on a nucleus with energy exactly corresponding to a particular ground state transition, the gamma radiation may be resonantly absorbed. Decay of the state would occur by re-emission of a gamma ray of very nearly the same energy. However, this does not immediately give the correct energy due to a small amount of recoil energy which must be supplied to the absorbing nucleus. Both these energy increments are $E_\gamma^2/2Mc^2$, where M is the mass of the radiating or absorbing nucleus, and E_γ is the excitation energy. Also the incident radiation is off resonance and excitation is only possible if the natural width of the level is large compared with the recoil energy loss. For most atomic transitions this last condition is fulfilled. Most nuclear transitions, on the other hand, are forbidden transitions in the atomic sense, i.e. they are not electric dipoles. For more detail information Metzger has given a extensive survey about nuclear resonance scattering and absorption[38]).

The cross-section for resonant absorption is given by[39])

$$\sigma^0(E) = g\frac{\lambda^2}{8\pi}\frac{\Gamma^2}{(E-E_0)^2+\frac{1}{4}\Gamma^2} \tag{32}$$

where E_0 is the energy of the level, Γ is the natural width of the level, E is the energy supplied by the incident gamma-ray, λ is the wavelength of the incident gamma-ray and g is a statistical weight factor equals to

$$g = \frac{1+2J_e}{1+2J_g} \tag{33}$$

J_e and J_g are the spins of the excited level and the ground state respectively.

If other de-excitation processes are possible, the total width of the excited state can be written as the sum of partial widths, i.e. $\Gamma = \Sigma_i \Gamma_i$, and the cross-section for photoexcitation followed by the i^{th} mode of the de-excitation is then[38])

$$\sigma_i^0(E) = g\frac{\lambda^2}{8\pi}\frac{\Gamma_0\Gamma_i}{(E-E_0)^2+\frac{1}{4}\Gamma^2} \tag{34}$$

where Γ_0 is the partial width for the direct gamma-ray transition to the ground state, and Γ_i is the partial width for the de-excitation of interest in the particular experiment.

[38]) Franz R. Metzger, Progress in Nuclear Physics, edited by O. R. Frisch **7** (1959) Ch. 2.

[39]) W. Heitler, The Quantum Theory of Radiations (Oxford University Press, 1936).

Summing over all possible modes of de-excitation, one obtains the cross-section for resonance absorption of photon of energy E

$$\sigma^0_{\mathrm{abs}}(E) = g\frac{\lambda^2}{8\pi}\frac{\Gamma_0\Gamma}{(E-E_0)^2+\frac{1}{4}\Gamma^2}. \qquad (35)$$

The actual absorption lines are, in general, much wider than is indicated by eq. (35), because of the Doppler effect. The Doppler width Δ is given[38]) by

$$\Delta = (E/c)\,(2kT/M)^{\frac{1}{2}} \qquad (36)$$

where c is the velocity of light, E is the energy of the gamma radiation, M is the mass of the nucleus, k Boltzmann's constant, and T the absolute temperature of the absorber.

Therefore the effective cross-section have the "Doppler form" is,

$$\sigma_{\mathrm{D}}(E) = \sigma^0_{\max}\,(\Gamma\pi^{\frac{1}{2}}/2\Delta)\exp\{-[(E-E_0)/\Delta]^2\}. \qquad (37)$$

It was pointed out by Kuhn that the resonance condition might be restored by a preceding beta- or gamma-emission. This argument was discussed in detail and studied experimentally by Pollard and Alburger[40]) then confirmed by I. Lacovac[41]) (1954).

not lost its velocity, the energy shift may be compensated by the Doppler effect. The resonance condition is exactly restored if the emitting nucleus

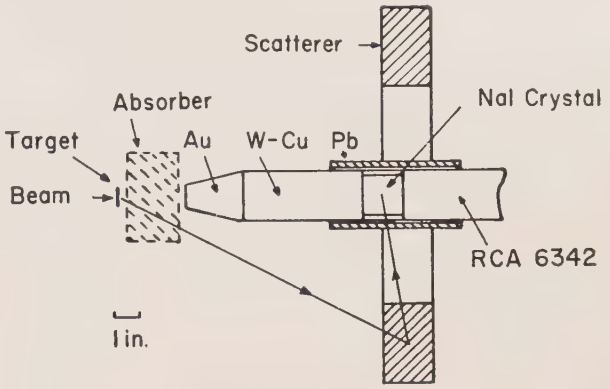

Fig. 18. Arrangement for detection of resonance scattering and absorption. The position shown for the scatterer corresponds to a scattering angle of 120°. [From C. P. Swann and F. R. Metzger, Phys. Rev. **108** (1957) 982.]

approaches the scatterer with the velocity $U = E/MC$. By measuring coincidences between the beta-particles and the scattered gamma rays, one might expect to find an increasing counting rate,

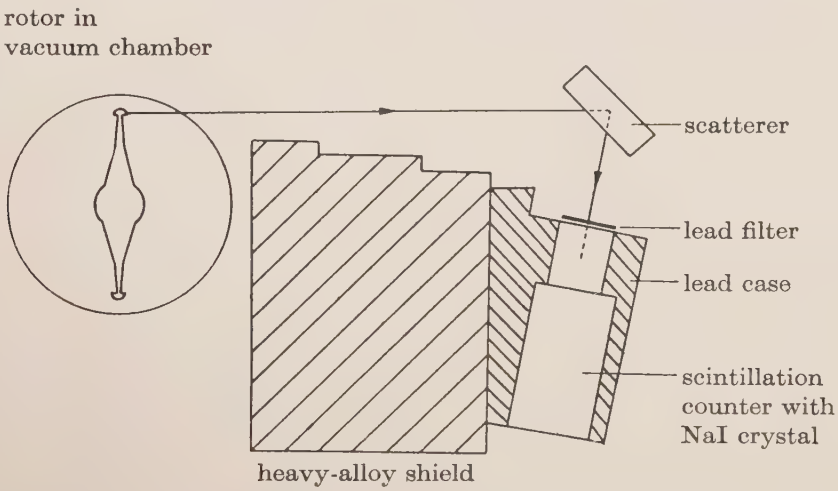

Fig. 19. Experimental arrangement for measuring resonance scattering intensity at various rotor speeds. [From P. B. Moon and B. S. Sood, Proc. Royal. Soc. **257**, No. 1228 (1960) 44.]

A nucleus emitting a beta-particle obtains a recoil velocity in the opposite direction. If the subsequent emission of the actual gamma-ray takes place within such a short time that the nucleus has

when the beta particles are measured at such an angle that the recoiling nucleus has the appropriate velocity component towards the scatterer, see fig. 18. This condition should be applied to measurements using beta or gamma recoil preceding the radiation under examination.

[40]) E. Pollard and D. E. Alburger, Phys. Rev. **74** (1948) 926.
[41]) K. I. Lakovac, Proc. Phys. Soc. Lond. A **67** (1954) 601.

Sources in gaseous and liquid form are used in most cases[42]) when the lifetime is of the order 10^{-11}–10^{-12} sec. Solid sources have been used when the transition is sufficiently fast[43]) (10^{-13} sec).

Another method for restoring the resonance by mechanical motion was proposed by Moon[44]). The energy shift is compensated by the Doppler-effect when the emitting nucleus moves towards the scatterer with the velocity $U = E/MC$. The method is restricted to heavy nuclei and gamma energies less than 500 keV. This velocity can be obtained at the edge of a high speed rotor. Moon derived an expression for the effective cross-section of resonance scattering taking into account the mechanical velocity of the gamma source and the thermal velocities of the nuclei in the source and the scatterer. It is supposed that the thermal velocities of the nuclei are distributed as in a gas at temperature T.

$$\sigma = g \frac{h^2c^2\Gamma}{4E^3} \sqrt{\frac{Mc^2}{4\pi kT}}\, e^{-\frac{M(U-E/Mc)^2}{4kT}}. \qquad (38)$$

The experimental arrangement used by Moon and Sood[45]) to study the intensity of resonant scattering as a function of rotor speed is shown, in fig. 19. The gamma-rays emitted in the forward direction from the source which is loaded in the tips of the high speed rotor were selected with the help of heavy alloy shielding and a gating arrangement which switches the counter on, only when the rotor tips are in the tangential position.

The temperature of the source or of the scatterer or both will result in a broadened energy distribution which increases the probability for two nuclei, having the appropriate relative velocities, to compensate the recoil. This possibility was pointed out and verified experimentally by Malmfors[46]).

The cross-section is given by

$$\sigma = g \frac{h^2c^4}{4\sqrt{\pi}} \frac{M}{E^4} \Gamma p\, e^{-p^2} \qquad (39)$$

where

$$p^2 = E^2/Mc^2 \frac{1}{2k(T_1 + T_2)}$$

T_1 and T_2 are the absolute temperatures of the source and the scatterer.

Recoiless emission and absorption (Mössbauer effect)

The technique of resonance absorption of gamma-rays by nuclei bound in crystals at low temperature has been shown by Mössbauer to be a valuable tool in the measurement of natural level width of nuclear isomers. Moon[44]) showed how to compensate for the recoil and Mössbauer[47,48,49]) showed how to eliminate it. Mössbauer found that it is possible for nuclei bound in a crystal to emit or absorb gamma radiation having an energy equal to that of the nuclear transition. The recoil momentum is taken by the crystal as a whole. The probability that there is no energy transfer to or from the lattice vibrations is given by Debye-Waller factor as applicable to elastic scattering of X-ray. The effect is described in terms of three characteristic temperatures or energies.

(1) The energy of the free recoil. (2) A characteristic temperature for the lattice. (3) The ambient temperature.

To obtain an effect, the lattice temperature should be of the same order as the free recoil energy and the ambient temperature should be low compared to these.

In his initial experiment Mössbauer measured the width of the 129 keV level in Ir^{191}. The emitting and absorbing nuclei were bound in crystals at a low temperature. The emissions which took place without energy transfer to the lattice give rise to a line of width 2Γ in the energy spectrum of gamma's emitted by the crystal. The height of this "no recoil line" was decreased rapidly as the temperature increased.

A recent survey by Nagle[50]), it would appear that about 75 stable nuclei have sufficiently low lying states which might be conveniently studied by this technique.

[42]) F. R. Metzger, Phys. Rev. **101** (1956) 286.
[43]) L. Grodzins, Phys. Rev. **109** (1958) 1014.
[44]) P. B. Moon, Proc. Phys. Soc. **64** (1951) 76.
[45]) P. B. Moon and B. S. Sood, Proc. Royal Soc. **257** (1960) 1288.
[46]) K. G. Malmfors, Arkiv för Fysik **6** (1952) 49.
[47]) R. L. Mössbauer, Z. Physik **151** (1959) 125.
[48]) R. L. Mössbauer, Naturwiss **45** (1958) 538.
[49]) R. L. Mössbauer, Z. Naturforschung **149** (1959) 711.
[50]) D. Nagle, "Mössbauer effect" Conference at the University of Illinois, Allerton house, 1960, Edited by Hans Frauenfelder.

To summarize:

Nuclear resonance and absorption offers a very valuable technique for the measurement of sub-nanosecond lifetimes. It is complementary to the delayed coincidence technique in so far as it becomes more suitable the shorter the lifetime is. Accurate measurements are often hampered by disturbing background radiation due to Compton and Rayleigh scattering. A severe and obvious limitation is that one can only study ground-state transition in nuclei available in bulk material (stable elements or isotopes possible to produce in weightable quantities).

3.2. COULOMB EXCITATION

Coulomb excitation is an indirect method of determining the half-life of a nuclear energy level. This process may be thought of as the interaction between the electric field of a nucleus and that of a closely passing bombarding particle. With a few exceptions the only excitations observed, so far, are of E2 character. From the measured absolute cross-section, one may derive the reduced transition probability $B(\mathrm{E2})$ by means of the theoretical expression given by Alder and Winther[51]).

$$\sigma = \frac{2\pi^2 m^2 v_f^2}{25 Z_2^2 \hbar^2} \cdot g_2(\xi) \cdot B(E2) \times 10^{-48} \qquad (40)$$

where $g_2(\xi)$ is a numerically tabulated function of the adiabatic parameter

$$\xi = \frac{Z_1 Z_2 e^2}{\hbar} \left(\frac{1}{v_f} - \frac{1}{v_i} \right) \qquad (41)$$

m is the mass of the bombarding particle, v_i and v_f are its velocities before and after the interaction, z_1 and z_2 are the charges of the bombarding particle and target nuclei, respectively.

The reduced transition probability determines the lifetime for the inverse radiative transition[52]) according to

$$T_\gamma(\mathrm{E2};\, I_f \to I_i) = 1.23 \times 10^{-2} (\Delta E)^5 \times$$

$$\times B(\mathrm{E2},\, I_i \to I_f) \cdot \frac{2I_i + 1}{2I_f + 1} \,\mathrm{sec}^{-1} \qquad (42)$$

where ΔE is measured in keV and $B(\mathrm{E2})$ in units of $e^2 \times 10^{-24}\,\mathrm{cm}^4$. From the Coulomb excitation experiments the partial reduced transition probability, $\varepsilon B(\mathrm{E2})$, is determined, where ε is the fraction of the excitations which decay through the observed mode, since the detected radiation can be either gamma-rays, conversion electrons or inelastically scattered protons.

Thus, if the detected radiation is a gamma ray (γ_i), the decay fraction is given by

$$\varepsilon(\gamma_i) = \frac{f_i}{\sum_i (1 + \alpha_i) f_i} \qquad (43)$$

where f_i are the relative intensities of the various gamma transitions by which the excited state may decay, and α_i are the corresponding total conversion coefficients.

In the case of conversion electron detection, the decay fraction is given by the above eq. (41) multiplied by the conversion coefficient for the conversion line in question, while for the inelastic protons $\varepsilon p' = 1$.

If the Coulomb excitation populates several levels in the same nucleus, the radiation from the lower levels may partly result from a cascade decay of a higher level. In the determination of $\varepsilon B(\mathrm{E2})$, it is necessary to establish what part of the measured radiation is due to the direct excitation of the radiating level. Coulomb excitation has proved to be a most valuable method for the determination of partial transition rates. An impressive amount of nuclear data has been obtained through Coulomb excitation experiments. The recent, very successful experiments on multiple Coulomb excitation[6]) has much widened the range of application. For obvious reason the method suffers from the same limitation as the nuclear resonance technique, i.e. it can only be applied to stable isotopes (or to long-lived isotopes that can be produced in weightable amount in nuclear reactors). Furthermore, Coulomb excitation is essentially limited to E2 excitations. This is not necessarily a disadvantage since it implies certain simplifications in the interpretation. Coulomb excitation renders itself to studies of general trends, such as the E2 enhancement factors in a series of neighbouring even-even nuclei. A comparison between the different methods for

[51]) K. Alder and A. Winther, Phys. Rev. **96** (1954) 237.

[52]) K. Alder, A. Bohr, T. Huus, B. Mottelson and A. Winther, Rev. Mod. Phys. **28**, No. 4 (1956).

measuring nano and sub-nanosecond lifetimes of nuclear level is shown in table 1. Also, to get an idea of the range of application of each method, an approximate number of nuclear lifetimes measured (up to 1960) by the various methods is given in table 2.

TABLE 1

Methods for measuring nuclear lifetimes

Method	Limit of measurable lifetimes
1. Delayed coincidence	$> 5 \times 10^{-11}$ sec
2. Direct timing	$> 10^{-12}$ sec
3. Recoil	$> 10^{-14}$ sec
4. Nuclear resonance Scattering and absorption "Mössbauer effect"	$< 10^{-9}$ sec $< 10^{-5}$ sec
5. Coulomb excitation	$> 10^{-12}$ sec

TABLE 2

Approximate numbers of nuclear lifetimes measured (up to 1960) by the various methods discussed above

Method	Number of nuclear lifetimes measured
1. Delayed coincidence	80
2. Direct timing	16
3. Recoil	19
4. Nuclear resonance scattering and absorption	24
5. Coulomb excitation	630

Acknowledgement

The author is greatly indebted to Dr. T. R. Gerholm for many illuminating discussions. My thanks are further expressed to Professor Kai Siegbahn for his kind interest in this work.

NUCLEAR INSTRUMENTS AND METHODS 12 (1961) 249–262; NORTH-HOLLAND PUBLISHING CO.

LEAKAGE CURRENT IN SEMICONDUCTOR JUNCTION RADIATION DETECTORS AND ITS INFLUENCE ON ENERGY-RESOLUTION CHARACTERISTICS

FRED S. GOULDING and WILLIAM L. HANSEN

Lawrence Radiation Laboratory, University of California, Berkeley, California

Received 3 March 1961

The theoretical limits of noise in detector-amplifier combinations are discussed and related to the bulk properties of the semiconductor (lifetime and resistivity). A new detector structure which includes a guard ring as an integral part of the detector is described and its effect in eliminating surface leakage is discussed. Experimental results in good agreement with theory for detector leakage and noise resolution are presented. The residual surface effects not eliminated by the guard ring are shown to be important in very-low-leakage detectors, and the results of surface treatments to reduce these effects are briefly mentioned.

Observations of the energy resolution of these detectors using various types of particles indicate that factors other than noise are important. Surface imperfections such as are encountered in polished surfaces may cause poor resolution when heavily ionizing particles are detected. Multiple peaks have also been observed in α spectra obtained with diffused junctions, possibly due to other surface effects. A brief description is given of the special electronic circuits used in these measurements.

Techniques used in producing the guard-ring counter are described in detail. These employ gaseous diffusion to produce a thin surface junction, followed by etching through a photoresistant mask to produce the desired geometry.

1. Introduction

Semiconductor junctions are finding increased use as radiation detectors. Although they are likely to be valuable replacements for existing types of detectors, possibly their main importance lies in the field of particle energy determination. Because absorption of a given amount of energy from the radiation produces about 10 times as much ionization in solids of interest as in gases used in ionization chambers, energy resolution can be improved by a similar factor. Existing methods of achieving energy resolutions comparable to the possible performance of silicon detectors are expensive and essentially use low geometric counting efficiencies. Therefore it is quite possible that experiments hitherto considered impossible will become practicable through use of these detectors. Their importance may be increased by their inherent short collection time, of great interest in the detection and timing of minimum ionizing particles.

The investigation described here was undertaken to determine the fundamental limits of performance of this type of detector. Literature has appeared describing various types of junction detector, some relying on surface barriers, while others use diffused junctions similar to those employed in commercial semiconductor devices. It has been our experience that the behavior of these simple detectors is unreliable. Excellent results do occur occasionally for no apparent reason, but the method of manufacture seems to be poorly controlled, and the detectors are seriously affected by their environment. For example, some detectors operate well in vacuum but not in air, while in other cases the reverse occurs. This example demonstrates that a major problem in these detectors arises at the edge of the junction where the p–n transition reaches a surface whose properties depend upon surface contaminants.

A major objective in our work was therefore to develop a device in which the surface problem is reduced. The suggestion that a guard ring be applied to a semiconductor junction edge is not new. However, because a suitable geometry was lacking, guard rings have not been used prior to the work described here. In practice, our guard ring is more complicated in its behavior than the simple insulator guard ring. This is discussed in detail later, but at this stage it is adequate to note that surface effects can be reduced to negligibility by

careful design. Once this is achieved, the bulk properties of the semiconductor become the limit to performance. In particular, the lifetime of the minority carrier is of great interest.

Relating the electrical parameters of the junction detector to its energy resolution, when used as a particle detector, involves consideration of the spread in output pulse amplitude from the detector-pulse amplifier system. Since electrical noise may in some circumstances be the primary limitation, the amount and behavior of this noise must be investigated under various conditions.

2. Amplifier Signal-to-Noise Ratio

A junction detector may be looked upon as a solid ionization chamber, and it is natural to consider how the electrical parameters compare with those of the gaseous ionization chamber. For noise calculations, ionization chambers may be regarded as very-high-impedance charge sources shunted by capacity. The junction detectors acts in a similar way. The detector impedance is somewhat lower than that of an ionization chamber, and its capacity is greater. Also, a significant leakage current flows across the junction. Despite these slight differences of behavior the general signal-noise considerations are the same as those developed for ionization chambers amplifiers, but the optimum design parameters of the system may differ with the particular detector. Formulae similar to those developed previously for ionization chamber amplifiers[1]) are presented in table 1. These formulae assume that the pulse amplifier contains single integrating and differentiating circuits having equal time constants, and that the detector collection time is very small compared with the amplifier time constant. Although a slight improvement in signal to noise can be obtained by using more complex pulse-shaping networks, the case considered here achieves almost the ideal result and lends itself to simple adjustment. This is essential if theory and experiment are to be compared. Note that the results given in table 1 assume that the ambient temperature is 25°C.

In table 1, note that the tube-flicker-effect contribution to total noise is independent of the actual value of amplifier time constant. Calculation also shows that it is small compared with the other terms in the practical case. Note, also, that any other noise having a $1/f$ frequency dependence (as

[1]) These formulae are derived in Appendix B. They are similar to ones developed in: A. B. Gillespie, Signal, Noise and Resolution in Nuclear Counter Amplifiers (Pergamon Press, London, 1953).

Table 1

Noise contributions from various sources

Noise source	Input equivalent ms noise (coulombs[2])	Input equivalent ms noise (keV[2])	Constants
Tube shot noise	$4 \times 10^{-35} \frac{C^2}{g_m \tau}$	$2 \times 10^{-2} \frac{C^2}{g_m \tau}$	C = total input capacity, picofarads (pF) i_g = tube grid current (mμ amp)
Tube flicker	$4 \times 10^{-37} C^2$	$2 \times 10^{-4} C^2$	g_m = tube mutual conductance (mA/V) τ = amplifier time constant (μ sec)
Grid Current	$3.2 \times 10^{-34} i_g \tau$	$1.6 \times 10^{-1} i_g \tau$	R = total input shunt R ($C \times R$ assumed $\gg \tau$)
Detector leakage	$3.2 \times 10^{-34} i_L \tau$	$1.6 + 10^{-1} i_L \tau$	i_L = dectector leakage (mμ amp)
Input resistance noise	$1.6 + 10^{-32} \frac{\tau}{R}$	$8 \frac{\tau}{R}$	

(a) Third column gives equivalent energy absorbed from an incident particle, assuming 3.6 eV/hole electron pair (correct for silicon).

(b) Full width at half maximum of a resolution curve is approximated by taking the square root of the sum of contributions in column 3 and multiplying by 2.3.

the flicker effect) would also result in a noise component independent of amplifier time constant. In our work we have assumed that no such $1/f$ noise apart from tube flicker noise is present; the justification for this assumption will be illustrated later when experimental results are presented. However, $1/f$ noise may be produced by semiconductor surface effects. The fact that we do not observe a $1/f$ noise term (i.e., independent of amplifier time constant) indicates that our surface effects are very small.

The remaining terms in table 1 all demonstrate some dependence on amplifier time constant. Tube shot noise^2 is inversely proportional to amplifier time constant, while grid current noise^2, detector leakage current noise^2 and resistance noise^2 are all linearly proportional to amplifier time constant. Thus, an optimum amplifier time constant exists at which the signal-to-noise ratio has its greatest value. This optimum time constant lies generally in the range 0.1 μsec to 2 μsec, depending upon the system parameters.

Fig. 1 presents curves calculated from table 1 illustrating the variation of the mean square noise with the various parameters in the equations. The curves assume a tube grid current of 2×10^{-9} amp

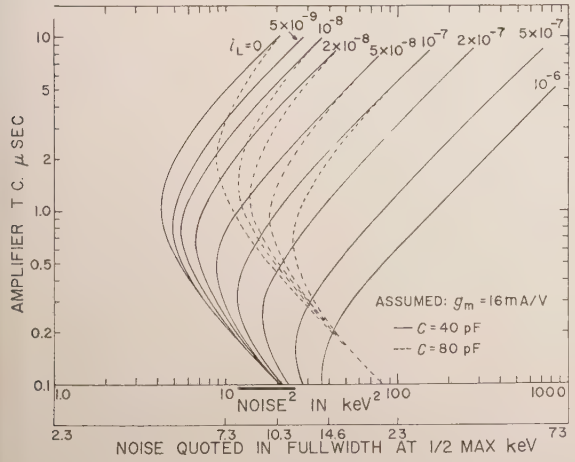

Fig. 1. Noise variation with amplifier T.C.

and a total shunt input resistance of 5 MΩ, each easily attained in practice. For short amplifier time constants, tube shot noise is dominant, whereas detector leakage-current noise is dominant for long amplifier time constants.

2.1. CHOICE OF INPUT TUBE AND SHUNT INPUT RESISTANCE FOR BEST RESOLUTION

In an ionization chamber amplifier, the grid current of the input tube, the shunt input resistance, and the tube mutual conductance determine the optimum circuit, since the detector exhibits no leakage. However, semiconductor junction detectors at present exhibit leakages much larger than the input-tube grid current. Therefore, grid current becomes less important and we choose a tube with a higher mutual conductance and grid current than would be optimum for ionization chamber uses. Measurements reported here use 417A input tubes operated at an anode voltage of 100 V and 10 mA current. Under these conditions the grid current is about 2×10^{-9} amp and mutual conductance 16 mA/V.

Table 1 may be used to determine a suitable value of input shunt resistance. Equating detector leakage current noise^2 to input resistance noise^2 permits the choice of R so as to make its noise contribution much smaller than that resulting from detector leakage. In our detectors $i_L > 25$ mμA under normal operating conditions, which means that a shunt impedance > 5 MΩ is desirable. The curves in fig. 1 are calculated for $R = 5$ MΩ. Ideally, a larger value of R should be used.

2.2. OPTIMUM AMPLIFIER TIME CONSTANT

Table 1 also permits ready practical calculation of the optimum amplifier time constant. Since tube shot noise and detector leakage current noise are dominant, the remaining terms may be neglected. Making this assumption, we have

$$\tau_{opt} = \frac{0.35C}{\sqrt{g_m i_L}} . \qquad (1)$$

By using this value of amplifier time constant, the optimum total mean square noise may be calculated. In the following equation, flicker effect, resistance noise, and grid current noise are neglected:

$$\langle \text{noise}^2 \rangle = 4 \times 10^{-2} \frac{C^2}{g_m \tau_{opt}} \text{ keV}^2$$
$$= 0.11\, C \sqrt{\frac{i_L}{g_m}} \text{ keV}^2 . \qquad (2)$$

For example:

If $g_m = 16$ mA/V,
$C = 80$ pF } (Typical in our experiments
$i_L = 50$ mμamp } using 1-cm diam detector)

$$\tau_{opt} = 1.0\ \mu\text{sec}$$
$$\langle \text{noise}^2 \rangle = 15\ \text{keV}^2.$$

Full width at half max of resolution curve = 9.2 keV.

This is in good agreement with the curves of fig. 1, if one considers that the curves include all noise contributions whereas the simplified calculations include only tube shot noise and detector leakage current noise.

2.3. SUMMARY OF THIS SECTION

Equations (1) and (2) express the theoretical optimum noise conditions in a detector-amplifier system. The curves of fig. 1 show the dependence of noise on amplifier time constant. The shape of these curves is used in the following work to show that the noise frequency spectrum agrees with this theory. Detector surface noise and detector series resistance noise have been omitted in this discussion. Our experience indicates that these are usually negligible in well-designed detectors, but the additional contribution due to series resistance can be calculated without difficulty if required.

3. Detector Parameters

The work described is confined to junctions manufactured by diffusing a donor impurity (phosphorus) into high resistivity p-type silicon. Phosphorus surface concentration, diffusion temperature and time were chosen to produce a very thin skin of highly doped n-type silicon on the face of the p-type wafer.

Table 2 presents formulae for calculating the depletion layer width, capacity, diffusion and generation currents in the types of junction used in this investigation. Appendix A shows how these formulae are derived from those appearing in the literature and gives general relationships which may be applied to any situation.

To illustrate the order of magnitude of the detector parameters, and using the formulae given in table 1 to calculate the predicted characteristics of a 1-cm-diam detector using 1500 ohm-cm p-type material having a equivalent[2]) minority carrier lifetime of

Table 2
Detector formulae

Depletion layer width	$W = 0.32\ (\rho V)^{\frac{1}{2}}$ microns
Detector capacity	$C_d = 3.3 \times 10^4\ (\rho V)^{-\frac{1}{2}}$ pF/cm^2
Generation	$I_g = 38 \dfrac{(\rho V)^{\frac{1}{2}}}{\tau_0}$ mμamp/cm^2
Diffusion current	$I_d = 2.75 \dfrac{\rho l}{\tau_0}$ mμamp/cm^2

500 μsec, and carrying out the calculation for an applied voltage of 200 V, we have

Detector area = 0.8 cm^2,
Depletion layer width = 176 μmicrons,
Detector capacity = 48 pF,
Generation current = 34 mμA,
Diffusion current = 0.6 mμA,
(taking l = wafer thickness = 35 mils = 900 microns).

Note that the diffusion current is very small compared with the current caused by generation of carriers at trapping centers in the depletion layer. In a well-designed detector this will always be so, and for this reason, we neglect discussion of diffusion currents.

By using eq. (2), which relates noise to detector characteristics, with the results of table 2 the following mean square noise at optimum amplifier time constant for the system can be derived:

$$\langle \text{noise}^2 \rangle = \left[\frac{A}{\tau_0 g_m}\right]^{\frac{1}{2}} 0.7 C_{in} (\rho V)^{\frac{1}{4}} + \frac{2.2 \times 10^4 A}{(\rho V)^{\frac{1}{4}}}\ \text{keV}^2 . \quad (3)$$

Where A = detector area in cm^2, C_{in} = input capacity of the system apart from the detector, and the remaining constants are as defined in tables 1 and 2.

The first term in eq. (3) is proportional to $(\rho V)^{\frac{1}{4}}$, while the second is inversely proportional to this quantity. Therefore an optimum operation voltage must exist from the point of signal to noise. This voltage is given by

$$v(\text{opt}) = \frac{10^9 A^2}{\rho C_{in}^2}\ \text{volts} . \quad (4)$$

[2]) This is not the normal minority carrier lifetime-see note in Appendix 1.

Inserting this into eq. (3) the best performance we can expect with a given semiconductor material and input tube in the amplifier is

$$\langle \text{noise}^2 \rangle \text{ (opt)} = 250A \sqrt{\frac{C_{in}}{\tau_0 g_m}}. \quad (5)$$

Using these equations to predict optimum performance for the type of detector used in the earlier example:

$A = 0.8$ cm^2,
$\rho = 1500\ \Omega$cm,
$\tau_0 = 500\ \mu$sec,
$g_m = 16$ mA/V,
$C_{in} = 25$ pF,
$\langle \text{noise}^2 \rangle$ (opt) $= 11.4$ keV^2,
Equivalent full width at half max $= 7.8$ keV,
Optimum applied voltage $= 614$ V,
Detector leakage current $= 72$ mμA
Detector capacity $= 35$ pF,
Optimum amplifier time constant $= 0.62\ \mu$sec.

3.1. SUMMARY OF THIS SECTION

Equations were developed permitting theoretical study of the ultimate noise performance of the detector-amplifier system. According to eq. (5), ultimate performance depends upon the lifetime of minority carriers in the material, and upon the input tube mutual conductance and its capacity. The resistivity of the material did not appear directly in this equation.

As an intermediate step in the development of the noise relationship, the leakage current of the detector as a function of resistivity and carrier lifetime in the bulk semiconductor were studied. We will now deal with practical detectors and use detector leakage current, capacity and noise to test agreement between theory and practice.

4. The Guard Ring Detector

In order to realize practically the theoretical behavior predicted in the foregoing sections, it is clear that surface leakage effects must be eliminated. Leakage current values predicted in table 2 are one or two orders of magnitude lower than is commonly measured in simple junction detectors. To decrease surface leakage as far as possible, the guard ring structure shown in fig. 2 was devised. Phosphorus was diffused into p-type silicon, then the wafer was etched through a photoresist mask to prevent etching in the detector and guard ring areas on the front face. This resulted in breaking of the n-type skin on the front face into two areas; a central area used as the detector, surrounded by a guard ring

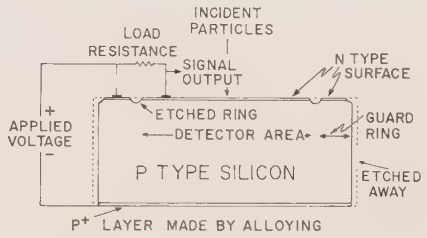

Fig. 2. Guard ring detector.

area. The space between guard ring and detector should be as small as practicable; we used 2.5 mils spacing in the work described here.

In some respects the behavior of the guard ring resembles that of the conventional insulator guard ring. Since no or only very small voltage exists between central areas and guard ring, no average current can flow out across the surface from the central region. However, although this applies for any guard-ring-to-central region spacing, it should be obvious that it is not the only condition for eliminating surface noise. Indeed, if the spacing is large, one might expect surface noise due to the edge of the central junction region to be increased by the presence of the guard ring, although average surface leakage out from the central region might still be zero. This anomaly can be explained by assuming equal and opposite currents to flow from central region to guard ring and vice-versa. Since each current contributes its noise component, the guard ring has, in fact, increased the surface noise instead of reducing it. This argument suggests that the guard-ring-to-central-region spacing should be very small. A little consideration shows that the spacing should be made very small compared with the depletion layer width at the operating voltage of the detector. In this case the depletion layer "pinches off" the space between guard ring and central region as the applied voltage is increased beyond a few volts. Therefore, the surface of the etched ring rises in potential as the applied voltage is increased.

Surface leakage in p–n junctions is generally attributed to two causes:

(a) Ionic conduction on the outside of an oxide film.

(b) Surface channeling produced by an inversion layer on the surface of the p- or n-type material.

Injection from the surface channel into the bulk of the material tends to result in an ohmic behaviour.

The guard ring entirely eliminates (a) and reduces (b) by a large factor since the surface channel is restricted in area to the region of the etched ring. The actual magnitude of the injected current due to (b) is dependant upon surface treatment but is much lower than in the simple detector.

4.1. EXPERIMENTAL RESULTS

Several guard ring counters were constructed, and, in general, the measurements on these counters agreed with theory. Leakage current measurements were carried out by using the potentiometer arrangement shown in fig. 3, ensuring that measurement was performed with the guard ring and detector areas at the same potential. It also permitted measurement of the impedance across the surface of the etched ring which shunts the detector load and may thereby increase the system noise.

A typical plot of detector capacity is shown in fig. 4, and the leakage current is shown in fig. 5. The improvement obtained by using the guard ring is

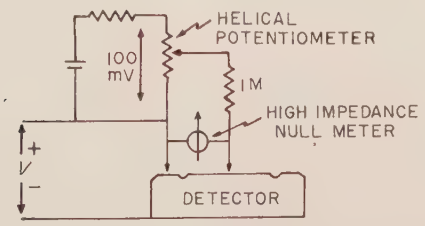

Fig. 3. Test circuit for leakage measurements.

apparent, since in this case the guard-ring leakage current was nearly 10 μA at 200 V and a simple type of detector with the same surface area would presumably also exhibit several μA leakage.

The detector capacity obeyed an inverse-square-root law with voltage, as predicted by table 2. This implies that the depletion layer width was proportional to $\sqrt{V}$. However, the detector leakage current obeyed the expected $\sqrt{V}$ law only at high voltages.

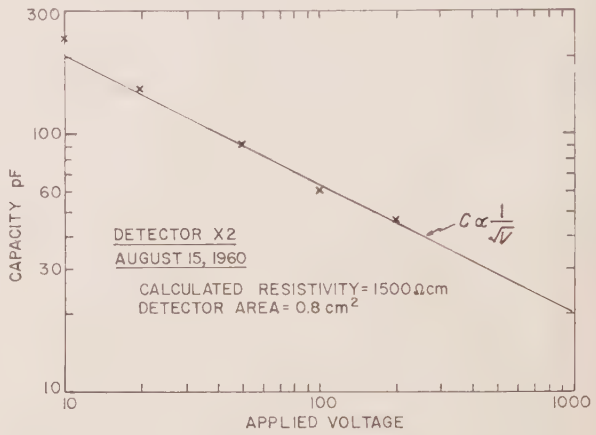

Fig. 4. Typical capacity-voltage relationship.

The departure at low voltages is believed due to injection effects where the p–n junction reaches the surface. This belief is strongly supported by the observation that operating the counter in different environments produced considerable change in the low voltage part of the curves in fig. 5. Small traces

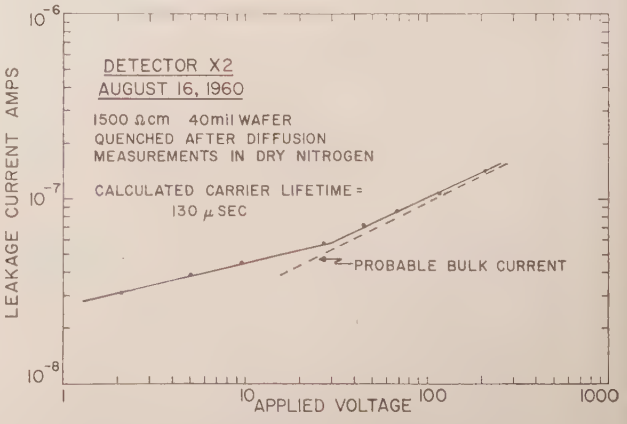

Fig. 5. Typical leakage current-voltage relationship.

of chlorine (known to produce a p-type surface) caused a large increase in the leakage current particularly at low voltages, while traces of ammonia (known to produce an n-type surface) caused the current at low voltages to fall almost to the value

expected on the basis of a $\sqrt{V}$ dependence. Therefore, to obtain the ultimate performance a surface treatment resulting in a stable, very light "n" surface in the etched ring is necessary. No quite satisfactory surface treatment has yet been found, but silicone resins and oxide film growth seem promising.

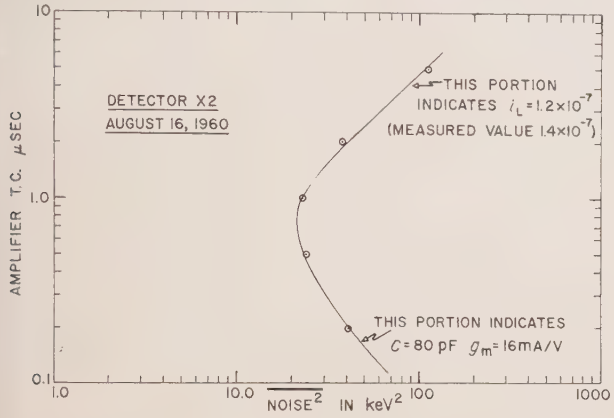

Fig. 6. Typical noise variation with amplifier time constant.

Measurements of the noise of a detector-amplifier system made by using the detector whose characteristics appear in figs. 4 and 5 are shown in fig. 6. Appendix C describes the low-noise preamplifier and biased amplifier units used for these measure-

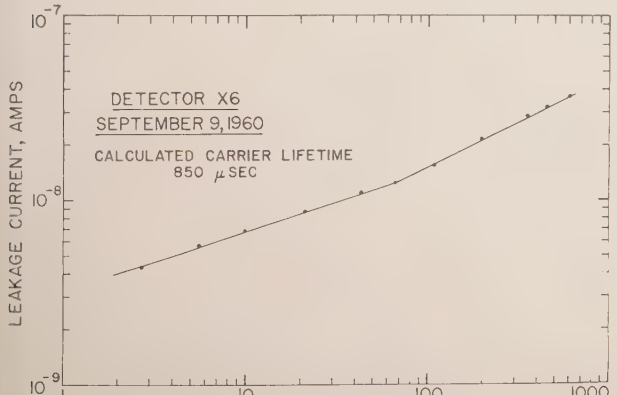

Fig. 7. Best leakage current curve yet attained.

ments. The curve shown in fig. 6 agrees very well with that predicted from fig. 1, which indicates that the equations given in table 1 accurately represent all noise sources and that no additional significant source of noise is present.

The leakage current curve of fig. 7 represents the best result. The current in fig. 5 corresponds to an effective lifetime of 130 μsec while that of fig. 7 corresponds to one of 850 μsec. As yet we have insufficient experience to indicate the best treatment, but the spread in lifetimes we apparently encountered showed that improvement may be

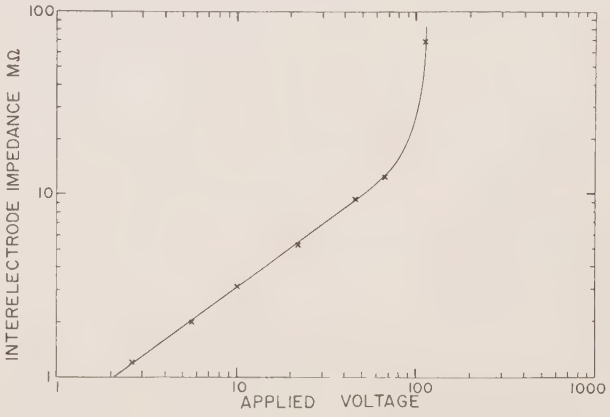

Fig. 8. Interelectrode impedance characteristic (n-type surface).

possible. Incidentally, the wafer used in the detector of fig. 5 was cooled quickly by withdrawing into air at room temperature after diffusion whereas that of fig. 7 was slowly cooled; however, the increase in lifetime in the latter case is probably fortuitous. One point to note is that no satisfactory method seems to exist for measuring minority carrier lifetime in thin wafers of high resistivity material.

Surface treatment of the etched ring affects the impedance measured between guard ring and detector as well as influencing carrier injection. The n-type surfaces tend to cause a low impedance, but guard ring and detector are virtually isolated if a p-type surface is produced. If the surface is only lightly n-type, impedance is small when a low voltage is applied to the detector, but increasing the applied voltage depletes the surface and impedance increases. Thus, as stated above, a light n-type surface is ideal. A typical impedance variation with applied detector voltage for what we believe to be a light n-type surface is shown in fig. 8.

4.2. SUMMARY OF THIS SECTION

Experimental results on guard ring detectors show good agreement with theory for high applied voltages, but discrepancies arise at low voltages due

to surface effects in the etched ring. Surface treatments to overcome these effects are being studied.

5. Energy Resolution as Particle Detector

The main purpose here has been to evaluate electrical noise in a detector amplifier system. It has been shown that, if surface problems are eliminated, reasonable agreement exists between theory using measured values of detector leakage and practical noise measurements. However, other limits to the particle energy resolution of practical detectors may exist.

In general, our energy-resolution experiments using β particles indicate that the limit to β-particle resolution is electrical noise and it appears that the equations derived in the earlier part of the paper may be used to determine the resolution. We measured an energy resolution (full width at half max) of 10 keV, using conversion electrons from an Hg^{203} source and a 0.8 cm^2 detector.

On the other hand, the measured resolution figures for α particles were much larger than is accounted for by electrical noise. The best resolution we obtained on 6-MeV α particles was 22 keV (full width at half max), and, in many cases, resolutions much worse than this were observed. Several early detectors were produced with mechanically polished surfaces and, since surface damage caused by the polishing appeared to penetrate 0.5 μ or more below the surface, it seemed reasonable to attribute some α-particle pulse-spread to absorption in this damaged layer. Recent detectors have used smooth etched surfaces, but the α-particle resolution was not greatly improved by this. Several detectors exhibited multiple peaks in α spectra when only a single peak should have been present. The reason for this multiple peaking is not clear, but it is likely that the poor resolution of even the best detectors is partly due to unresolved multiple peaks. Observation that the spectrum resolution was improved by using long amplifier time constants indicated that the multiple peaks were due to slight changes in charge collection time at different points on the detectors surface. This may have been due to a trapping phenomenon.

An intensive investigation of effects just under the detector surface is required before the ultimate α-particle resolution can be realized. This presumably also applies to other heavily ionizing particles.

6. Construction Details of Guard Ring Counter

All guard ring counters constructed have used phosphorus diffusion into 1500- or 5000-ohm-cm p-type silicon and have had identical guard ring geometries. Wafers 15 to 40 mils thick were cut parallel to the 1,1,1 plane from single optically oriented 2-cm diam silicon crystals. Saw damage was removed by lapping several mils from each side with "Lapmaster" 1950 grinding compound. One side of each wafer was masked with Picein sealing wax and 2 to 5 mils etched from the other side with a polishing HNO_3-HF mixture (10 parts HNO_3 to one part HF). The etched wafers were then cleaned successively in trichloroethylene, methyl alcohol, and deionized water, in preparation for phosphorus diffusion.

Phosphorus diffusion was performed in the quartz-lined 2-in.-diam tube furnace at 900°C. The phosphorus source was P_2O_5 from a furnace-preheated zone held at 210 to 220°C, and carried with about 2 liters per minute of dry nitrogen gas obtained by boiling liquid nitrogen. The P_2O_5 source was aged for at least 1 h prior to diffusion. A typical diffusion schedule is 5 min at 900°C, followed by turning off the furnace and allowing the wafers to anneal. This diffusion schedule was intended to give a calculated junction depth of about 0.05 μ. The junction depth has not been measured, but controlled etching tests showed that it was less than 0.5 μ. The sheet resistance of the diffused layer is found by fourpoint probe measurement to be 4 to 5 ohms per square, which indicates a surface phosphorus concentration of between 5×10^{21} and 10^{22} phosphorus atoms per cm^3 (ref.[3])). The phosphosilicate glass grown on the silicon was not thick enough to interfere with resistivity measurements.

A P^+ back-contact was made for each wafer by removing the phosphorus diffusion from the lapped side by hand-lapping, then by alloying with aluminum or gold-gallium. In each case, about 2 μ of the contact metal was applied by vacuum vaporization

[3]) If the sheet resistance and junction depth are known, the surface concentration can be found from curves given by G. Bakenstross, Bell System Tech. J. (May 1958) pp. 699–709.

and the alloying performed in dry nitrogen at 600°C for Al and 500°C for Au-Ga.

The guard-ring structure was formed by a modified photo-engraving technique. All counters made to date have used the same engraving negative or stencil. The stencil was made on a glass Kodalith plate by a 20-fold reduction of a line drawing that gave a guard ring diam of 0.6 in., a counting area diameter of 0.4 in., and an interelectrode spacing of 2.5 mils. Several attempts were made to use Kodak Photo Resist (KPR) as the etching mask, without success. In all cases the resist was penetrated in about 30 sec with even the weakest silicon etches. The etching procedure which has proved most effective was a mask with Kodak Metal Etch Resist (KMER) followed by etching in silver-glycol[4]). One part of KMER was diluted with two parts of thinner and applied according to the manufacturer's literature. Exposure time was 12 min at 12 in. from a 100-watt mercury arc, with the sensitized wafer and stencil held in contact by a vacuum frame. It is important that the counter be washed with HF just prior to resist application, or the etch will quickly undercut the resist.

Etching was carried out in silver-glycol etch maintained at 25°C in a water bath for times ranging from 5 to 30 min, giving etching depths ranging from 0.5 to 3 μ. No significant differences in performance were noted that were a function of the etching depth. The etching time routinely used was 10 min, which gave 1 μ depth. Before etching, the back contact was protected with Picein wax, as both Al-Si and Au-Si eutectics are soluble in the etchant.

After etching, the counter was washed with deionized water and then methyl alcohol and the resist was removed with trichlorethylene on a cotton swab. A final wash with deionized water followed by drying with a blast of dry nitrogen completed the procedure required before testing the counter.

Several attempts have been made to protect the junction edges with various resins, waxes, and varnishes, but our experience is that these only delayed the absorption of ionic contaminants. The most successful material, yet used has been Dow-Corning XR-6-2044 Silicone resin.

Appendix A

DERIVATION OF NOISE FORMULAE

The general formula for depletion-layer width in an abrupt semiconductor junction is given in all textbooks on the subject as

$$W = 1.05 \times 10^{-6} \left[\frac{E(V_0 - V)}{2\pi q(N_a + N_d)}\right]^{\frac{1}{2}} \left[\left(\frac{N_a}{N_d}\right)^{\frac{1}{2}} + \left(\frac{N_d}{N_a}\right)^{\frac{1}{2}}\right] \text{cm.}$$

where:

E = dielectric constant of material,
V_0 = built-in potential barrier at junction,
q = electronic charge,
V = applied voltage (negative for reverse bias),
N_a = acceptor concentration on "p" side of junction,
N_d = donor concentration on "n" side of junction.

In a junction where the "n" side is much more heavily doped than the "p" side, and where the applied reverse bias is much greater than V_0,

$$W = 1.05 \times 10^{-6} \left[\frac{EV}{2\pi q N_a}\right]^{\frac{1}{2}} \text{cm.}$$

The acceptor concentration is related to the resistivity of the material and to carrier mobility by the equation

$$N_a = \frac{1}{q\mu_h \rho}$$

where ρ = resistivity of p-type material, μ_h = hole mobility.

Therefore,

$$W = 1.05 \times 10^{-6} \left[\frac{EV\rho\mu_h}{2\pi}\right]^{\frac{1}{2}}.$$

For silicon: $E = 12$, and $\mu_h = 480$ cm^2 sec^{-1} V^{-1}
So, $W = 0.32\ (\rho V)^{\frac{1}{2}}$.

A similar equation can be derived where the "p" type material is much more heavily doped than the "n" type material.

To determine the junction capacity we regard the junction as a parallel plate capacitor with plate spacing W:

$$C = \frac{AE}{4\pi W} = 3.3 \times 10^4 (\rho V)^{-\frac{1}{2}} \text{ pF/cm}^2.$$

[4]) For the formula and method of using silver-glycol etch, see Transistor Technology, Vol. III, F. J. Biondi, Ed. (D. Van Nostrand, Princeton, N.J. 1958) p. 158.

To determine the leakage current of the junction, we refer to the work of Sah, Noyce, and Shockley[5]). They show the junction leakage as containing one component due to diffusion of carriers into the depletion layer, and another due to generation of carriers at trapping centers in the depletion layer itself. The probability of generation by direct excitation of electrons from valency to conduction bands is very small, and the trapping centers are necessary to explain the observed lifetimes in silicon. Sah, Noyce, and Shockley derive the following equations for the two leakage-current components:

$$I_g = \frac{q \times n_i \times W}{2\tau_0} \text{ per cm}^2 ,$$

$$I_d = \frac{q \times n \times l}{\tau_0} \text{ per cm}^2 ,$$

where

n_i = number of holes or electrons in intrinsic material,
l = distance from which carriers may diffuse into the depletion layer (the diffusion length in a large volume sample),
τ_0 = minority-carrier lifetime,
n = number of minority carriers in the material,
I_g = generation current,
I_d = diffusion current.

A value of 1.5×10^{10} per cm^3 is assigned to n_i for silicon[6]). Inserting the value of W derived earlier, we have

$$I_g = 38 \frac{(\rho V)^{\frac{1}{2}}}{\tau_0} \text{ m}\mu \text{ amp/cm}^2 .$$

The value to use for n in the diffusion current equation is that for electrons (n_e) in the p region of the detector (if the high-resistivity material is p-type).

We have $n_e \times n_p = n_i^2$,

$$n_e = \frac{n_i^2}{n_h} = n_i^2 \times p\mu_h \times q .$$

Including this in the equation for I_d and putting in values for the constants, we have

$$I_d = 2.75 \frac{\rho \times l}{\tau_0} \text{ m}\mu \text{ amp/cm}^2 .$$

Note added in proof

A private communication received from T. R. Kohler and E. S. Rittner points out an error in this appendix. Sah, Noyce and Shockley assume that the trap level and the Fermi level coincide in position in order to derive the equations relating I_g and I_d to the carrier lifetime. This is not the normal situation and this fact accounts for the unusually long lifetimes indicated by our measurements. We may regard the lifetime τ_0 used in this report as an equivalent lifetime which would apply if the trap and Fermi levels did coincide. The relationship between τ_0 and the true carrier lifetime in the material can then be used to deduce something about the level of the trapping centers.

Appendix B

DERIVATION OF DETECTOR FORMULAE

Several sources of noise are present in a detector-amplifier combination, and the frequency dependence of each may differ from that of the others. Since the amplifier shaping networks limit its frequency response, computation of the noise output of the amplifier involves integration of the product $N(\omega) \times G(\omega)$ (ref.[7])) in the range $\omega = 0$ to $\omega = \infty$ for each source of noise. Individual noise outputs may then be compounded into a single rms noise output by summing the mean square values of all individual terms and taking the square root of the total.

The noise output in itself is unimportant, the quantity of real interest being the signal-to-noise ratio, usually expressed by quoting the input signal charge required to produce an output signal equal to the rms noise. To calculate this, we consider the effect of the amplifier-shaping networks on signal as well as on noise. In outline, this is the procedure used to derive the formulae appearing in table 1. To simplify, we have considered only that case in which the integrating and differentiating networks in the amplifier have the same value of time constant τ.

[5]) C. T. Sah, R. N. Noyce, and W. Shockley, Carrier Generation and Recombination in p–n Junctions, Proc. I.R.E. **45** (1957) 1228.

[6]) See E. M. Conwell, Properties of Silicon and Germanium, Proc. I.R.E. **46** (1958) 1281.

[7]) $N(\omega)$ = frequency-dependent noise input term; $G(\omega)$ = frequency-dependent amplifier gain, where $\omega = 2\pi f$.

1. Sources of Noise

(a) *Tube Shot Noise.* It is usual to represent this by including an equivalent resistance R_{eg} in series with the grid of the tube. For a triode, $R_{eg} = 2.5/g_m$. The mean square noise generated by this resistor at the input in a small bandwidth is given by

$$\langle e_T^2 \rangle = 4KT\, R_{eq}\, \Delta f = \frac{10KT}{g_m} \Delta f = \frac{5KT}{\pi g_m} \Delta\omega\,.$$

(b) *Tube Flicker Noise.* This is caused by fluctuations in the cathode of the tube and the mean square noise due to this source obeys a $1/f$ law.

Thus

$$\langle e_F^2 \rangle = \frac{A}{f} \Delta f = A \frac{\Delta\omega}{\omega}\,,$$

where A is a constant found experimentally to be approximately 10^{-13}.

(c) *Tube Grid Current Noise.* The tube grid current is subject to the usual statistical fluctuations:

$$\langle i_G^2 \rangle = 2q \times i_g\, \Delta f\,.$$

In the frequency range passed by the amplifier, if the detector load resistance and tube grid leak are made large in value, the impedance in which grid current fluctuations can develop voltage is almost entirely capacitive (due to the total capacity of tube and detector), and we have

$$\langle e_G^2 \rangle = \frac{2 \times i_g}{\omega^2 C^2} \Delta f = \frac{q \cdot i_g}{\pi\omega^2 C^2} \Delta\omega\,.$$

(d) *Detector Leakage Noise.* This, like the grid current of the tube, is subject to statistical fluctuations, resulting in a noise given by

$$\langle e_L^2 \rangle = \frac{q \times i_L}{\pi\omega^2 C^2} \Delta\omega\,.$$

(e) *Input Resistance Noise.* Shunt resistance in the input circuit produces resistance noise, and a portion of this noise appears across the input capacity of the amplifier. If shunt resistance is large, the current mean square noise produced by it is given by

$$\langle i_R^2 \rangle = \frac{4KT}{R} \Delta f = \frac{2KT}{\pi R} \Delta\omega\,,$$

where T is absolute temperature.

The noise voltage^2 produced across the input capacity is therefore

$$\langle e_R^2 \rangle = \frac{2KT}{\pi R} \Delta\omega \cdot \frac{1}{\omega^2 C^2} = \frac{2KT}{\pi\omega^2 RC^2} \Delta\omega\,.$$

(f) *Total Noise at Input to Amplifier.* Summing the noise terms described above, we have

$$\langle e_I^2 \rangle = \langle e_T^2 \rangle + \langle e_F^2 \rangle + \langle e_G^2 \rangle + \langle e_R^2 \rangle$$
$$= \left[\frac{5KT}{\pi g_m} + \frac{10^{-13}}{\omega} + \frac{1}{\pi\omega^2 C^2}\left(q(i_g + i_L) + \frac{2KT}{R}\right)\right] \Delta\omega\,.$$

2. Effect of Amplifier Bandwidth on Signal and Noise at Output

The gain of an amplifier having equal integrating and differentiating circuits varies with frequency

$$G = G_0 \frac{2\pi f\tau}{1 + 4\pi^2 f^2 \tau^2} = G_0 \frac{\omega\tau}{1 + \omega^2\tau^2}\,.$$

Thus the mean square moise at the amplifier output is given by

$$\langle e_0^2 \rangle = \int_{\omega=0}^{\omega=\infty} G_0^2 \left[\frac{5KT}{g_m} \frac{\omega^2\tau^2}{(1 + \omega^2\tau^2)^2} + \right.$$
$$\left. + \frac{10^{-13}\,\omega\tau^2}{(1 + \omega^2\tau^2)^2} + \frac{\tau^2}{C^2(1 + \omega^2\tau^2)^2}\left((i_g + i_L) + \frac{2KT}{R}\right)\right] d\omega\,.$$

Note that each of the three major terms in the integral has a different frequency dependence.

Performing the integration yields the result

$$\langle e_0^2 \rangle = G_0^2 \left[\frac{1.25KT}{g_m\tau} + 0.5 \times 10^{-13} + \right.$$
$$\left. + \frac{\tau}{4C^2}\left(q(i_g + i_L) + \frac{2KT}{R}\right)\right].$$

If the input signal consists of a very small pulse of charge, the output signal produced by the amplifier is given by

$$\text{Output Signal} = \frac{Q}{2.73} \times \frac{G_0}{C}\,.$$

where Q is the charge produced by the ionizing event in the detector.

Thus the detector charge input producing an output signal equal to the rms noise level at the output is given by

$$\langle Q_{eff}^2 \rangle = 8C^2 \left[1.25 \frac{KT}{g_m\tau} + 0.5 \times 10^{-13} + \right.$$
$$\left. + \frac{\tau}{4C^2}\left(q(i_g + i_L) + \frac{2KT}{R}\right)\right].$$

Putting:

$$q = 1.6 \times 10^{-19} \text{ coulombs}$$

$$\frac{KT}{q} = 25 \text{ mV} \qquad i_g \text{ in m}\mu\text{amp}$$

$$t \text{ in } \mu \text{ sec} \qquad i_L \text{ in m}\mu\text{amp}$$

$$R \text{ in M}\Omega \qquad g_m \text{ in mA/V},$$

we have

$$\langle Q_{\text{eff}}^2 \rangle = 4 \times 10^{-35} \frac{C^2}{g_m \tau} + 4 \times 10^{-37} C^2 + $$

$$+ 3.2 \times 10^{-34} \tau (i_g + i_L) + 1.6 + 10^{-32} \frac{\tau}{R} \text{ coulomb}^2 .$$

The various contributions listed in table 1 are items in this equation. In order to express the input signal equivalent to noise in terms of energy absorbed from the incident radiation it is necessary to establish a value for the energy absorption per hole electron pair produced in the detector. The generally accepted value for silicon is 3.6 eV/hole-electron pair.

$\langle E_{\text{eff}}^2 \rangle$ = Mean square energy spread due to noise

$$= \frac{\langle Q_{\text{eff}}^2 \rangle}{1.6^2 \times 10^{38}} \times 3.6^2 = 5 \times 10^{38} \times \langle Q_{\text{eff}}^2 \rangle .$$

If $\langle E_{\text{eff}}^2 \rangle$ is expressed in keV^2 we have

$$\langle E_{\text{eff}}^2 \rangle = 5 \times 10^{32} \langle Q_{\text{eff}}^2 \rangle \text{ keV}^2 .$$

This equation is used to convert the values in the first column of table 1 to those in second column.

Appendix C

SPECIAL ELECTRONIC CIRCUITS

A standard linear pulse amplifier (Berkeley Model V) was used for noise and resolution measurements. This was preceded by a special low-noise preamplifier and followed by a biased amplifier unit. These two units are described below. The main amplifier was modified to contain equal integrating and differentiating time constants, the actual value of the time constant being controlled by a switch giving values of 0.2, 0.5, 1, 2, and 5 μsec. The gain stability of this system was not really adequate for accurate α-particle resolution measurements, but in the experiments described here, a standard pulse was always fed into the input of the preamplifier and the spectrum of the reference pulses was examined to determine that the gain drift during any particular experiment was negligible. We are now developing a more stable amplifier.

1. Low-Noise Preamplifier

The schematic of this unit is shown in fig. 9. A 417A tube V1 is used in a cascode connection with tube V2(a) to give good noise performance. Tubes V1, V2(a), and V2(b) are arranged as a feedback integrator, capacitor C5 acting as the integrator capacitor. The anode load of V2(a) is "bootstrapped" from the cathode of V2(b) to increase the feedback loop gain, thereby increasing the effective capacity (looking into the input of the amplifier) to a large value (about 500 pF). The output signal from the anode of V2(b) feeds the White cathode-follower V3(a, b) which provides a low-output-impedance driver for the cable connecting the preamplifier to the main amplifier.

Note that an integrator arrangement is preferred to a conventional amplifier. This is convenient, since the output from the integrator is less dependent on detector capacity than it would be with a conventional amplifier. The integrator is slightly worse with respect to noise, since the integrating capacitor (C5) must be added to the tube input capacity used in the noise calculation. However, we feel the convenience of the integrator arrangement more than offsets its slightly degraded noise performance.

2. Biased Amplifier

The purpose of this unit, which follows the main pulse amplifier, is to provide a method of subtracting a selected dc voltage from all pulses at the amplifier output and of linearly amplifying the part of pulses exceeding the dc voltage by preselected factors. The particular unit described here also shapes the pulses suitable for feeding any common type of multichannel pulse-amplitude analyzer.

The range of bias voltages available in the circuit shown in fig. 10 is 0 to + 50 V. Post-bias gains of $\times 1$, $\times 2$, $\times 5$, and $\times 10$ are provided. The signal obtained at the output of the unit is of almost constant amplitude for a 1-μsec period at the peak of the pulse. Performance of the unit was satisfactory when

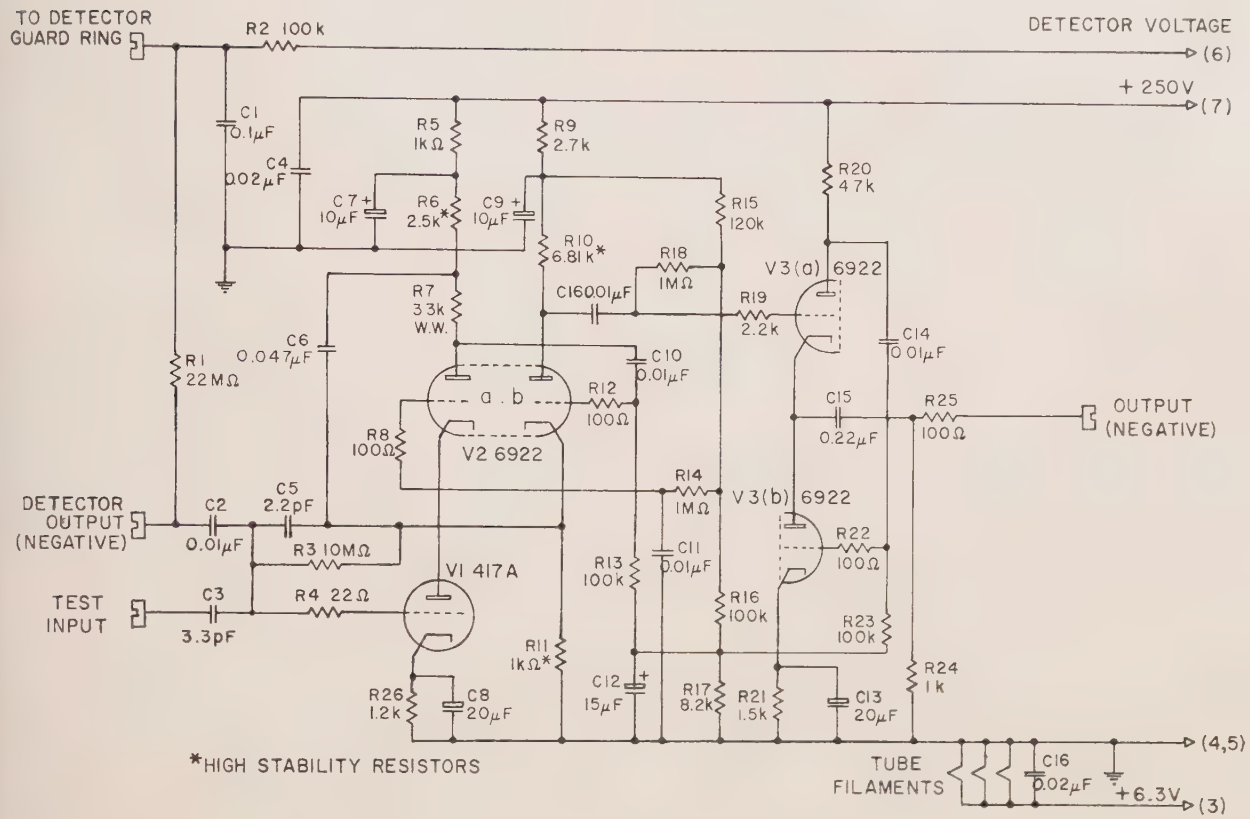

Fig. 9. Low-noise preamplifier for S-C detectors.

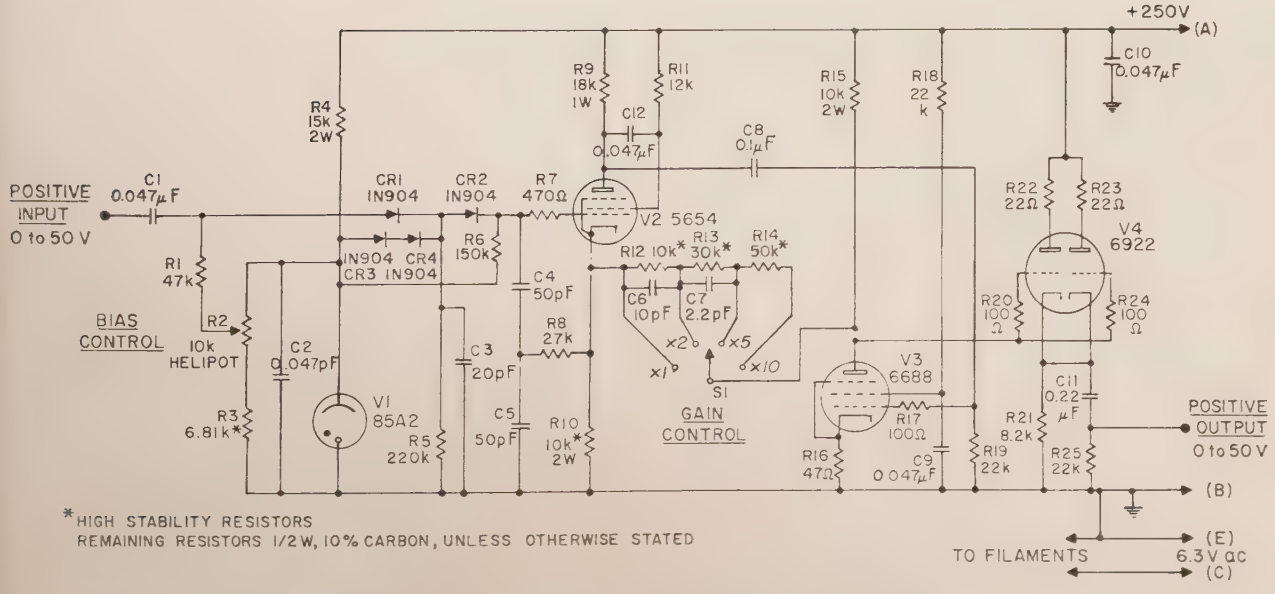

Fig. 10. Biased amplifier for α-particle resolution measurements.

fed with input pulses produced by an equal-time-constant amplifier having time constant values in the range 0.2 μsec to 5 μsec.

In the circuit of fig. 10, diode CR1 is back-biased by the bias supply, and only those pulses exceeding the bias cause it to conduct. Diode CR2, combined with the capacitors in the grid circuit of V2, lengthens the pulse and shapes it for analysis. Diodes CR3 and CR4 are included to compensate for the effects of temperature changes on the voltage drops in CR1 and CR2.

The signal appearing at the grid of V2 is amplified by the feedback amplifier containing V2 and V3. Switch S1 controls the degree of feedback and therefore the gain. Tube V4 acts as an outputcathode follower providing a low-impedance-output source.

The method used to achieve to flat-topped pulse at the grid of V2 is of interest. A normal diode lengthener containing a single capacitor to ground would produce an exponential fall in potential at the grid of V2. It may be shown that by applying feedback through R8, and by splitting the lengthener capacitor into the series combination C4 and C5, a pulse having almost a flat top for a large fraction of its total recovery time can be produced. The value of R8 must be chosen to achieve this result.

Acknowledgements

The assistance of L. Shifferle, E. Woo, and F. Gin in constructing counters and apparatus used in these experiments is gratefully acknowledged. The authors also thank Prof. A. English for helpful suggestions as the work proceeded, and Mrs. E. Potter for preparing the diagrams used on this report. This work was performed under the auspices of the U.S. Atomic Energy Commission.

NUCLEAR INSTRUMENTS AND METHODS 12 (1961) 263–277; NORTH-HOLLAND PUBLISHING CO.

A PAIR SPECTROMETER FOR ENERGIES UP TO 2 GeV

G. BOLOGNA, G. DIAMBRINI, R. TOSCHI†

C.N.E.N. – Laboratori Nazionali di Frascati

and

A. S. FIGUERA††, U. PELLEGRINI §, B. RISPOLI §§, A. SERRA

C.N.E.N. – Laboratorio Elettronica

Received 28 February 1961

A pair spectrometer, having the capacity of analyzing photon energies up to 2 GeV is described.

The optical properties of the instrument are examined by calculating the horizontal and vertical deviation matrices.

Further, the magnetic measurements that were made both inside and outside the magnet gap in order to obtain information on the electron trajectories, are described. The method used in calculating the trajectories is given. The calculated trajectories are compared with the ones obtained experimentally by means of the floating wire technique, a description of which is also given.

Last, the electronic devices used in the electron detection are described.

1. Introduction

An electron pair spectrometer has been developed chiefly with the purpose of determining the energy spectrum of the Frascati 1 GeV electronsynchrotron γ-ray beam and with characteristics such as to allow also various experiments on electrodynamics. The maximum measurable photon energy is 2 GeV.

The pair spectrometer consists of the following parts:

a. magnet, for the deflection of electron pairs;

b. vacuum chamber;

c. converter, in which the γ-rays produce the electron pairs;

d. scintillation detector telescopes and electronic equipment for the detection of electron pairs.

2. Description of the Instrument

2.1. MAGNET DESCRIPTION

Fig. 1 shows the magnet and the exit side of the vacuum chamber. The magnet is of the shell type, with the two flux return paths placed on both sides of the path of the γ-ray beam.

Fig. 2 shows a cross section of the upper yoke obtained with a plane parallel to the pole surfaces.

In contrast to the design of previous spectrometers[1,2]), the high momentum trajectories pass out of the field through the exit face of the magnet rather than a side. Hence there is essentially no focusing in the horizontal plane. With this design it is possible to keep the size of the instrument a minimum.

The technical details of the magnet are as follows:

Maximum induction in the gap:	20 kgauss
Iron quality:	T 11 S Terni, forged at low C content (30 KAT/m, 20 kgauss)
Iron weight:	17.8×10^3 kg
Magnet height:	1326 mm
Pole faces:	flat and parallel within $\pm$ 0.1 mm
Gap height:	100 $\pm$ 0.1 mm
Pole height:	15 mm
Excitation coil:	120 turns around each pole
Maximum current:	2100 A
Coil:	square copper bars (13.5×13.5) mm² with a central hole 7 mm in diameter
Winding weight:	0.75×10^3 kg
Resistance (at 70° C):	0.90 Ω
Inductance:	57 mH
Cooling water:	flow 1.3 l/s; pressure 3 kg/cm² .

† Now at C.N.E.N.-Laboratorio Gas Ionizzati, Frascati.

†† Now at the Physics Department, University of Maryland.

§ Now at LABEN, Milano.

§§ C.N.E.N.-Laboratorio Elettronica and Istituto di Fisica, Università di Roma.

[1]) K. M. Crowe and R. H. Phillips, Phys. Rev. 96 (1954) 470; K. M. Crowe, Thesis-Report UCRL 2050 (1952) (unpublished).

[2]) D. H. Cooper, Thesis-Cal. Inst. Techn. (1955) (unpublished).

The above characteristics are justified by the following considerations.

Owing to the high induction value required in the gap, the use of high poles must be avoided to prevent saturation at the pole bases; poles only 15 mm high have therefore been used. Because of the high induction value, and of the limitation of the number of turns possible, the current density in the coil must be very high (15 A/mm²) and requires a considerable flow of cooling water. Due to the small coil window ((230 × 130)mm²), the magnetic flux loss in this magnet is small. Thus the magnet weight (18.5 ton) is maintained to a minimum for the required stored energy.

Fig. 2 shows the holes bored in the upper yoke, which permit the introduction of the light pipes for scintillation detectors inside the magnet gap†. With the exception of two, these holes are set in pairs with their centers on circles which are tangential to the direction of the photon beam at the point C of the converter††. All the holes can be plugged when not used so as to restore the iron continuity; the plugs are flanged on the top and provided with a vacuum gasket.

† These counters have not been used to determine the bremsstrahlung spectrum of the electronsynchrotron.

†† Double coincidences for each branch of a pair may be obtained in this manner, and spurious counts generated by back scattering of the walls may mostly be eliminated.

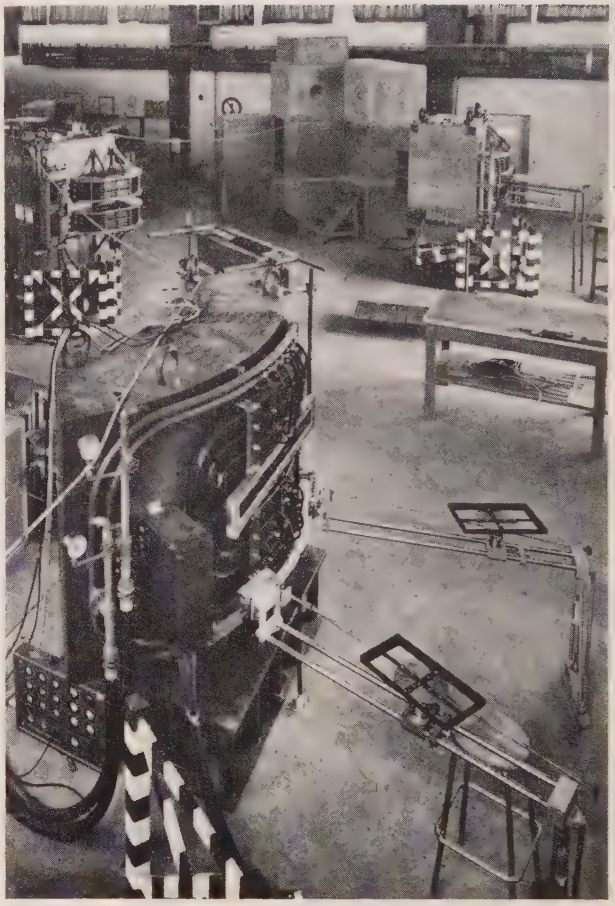

Fig. 1.
Pair spectrometer: the magnet and the vacuum chamber.

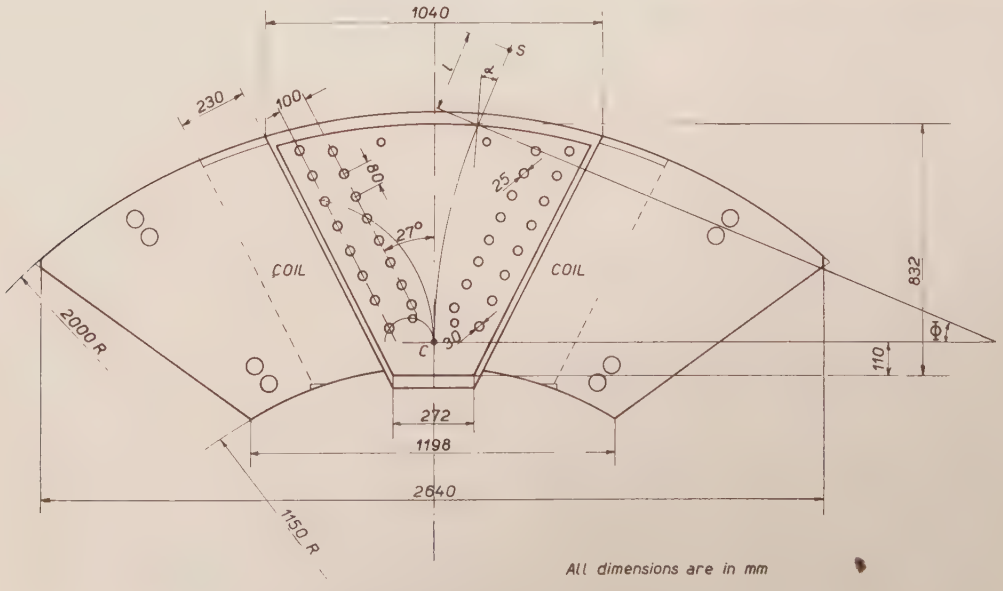

Fig. 2. Magnet: cross section of the upper yoke.

2.2. DESCRIPTION OF THE VACUUM CHAMBER

Fig. 1 shows the vacuum chamber projecting from the gap.

In fig. 3 the vacuum chamber can be seen laying on the lower yoke. It is made of stainless steel and consists of two walls connected by two flanges. This chamber is introduced into the space left between the poles when the upper yoke is lifted. The walls of the chamber are fitted in appropriate grooves made around the poles and provided with vacuum gaskets. The chamber is screwed to the lower and upper yokes. A vacuum of 0.03 mm Hg may be maintained with the help of a conventional rotary pump having a speed of 10^3 l/min. Since the polar faces were used as upper and lower chamber walls, we are not losing any height or precision in the gap.

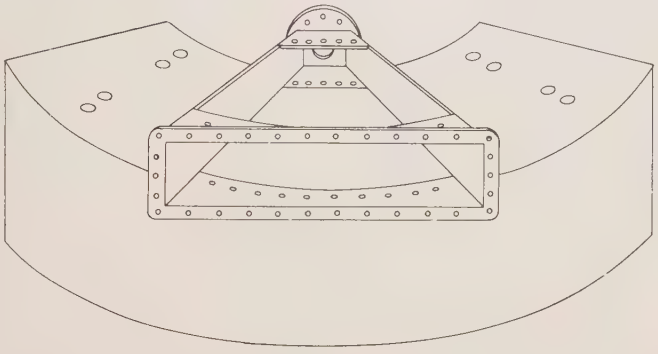

Fig. 3. Vacuum chamber.

Applied to the two flanges are: at the entrance a tube 15 cm in diameter, 4 m long, passing through a broom magnet to a collimator†, and at the exit a mylar foil 0.2 mm thick (equal to about 5×10^{-4} radiation lengths). The equivalent thickness of the residual air and of the mylar foil is so small that no background disturbances arise, owing to the characteristics of the counter telescopes (see section 7).

2.3. DESCRIPTION OF THE CONVERTERS – SPECTROMETER ALIGNMENT

We use three aluminum converters 1; 0.1; 0.01 mm thick, equal to 0.011; 0.0011; 0.00011 radiation lengths, respectively. They are applied to plexiglass rings, each having a diameter of 6 cm. The rings are mounted on a turntable which can be positioned remotely, so that they may be interposed in the path of the beam; each ring is automatically turned up within the beam when it reaches the proper position.

Fig. 4 shows one of these converters†† intercepting the γ-ray beam; the others are laying on the turntable and do not disturb the beam. On this device a place is reserved for a brass ring 3 mm thick, for adjusting the position of the beam and collimators. The initial alignment of the spectrometer along the γ-ray beam has been obtained by placing another brass ring, slightly larger in diameter than the one mentioned above, at the exit of the spectrometer, with its center on the spectrometer axis. The position of the spectrometer was adjusted so that the shadows of the two rings in a radiograph of the γ-ray beam appeared concentric. Thereafter, the spectrometer was no longer shifted and, in order to align the beam, one had to make little adjustments of the tantalum target inside the synchrotron and of the two collimators inserted in the γ-ray beam, until the photographed shadow of the first ring alone appeared centered on the beam.

3. Optical Properties of the Spectrometer

The optical properties of the spectrometer were determined during the design by calculating the

† The general experimental arrangement is described in other papers[3]).

†† The figure shows also another device used to control a monocristalline sylicon converter employed in an another experiment[4]). At present the single crystal is removed and does not disturb the beam. A scintillation detector used for the same experiment may also be seen.

[3]) G. Diambrini, A. S. Figuera, A. Serra and B. Rispoli, Nuovo Cimento **15** (1960) 500, and Nuovo Cimento **19** (1961) 250.

[4]) G. Bologna, G. Diambrini and P. G. Murtas, Phys. Rev. Letters **4** (1960) 134.

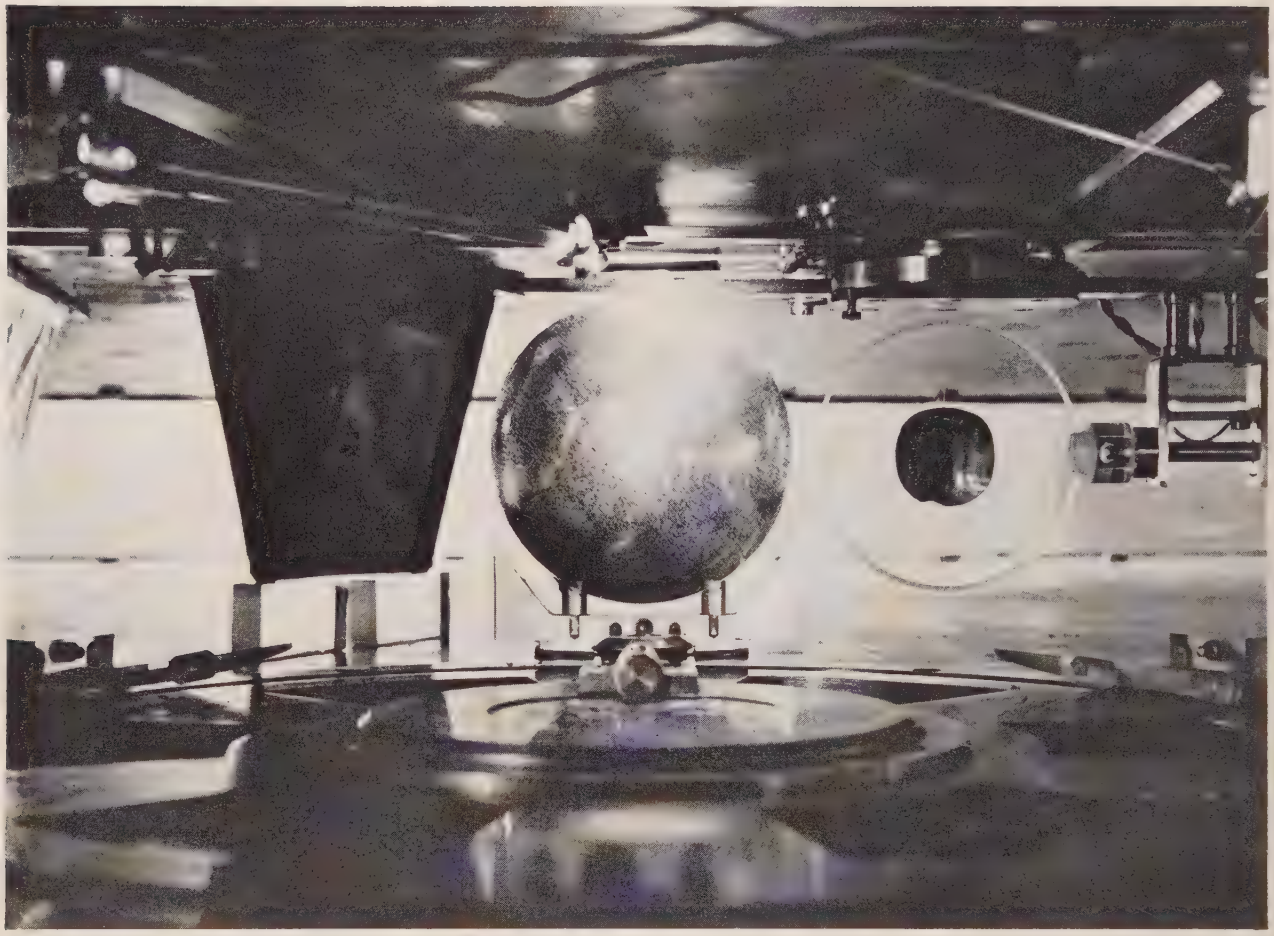

Fig. 4. View of the converter turntable, showing one aluminum converter in position.

matrix elements $H_{ij}(i, j, = 1, 2, 3)$; $V_{hk}(h, k = 1, 2)$ of the horizontal and vertical deflections in the Gauss linear approximation, obtained by resolving the equation of motion[5]). The field was assumed $B = \text{const.} \neq 0$ in the gap of the magnet, and $B = 0$ outside.

Let us consider an electron of momentum p emerging from the center C of the converter and directed, initially, along the spectrometer axis; the trajectory lies in the median plane (M.P.), which is horizontal. Let r be the radius of curvature of that portion of the trajectory internal to the spectrometer; ϕ be its deflection angle; α be the angle between the trajectory and the normal to the edge of the spectrometer; l be the distance of a point S from the edge, measured along the trajectory—point in which will be placed the center of the first detector (see fig. 2). We shall call this the principal trajectory.

The quantities r, ϕ, α are assumed positive for all trajectories bending to the right of the spectrometer axis and negative for those to the left. Let $p + \Delta p$ be the momentum of an electron which emerges from the point (ξ_0, ζ_0) of the convertor, measured with respect to the point C. The coordinates (ξ, ζ) of this electron at the detector, relative to the point S are given by

$$\begin{pmatrix} \xi \\ \xi' \\ \Delta p/p \end{pmatrix} = \begin{pmatrix} H_{11} & H_{12} & H_{13} \\ H_{21} & H_{22} & H_{23} \\ H_{31} & H_{32} & H_{33} \end{pmatrix} \begin{pmatrix} \xi_0 \\ \xi'_0 \\ \Delta p/p \end{pmatrix}$$

$$\begin{pmatrix} \zeta \\ \zeta' \end{pmatrix} = \begin{pmatrix} V_{11} & V_{12} \\ V_{21} & V_{22} \end{pmatrix} \begin{pmatrix} \zeta_0 \\ \zeta'_0 \end{pmatrix}.$$

[5]) P. G. Sona, Internal note no. 3 (1958) – I.N.F.N., Laboratori Nazionali di Frascati.

The primes signify the derivative with respect to s, the distance measured along the principal trajectory. Then we have:

$$H_{11} = \left(1 + \frac{l}{r}\tan\alpha\right)\cos\phi - \frac{l}{r}\sin\phi$$

$$H_{12} = r\left(1 + \frac{l}{r}\tan\alpha\right)\sin\phi + l\cos\phi$$

$$H_{13} = r\left(1 + \frac{l}{r}\tan\alpha\right)(1 - \cos\phi) + l\sin\phi$$

$$H_{21} = \frac{l}{r}(\tan\alpha\cos\phi - \sin\phi)$$

$$H_{22} = \tan\alpha\sin\phi + \cos\phi$$

$$H_{23} = \tan\alpha(1 - \cos\phi) + \sin\phi$$

$$H_{31} = H_{32} = 0\,; \qquad H_{33} = 1\,. \tag{1}$$

$$V_{11} = 1 - \frac{l}{r}\tan\alpha$$

$$V_{12} = \left(1 - \frac{l}{r}\tan\alpha\right)r\phi + l$$

$$V_{21} = -\frac{l}{r}\tan\alpha$$

$$V_{22} = 1 - \phi\tan\alpha\,. \tag{2}$$

Since the spectrometer has a symmetry plane, horizontal and vertical deviations are quite independent and decoupled, so that we may take them into account separately.

3.1. DEVIATION IN THE HORIZONTAL PLANE

The following factors influence the dispersion and resolving power:

1. Finite width of the converter and angular spread of the γ-ray beam.

2. Multiple scattering of the particles in the converters and pair emission angle different from zero.

3. Energy loss by ionization and radiation of the particles in the converter.

Let us consider an electron having a momentum $p + \Delta p$, emerging from C in the direction of the principal trajectory. Let us call this new trajectory "varied".

The dispersion and resolving power are given, respectively, by:

$$D = \frac{\xi}{\Delta p} = \frac{|H_{13}|}{p}$$

$$P = \frac{p}{\Delta p} = \frac{|H_{13}|}{\xi}\,. \tag{3}$$

Let us show now that the first factor cited above does not introduce any aberration, as far as the measurement of the γ-ray beam energy spectrum is concerned. As may be seen later on (see section 7), only one counting channel is being used and it consists of two counter telescopes placed in a symmetrical position with respect to the spectrometer axis; the detectors are placed perpendicularly to the principal trajectory passing through their center. Let us assume that the cross section of the γ-ray beam at the converter is circular with a radius c (we shall call $2c$ the "width" of the converter) and that 2ω is the angular spread of the beam. Let $2a$ be the width of the first detector of each telescope. At point P_- of the detector, a distance ξ from point $S_- \equiv S$, the momentum spread of an electron leaving the edge of the converter in the same direction as the creating photon, is:

$$\frac{\delta_- p}{p} = \frac{\xi_- \mp cH_{11} \mp \omega H_{12}}{H_{13}}\,.$$

Let us assume that the positron created simultaneously with the preceding electron crosses the detector in a point P_+, ξ_+ distant from S_+, symmetric point of S_-, with respect to the spectrometer axis. Taking into account the algebraic signs of r, ϕ, and α, we have from (1):

$$\frac{\delta_- p}{p} + \frac{\delta_+ p}{p} = \frac{\xi_-}{H_{13}} - \frac{\xi_+}{H_{13}}\,,$$

H_{13} being relative to S_-; therefore we obtain the algebraic sum of the momentum spreads that we would have for the principal trajectories. This means that, *in linear approximation*, the photon is detected as it passed through the center of the converter directed exactly as the axis of the spectrometer, i.e. as if the source were a point.

It is useful to calculate the maximum angle β between the principal trajectory and the one leaving from the edge of the converter, when they cross the first detector: this angle enables us to calculate the dimensions that the following detectors should

have in order to collect all the electrons passing through the first detector†.

We obtain:

$$\beta = \frac{H_{23}}{H_{13}}(a + cH_{11} + \omega H_{12}) - (cH_{21} + \omega H_{22}) . \quad (4)$$

As far as the second factor is concerned, we can say that the aberrations caused by the multiple scattering and by the emission angle of the electrons in the converter modify the triangular resolution function of the detectors[2]). With the thickness of the converters now used and at the energies that concern us, this effect may be neglected as compared with the aberrations produced by the same causes in the vertical plane. In such cases the ionization and radiation energy losses in the converter are also negligible.

3.2. DEVIATION ON THE VERTICAL PLANE

The limiting angles with respect to the spectrometer axis, at which an electron can be emitted in the vertical plane at a height z above the M.P., so that it may be collected by the first detector, $2h$ in height, are given by:

$$\theta_{l_{1,2}} = \frac{1}{V_{12}}[\pm h - zV_{11}] , \quad (5)$$

with $|z| < c$.

Taking these angles into account, we may determine the vertical counting losses due to the multiple scattering and the emission angle of the electrons, as a function of the photon energy and of the converter and detector heights. The calculation is given in the second paper of ref.[3]).

The maximum γ angle defined similarly to the β angle, but in the vertical plane is given by:

$$\gamma = \frac{V_{22}}{V_{12}}[h + cV_{11}] - cV_{21} . \quad (6)$$

3.3. APPLICATION TO OUR TELESCOPES

For the counting channel being used we took:

$$r = 1.67\ m \qquad l = 1\ m$$
$$\phi = 26°30' = 0.464\ \text{rad} \qquad \alpha = 21°50' . \quad (7)$$

† Actually one should also take into account the multiple scattering in the detectors.

We therefore obtain from (1) and (2):

$$\| H_{ij} \| = \begin{pmatrix} 0.84 & 1.82 & \mp 0.67 \\ -0.054 & 1.07 & \mp 0.49 \\ 0 & 0 & 1 \end{pmatrix}$$

$$\| V_{hk} \| = \begin{pmatrix} 0.76 & 1.59 \\ -0.24 & 0.81 \end{pmatrix} , \quad (8)$$

with the upper or lower algebraic sign, depending on whether it concerns point S of fig. 2 or its symmetrical with respect to the spectrometer axis. From the value of V_{11}, which represents the linear vertical magnification, we deduce that, for $l = 1$ m, the spectrometer has weak focusing properties on the vertical plane.

From (3) we obtain:

$$\frac{1}{pD} = \frac{\Delta p/p}{\xi} = 1.5\,\%/\text{cm} . \quad (9)$$

As can be seen from section 7 and from ref.[3]), we have:

$$2a = 1.8\ \text{cm} \qquad 2h = 5.4\ \text{cm}$$
$$2c = 5.3\ \text{cm} \qquad 2\omega = 3.6\ \text{mrad} . \quad (10)$$

We obtain therefore from (4) and (6):

$$\beta = 25\ \text{mrad}$$
$$\gamma = 31\ \text{mrad} . \quad (11)$$

Further, we have from (5):

$$\theta_{l_{1,2}} = [\pm 17.7 - 4.78z] \times 10^{-3}\ \text{rad} , \quad (12)$$

z being measured in cm.

4. Magnetic Measurements

4.1. GENERAL CONSIDERATIONS

It is very likely that the assumption of a step function field, although sufficient for the calculation of the deviations from the principal trajectory, i.e., of the matrices $\| H_{ij} \|$, $\| V_{hk} \|$, does not apply to the calculation of the principal trajectory itself.

A better approximation could be obtained by substituting the mechanical length of the magnet by its "magnetic" length, thus taking into account also the fringing field.

For this purpose it is necessary to measure the behaviour of the magnetic field. We preferred to have the measurements analyzed directly by an

electronic computer, so as to obtain a higher precision. As one may see in section 5, the computation has given us both the principal and the varied trajectories. As a further check, these trajectories have been compared with the ones obtained by means of the floating wire technique (see section 6).

For determining the principal trajectories it is sufficient—owing to the existence of a symmetry plane—to determine the distribution B_z of the field component perpendicular to the M.P. on the M.P. itself. The B_z distribution ought to be measured with several excitation currents, but since it was observed that at the converter center C the field is a linear function of the current, at least up to 15 kgauss, we assumed that the B_z distribution, with respect to the value B_c at the converter, was independent of the excitation current. The measurements were therefore taken when the value B_c was 10 kgauss.

Different methods were employed for the inner and outer positions.

4.2. MEASUREMENTS INSIDE THE GAP

Inside the gap we measured the relative difference of magnetic field:

$$\rho = \frac{B_z - B_c}{B_c} = \frac{\Delta B}{B_c} \qquad (13)$$

B_z being the vertical component of the field (coincident now with the field itself) existing at a certain position in the M.P. and $B_c = 10$ kgauss the field existing at the center C of the converter.

The measurements were performed with an electronic fluxmeter of the Dicke type[6]) and a coil, 12 mm in diameter and 20 mm in height. The coil dimensions are justified by the field homogeneity (see later on). In the tested region the coil electric axis always coincides with its geometrical axis.

In order to determine the coil position, we used a plexiglass plate, fitted to the lower pole. On it we made a square grid of holes, in which the coil support could be inserted. The centers of the holes were spaced by 1 cm. The geometric center of the coil was always on the M.P. within $\pm$ 0.1 mm, its axis being vertical within $\pm$ 30′.

[6]) G. Diambrini and G. Ghigo (to be published).

In order to obtain ρ, the flux variation corresponding to ΔB was measured by moving the coil on the plate and that corresponding to B_c by rotating it through 180° $\pm$ 30′, at C. With such an angular uncertainty the measurements of the vertical components was achieved with an error lower than $\pm$ 0.05%.

During the measurements the excitation current was maintained stable within $\pm$ 0.1%, but the field fluctuations were, however, still of the order of ΔB. Hence we tried to compensate them by means of a fixed coil connected to the movable one, and identical to it, in such a way that the flux variations with time tend to compensate one another. Thus the error in the determination of ΔB could be maintained within $\pm$ 1 gauss. To minimize the fluxmeter error we always used the same scale. In order that the instrument indication corresponding

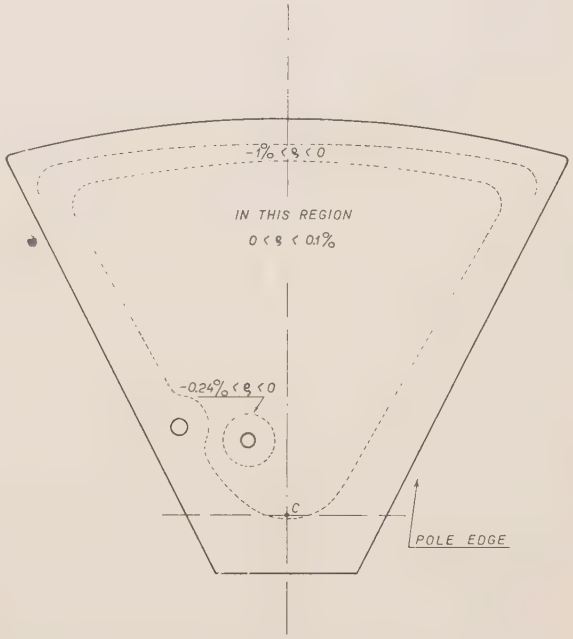

Fig. 5. Plot of the magnetic field distribution. The variation of the field within several regions is indicated.

to ΔB and B_c had about the same value, in measuring B_c, we used a resistive divider, from which one may derive a convenient fraction (having an error of $\pm$ 0.1%) of the voltage induced at the coil ends.

Taking into account all the errors, the maximum absolute error in the determination of $\delta\rho$ is:

$$\delta\rho = \pm\, 0.0001\,.$$

In the central region of the gap, where the magnetic field varies little, the distance between two successive measurements was 5 cm; towards the edges, where the field variation is stronger, steps of 1 cm was chosen. There were 600 measurements altogether.

Fig. 5 shows the results; it indicates the M.P. regions inside of which ρ lies between the values written in the figure. At the point C we determined the dependence of the magnetic field upon the excitation current by using a nuclear magnetic resonance method[7]). The error in the field measurement was $\pm$ 0.02%; the one in the current $\pm$ 0.1%.

4.3. MEASUREMENTS OUTSIDE THE GAP

Towards the edge of the magnet the use of the fluxmetric method previously mentioned did not prove convenient, inasmuch as the magnetic field variation is no longer linear with the displacement and it is therefore difficult to ascertain the exact position of the coil electric axis. Further, the use of a coil outside the magnet requires too much time.

We have therefore used a Hall probe[8]) of $11 \times 3 \times 1$ mm^3 in size. A 150 mA current, stabilized within $\pm$ 0.1%, supplied by a current generator, was sent to one electrode pair. The other electrodes, which supplied the Hall voltage, were connected to a suitable resistor, with the purpose of linearizing the probe output. The voltage across the terminals of this resistor was measured with a L & N K3 potentiometer. The probe had previously been calibrated with the nuclear magnetic resonance method. An error of $\pm$ 0.1% was included, due to the Hall constant variation with the temperature.

The probe was mounted on an appropriate arm that enabled us to introduce it up to where the magnetic field did not differ more than 0.1% from the value B_c. In view of the circular sector shape of the magnet, it proved convenient to move the probe on the M.P. along straight lines converging at the curvature center. Measurements were made along 16 radial lines; altogether 600 points were tested.

Fig. 6 shows the behaviour of the ratio (measured along the spectrometer axis)

$$\sigma = \frac{B_z}{B_c} . \tag{14}$$

Bearing in mind all the causes of error described above, we can say that the maximum error in the determination of σ was

$$\frac{\delta\sigma}{\sigma} = \pm 0.3\% .$$

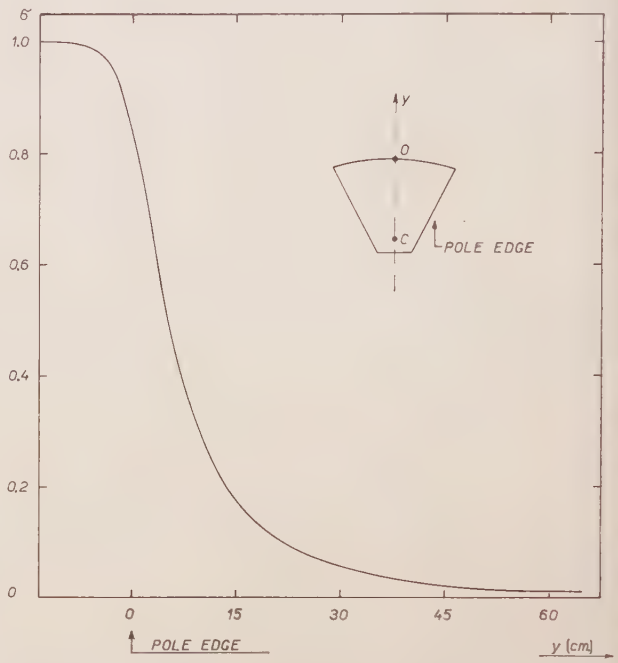

Fig. 6. Results of the magnetic measurements outside the gap, along the spectrometer axis.

From fig. 6 one can deduce that the equivalent magnetic length along the spectrometer axis exceeds the mechanical length of the magnet by an amount of 8.7 $\pm$ 0.1 cm. In the other useful directions, the variation of σ never exceeds $\pm$ 0.005. This figure corresponds to a variation of the magnetic length less than $\pm$ 0.3 cm.

5. Calculation of the Trajectories

5.1. GENERAL CONSIDERATIONS

The particle trajectories have been obtained from the magnetic measurements with an electronic computer†.

[7]) G. Bologna, Thesis – (1955) (unpublished).
[8]) J. L. Symonds, Rep. Progr. Phys. **18** (1955) 83.
[9]) G. Pesamosca, Thesis – (1960) (unpublished).

† The magnetic measurement data and the equations for the principal and varied trajectories were programmed by Dr. G. Pesamosca[9]) on the Ferranti electronic computer of the Instituto Nazionale per le Applicazioni del Calcolo – Roma.

For the principal trajectories the differential equation of motion to be integrated is[1]):

$$\frac{\mathrm{d}^2y}{\mathrm{d}x^2} = \frac{\left[1 + \left(\frac{\mathrm{d}y}{\mathrm{d}x}\right)^2\right]^{\frac{3}{2}}}{r(x, y)}$$

$$r(x, y) = \frac{pc}{eB_z(x, y)}, \qquad (15)$$

y being the cartesian coordinate directed along the spectrometer axis and x the other rectangular coordinate; the origin is fixed at point C of fig. 2.

In view of its numerical resolution, the Milne method was adopted, using as a starting method the Runge-Kutta method[10]).

For the varied trajectories the Kerst-Serber equations[11]) were used:

$$\frac{\mathrm{d}^2\xi}{\mathrm{d}s^2} + [\,1 - n(s)\,]\frac{\xi}{r^2(s)} = \frac{1}{r(s)}\frac{\Delta p}{p}$$

$$\frac{\mathrm{d}^2\zeta}{\mathrm{d}s^2} + n(s)\,\zeta = 0\,, \qquad (16)$$

s being the curvilinear abscissa on the principal trajectory, ξ and ζ being, respectively, the deviations on the horizontal and vertical planes of the varied from the principal trajectory, $n(s)$ being the field index defined by:

$$n(s) = -\left[\frac{\partial B_z(s)}{\partial \xi}\right]_{\xi,\,\varsigma\,=\,0}\frac{r(s)}{B_z(s)}$$

and $B_z(s)$ being the vertical component of the field on the principal trajectory.

Equations (16) hold in the Gauss linear approximation, i.e.:

$$|\,\xi\,| \ll r \qquad |\,\zeta\,| \ll r$$

$$\left|\frac{\mathrm{d}\xi}{\mathrm{d}s}\right| \ll 1 \qquad \left|\frac{\mathrm{d}\zeta}{\mathrm{d}s}\right| \ll 1\,.$$

Both the Milne and Runge-Kutta methods were used to solve equations (16), after having made the substitution:

$$s(x) - \int_0^x \left[1 + \left(\frac{\mathrm{d}^2y}{\mathrm{d}t^2}\right)^2\right]^{\frac{1}{2}}\mathrm{d}t\,.$$

The field index $n(s)$ was evaluated along the principal trajectory from the measurements of $\Delta B_z/B_z$ nearby.

5.2. RESULTS

The integration error in (15) and (16) was estimated as being less than the one due to the experimental errors in the magnetic measurements. The error propagated from these latter to the momentum value corresponding to a principal trajectory is:

$$\frac{\delta p}{p} = \pm\, 0.15\,\%\,.$$

Once calculated, the principal trajectories were compared with the ones obtained by means of the floating wire technique (see section 6).

Five varied trajectories were then calculated, three of which were horizontal and two vertical, i.e. the ones required for the calculation of the matrix elements (1), (2). The varied horizontal trajectories were calculated also as principal trajectories, by using (15). A comparison with the trajectory obtained by means of the first of (16) showed perfect agreement.

We obtained:

$$\| H_{ij} \| = \begin{pmatrix} 0.824 & 1.779 & \mp\, 0.678 \\ -\,0.0639 & 1.075 & \mp\, 0.525 \\ 0 & 0 & 1 \end{pmatrix}$$

$$\| V_{hk} \| = \begin{pmatrix} 0.790 & 1.573 \\ 0.226 & 0.815 \end{pmatrix}. \qquad (17)$$

We note the good agreement between these values and the ones given by (8), calculated in the step function field approximation.

Naturally, the values given by (17) are the more reliables ones, according to which the various quantities of section 3 may be calculated once more.

We obtain:

$$\frac{\Delta p/p}{\xi} = 1.47\%/\mathrm{cm}$$

$$\beta = 26\ \mathrm{mrad}$$

$$\gamma - 31\ \mathrm{mrad}$$

$$\theta_{t_{1,2}} = [\,\pm\, 17.2 - 5.02z\,] \times 10^{-3}\ \mathrm{rad}\,. \qquad (18)$$

[10]) F. B. Hildebrand, Introduction to numerical analysis (MacGraw-Hill, New York, 1956).

[11]) D. W. Kerst and R. Serber, Phys. Rev. **60** (1941) 53.

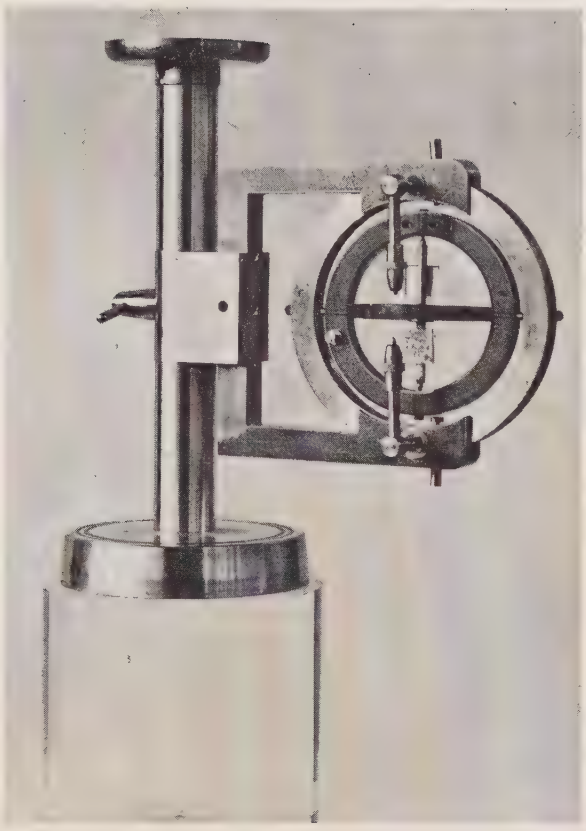

Fig. 7a.

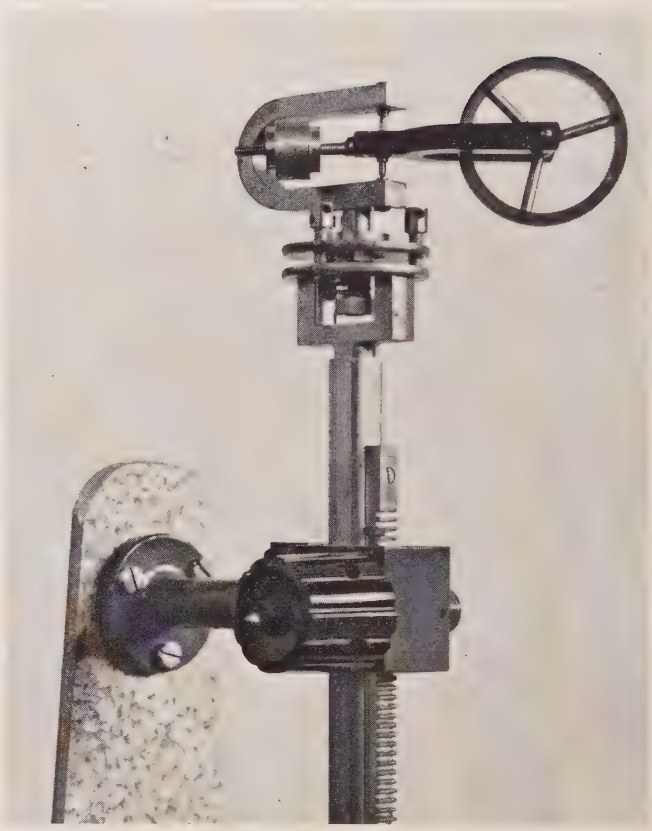

Fig. 7b.

Fig. 7a, 7b. Devices employed in the measurements performed with the floating wire technique.

6. The Floating Wire Technique

6.1. DESCRIPTION OF THE APPARATUS. MEASUREMENT METHOD

The floating wire technique[8]) has been employed with a view to determining the position to be assigned to the counter telescope when the trajectories—calculated by means of the electronic computer—were not yet known. Some of the matrix elements (1) and (2) were also determined.

We used the devices of fig. 7.

Fig. 7a shows two araldite wheels, the inner one having its rotation axis perpendicular to its plane, while the outer has it coplanar. The two axes are coplanar and perpendicular to each other. The whole system is supported by an external brass ring, by two arms and by a support which may be wedged between the spectrometer poles. The inner wheel has an external diameter of 2.4 cm; two small mirrors are affixed to its axis: only the upper mirror is used, while the lower one serves for balancing the system.

The system is built in such a way as to be in neutral equilibrium; 1 mg applied to one of the wheels will suffice to unbalance it. The materials used are all diamagnetic; the bearings are made of tungsten.

The copper wire used in the measurements, 0.08 mm in diameter, is clamped in a hole bored in the rim of the internal wheel. Two silver wire segments, 1 cm long and 0.02 mm in diameter are soldered to the copper wire at the wheel; their ends are connected to the two vertical terminals shown in fig. 7a, so as to allow the pulley to be rotated about 30°.

The whole system was wedged between the poles in such a position that the point of the internal wheel, where the wire was secured, could be moved along a vertical line passing through C.

The wire passes through the magnet gap and

then passes to the pulley of the device shown in fig. 7b, which is built according to criteria similar to the preceding ones and placed outside the gap, in about the same position as the counter telescopes. The tension applied to the wire was 30 g. The wire could be supplied with a maximum current of 0.5 A without the danger of breaking.

The device shown in fig. 7a allows the wire to move freely both vertically and horizontally. In order to determine its position from outside the spectrometer, a light beam is sent, by means of a projector, to the posterior mirror seen in fig. 7a. The image is projected on an suitable screen. At first, with no current on, the wire is placed coincident with the spectrometer's axis, and the position of the light spot is observed.

In order to determine a principal trajectory in a certain field, the wire is supplied with the required current and the device seen in fig. 7b is moved until the spot comes back to its initial position.

Under these conditions the wire emerges (with a certain curvature) tangent to the spectrometer axis from the position corresponding to the converter center.

A varied trajectory may also be determined by either slightly changing the wire current, or by changing the emergency position of the wire or, last, by assigning a certain angle, measurable by the displacement of the light spot, to the initial direction of the wire.

6.2. DISCUSSION OF MEASUREMENT ERRORS

The following considerations may be made as regards possible measurement errors: by moving the device of fig. 7b vertically and horizontally and by taking it back to the initial position, the pulleys of fig. 7a return to their initial position with an error $\delta\theta = \pm 1$ mrad, both on the horizontal and vertical planes. The error propagated in the momentum measurement is then:

$$\frac{\delta' p}{p} = \frac{H_{12}}{H_{13}} \delta\theta \simeq \pm 0.26\% \,.$$

As a confirmation, we can say that a minimum weight of 70 mg had added to or subtracted from the initial 30 g to observe a motion of the light spot. This means a momentum variation of $\pm$ 0.23%.

The quota error in determining the position of the detector center is:

$$\delta'\zeta = V_{12}\,\delta\theta \simeq \pm 1.6 \text{ mm} \,.$$

By varying the field from 0 to 10 kgauss, with no current in the wire, the external wheel of fig. 7a rotates around its horizontal axis $\pm$ 1 mrad, owing to ferromagnetic impurities contained in the internal wheel axis. However there is no horizontal wire motion. The wire weight produces negligible effects, owing to the small deviation (less than 1 mm) from an horizontal plane.

The constraint imposed by the silver wire segments to the internal wheel is negligible because the segments have the same length and the same current flows in opposite directions. During the measurements we set the wires as symmetrically as possible with respect to the spectrometer axis.

The last error source is the uncertainty in the current determination, which is measured by the L& N K3 potentiometer, with an error of $\pm 0.05\%$.

Bearing all these errors in mind we may say that the momentum determination uncertainty amounts to:

$$\frac{\delta p}{p} = \pm 0.3\% \qquad (19)$$

and that the maximum error in the vertical coordinate of the wire with respect to the M.P. is:

$$\delta\zeta \simeq \pm 3 \text{ mm} \,. \qquad (20)$$

6.3. EXPERIMENTAL RESULTS

Measurements of principal trajectories were made with a magnetic field of $B_c = 10$ kgauss for a momentum $p = 500$ MeV/c (with a wire tension $F = 30$ g). The trajectory deviation from the M.P. was found to be less than 1 mm. The wire configuration in the horizontal plane was recorded on sensitive drawing paper; later on this was compared with the one obtained by means of the electronic computer, and the deviations were found to be in accordance with the experimental errors.

Further, the magnetic field and, at the same time, the wire current were varied so as to measure the momentum corresponding to the same wire configuration.

The results obtained are shown in the following table:

Momentum p(MeV/c)	Current in the wire (mA)	Field B_c (gauss)	B_c/p $\left(\frac{\text{gauss}}{\text{MeV}/c}\right)$
500	176.3	9943	19.89
450	195.9	8914	19.81
400	220.4	7951	19.88
350	251.9	6964	19.90
300	293.9	5966	19.89
250	352.7	4963	19.85

From the above table it may be seen that the ratio between the magnetic field and the momentum remains constant within the experimental errors.

A vertical varied trajectory was then measured, with the wire starting parallel to and 1 cm above the principal trajectory; the elevation at the detector was 0.7 cm; thus we have:

$$V_{11} = 0.7 \,, \tag{23}$$

which is in good agreement with (17), and better than one would expect from (20).

Last, we measured the varied vertical trajectory starting from the converter center and forming with the principal trajectory an angle of 10 mrad; a rise of 23 mm was found at the first detector. Thus we have:

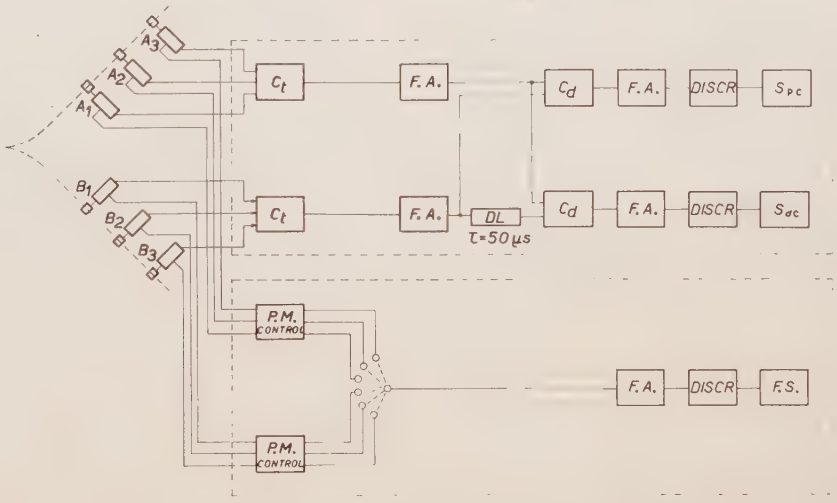

Fig. 8. General block diagram of the electronic apparatus.

Determinations of varied trajectories were then made; an increment Δi was given to the current and the distance ξ by which the wire was displaced, at the position of the first detector, was measured. We found:

$$\frac{\Delta p/p}{\xi} = 2.3\,\%/\text{cm} \,. \tag{21}$$

Taking into account formula (19) and the error in ξ ($\pm$ 0.3 mm), we may conclude that (18) and (21) agree.

As a result of (21) we have:

$$H_{13} = \pm\, 0.43 \text{ m} \,. \tag{22}$$

$$V_{12} = 2.3 \text{ m/rad} \,. \tag{24}$$

Taking into account the usual errors, this is in agreement with (17). It is reasonable to expect considerable differences between the results found by the wire and those obtained by the electronic computer. It should be borne in mind that these errors are determined by small increments in current and position. Naturally, the most reliable values are the ones obtained by means of the electronic computer.

The values (23) and (24) were used to determine the limiting angles (5) in the work on the γ-ray spectrum (see ref.[3])), at the time when the results of the computer were not yet known.

7. Apparatus for Detecting Electron Pairs

7.1. GENERAL BLOCK DIAGRAM

For detecting electron pairs of a certain energy, one channel has been used, with the detectors outside of the magnetic field.

A block diagram of the detectors and electronics is sketched in fig. 8. The channel consists of two telescopes of scintillation counters placed along the trajectories of the positive and negative electrons, having the same energy (symmetric pairs). Each telescope consists of three counters, the first of which is roughly at 1 meter from the magnet edge. This distance is determined by the conditions established for the spectrometer resolution.

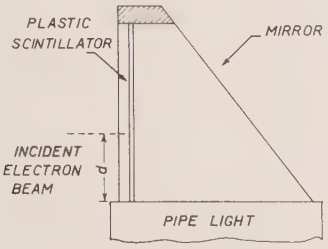

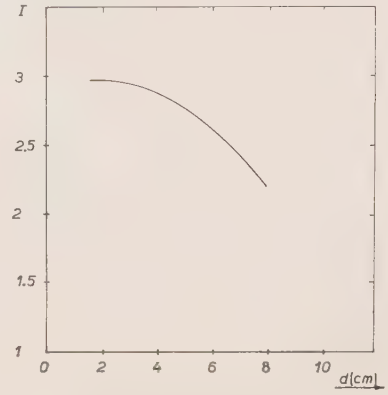

Fig. 9. On the left: Geometry of the detectors. On the right: Intensity of the collected light (arbitrary units) vs. the distance of the point of incidence from the edge of the scintillator.

The output pulses of the photomultipliers from both the anode and the last dinode are sent separately to two different electronic channels.

The outputs from the photomultipliers anodes of each telescope are sent to the input of a triple coincidence (C_t). The outputs of the two triple coincidence go, through a fast distributed amplifier (F.A.), to two double coincidences channels (C_d), giving both prompt and delayed coincidences (delay time $\tau = 50\ \mu s$) recorded by scalers S_{pc} and S_{dc}.

The outputs of dynodes are sent to a second electronic chain which enables us to check the behaviour of the detectors during the measurements. This chain consists of a fast distributed amplifier, a fast discriminator with a dead time of 100 ns, and a fast scaler (F.S.) with a resolution time of 50 ns.

7.2. DESCRIPTION OF THE DETECTORS

Each counter consists of a plastic scintillator, a light pipe, and a photomultiplier. The sizes of the plastic scintillators to obtain a momentum resolution $\Delta p/p \simeq 2.7\%$ were:

Scintillators $A_1 - B_1$ ($18 \times 54 \times 1$) mm^3;
Scintillators $A_2 - B_2$ ($40 \times 76 \times 1$) mm^3;
Scintillators $A_3 - B_3$ ($72 \times 106 \times 1$) mm^3;

In order to obtain a reasonable response uniformity from the scintillator and the best light collection, we used the geometry of fig. 9, placing the scintillator in optical contact with the pipe-light.

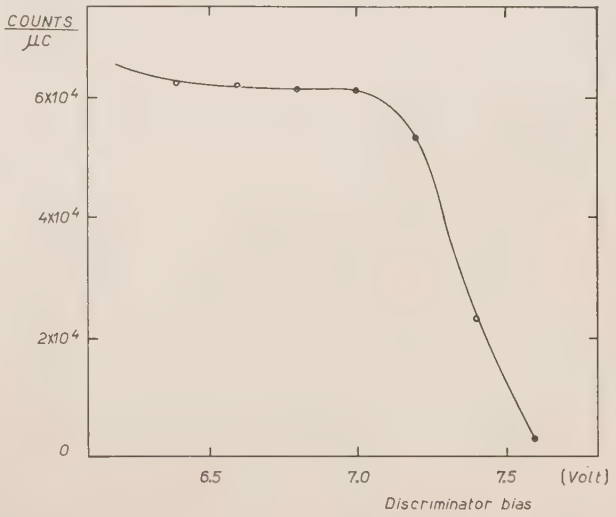

Fig. 10. Counting rate of the 1–2 double coincidence channel of the triple coincidence vs. delay time.

In the same figure the efficiency of light collection is plotted versus the distance of the point of incidence from the near edge of the scintillator.

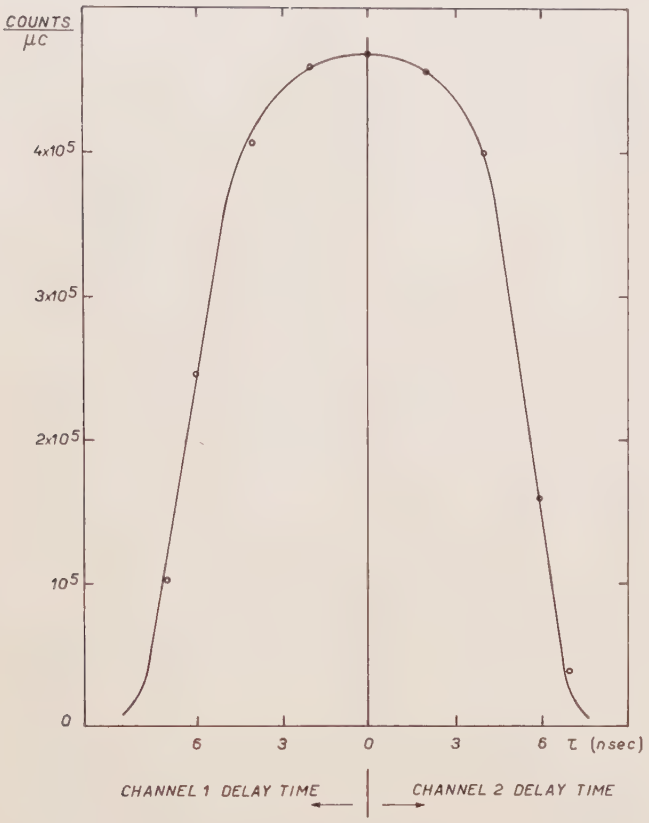

Fig. 11. Counting rate of the triple coincidence as a function of the discriminator voltage level.

The photomultipliers used are of the RCA 6810A type. Supply voltage and potentials partition for dynodes and focusing as well as accelerating grids are so chosen in order to obtain the same gain for the six P.M.

In the actual measuring conditions all the various coincidence channels are fed with signals having an amplitude greater than 5 V.

Magnetic shielding is given by two cylinders: the inner one of μ-metal and the external one of soft iron 0.5 cm thick.

7.3. CHARACTERISTICS OF THE ELECTRONIC APPARATUS

Triple coincidences are of the line type with distributed constants, which have been already described[12]). The resolution time was fixed at 6 ns. Fig. 10 shows the characteristic of the 1–2 double channel of the triple.

In fig. 11 the number of counted events is plotted against the level of the discriminator inside the coincidence.

[12]) U. Pellegrini, B. Rispoli and A. Serra, Nuovo Cimento **9** (1958) 171.

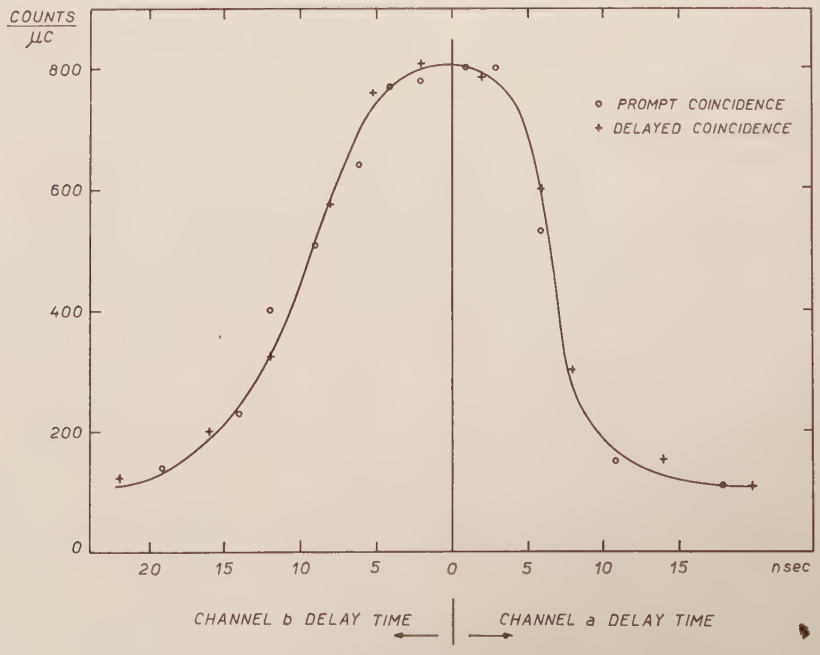

Fig. 12. Counting rate of the double coincidence vs. delay time.

The signals incoming from the two triple coincidences trigger the first double coincidence and the second one after a time shift of 50 ns. From the output of the first coincidence we take the simultaneous coincidences, while from the output of the second one we get the delayed one. The coincidence characteristics drawn in fig. 12 and in fig. 13 have the same shape for the two double circuits.

With a view of avoiding possible integration effects, we placed at the output of both double coincidence circuits distributed amplifiers followed by trigger circuits having the input sensitive to fast pulses 20 ns long.

The scalers following the discriminators are of the conventional type, having 1 μs as resolution time.

This electronic assembly has been working continuously more than 600 hours without any trouble.

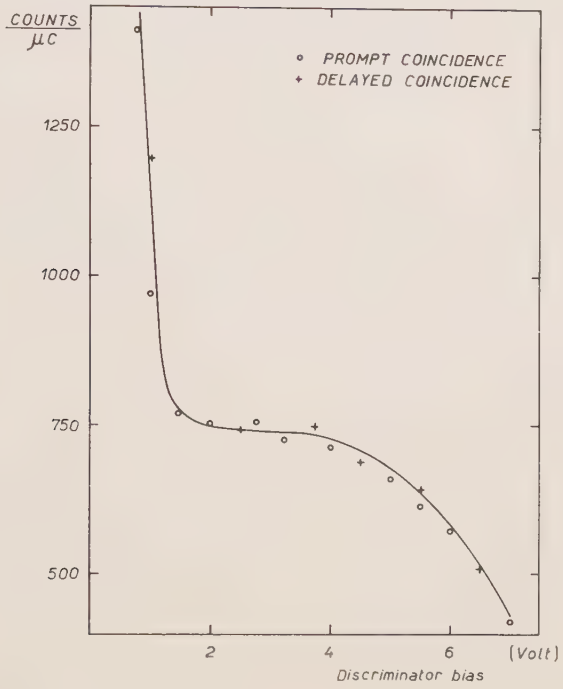

Fig. 13. Counting rate of the double coincidence as a function of the discriminator voltage level.

One of us (G.B.) is very indebted to Prof. J. De Wire for helpful discussion.

NUCLEAR INSTRUMENTS AND METHODS 12 (1961) 278–290; NORTH-HOLLAND PUBLISHING CO.

TRANSIT TIME OF CHARGE CARRIERS IN THE SEMICONDUCTOR IONIZATION CHAMBER

P. A. TOVE and K. FALK

Institute of Physics, University of Uppsala, Uppsala, Sweden

Received 31 January 1961

The transit time of charge carriers and the resulting pulse rise time are considered theoretically for a semiconductor particle detector, with particular reference to silicon detectors. Results are given in nomogram form for n- and p-type detectors, assuming constant mobility and specific ionization loss. The influence of various design factors is discussed, and the effect of non-constant mobility and ionization loss is calculated for typical cases.

1. Introduction

The silicon junction detector has become of great interest because of its simplicity and possible high energy resolution. In the latter respect it surpasses the scintillation detector for detection of charged particles within a certain energy range, and competes with simpler types of magnetic spectrometers. An essential point of view for a detector used in nuclear physics research is the time definition possible which is essentially determined by the rise time of the pulses and their uniformity. In the semiconductor detector the speed of the pulses is fundamentally limited by the travel time of the charge carriers in the depletion region of the junction. The pulse shape is also influenced by the presence of any resistance, such as bulk and contact resistance, in series with the input capacity of the sensing amplifier. The motion of the carriers is not as simple to treat as for the corresponding case of the gaseous ionization chamber. Thus the electric field varies with position in the junction and the mobility of the carriers may also not be constant. In the following various conditions determining the rise time will be discussed and specific examples treated in some detail.

2. Stopping Time for the Ionizing Particles

This is the ultimate factor determining the speed. The stopping time is

$$t_s = \int_0^{x_{0s}} \frac{dx}{v} \qquad (1)$$

where v is the velocity of the particle and x_{0s} its range. An upper limit for t_s is obtained by considering the retardation to be constant in which case we obtain $t_s = 2x_{0s}/v_0$ where v_0 is the starting velocity.

If we assume particles corresponding to a range of 0.5 mm, which is a typical case, we get for electrons $t_s = 4 \times 10^{-12}$ sec. and for protons and α-particles $t_s = 2.6 \times 10^{-11}$ sec.

Constant retardation corresponds to $dE/dx =$ const. in the non-relativistic case.

In the actual case dE/dx increases with x and the actual stopping time can be determined graphically from (1) knowing the plot of E or dE/dx versus x. For the above case of electrons with a range of 0.5 mm the stopping time turns out to be 2.8×10^{-12} sec (relativistically corrected) instead of 4×10^{-12} sec.

The stopping time turns out to be negligible in most cases compared to the drift time of the charge carriers.

Many of the primarily formed electrons and holes correspond to energies high up in the conduction bands, resp. deep in the valence band. The interaction among the electrons (and holes) make the electrons fall to the bottom of the lowest lying unoccupied band and the holes rise to the top of the highest full band[1]). During this process, which takes a time of the order of 10^{-12} sec many new electrons and holes are formed.

[1]) W. L. Brown, IRE Transactions on Nuclear Science Vol. NS-8 (1961) 2.

3. Collection Times for Electrons and Holes

In the calculation of these, complications arise if the non-constant carrier mobility at high fields is considered. The mobility appears to be constant, for electrons in Si up to about 2500 V/cm and for holes in Si up to 7500 V/cm[2,3]). For higher fields the mobility approximately follows

$$\mu \sim \frac{1}{\sqrt{E}}$$

up to at least a few times 10^4 V/cm. The ionizing particles are considered to enter a slab of high-resistivity p-type Si with a thin n-type layer on the surface. The variation of the electric field is determined by solution of Poissons eq.

$$\frac{d^2\psi}{dx^2} = \frac{-\rho(x)}{\varepsilon\varepsilon_0}.$$

ψ is the potential and $\rho(x)$ is net space charge in the depletion layer arising from the ionized donor and acceptor atoms. The permittivity ε is ≈ 11 for Si and ε_0 is the permittivity of free space. The geometry assumed is shown in fig. 1. V is the externally applied voltage and V_d is the built-in diffusion potential. With good approximation we have $\rho = -qN_a$ for $0 \leqslant x \leqslant x_p$ (N_a is density of acceptors in the p-region. In the n-region $\rho = qN_d$ ($-x_n \leqslant x \leqslant 0$) where N_d is the density of donors.

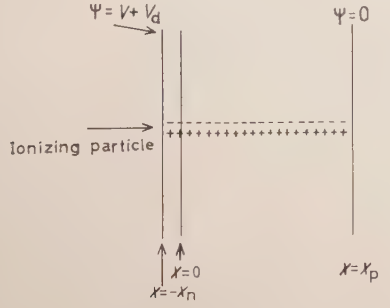

Fig. 1. Silicon particle detector consisting of a thin n-type layer on p-type silicon.

In actual devices the density of donors varies with x, following a Gaussian relationship, because the n-layer is formed by diffusion. The extension of the n-layer is typically only $\frac{1}{1000}$ of that of the p-layer. Hence the part of the output pulse arising from travels of the carriers in the n-region will play a negligible role. For simplicity assuming a stepjunction with N_a and N_d const. one obtains for the fields and potentials in the two regions.

field	potential
n-region	n-region
$F = \frac{qN_d}{\varepsilon\varepsilon_0}(x + x_n)$	$\psi_n = (V_d + V) - \frac{qN_d}{2\varepsilon\varepsilon_0}(x + x_n)^2$
p-region	p-region
$F = \frac{qN_a}{\varepsilon\varepsilon_0}(x_p - x)$	$\psi_p = \frac{qN_a}{2\varepsilon\varepsilon_0}(x_p - x)^2$

Because the total charge on the p-side equals that on the n-side one has $x_p/x_n = N_d/N_a$ and the ratio of the potential differences across the p-region and the n-region, respectively, also equals (N_d/N_a). (N_d/N_a) is normally high, of the order of 1000.

The motion of the carriers is conveniently divided into

A. The motions of the holes formed in the p-region (those formed in the n-region can be neglected for a particle with not too small a range) toward the right in fig. 1.

B. The motions of the electrons formed in the p-region (for the same reason as above those in the n-region can be neglected) toward the left in fig. 1.

A. The holes are moving with the velocity

$$v_h = \frac{dx}{dt} = \mu_h F = -\mu_h \frac{d\psi}{dx}.$$

Because of the short times involved in the processes mentioned in § 2 the charge carriers will be considered to be created all at one time. For a hole formed at the point x_0 the time for travel to point x is obtained from

$$\frac{dx}{dt} = \mu_h \frac{qN_a}{\varepsilon\varepsilon_0}(x_p - x)$$

$$= \mu_h k_a (x_p - x), \quad \text{where} \quad k_a = \frac{qN_a}{\varepsilon\varepsilon_0}$$

$$t = \frac{1}{\mu_h k_a}\int_{x_0}^{x} \frac{dx}{x_p - x}$$

$$= \frac{1}{\mu_h k_a} \ln\left(\frac{x_p - x_0}{x_p - x}\right) \quad (x_0 \geqslant 0)$$

$$x_p - x = (x_p - x_0)\, e^{-\mu_h k_a t}.$$

[2]) E. J. Ryder, Phys. Rev. **90** (1953) 766.
[3]) A. C. Prior, J. Chem. Phys. Solids **12** (1960) 175.

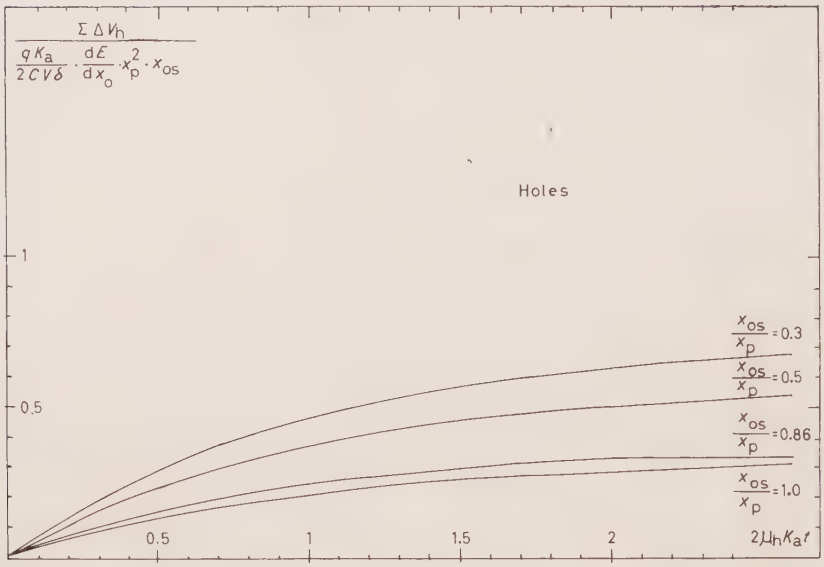

Fig. 2a.

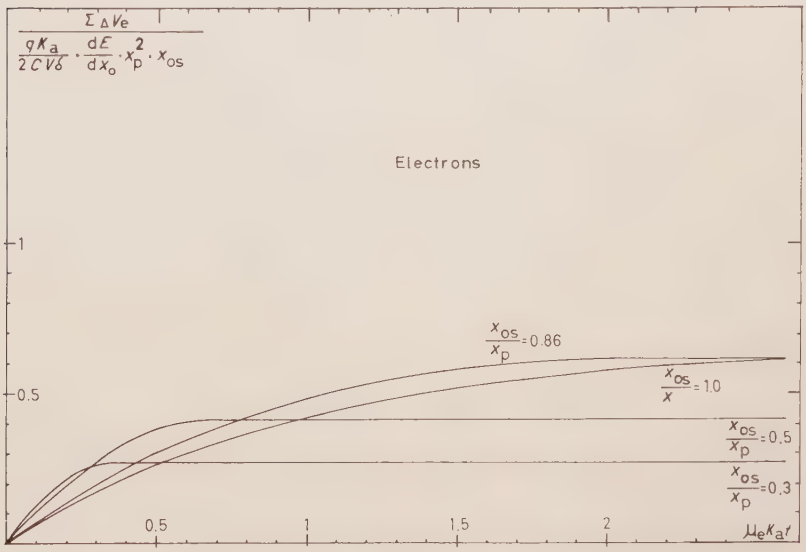

Fig. 2b.

Fig. 2. Pulse shapes from hole (fig. 2a) and electron motion (fig. 2b) in a p-type detector. The time scale involves the mobilities μ_h and μ_e and $k_a = qN_a/\varepsilon\varepsilon_0$ where N_a is density of acceptor, q electron charge and $\varepsilon\varepsilon_0$ dielectric constant. The vertical scale is normalized so that the final value of the sum of the hole and electron pulses equals 1. The figure also applies to an n-type detector in which case fig. 2a would correspond to the motion of the electrons, with time scale $2\mu_e k_d t$ and vertical scale

$$\frac{\sum \Delta V_e}{\frac{qk_d}{2CV\delta}\left(\frac{dE}{dx_0}\right) x_n^2 \, x_{os}},$$

and fig. 2b to the motion of the holes, the time scale being $\mu_h k_d t$ and the vertical scale

$$\frac{\sum \Delta V_h}{\frac{qk_d}{2CV\delta}\left(\frac{dE}{dx_0}\right) x_n^2 \, x_{os}}.$$

This motion of the particle corresponds to a current i and hence a change of charge Q and voltage V of the condenser. The time rate of energy delivered to the charged particle is $\mathrm{d}E/\mathrm{d}t = qvF$ and we also have $\mathrm{d}E/\mathrm{d}t = Vi$ whence

$$i = \frac{qvF}{V} = \frac{q}{V}\frac{\mathrm{d}x}{\mathrm{d}t}\frac{\mathrm{d}\psi}{\mathrm{d}x} = \frac{q}{V}\frac{\mathrm{d}\psi}{\mathrm{d}t}$$

where the infinitesimals are taken following the motion of the particle.

The motion of the particle through a potential change of $\Delta\psi$ thus gives a change in the charge of the capacity of $\Delta Q = \int i\mathrm{d}t = (q/V)\,\Delta\psi$ and thus a voltage change ΔV of $\Delta Q/C = (q/CV)\,\Delta\psi$ if the condenser can be considered isolated from external connections (leakage neglected) during the motion of the particle. This result is also easily seen considering the change of stored condenser energy $\Delta(\frac{1}{2}CV^2)$ to be equal to the energy $q\cdot\Delta\psi$ delivered to the particle.

For a hole created at point x_0 and moving to point x we thus get a potential change

$$\Delta V_\mathrm{h} = \frac{q}{CV}(\psi_{x_0} - \psi_x) \qquad (\Delta V_\mathrm{h} \ll V) \tag{2}$$

$$= \frac{qk_\mathrm{a}}{2CV}[(x_\mathrm{p} - x_0)^2 - (x_\mathrm{p} - x)^2]$$

$$= \frac{qk_\mathrm{a}}{2CV}(x_\mathrm{p} - x_0)^2\,(1 - \mathrm{e}^{-2\mu_\mathrm{h}k_\mathrm{a}t}). \tag{3}$$

This is the potential change caused by a single hole created at x_0. In the small distance $\mathrm{d}x_0$ the number of holes formed are

$$\frac{\mathrm{d}E}{\delta} = \frac{1}{\delta}\left(\frac{\mathrm{d}E}{\mathrm{d}x_0}\right)\mathrm{d}x_0$$

where δ is the energy loss per electron-hole pair ≈ 3.6 eV in silicon. The total pulse from the holes thus becomes

$$\sum\Delta V_\mathrm{h} = \frac{qk_\mathrm{a}}{2CV\delta}(1 - \mathrm{e}^{-2\mu_\mathrm{h}k_\mathrm{a}t})\int_0^{x_{0\mathrm{s}}}(x_\mathrm{p} - x_0)^2\left(\frac{\mathrm{d}E}{\mathrm{d}x_0}\right)\mathrm{d}x_0\,. \tag{4}$$

Here $x_{0\mathrm{s}}$ is the stopping coordinate for the particle. If we assume $\mathrm{d}E/\mathrm{d}x_0 = \text{const.}$ we get

$$\sum\Delta V_\mathrm{h} = \frac{qk_\mathrm{a}}{6CV\delta}(1 - \mathrm{e}^{-2\mu_\mathrm{h}k_\mathrm{a}t})\left[x_\mathrm{p}^3 - (x_\mathrm{p} - x_{0\mathrm{s}})^3\right]\frac{\mathrm{d}E}{\mathrm{d}x_0}\,. \tag{5}$$

If the particle traverses to x_p this becomes

$$\sum\Delta V_\mathrm{h} = \frac{qk_\mathrm{a}}{6CV\delta}(1 - \mathrm{e}^{-2\mu_\mathrm{h}k_\mathrm{a}t})\,x_\mathrm{p}^3\frac{\mathrm{d}E}{\mathrm{d}x_0} \tag{6}$$

B. For the electrons, the speed is

$$v_\mathrm{e} = \frac{\mathrm{d}x}{\mathrm{d}t} = -\mu_\mathrm{e}F = \mu_\mathrm{e}\frac{\mathrm{d}\psi}{\mathrm{d}x} = -\mu_\mathrm{e}k_\mathrm{a}(x_\mathrm{p} - x)$$

and the time for travel from x_0 to x is

$$t = -\frac{1}{\mu_\mathrm{e}k_\mathrm{a}}\int_{x_0}^{x}\frac{\mathrm{d}x}{x_\mathrm{p} - x} = \frac{1}{\mu_\mathrm{e}k_\mathrm{a}}\ln\left(\frac{x_\mathrm{p} - x}{x_\mathrm{p} - x_0}\right)$$

from which $x_\mathrm{p} - x = (x_\mathrm{p} - x_0)\,\mathrm{e}^{\mu_\mathrm{e}k_\mathrm{a}t}$.

For an electron created at point x_0 and moving to point x (this x-value is different from that for the holes) we thus get a potential change

$$\Delta V_\mathrm{e} = \frac{q}{CV}(\psi_x - \psi_{x_0})$$

$$= \frac{q}{CV}\frac{k_\mathrm{a}}{2}[(x_\mathrm{p} - x)^2 - (x_\mathrm{p} - x_0)^2]$$

$$= \frac{qk_\mathrm{a}}{2CV}(x_\mathrm{p} - x_0)^2\,(\mathrm{e}^{2\mu_\mathrm{e}k_\mathrm{a}t} - 1)\,. \tag{7}$$

This expression is valid only until the electrons traverse $x = 0$, at the junction, which happens for

$$t' = \frac{1}{\mu_\mathrm{e}k_\mathrm{a}}\ln\frac{x_\mathrm{p}}{x_\mathrm{p} - x_0}\,.$$

Thereafter, ΔV_e is assumed to remain at the value obtained at $x = 0$. This means neglecting the small extra voltage increase from the traversal of the thin n-region, the voltage across which is only a small fraction of that across the p-region. Thus the electrons formed at x_0-values less than $x_\mathrm{p}\,[\,1 - \exp(-\mu_\mathrm{e}k_\mathrm{a}t)\,]$ at time t' all have arrived at $x = 0$ and have given their contribution to the voltage pulse. The contribution of each is

$$\Delta V_\mathrm{e} = \frac{q}{CV}(\psi_0 - \psi_{x_0})$$

$$= \frac{qk_\mathrm{a}}{2CV}[x_\mathrm{p}^2 - (x_\mathrm{p} - x_0)^2]$$

$$= \frac{qk_\mathrm{a}}{2CV}x_0(2x_\mathrm{p} - x_0) \tag{8}$$

and thus for all electrons

$$\frac{qk_\mathrm{a}}{2CV\delta}\int_0^{x_\mathrm{p}(1-\mathrm{e}^{-\mu_\mathrm{e}k_\mathrm{a}t})} x_0(2x_\mathrm{p} - x_0)\frac{\mathrm{d}E}{\mathrm{d}x_0}\mathrm{d}x_0\,.$$

This adds to the contribution

$$\frac{qk_a}{2CV\delta}(e^{2\mu_e k_a t}-1)\int_{x_p(1-e^{-\mu_e k_a t})}^{x_{0s}}(x_p-x_0)^2\left(\frac{dE}{dx_0}\right)dx_0$$

from the electrons still on flight to $x = 0$. Hence the total electron pulse $\Sigma\Delta V_e$ is

$$\sum\Delta V_e=\frac{qk_a}{2CV\delta}\left\{\int_0^{x_p(1-e^{-\mu_e k_a t})}x_0(2x_p-x_0)\left(\frac{dE}{dx_0}\right)dx_0 + (e^{2\mu_e k_a t}-1)\int_{x_p(1-e^{-\mu_e k_a t})}^{x_{0s}}(x_p-x_0)^2\left(\frac{dE}{dx_0}\right)dx_0\right\}. \quad (9)$$

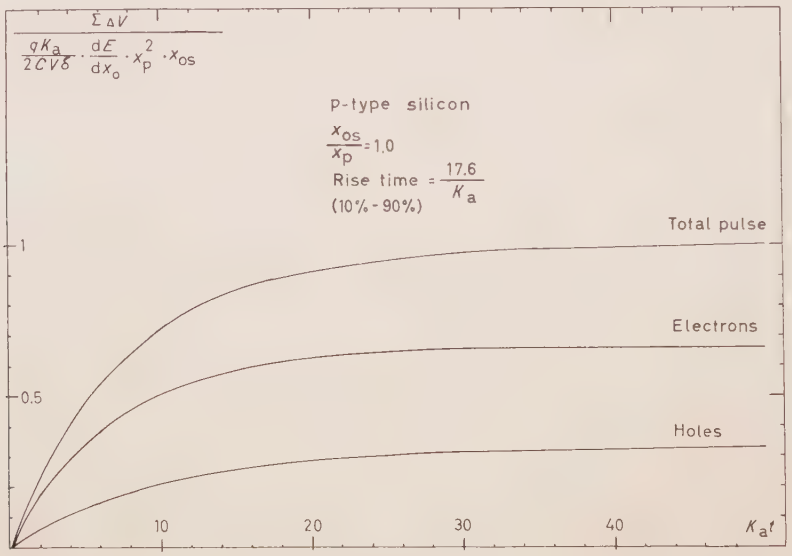

Fig. 3a.

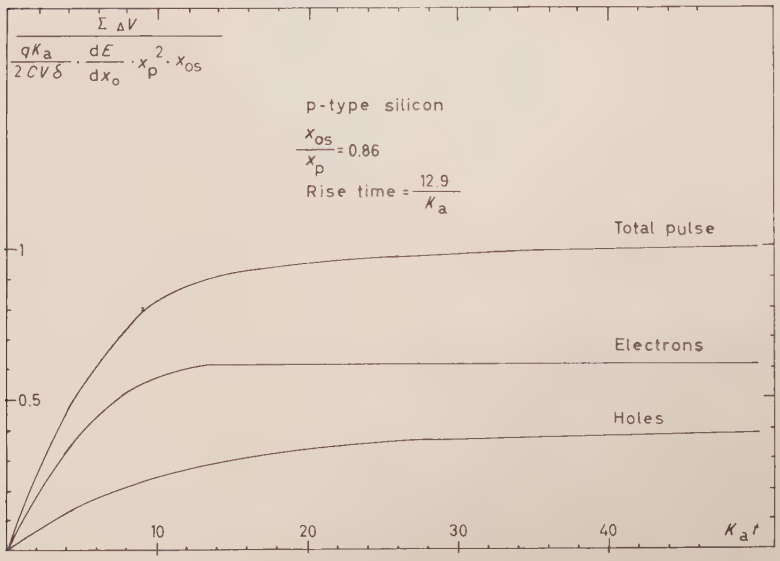

Fig. 3b.

This is valid until

$$t = \frac{1}{\mu_e k_a} \ln \frac{x_p}{x_p - x_{0s}}$$

(meaning that the integration boundary $x_p [1 - \exp(-\mu_e k_a t)]$ reaches x_{0s}) after which time

$$\sum \Delta V_e = \frac{q k_a}{2CV\delta} \int_0^{x_{0s}} x_0(2x_p - x_0) \left(\frac{dE}{dx_0}\right) dx_0 . \quad (10)$$

If we assume $dE/dx_0 = \text{const.}$ we get

$$\sum \Delta V_e = \frac{q k_a}{6CV\delta} \left(\frac{dE}{dx_0}\right) \times$$

$$\times \{ 2x_p^3 (1 - e^{-\mu_e k_a t}) - (x_p - x_{0s})^3 (e^{2\mu_e k_a t} - 1) \} . \quad (11)$$

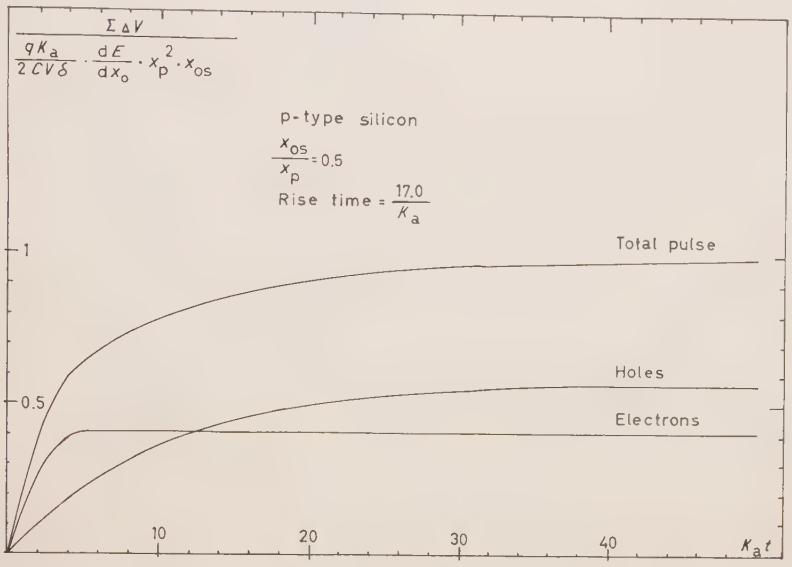

Fig. 3c.

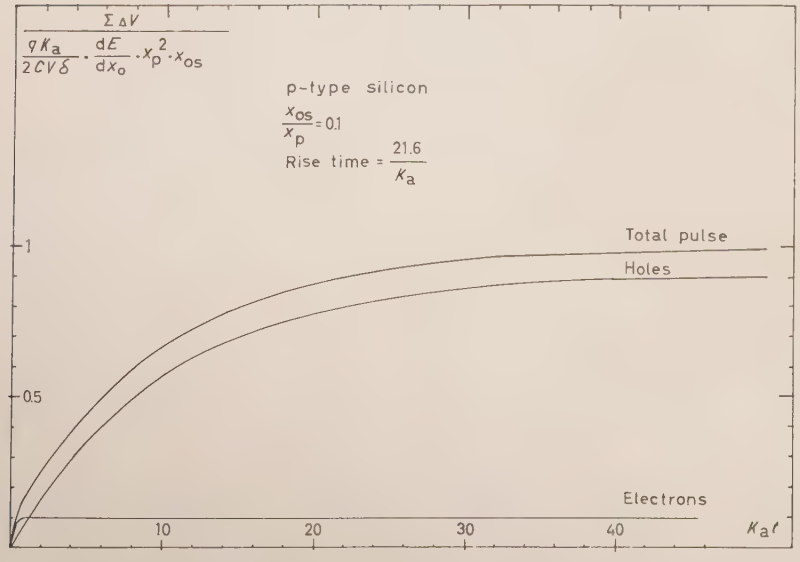

Fig. 3d.

Fig. 3. Pulse shape from the motions of the holes, the electrons, and their sum, respectively, for a p-type silicon detector for various values of relative range x_{0s}/x_p. The time scale $k_a t$ (in seconds) involves factor k_a which is inversely proportional to resistivity. For 10 kΩcm p-material $k_a = 2.1 \times 10^9$.

This is valid to

$$t = \frac{1}{\mu_e k_a} \ln \frac{x_p}{x_p - x_{0s}}$$

and after that time

$$\sum \Delta V_e = \frac{q k_a}{2CV\delta} \left(\frac{dE}{dx_0}\right) x_{0s}^2 \left(x_p - \frac{x_{0s}}{3}\right). \quad (12)$$

For a particle traversing to x_p we obtain

$$\sum \Delta V_e = \frac{q k_a}{3CV\delta} \left(\frac{dE}{dx_0}\right) x_p^3 \left(1 - e^{-\mu_e k_a t}\right). \quad (13)$$

The hole pulse, as given by (5) is drawn in fig. 2a while fig. 2b depicts the electron pulse, for four values of x_{0s}/x_p, the relative range of the particle. In all cases the sum

$$\sum \Delta V_h + \sum \Delta V_e = \frac{q k_a x_p^3}{2CV\delta} \left(\frac{x_{0s}}{x_p}\right) \left(\frac{dE}{dx_0}\right).$$

In fig. 3a–d are drawn the pulse shapes resulting from the motions of the electrons, the holes, and their sum for four values of x_{0s}/x_p, in silicon, assuming $\mu_h = 0.05$ m²/Vs and $\mu_e = 0.145$ m²/Vs. In all cases $dE/dx_0 = \text{const.}$ is assumed and the curves thus correspond to (5), (6), (11), (12) and (13).

The curve corresponding to full traversal of the depletion layer, fig. 3a, represents a simple exponential relationship. The time scale for the hole and electron pulse respectively are nearly the same because the exponential in (6) is exp $(-2\mu_h k_a t)$, in (13) is exp $(-\mu_e k_a t)$, and in silicon $2\mu_h$ happens to be not very different from μ_e. That the contribution from the holes is one-half of that from the electrons in fig. 3a reflects the fact that, on the mean, electrons traverse twice as high potential difference as the holes, due to the quadratic shape of the potential curve. The curves in figs. 3b–d have some breaks because the contribution from the electrons reaches its final value at an early stage. The rise time τ_r of the pulse depends on μ_e, μ_h, k_a and the ratio x_{0s}/x_p. The variation with the latter quantity can be seen by comparing figs. 3a–d. τ_r has a rather weak minimum for $x_{0s}/x_p \approx 0.86$, being somewhat larger for greater or smaller values of x_{0s}/x_p. The minimum can be shown to correspond to the case where the electron pulse is flattened out at the point corresponding to 90% of full height, which was the upper reference point for determination of τ_r. For other values of μ_e/μ_h the minimum would occur at a different value of x_{0s}/x_p.

In a surface barrier junction, on n-type material, the contribution (for $x_{0s} = x_n$) of the holes would be twice that of the electrons while the time constant for the holes would be exp $(-\mu_h k_d t)$ and for the electrons exp$(-2\mu_e k_d t)$, because the motions of the two kinds of particles are simply interchanged implying that in fig. 2 the markings "electrons" and "holes" should be interchanged, together with the appropriate indices in μ, k and x. The change of relative time scale would mean that separation of pulses due to electron and hole motion respectively is facilitated. Selecting the electron pulse would however mean that the pulse height becomes dependent on direction (and range) of the ionizing particle, just as in the corresponding case of the non-gridded gas ionization chamber.

The pulse shapes for an n-type detector are shown in fig. 4a–d. The pulse rise time τ_r is found to be more strongly dependent, changing more than a factor 5, on the fractional range x_{0s}/x_n, than for the curves in fig. 3 for a p-type detector. Minimum τ_r occurs for $x_{0s}/x_n = 0.30$ and corresponds to the case where the hole pulse flattens off at the 90%-point of the total pulse. When comparing an n-type detector with a p-type under the assumption of $k_d = k_a$, corresponding to the same depletion layers for a given voltage, it is found that the minimum τ_r in n-type Si is about $\frac{1}{2}$ of minimum τ_r for p-type Si. It is apparent that for a given detector and particle energy the fastest pulses would be obtained if the detector bias is adjusted so that $x_{0s}/x_n \approx 0.30$ for the n-type detector. Other factors may however be more important in this choice.

Assuming a certain material and optimizing the resistivity one has for p-type material $\mu_h k_a = \sigma_p/\varepsilon\varepsilon_0$; $\mu_e k_a = (\sigma_p/\varepsilon\varepsilon_0)\,(\mu_e/\mu_h)$ and depletion layer width $x_p = \sqrt{2V\mu_h\varepsilon\varepsilon_0/\sigma_p}$ and for n-type material $\mu_e k_d = \sigma_n/\varepsilon\varepsilon_0$; $\mu_h k_d = (\sigma_n/\varepsilon\varepsilon_0)\,(\mu_h/\mu_e)$ and depletion layer width $x_n = \sqrt{2V\mu_e\varepsilon\varepsilon_0/\sigma_n}$.

Increase of σ, which is the evident way to get shorter τ_r, thus decreases x, which in principle can be compensated for by increasing the bias.

Considering different materials one would prefer

o have high σ but increase μ in the same proportion. High values for μ_e/μ_h (p-type) and μ_h/μ_e (n-type) would be favourable when electrons and holes

and the other of low resistance, with $x_{0s} = x_n$, one would prefer the latter as it turns out to give half the rise-time of the former. The corresponding

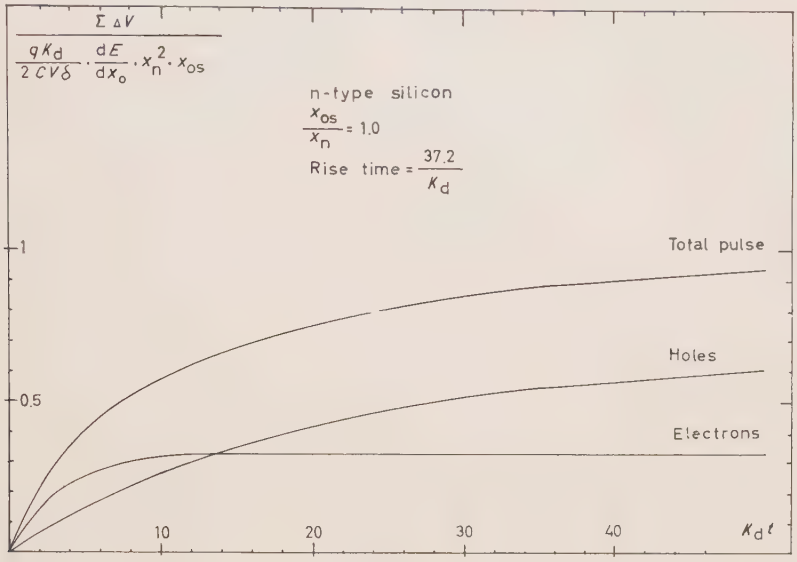

Fig. 4a.

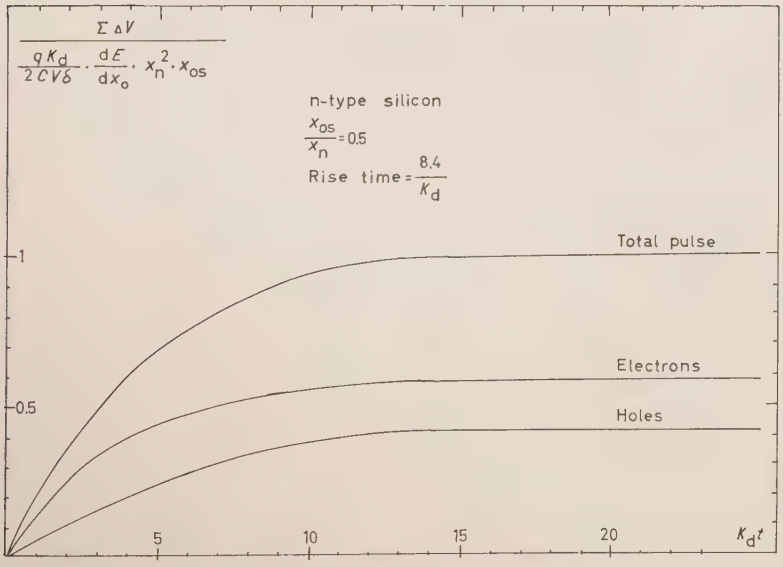

Fig. 4b.

respectively contribute appreciably, that is when x_{0s} is a large fraction of x_p resp. x_n.

If one, for n-type Si detectors, would make the choice between *two* detectors, both with the same bias, one of high resistance such that $x_{0s}/x_n = 0.3$ comparison for two p-type Si detectors, (with $x_{0s} = 0.86\, x_p$ resp. $x_{0s} = x_p$) gives the expected result that the τ_r's are nearly equal.

As a typical example of the expected rise times we may choose 10 k Ω cm p-type Si which gives $\tau_r =$

6.4 ns for the optimum choice of x_{0s}/x_p. Such a detector should, with 500 V bias, give a depletion layer of 700 μ, sufficient for 10 MeV protons. If one wants to measure particles of much shorter range, say α's up to 10 MeV, and assumes the same bias of 500 V, one could in principle use a detector with a

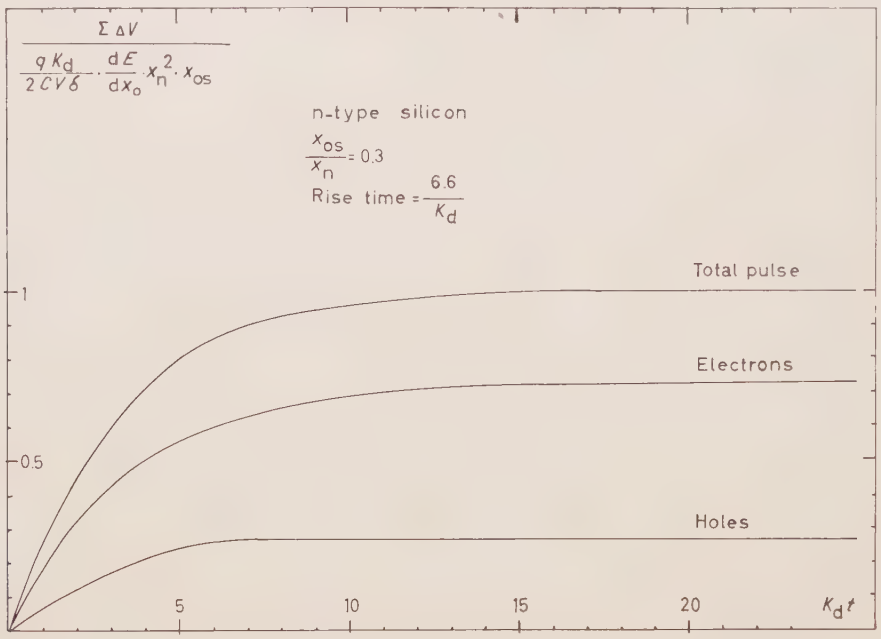

Fig. 4c.

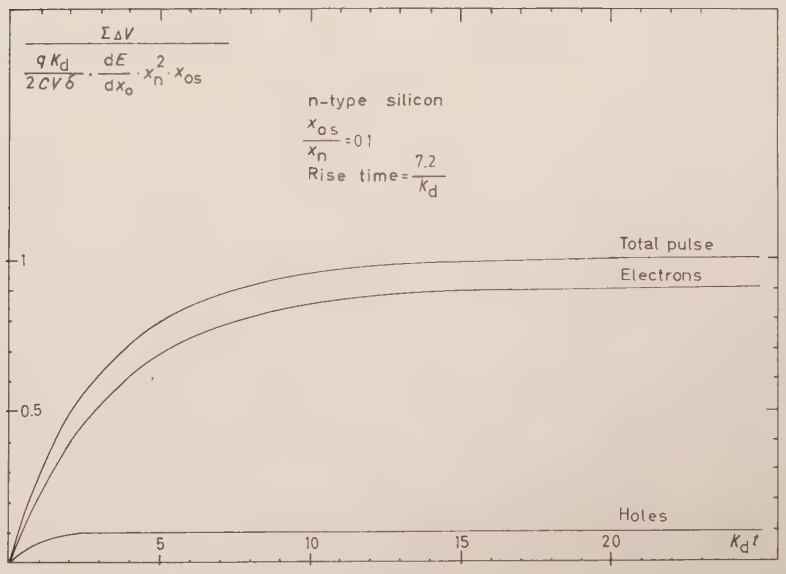

Fig. 4d.

Fig. 4. Pulse shape from the motions of the electrons and the holes, and their sum, for an n-type silicon detector for various values of relative range x_{0s}/x_n. The time scale $k_d t$ (in seconds) involves factor k_d which is inversely proportional to resistivity. For 3.6 kΩcm n-material k_d is 2.1×10^9.

resistivity as low as 80 Ω cm and this should give $\tau_r \approx 5 \times 10^{-11}$ sec.

An n-type counterpart to the above detector should make use of $\approx 3600\,\Omega$ cm n-type Si to give the same depletion layer with 500 V bias. When detecting particles with a range $x_{0s}/x_n = 0.3$ (which means e.g. 5.5 MeV protons) the resulting τ_r is 3.3 nsec. Used for 10 MeV protons it should give 18.4 nsec. For detecting 10 MeV α's 30 Ω cm n-type Si would be sufficient and the resulting τ_r is 15×10^{-11} sec.

These rise times can be found with the help of the nomogram in fig. 5.

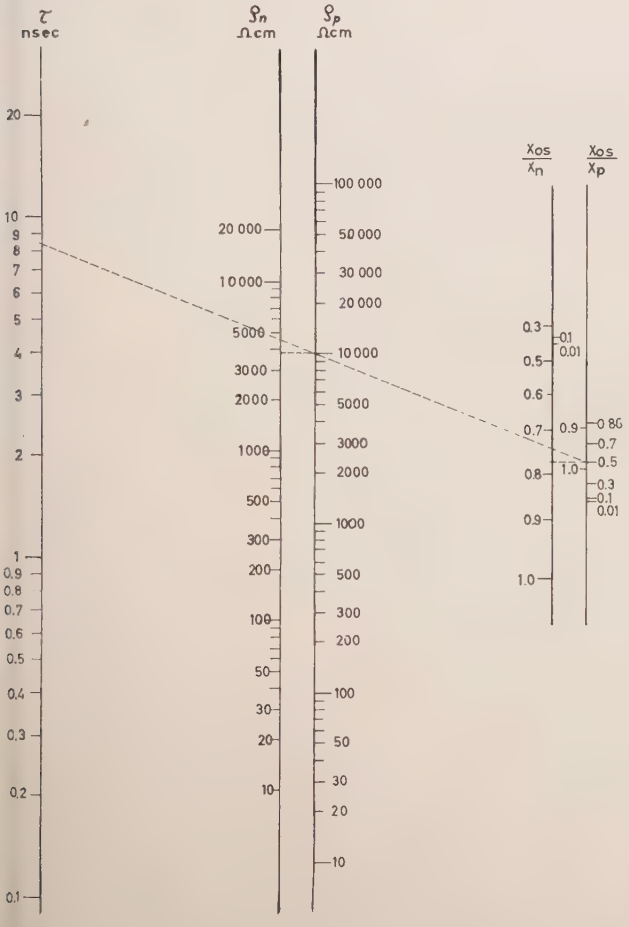

Fig. 5. Nomogram, showing the 10 to 90 % theoretical pulse rise time in p- and n-type silicon detectors due to the finite travel time of electrons and holes. The mobilities and dE/dx are assumed constant. The rise-time is obtained by extending, to the time scale, the line between the applicable points of resistivity and relative range x_{0s}/x_p (or x_{0s}/x_n). The scales to the right have upper turning points corresponding to the optimum relative range values of 0.86 and 0.3 resp. Both lower and higher values of relative range lie lower on the scales.

4. Influence of non-constant dE/dx

Non-constant dE/dx_0 changes the proportion between the pulses from holes and electrons respectively. If dE/dx increases towards the end of the range in a p-type detector this means that the mean voltage difference traversed by the holes is decreased while that for the electrons is increased. This means a decreased hole pulse and increased electron pulse because the heights are proportional to the number of charges times the mean traversed potential difference as indicated by (2) and (8). Also, the rise time of the electron pulse is increased because the mean travel time of the electrons increases. The rise time of the hole pulse is not changed as can be seen from (4). For an n-type detector the corresponding would hold, interchanging electrons and holes.

The quantitative influence of non-constant dE/dx can be deduced either graphically or analytically. In the first case, considering a p-type detector and starting from (9), the known dE/dx curve is multiplied with $x_0(2x_p - x_0)$ and $(x_p - x_0)^2$ respectively and the integrals obtained by measuring areas. The dE/dx curve can also be approximated by a simple function, e.g. for protons having a range of 1 mm or less $^{10}\log\,(dE/dx) = 8.51 - 0.442 \log\,(x_p - x_0)$ is a suitable expression. This can be put into (4), (9) and (10). The result, for 8 MeV protons having a range of 0.5 mm, and for $x_{0s} = x_p$, is shown in fig. 6 which can be compared with fig. 3a. The increase in rise time is seen to be $\approx 50\%$. The corresponding result for electrons in the same detector, which means that the electron energy should be ≈ 375 keV, is shown in fig. 7. However, the fact that the trajectories of the electrons can be deflected considerably during the retardation, due to the small mass of the electron, and also the production of high-energy secondary electrons, will mean that a fraction of the electrons will not follow paths assumed in the calculations.

5. Influence of Non-Constant Carrier Mobility

The carrier mobility is constant $= \mu_0$ up to a field strength F_{ch} of 7.5×10^5 V/m for holes and $F_{ce} = 2.5 \times 10^5$ V/m for electrons. Above these values $\mu = \mu_0\,(F_c/F)^{\frac{1}{2}}$. For still higher values, not reached in typical detectors, the velocity

approaches a constant value. In fig. 8, assume that in the p-type detector $F = F_c$ at $x = x_c$. The voltage pulse from the motion of holes (or electrons respectively) is obtained by summing three types of contribution for each kind of particle.

1) or 4) Contribution from holes, (electrons) formed in the region $0 \leqslant x_0 \leqslant x_c$ (where $F > F_c$) as long as the carriers are in this region.

2) Contribution from holes formed in the region $0 \leqslant x_0 \leqslant x_c$, during the time they traverse the region from x_c to x_{0s} (which is here assumed to be equal to x_p).

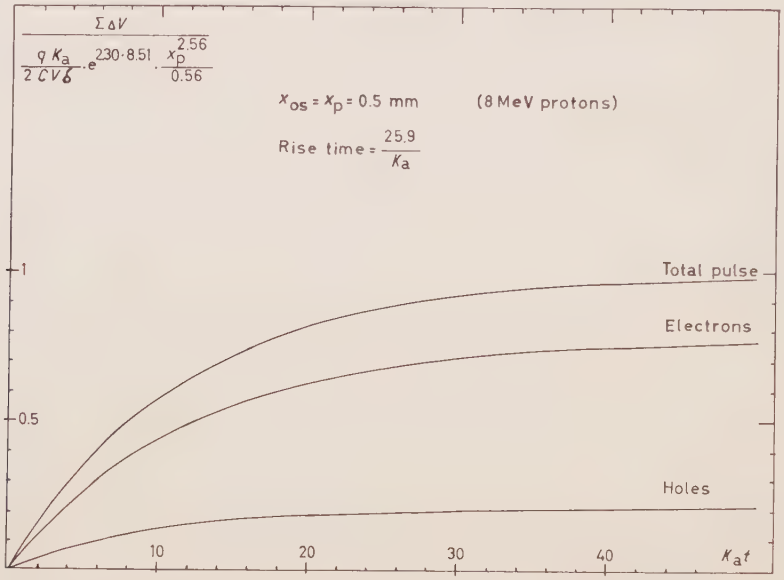

Fig. 6. Pulse shape from the motions of holes and electrons for a p-type silicon detector, with consideration to the fact that dE/dx is non-constant. The curve is calculated for 8 MeV protons having a range of 0.5 mm and with $x_{0s} = x_p$. Comparison should be made with fig. 3a which is for dE/dx = constant. Rise time increases in proportion 25.9/17.6.

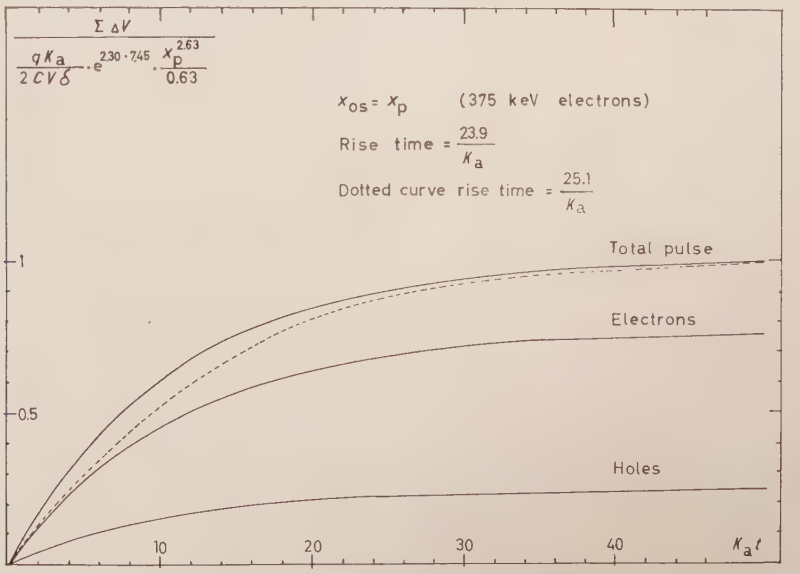

Fig. 7. Pulse shape, calculated for the case of an incident electron for the same detector as in fig. 6 and with $x_{0s} = x_p = 0.5$ mm. The dotted curve is calculated for a 10 kΩcm detector with a bias of 250 V and under consideration of non-constant carrier mobility and dE/dx. The increase in τ_r is only 6 % relative to the solid curve for which only the variation in dE/dx is considered.

5) Contribution from electrons formed in the region $x_c \leqslant x_0 \leqslant x_{0s}$ and traversing the region $x = x_c$ to $x = 0$.

3) or 6) Contributions from holes (electrons) formed in the region $x_c \leqslant x_0 \leqslant x_{0s}$ as long as the carriers are in this region.

The equations for the motions corresponding to the different contributions are

$$1)\ \frac{dx}{dt} = \mu_h F = \mu_{0h}\sqrt{F_c F} = \mu_{0h}\sqrt{F_c k_a (x_p - x)} = k_{ch}\sqrt{x_p - x}$$

where μ_{0h} and k_{ch} are constant.

Thus

$$t = \frac{1}{k_{ch}}\int_{x_0}^{x}\frac{dx}{\sqrt{x_p - x}} = \frac{2}{k_{ch}}\left(\sqrt{x_p - x_0} - \sqrt{x_p - x}\right) \qquad (0 \leqslant x_0 \leqslant x \leqslant x_c)$$

and $\sqrt{x_p - x} = \sqrt{x_p - x_0} - \frac{1}{2}k_{ch}t$

$$2)\qquad \int_{x_c}^{x}\frac{dx}{x_p - x} = \int_{t_0}^{t}\mu_{0h}k_a\,dt$$

$x_p - x = (x_p - x_c)\,e^{-\mu_{0h}k_a(t-t_0)}$. (At $t = t_0$ the holes have arrived at $x = x_c$.)

3) Here the mobility is constant.

$$\frac{dx}{dt} = \mu_{0h}F = \mu_{0h}k_a(x_p - x) \text{ and } x_p - x = (x_p - x_0)\,e^{-\mu_{0h}k_a t}$$

$$4)\ \frac{dx}{dt} = -\mu_e F = -k_{ce}\sqrt{x_p - x} \text{ where } k_{ce} = \mu_{0e}\sqrt{F_c k_a}$$

$$\sqrt{x_p - x} = \sqrt{x_p - x_0} + \tfrac{1}{2}k_{ce}t \quad (0 \leqslant x \leqslant x_0 \leqslant x_c)$$

$$5)\ \int_{x_c}^{x}\frac{dx}{\sqrt{x_p - x}} = -\int_{t_0}^{t}k_{ce}\,dt \qquad (0 \leqslant x \leqslant x_c)$$

$$\sqrt{x_p - x} = \sqrt{x_p - x_c} + \tfrac{1}{2}k_{ce}(t - t_0)\,.$$

6) The mobility is constant

$$\frac{dx}{dt} = -\mu_{0e}F = -\mu_{0e}k_a(x_p - x)$$

$$x_p - x = (x_p - x_0)\,e^{\mu_{0e}k_a t} \quad (x_c \leqslant x \leqslant x_0 \leqslant x_{0s}).$$

The values for $x_p - x$ obtained from 1) 2) and 3) are to be inserted in eq. (3) and those from 4) 5) and 6) in eq. (7).

The calculations turn out to be rather laborious. For the case of electrons as the ionizing particles and $x_{0s} = x_p$ the result is shown as the dotted curve in fig. 7. The modification introduced is seen to be slight, amounting to a 6% increase.

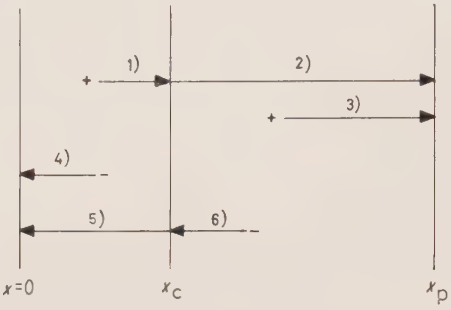

Fig. 8. Different contributions to the voltage pulse for the case of non-constant mobility. + refers to created holes and — to electrons. Three types of contribution, described by different expressions, exist for each kind of carrier as discussed in text. It is implied that x_c for holes and electrons are unequal.

6. Discussion

The calculations indicate that under favourable conditions pulses with very fast rise could be expected. Low-resistivity material is desired for this, but this is in contradiction to the desire for thick depletion layers. The small size of the pulses means that it will be more difficult to develop fast coincidence circuitry than for the large pulses obtainable from photomultiplier tubes with scintillators. Compared with the latter arrangement, the semiconductor detector has the advantage of having no time jitter, which the multiplier has, particularly at low energies, due to the statistical uncertainty in the emission time of the first photoelectrons[4]).

An important question is to what extent the effective field on the carriers will be changed by the fact that the ionization column is rather dense, causing a shielding of carriers inside the column and also a change of the potential distribution because of the high conductivity of the column[1]). These circumstances would imply a correction of

[4]) See e.g. I. A. D. Lewis and F. H. Wells, Millimicrosecond techniques (Pergamon Press, 1959) p. 316.

the simple theory of particles moving in an undisturbed junction field. From simple theory for particle ionization[5]), most electrons, at the instant of release, are within an atomic distance of the track of the particle but the irregular motion of the carriers will imply a track width of the order of their mean free path, which is of the order of a few times 10^{-8} m. This leads to a carrier density of 10^{22}–10^{23} per m^3 for minimum-ionizing particles. The time spent on a mean free path is of the order of 10^{-12} sec. Because of the diffusion, the column will rapidly widen, being 5×10^{-7} m after 10^{-10} sec and 1.5×10^{-6} m after 10^{-9} sec. At these times the microfield[6]) strength in the column will only be a small fraction of the junction field, which would indicate that the latter is the determining factor. It could also be pointed out that the number of created free charges is only a negligible fraction of the number of charges due to ionized impurity atoms in a detector. Deformation of the junction field occurs to an extent determined by the relation between the conductivity of the ionized column and that of the silicon. The deformation is such as to cause less field along the column. The effect will be less important with low resistivity material.

In detector arrangements, the resistance of the non-depleted part of the silicon and the contact resistance is in series with the junction capacity and the external capacitance to be charged by the current pulse[7,8]). These resistances can be minimized by special precautions and arrangements, decreasing the resulting slowing-down of the pulse.

[5]) E. Fermi, Nuclear Physics (University of Chicago Press, 1951).

[6]) J. D. Cobine, Gaseous Conductors (Dover, 1958).

[7]) C. T. Raymo, J. W. Mayer, IRE Transactions on Nuclear Science Vol. NS-8 (1961) p. 157.

[8]) H. M. Mann, J. W. Haslett and G. P. Lietz, *ibid* p. 151.

NUCLEAR INSTRUMENTS AND METHODS 12 (1961) 291–298; NORTH-HOLLAND PUBLISHING CO.

PROTON RESONANCES SUITABLE TO SHAPE CALIBRATE A SCINTILLATION γ-RAY SPECTROMETER

ROLF NORDHAGEN

Fysisk Institutt, Universitetet i Oslo

Received 18 April 1961

A number of resonances in the reactions (p γ), (p p' γ) and (p α' γ) are found to yield monoenergetic γ-rays with only small relative intensities of interfering radiations. The method by which these γ-rays are used to provide *in situ* scintillation counter pulse-height distribution shapes for γ-rays of arbitrary energy is described, and a detailed description of the resonance reactions and the γ-rays they provide is given. The results of shape calibrating a 5″ by 5″ NaI scintillation counter is presented as an example.

1. Introduction

A method for unravelling an unknown γ-ray distribution observed by a NaI(Tl) scintillation counter is now standard practise in several laboratories[1,2,3]). By this method use is made of knowing the detailed shapes of the pulse height distributions from monoenergetic γ-rays of known energies. These standard shapes can then be successively folded into a distribution observed from a mixture of many γ-transitions and thus the γ-rays present and their relative number of counts can be found. To obtain relative and absolute intensities use can be made of one of the many good tables of γ-rays absorption efficiencies for all sizes of NaI crystals[4–7]).

The present study gives the result of a search for γ-rays which could provide standard shapes for a scintillation spectrometer to be used in proton capture work. Before the actual reactions providing the γ-rays are described, a discussion of the conditions under which the γ-rays are to be observed is given. This necessitates mentioning the useful way the standard spectra can be plotted.

The scintillation spectrometer itself consists of two 5 inch by 5 inch NaI(Tl) counters and is used for observing directly or by coincident cascades the γ decay of resonance levels excited by proton capture. The bombarding protons are provided by the Oslo University Van de Graaffs, one small running up to between 400 and 500 keV, and another larger machine presently being used between 800 and 1900 keV.

2. The γ-Ray Spectra

2.1. GENERAL CONSIDERATIONS

The excitation energies of the resonance levels encountered extend with a few exceptions up to around 12 MeV. The well known multipeaked distributions observed in the corresponding region of γ-ray energy are shown in fig. 1, and has been thoroughly described and explained[8,9]).

The following regions in the shape of the pulse-height distributions from our counters are indicated in this figure.

A: *The low energy tail*, due mainly to Compton absorption processes in the scintillation crystal. Added to this is absorption of quanta scattered

[1]) P. M. Endt and A. Heyligers, Physica **26** (1960) 230.

[2]) C. Broude, L. L. Green, J. C. Willmott, Proc. Phys. Soc. **72** (1958) 1097.

[3]) Kotoyoki Okano, Journ. Phys. Soc. Japan **15** (1960) 28.

[4]) P. R. Bell, The Scintillation Method in Beta and Gamma Ray Spectroscopy, ed. K. Siegbahn (North-Holland Publ. Co. Amsterdam, 1955).

[5]) A. L. Stanford, Jr. and W. K. Rivers, Jr., Rev. Sci. Instr. **29** (1955) 406.

[6]) S. H. Vegors, Jr., L. L. Marsden and R. L. Heath, Calculated Efficiencies of Cylindrical Radiation Detectors, A.E.C. Report. IDO-16370 (1958);
and R. L. Heath, Scintillation Spectrometry Gamma-Ray Spectrum Catalogue, A.E.C. Report IDO-16408 (1957).

[7]) H. E. Gove and A. R. Rutledge, Finite Geometry Corrections to Gamma Ray Angular Correlations Measured with 5″ Diameter by 4″ long NaI(Tl) Crystals, A.E.C.L. Report CRP-755 (Chalk River, Ontario, 1958).

[8]) D. Maeder, R. Müller and V. Wintersteiger, Helv. Phys. Acta **27** (1954) 3.

[9]) M. J. Berger and J. Doggett, Journ. Res. Nat. Bureau of Standards **5** (1956) 355.

into the crystal from the shielding, a collimator or the surroundings in general. The increase of this tail at low energies is especially sensitive to the amount of this scattering.

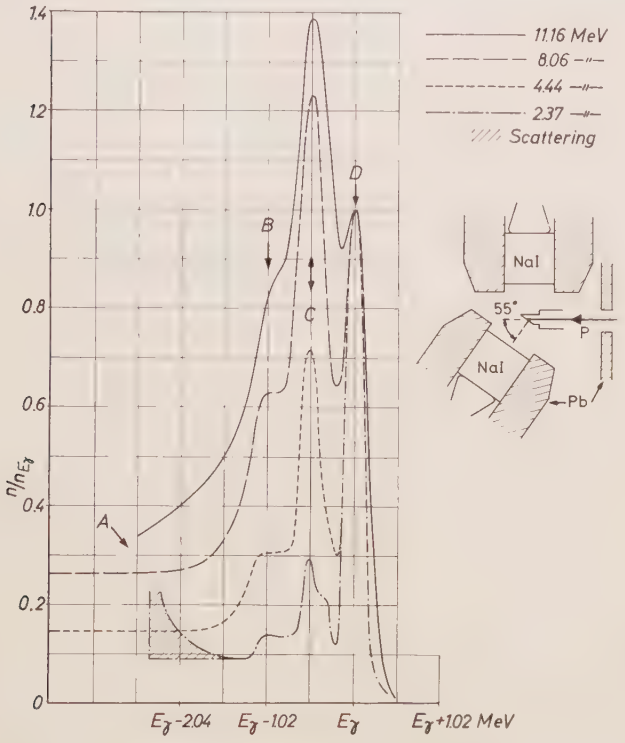

Fig. 1. Pulse-height distribution from a 5″ by 5″ NaI(Tl) scintillation counter† shown for different energies. Configuration as in inset, the distributions being for the lower crystal at 55° to beam direction. Distance 7 cm from target to both crystals.

B: *The pair peak*: At energies above the threshold for pair production, a peak due to the absorption of the pair kinetic energy can be seen. With 5″ × 5″ crystals this peak is very small and due to absorption events near the edge of the crystal where both annihilation quanta escape.

C: *"Annihilation" peak*. Absorption by pair production inside these crystals is strongly accompanied by simultaneous absorption of one or both of the annihilation quanta. The farther from the crystal center the absorption takes place, the larger the probability of one of the quanta escaping and the absorption event giving rise to a pulse in this peak. As the primary γ-ray moves to higher values this peak is broadened in energy due to brehmsstralung processes giving increasing tails on all peaks. This effect is clearly visible from around 10 MeV and increasing with energy. The Compton edge from the secondary annihilation quantum is mixed into the pair peak, and the annihilation peak itself has a similar Compton edge from the full energy peak riding on its upper slope.

D: *Photo peak or full energy peak*: At energies where pair production is small and photoproduction still large, absorption by the last process gives rise to the strong peak revealing the full energy of the primary γ-ray. As pair production increases and photoabsorption diminishes with increasing energy, the full energy peak is mainly due to simultaneous absorption of the two annihilation quanta and other multiple processes.

From the preceding considerations the following points emerge:

(i) To obtain standard line shapes to be compared with unknown distributions care must be taken to keep the counter surroundings identical in both cases to preserve the shape of the low energy tail. The standard shapes† should be observed "in situ".

(ii) To preserve the same proportions between the different peaks, the same amount of collimation and the same solid angle must be used to confine especially pair production to the same regions of the crystal. The enhancement by collimation on the relative size of the full energy peak is shown in fig. 2††.

(iii) The relative sizes of the peaks and the dip between them are markedly energy dependent, the features of the low energy tail are a more slowly varying function of energy.

2.2. CALIBRATION METHOD

When the necessary precuations are taken the standard shapes can be used in the following manner: Of the large number of resonance levels available only a limited number have transitions giving γ-ray lines useful for obtaining standard shapes. In the present study in the mean only one such line is found per MeV γ-ray energy. The

† Counter obtained from Harshaw Chemical Co., Matched Window Assembly with selected 3″ photomultiplier, resolution 9.2 % at 661 keV.

†† This feature of collimation can be used to indicate full energy peaks in complicated spectra by comparing collimated and uncollimated distributions.

features of the distribution shapes therefore have to be plotted as a function of energy to enable us to fit all γ-ray energies. One useful obvious method is

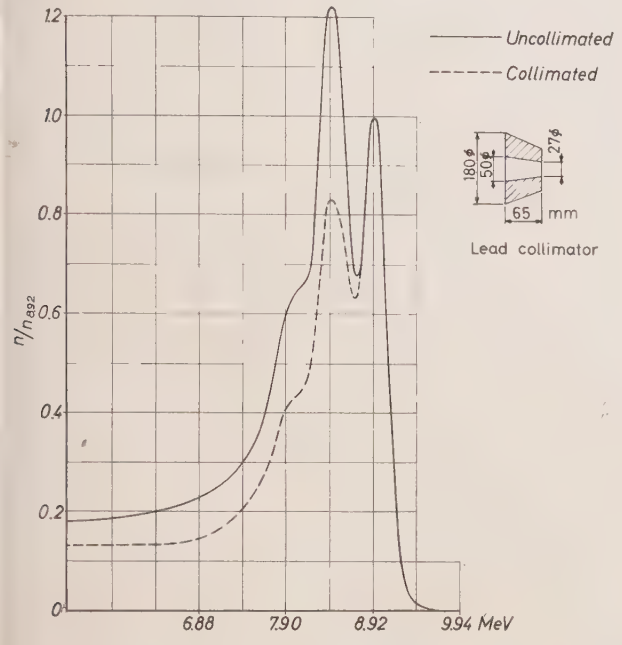

Fig. 2. Collimated and uncollimated distributions of a 8.92 MeV γ-ray. Same crystal and configuration as in fig. 1, except the distance to both crystals are 10 cm, and both are equipped with collimators in the collimated distribution. Collimator shown in inset.

to plot the ordinate of prominent points in a distribution, as the annihilation peak (full energy — 0.51 MeV) and the pair peak (full energy — 1.02 MeV). The values plotted can for instance be the number of counts at that point relative to the number of counts at the full energy peak. A large number of chosen points has to be plotted to preserve the distribution shape, and it is found that an interval of 0.17 MeV ($\frac{1}{3}$ of 0.51), starting a few intervals above full energy, covers the peak region well[1]). In the tail wider spacing is possible. From such plots any monoenergetic γ-ray distributions can be constructed and successively folded into an unknown distribution, starting in the high energy end. A set of plotted curves has to be prepared for every experimental configuration of counters, collimators and target systems. The labours involved in preparing the curves necessiates a limited number of configurations to be used. For instance so far only four have been considered by us: a distance of 10 cm for both 5 inch counters, both collimated and uncollimated, for use with angular correlation studies, and one distance 7 cm, with and without an anti Compton shield[4]) between the counters, for general and coincidence work. As an example the curves for our best counter (9.2% resolution of the

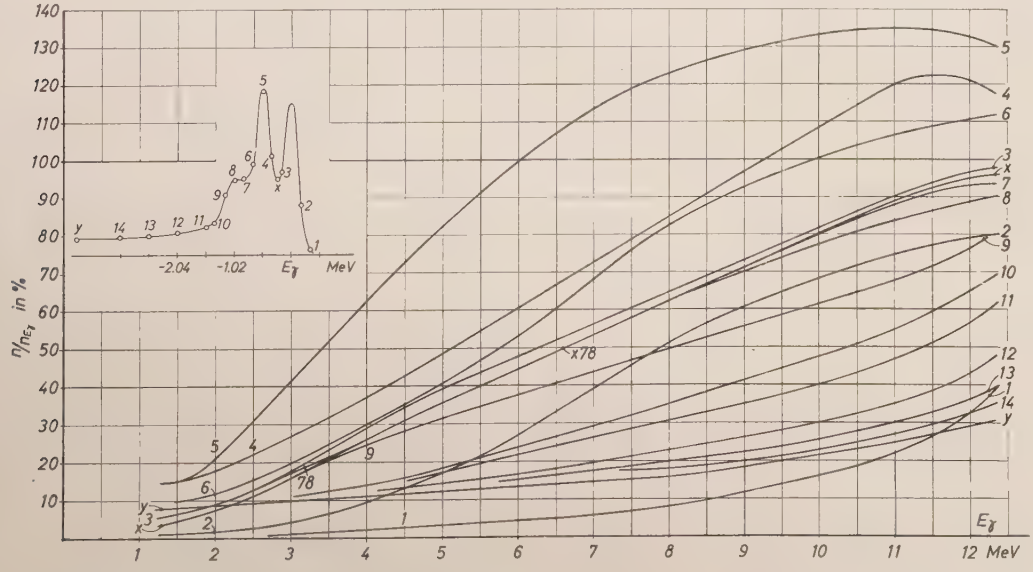

Fig. 3. Shape callibrationc urves for 9.2% res. crystal in the geometry shown on fig. 1. (Both crystals at 7 cm, 9.2% res. crystal in lower position at 55° to the beam.) The curve parameters shown are the position of the distribution points for which the corresponding number of counts relative to the full energy point are given.

0.66 MeV Cs^{137} photo-peak) are shown in fig. 3 for 7 cm distance and no shield in front. The counters are covered with a close fitting cylindrical lead shield, 8 cm thick around the crystal.

To find the total number of counts due to a single γ-ray in a mixed distribution, an estimate of of the tail area has to be made. To avoid this the customary method is to consider the area of the γ-ray full energy peak only, and compare this with a plot of the peak area to total area ratio (peak to total ratio) which can be prepared from the standard monoenergetic shapes[6,10,11]).

The total numbers found in this manner are multiplied by solid angle and efficiency factors to give the intensity of the observed γ-rays. This total intensity is dependent on how the total areas of the standard shapes are evaluated, and as the tabulated efficiencies only take into account γ-rays reaching the crystal directly from the source, counts due to scattering should not be included in the evaluated total areas. This is achieved by extrapolating the low tail of the Compton distribution as a straight line to zero energy, and only include in the tail area the part below this line. Any sharp rise at low energies is not included. The peak to total ratios found in this manner and multiplied by the crystal efficiencies are shown in fig. 4 as the peak efficiencies for the same counter and configuration as above. The crystal efficiencies were found from refs.[5]) and[7]).

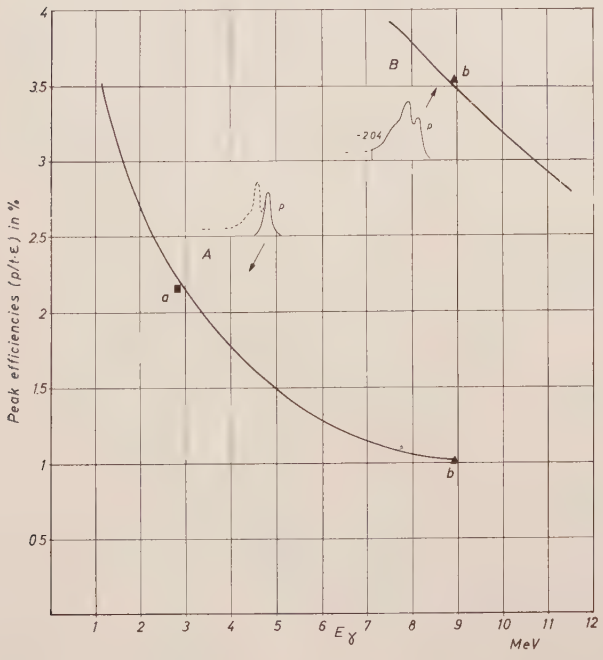

Fig. 4. The peak efficiencies of the distributions plotted in fig. 3. Above 7.48 MeV the ratio is also given for the peak region down to the — 2.04 MeV point (curve B). Experimentally determined peak efficiencies shown (a) at 2.75 MeV relative to 1.37 MeV and (b) at 8.92 MeV relative to 2.75 MeV (Sects 3.6 and 3.10).

Strong distortions of the standard shapes can be found from the following effect. A strong cascade through an intermediate state linking the same two levels as between which the observed γ-ray is emitted may give rise to accidental summing. Both members of the cascade with energies much lower than the observed line will be detected simultaneously in the same counter crystal. Folded together the two low energy distributions will give the accidental sum distribution. As both have higher peak to total ratios than the crossover the accidental sum will be quite different from the standard shape pertaining to the observed energy, and also from the low energy distribution, the extreme case being the square of the half energy distribution. The effect can be clearly seen for instance when observing in bad geometry the 4.43 MeV line in B^{11} (pγ)C^{12} as described in section 3.3. A weak 16 MeV crossover is seen to have a substantially better full energy peak than the 12 MeV line feeding the 4.43 MeV state. Where such cascades exsist the application of corrections should be considered.

3. The Resonance Reactions

3.1. GENERAL

The γ-ray spectrum emitted from the chosen resonances should preferably contain only the single γ-ray to be used for calibration. Interfering radiation should be at a minimum, and if present of low intensity and easily recognised and subtracted. The resonances should be of intensity at least one order of magnitude above general and machine background. These demands heavily limits the

[10]) N. H. Lazar, R. C. Davis, and P. R. Bell, Nucleonics **14**, 4 (April 1956) 52;
and N. H. Lazar and H. B. Willard, in Physics Division Semiann. Prog. Rep. March 10, 1956, A.E.C. Report ORNL-2076 (1956) 55.

[11]) I. E. Draper and A. A. Fleischer, Nucl. Instr. and Meth. **9** (1960) 67.

choice of useful reactions. When sufficient resonances are not available, resonances with one strong transition to a low excited state and a fair distance in energy to the next transition can be used to provide calibration points for the essential peak region only.

Some care has to be taken when using a primary γ-ray from a resonance broad (in eV) with respect to the spectrometer resolution. Then the target thickness (in eV) and beam energy spread have both to be small compared to the resolution. The mean excitation energy of the reaction, and thus the energy of the γ-ray, will be given by the energy of the proton beam and not by the energy of the resonance peak, except when they coincide. If the resonance width is not too large compared with the resolution, but still large enough to give an measurable energy shift when bombarding off resonance maximum, one can still work with a thick target. However, in this case the bombarding energy should be chosen well above resonance to avoid shifts.

The resonance reactions found suitable to use for shape calibration are listed in table 1 according to the calibration lines they provide. The majority of γ-rays listed can be utilised even with moderate currents of protons down to 1 or 2 μA. The fair number of resonances accesible make the use of isotopic targets unneccessary. For a resonance lying below the low energy limit of a machine, a higher mass beam can be used.

The region of low γ-ray can be extended by using radioactive sources useful for calibration[12]). The sources should be prepared on target discs and situated in target position.

In the following the reactions will be rewieved in light of our purpose, and are presented in an order following mass number. Most of the information is taken from the well known reviews of F. Ajzenberg-Selove and T. Lauritsen[13]) and P. M. Endt and C. M. Braams[14]).

Table 1
Calibration γ-rays from proton capture reactions

Calibration γ-ray energy (MeV)	Resonance reaction	Proton bombarding energy (keV)	Described in section
0.44	$Na^{23}(pp'\gamma)Na^{23}$	1281	3.6
1.63	$Na^{23}(p\alpha'\gamma)Ne^{20}$	1161 or 1252	3.6
2.37	$C^{12}(p\gamma)N^{13}$	457	3.4
3.51	$C^{12}(p\gamma')N^{13}$	1698	3.4
4.43+	$B^{11}(p\gamma)C^{12}$	163 or 675	3.3
(5.28)+	$Si^{29}(p\gamma)P^{30}$	414	3.8
6.14	$F^{19}(p\alpha'\gamma)O^{16}$	341	3.5
7.48*	$Be^{9}(p\gamma)B^{10}$	991	3.2
(7.89)	$Si^{30}(p\gamma)P^{31}$	620	3.8
8.06	$C^{13}(p\gamma)N^{14}$	554	3.4
8.92+	$Na^{23}(p\gamma)Mg^{24}$	1415	3.6
9.17	$C^{13}(p\gamma)N^{14}$	1747	3.4
10.54*	$Al^{27}(p\gamma)Si^{28}$	759	3.7
10.61*	$Na^{23}(p\gamma)Mg^{24}$	309	3.6
10.71*	$Al^{27}(p\gamma)Si^{28}$	922	3.7
10.88*	$Na^{23}(p\gamma)Mg^{24}$	592	3.6
11.10*	$Al^{27}(p\gamma)Si^{28}$	1326	3.7
11.15*	$Al^{27}(p\gamma)Si^{28}$	1380	3.7
11.16*		1387	3.7
11.58+	$Na^{23}(p\gamma)Mg^{24}$	1317	3.6
11.68+	$B^{11}(p\gamma)C^{12}$	163	3.3
12.15+	$B^{11}(p\gamma)C^{12}$	675	3.3

* For peak region only.

( ) Not studied by the author. Isotopic targets presumably necessary.

+ Members of intense cascades and useful for other calibrational purposes.

3.2. $Be^{9}(p\gamma)B^{10}$

Of the three strong, easily located resonances in this reaction, at 330, 991 and 1084 keV, only the one at 991 can be used for shape calibration. The spectrum at 330 keV is too complicated, and the 1084 keV res. is too close to the 90 keV broad 991 keV res. to easily yield a clean spectrum. The 991 keV res. yield a ground state transition of 7.48 MeV.

Some doubt can be thrown on the usefulness of this γ-ray, as the intensity of cascades with lower energy is not too well known. Recent research has shown the broad resonance to be composed of two wide levels, the lower and least intense member

[12]) A. H. Wapstra, G. J. Nijgh and R. van Lieshout, Nuclear Spectroscopy Tables (North-Holland Publ. Co., Amsterdam, 1959) 133.

[13]) F. Ajzenberg-Selove and T. Lauritsen, Nucl. Phys. **11** (1959) 1.

[14]) P. M. Endt and C. M. Braams, Revs. Mod. Phys. **29** (1957) 683.

decaying through the first excited state at 0.72 MeV[15]).

3.3. $B^{11}(p\gamma)C^{12}$

Two important calibration lines are yielded by this reaction, 4.43 MeV and approximately 12 MeV in cascade. This cascade through the first excited state of C^{12} resonates strongly at 163 ($\Gamma = 7$ keV) and 675 keV ($\Gamma = 322$ keV) proton energy. A crossover of around 16 MeV also exists, revealing the full excitation energy of the reaction. This line has a different resonant behaviour. To obtain a good energy assignment of the 12 MeV line (a primary) at 675 keV it is important here to bear in mind the previous remark on the use of a broad resonance. At a proton energy of 675 keV and with a thin target this line will have an energy of 12.15 MeV. At this energy the tail from the 16 MeV line is small.

To obtain a 4.43 MeV line free from tails of higher lines, a gated coincidence spectrum can be taken. In our case a very thick target and a high mass 2 beam energy (near 1.4 MeV) was used to obtain a high intensity. This can be done as the line in question is a secondary.

3.4. $C^{12}(p\gamma)N^{13}$ and $C^{13}(p\gamma)N^{14}$

The C^{12} reaction yields two strong resonances, 457 and 1698 keV. The low resonance which is the first excited state of N^{13} yields the well known 2.37 MeV γ-line contaminating most low energy ($p\gamma$) reactions. A thick target of lamp black sufficed for observing this line, and the mass 2 beam was used for bombardment. The small admixture of deuterons in this beam was sufficient to give an observable contamination of the 3.09 MeV γ-ray deexciting the first excited state of C^{13}. This level is excited in $C^{12}(dp)C^{13}$. The 3.09 MeV line was small and easily subtracted, but only when a low bombarding energy was used (< 950 keV), as the yield is strongly increasing with energy.

The 1698 keV resonance yields a line of 3.51 MeV, but here a thin target has to be used to avoid the large number of strong C^{13} resonances otherwise adding up to a sizeable background. Both C^{12} resonances has sufficient widths (39 and 70 keV respectively) to consider the previous remarks on the bombarding energy.

Even with the small isotopic abundance of C^{13} in natural carbon (1.12%) the C^{13} ($p\gamma$) resonances have sufficient yield to give calibration γ-rays. However, at least 5 to 10 μA of protons ought to be available. The 554 keV resonance ($\Gamma = 32$ keV) will give a line of 8.06 MeV on a thick target, and the resonance at 1747 keV ($\Gamma = 0.075$ keV) will give 9.17 MeV on a semi-thin target. Both lines are direct ground state transitions. The remaining important resonances, at 1160 ($\Gamma = 6$ keV), 1250 (500 keV), 1466 (16 keV), 1150 (7 keV) and 2000 keV (20 keV) are all either too weak or too complicated to be of any value.

3.5. $F^{19}(p\alpha'\gamma)O^{16}$

This strong contaminant of most resonance reaction measurements yields the prominent 6.14 MeV line deexciting the 2nd excited state of O^{16}. Also the 3rd and 4th excited state are fed by the same resonances as feed the 2nd. In some resonances the lines deexciting these other states strongly disturbs the shape of the 6.14 MeV line. The most satisfactory situation is found in the resonance at 341 keV, where the other lines, at 6.92 and 7.12 MeV, can hardly be seen. To reach this low energy on our large machine we had to use the mass 3 beam. The weak current of this beam kept the counting rate of this intense reaction down on the same level as most of the other measurements†.

3.6. $Na^{23}(p\gamma)Mg^{24}$, $(p\alpha'\gamma)Ne^{20}$, and $(pp'\gamma)Na^{23}$

Of the vast number of resonances in the mass region $A = 20$ to 40 only these reactions provide good calibration lines of appreciable intensity. By bombardment of sodium targets very intense ($pp'\gamma$) and ($p\alpha'\gamma$) resonances are found at several energies. These give γ-rays of 0.44 and 1.63 MeV respectively. We used the (pp') resonance at 1218 keV and the ($p\alpha'\gamma$) resonances at 1161 or 1252 keV[16]).

† To avoid contaminating our target chamber with fluorine the targets were covered with a thin evaporated layer of aluminium.

[15]) J. Kantelle, Ann. Acad. Sci. Fennicae VI, **37** (1959); L. Simons, Soc. Sci. Fennica, Comm. Phys.-Math. XXIV, **8** (1960).

[16]) S. L. Andersen, O. Dørum, E. Gautvik and T. Holtebekk, Nucl. Phys. **22** (1961) 245.

Table 2
Resonances in $Al^{27}(p, \gamma)Si^{28}$ (ref.[19]))

E_p (keV)	$\omega\gamma$ (eV)*	$E_x - 1.78$ (MeV)	E_p (keV)	$\omega\gamma$ (eV)*	$E_x - 1.78$ (MeV)	E_p (keV)	$\omega\gamma$ (eV)*	$E_x - 1.78$ (MeV)
731	1.8		991	18		1212	5	
736	2.0		1002	0.5		1261	5	
741	0.17		1024	4		1274	0.5	
759	1.6	10.54	1089	0.5		1315	5	
766	1.9		1096	0.5		1326	5	11.10
773	4.7		1117	3		1362	5	
884	0.5		1171	1		1380	30	11.15
922	2.0	10.71	1182	3		1387	25	11.16
936	2		1198	4				

* Up to and including 773 from Endt and Heyligers[1]), above 773 rough values for guidance only[17]).

The strong (pγ) resonance at 1317 keV has what seems a pure transition of 11.58 MeV to the first excited state, and another strong (pγ) resonance at 1415 keV shows only one cascade deexciting the resonant level through the 4.12 MeV state of Mg^{24} (ref.[17])). The latter gives rise to a line of 8.92 MeV, the primary, and secondaries of 2.75 and 1.37 MeV de-exciting the 4.12 MeV level through the first excited state at 1.37 MeV. No fine structure due to any other line of appreciable intensity could be seen in the γ-ray spectrum from these resonances, and the 11.58 and 8.92 MeV lines were considered useful for our purpose. The use of the 2.75 MeV line would require either careful tail subtraction, or good intensity and coincidences, which was more cumbersome than the use of the good carbon line at 2.37 MeV.

A few of the other (pγ) resonances, notably the ones at 309 and 592 keV have their strong transitions to the first excited state of Mg^{24} sufficiently removed from any lines of appreciable intensity (at $\approx$ 8 MeV) to yield calibration lines at 10.61 and 10.88 MeV. These lines can only be used for the peak area. At large solid angles a correction for accidental summing should be considered. The cascades of any intensity connecting the resonance level and the first excited state are through the 4.24 and 5.22 MeV levels having secondaries of 2.87 and 3.86 respectively. Their relative intensities to the calibration line are at both resonances 40% through 4.24 and 20% through 5.22 MeV[18]).

The large number of resonances in these reactions makes the use of thin targets necessary.

3.7. $Al^{27}(p\gamma)Si^{28}$

A few of the numerous resonances in this reaction has strong first excited state transitions again removed fairly well from the next transition of any intensity. A list of the Al^{27} resonances in the region of interest is given in table 2. The suitable resonances are underlined, and the relative intensities are given. The values of $\omega\gamma$ above 773 keV are only approximate and for guidance. The most satisfactory tails are found at 922 and 1326 keV. Neither of these resonances are particularly strong, but readily observable with good resolution and on a thin target. By far the strongest are the 1380 and 1387 keV resonances. These two are sufficiently similar so that no separation is necessary. At all underlined resonances except 759[1]) competing cascades are sufficiently weak to make accidental summing corrections unnecessary[17]).

3.8. Si(pγ)P

The resonance at 414 keV in $Si^{29}(p\gamma)P^{30}$ is reported to have a 90% cascade with members of

[17]) Recent measurement in this laboratory (unpublished).
[18]) P. M. Endt, Nucl. Instr. and Meth. **11** (1961) 3.
[19]) S. L. Andersen, H. Bø, T. Holtebekk, O. Lønsjø and R. Tangen, Nucl. Phys. **9** (1958/59) 509.

5.28 and 0.68 MeV[20]). The 5.28 MeV line should presumably be useful for shape calibration.

Also the strong 620 keV[21]) resonance in the $Si^{30}(p\gamma)P^{31}$ reaction should yield a calibration line. The energy is 7.89 MeV, the ground state transition of the resonant level.

When more is known about the large number of $(p\gamma)$ resonances above 1 MeV in these reactions, more calibration lines probably can be found.

None of these resonances have been studied in the present work, and strong currents or isotopic targets presumably have to be used.

3.9. OTHER REACTIONS

Of the $(p\gamma)$ resonances in higher Z elements none have so far been used for shape calibration. Especially the $P^{31}(p\gamma)S^{32}$ reaction has been the subject of much study, and only the γ-spectra of the resonances below 800 keV are not known. However, recent experiments[17]) indicate the existence of a strong ground state transition in the 650 keV resonance, of 9.48 MeV excitation energy. By the use of isotopic targets of N^{15} the 4.43 MeV γ-ray of C^{12} (sec. 3.3) can be observed through the reaction $N^{15}(p\alpha'\gamma)C^{12}$ (ref.[10])). At higher bombarding energies new $(pp'\gamma)$ and $(p\alpha'\gamma)$ reactions occur. The lines from these reactions are however mainly in the region 1.5 to 4 MeV, where ample coverage is found from the described reactions.

Reactions with bombarding particles other than protons may yield γ-rays useful for shape calibration. The (d p) and (d n) reactions has been considered, but in general seem to yield rather complicated spectra, especially since they both occur simultaneously. The 3.09 MeV line excited in C^{12}(d p)C^{13} (sec. 3.4) seems a possibility. As no deutron beam is presently available these reactions have not been studied. The same applies to α-excited reactions, which is anyhow easily contaminated by $(\alpha\, n)$ reactions.

3.10. OTHER APPLICATIONS

The absence of interfering γ-radiations in these reactions should extend their usefulness to other calibrational purposes. For instance pure cascades are much in demand for experimental determination of the variation in scintillation counter efficiency with energy. Of the resonances studied here both the $B^{11}(p\gamma)C^{12}$ resonances and the $Na^{23}(p\gamma)Mg^{24}$ reaction at 1317 and 1415 keV should be suitable for this purpose. In particular the last resonance has a triple cascade yielding two simultaneous determinations, at 2.75 and 8.92 MeV, relative to an energy of 1.37 MeV. Possible interference from the 1.63 MeV $(p\alpha'\gamma)$-line can easily be subtracted. With a little care probably some of the underlined $Al^{27}(p\,\gamma)Si^{28}$ resonances in table 2 can also be used.

These cascades should presumably also be helpful when studying the properties of sum-coincidence spectrometers[11]).

Acknowledgements

The author is greatly indebted to Mr. S. L. Andersen and Dr. A. Storruste for valuable discussions, and to Professor Dr. R. Tangen for continuing interest and help. The valuable assistance by Mr. A. Tveter is especially appreciated. The work was sponsored by the Royal Norwegian Council for Industrial and Scientific Research which is gratefully acknowledged.

[20]) K. J. van Oostrum and A. C. Meijer, Nucl. Instr. and Meth. **10** (1961) 37.

[21]) J. Kuperus, P. J. M. Smulders and P. M. Endt, Physica **25** (1959) 600.

UCLEAR INSTRUMENTS AND METHODS 12 (1961) 299–306; NORTH-HOLLAND PUBLISHING CO.

A METHOD OF ALPHA PARTICLE SPECTROSCOPY FOR MATERIALS OF VERY LOW SPECIFIC ACTIVITY

C. R. HILL

Physics Department, Institute of Cancer Research: Royal Cancer Hospital, London

Received 13 April 1961

his paper describes a pulse ionisation chamber technique that as been developed in order to identify the alpha radioactivity hat occurs as a natural constituent of many biological tissues nd environmental materials. The chamber has a gridless, oncentric cylindrical configuration, in which the 15000 sq. cm source forms the outer electrode. Nuclides occurring in a material at a specific activity of a few tenths of a picocurie per gramme can be identified and spectral line widths of the order of 150 keV are obtainable.

. Introduction

Natural alpha activity commonly occurs in bio-ogical ashes at concentrations of a few tenths of a picocurie per gramme and in determinations of the ature of such activity it is often desirable to avoid methods that rely on chemical concentration, which may be very laborious if adequate care is to be aken to eliminate all possibility of contamination r loss of material. In order to analyse directly such ow specific activities, in a reasonable period of ime, it is necessary to observe a large fraction of he alpha particles produced in a quantity of ma-erial at least of the order of a gramme and a funda-mental requirement of such an analysis is that this material shall be so disposed physically that alpha particles originating within it will transfer a large and sensibly constant fraction of their energy to a suitable transducer. To satisfy this requirement in practice it is necessary to spread the source material n a film having a surface density of the order of 0.1 mg per sq.cm. It is also necessary that the ma-erials employed both in the transducer and in the mechanical support for the source should them-elves give rise to the least possible background counting rate.

Of the many available methods of alpha spectro-copy, only the pulse ionisation chamber appears to provide the possibility of a source-transducer ystem capable of accomodating more than a few milligrammes of material. Parallel plate, gridded pulse ionisation chambers have been described by several authors[1–4]) but their application to very low specific activities is limited in view of the un-acceptably large collector capacitance which occurs with a source area of more than a few hundred sq.cm. By using a cylindrical, gridded arrangement Lonati[5]) has been able to construct an instrument with a source area of 2800 sq.cm, capable of accom-modating about a quarter of a gramme of source material. With a concentric arrangement of elec-trodes, however, the need for a grid as a means of reducing "positive ion effect" can be largely ob-viated if the alpha tracks and their associated posi-tive ion columns can be confined to the region of comparatively low field close to the negative outer electrode. A spherical electrode arrangement was in fact used in this way, for small, high specific acti-vity sources, by Ghiorso[6]) before the Frisch grid had come into common use. For use with very low specific activity materials a concentric arrangement has the advantage of providing a low collector ca-pacitance even with source areas of 10^4 sq.cm or more, while elimination of the grid greatly simpli-fies the construction and also dispenses with a

[1]) T. E. Cranshaw and J. A. Harvey, Canad. J. of Research 26 A (1948) 243.

[2]) O. Bunemann, T. E. Cranshaw and J. A. Harvey, Canad. J. of Research 27 A (1949) 191.

[3]) D. H. Wilkinson, Ionisation Chambers and Counters (Cambridge, 1950).

[4]) K. M. Glover, AERE C/R 2091 (1957).

[5]) R. D. Lonati *et al.*, Nuovo Cim. 10 (7) (1958) 133.

[6]) A. Ghiorso *et al.*, The Transuranium Elements, Ed. G. T. Seabourg *et al.*, Part 2 (Mc Graw-Hill, 1949) p. 1266.

large surface area that is liable to accumulate surface contamination.

2. Theoretical Considerations

The principle of the gridless alpha pulse ionisation chamber can be employed with either a cylindrical or a spherical electrode arrangement. An uncollimated alpha emitting source on the inner surface of the outer electrode of such an arrangement will give rise in its vicinity to randomly oriented ionisation tracks consisting, in the presence of a free-electron gas, of positive ions and electrons. The collection of electrons on to the inner electrode from an ionisation track which grazes the surface of the outer electrode will give rise to a fast voltage pulse of magnitude dependent on the initial energy

Curve	Inner electrode radius (cm)	Outer electrode radius (cm)	Electrode configuration	Ratio between field strengths at surfaces of inner and outer electrodes	Applied potential required to provide field strength of 20 v/cm at surface of outer electrode
a	0.025	15	Cylindrical	600	1900V
b	0.5	30	Cylindrical	60	2500V
c	0.05	30	Cylindrical	600	3800V
d	2.0	30	Spherical	225	8400V
e	1.0	30	Spherical	900	17400V

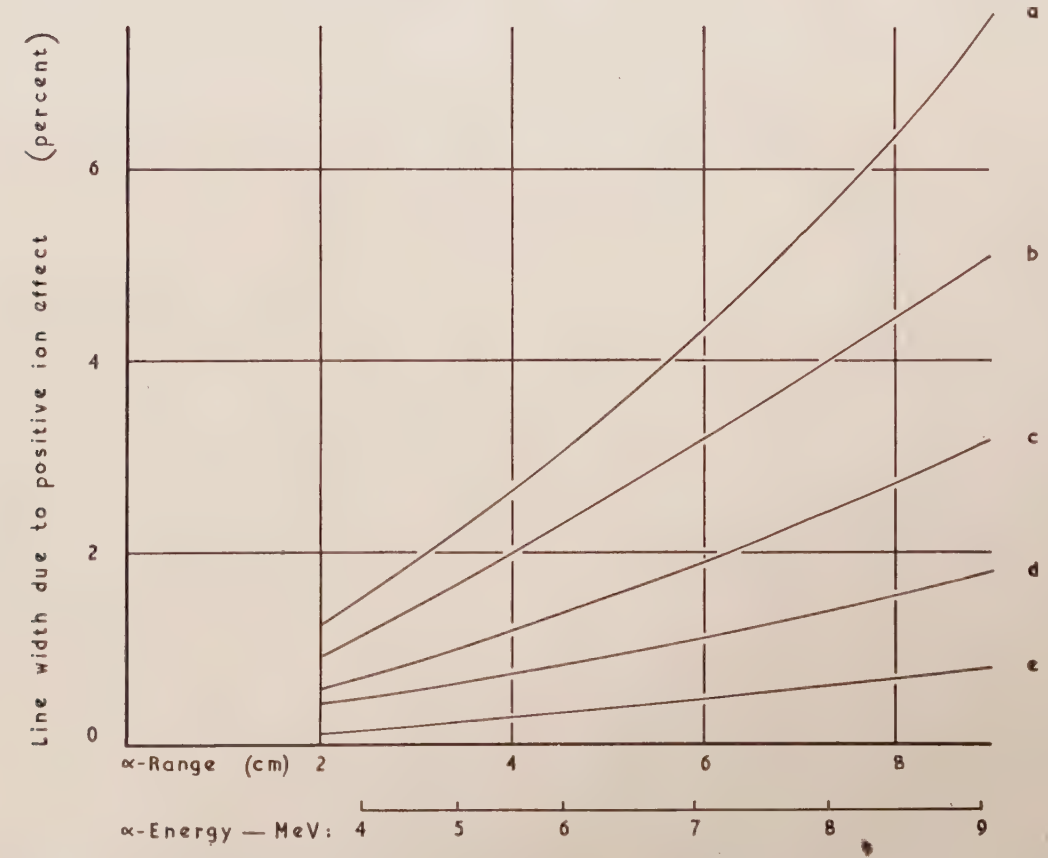

Fig. 1. "Positive Ion Effect" in concentric, two-electrode pulse ionisation chambers.

of the alpha particle. Tracks having other orientations will give rise to somewhat smaller pulses, since all of the electrons will not move through the full electrode potential difference. In particular, a radially orientated track of length R will give rise to a fast pulse reduced in magnitude by a percentage P,

$$= \frac{100}{V} \int_{b-R}^{b} V(r) \cdot B(r) \cdot \mathrm{d}r ,$$

where:

V is the potential applied between the electodes,

$V(r)$ is the potential at radius r, relative to the outer electrode,

$B(r)$ is the distribution function for ionisation density along the alpha track (the Bragg function),

b is the radius of the outer electrode.

Provided that the electrode spacing is several times greater than the length of the alpha track, there will be a substantially rectangular distribution for the numbers of particles whose orientations result in pulse height reductions between zero and P, and it can thus be seen that P represents the spread in pulse heights due to "positive ion effect" in the system. Values of P have been calculated for various electrode systems and are shown in fig. 1.

In a system of given outer electrode radius, a fundamental limitation on inner electrode radius, and therefore on the extent to which "positive ion effect" can be reduced, is imposed by the requirement that field strengths should everywhere be adequate to ensure complete collection of electrons, without anywhere being so great as to give rise to gas multiplication. From this point of view a spherical system is evidently superior but its use for large sources is in practice ruled out by difficulties in source preparation. In pure argon, complete collection of electrons occurs with field strengths greater than 7 V per cm per atm[7]) and the addition of about 2% of methane does not increase this figure to more than 20 V per cm per atm, while gas multiplication does not take place in such gases with field strengths less than about 2×10^4 V per cm per atm. A ratio of about 1000:1 thus exists between the maximum and minimum allowable field strengths and it is therefore evident from the data of fig. 1 that cylindrical systems can, in principle, be designed to provide "positive ion effects" of less than two per cent over the practically important range of alpha particle energies between 4 and 6 MeV.

3. Description of the Instrument

An instrument based on the above principles has already been briefly described by Mayneord and the present author[8]) and another, improved model has now been constructed. The new instrument consists essentially of two concentric cylindrical electrodes of length 90 cm and radii 30 and 0.45 cm respectively (fig. 2). The material to be analysed is mounted on the metallized surface of a sheet of 0.1 mm thick aluminized cellulose acetate, lining the inner surface of the outer electrode and providing a useful area of 15000 sq. cm for the unknown source. A negative potential is applied to the source, and the inner, collecting electrode is earthed through the grid leak capacitor of the associated amplifier. A set of four concentric guard rings is placed at each end in order to maintain approximately radial field conditions throughout the length of the cylinder.

A standard calibrating source is provided on one side of a rotatable strip whose surface is located geometrically in the surface of the sample cylinder, in a notch cut lengthwise from the main sample holder. The other side of the standard source strip is bare aluminized cellulose acetate and, by means of a control shaft passing through the wall of the gas chamber, the standard can be exposed at will. When exposed, its spectrum is analysed under conditions identical to those applying to the unknown spectrum, on which it is superimposed. The standard source, which consists of U^{238} (4.19 MeV), U^{234} (4.77 MeV), Am^{241} (5.48 MeV) and Cm^{242} (6.10 MeV) and carries a total activity of the order of a few millimicrocuries, is located at the bottom of the cylinder in order to minimise any possible contamination of unknown samples as a result of radioactive material becoming detached from its backing. A view of the electrode structure in position in the gas chamber is given in fig. 4.

The electrode structure is designed to provide a low collector capacitance and the calculated value

[7]) E. D. Klema and H. H. Barschall, Phys. Rev. **63** (1943) 18.

[8]) W. V. Mayneord and C. R. Hill, Nature **184** (1959) 667.

for the cylindrical capacitor formed by the source and the collector (assumed semi-infinite) in the absence of guard rings is 12 pF. The measured capacitance of the chamber with guard rings in place and including the connection to the head amplifier is 22 pF, to which must be added the input capacitance of the head amplifier, equal to 10 pF, giving a total of 32 pF. This figure is comparable to the value to be expected in a parallel plate gridded chamber having about 1% of the available source area of the present instrument.

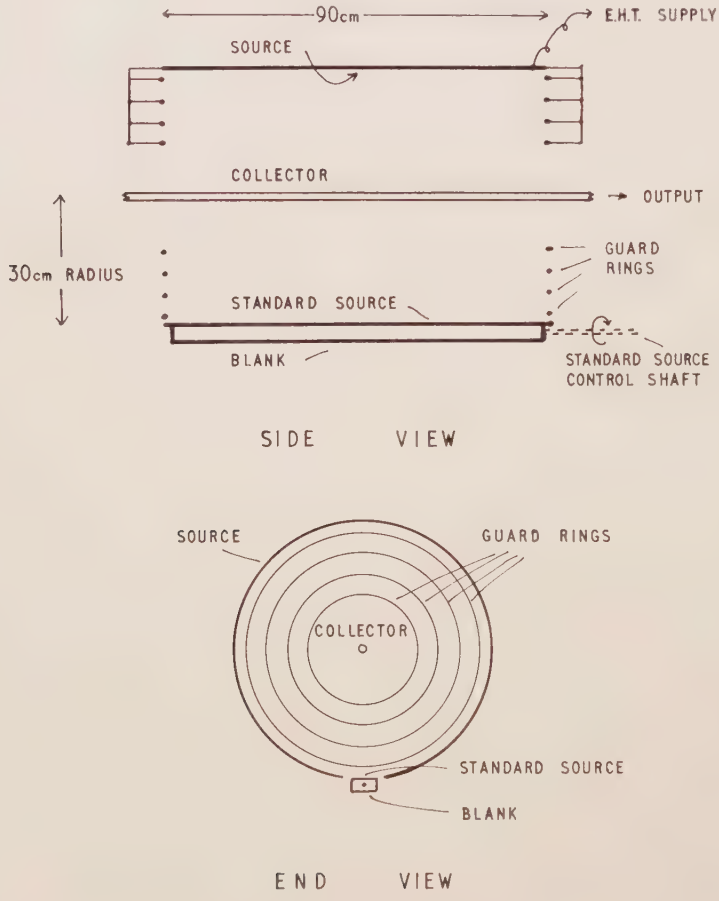

Fig. 2. Electrode arrangement.

4. Gas Chamber

The electrode structure is contained in a vacuum tight gas chamber which is made of stainless steel in order to achieve a low equilibrium radon concentration (fig. 3 and 5). One end of the chamber can be removed and the cylindrical Perspex framework supporting the unknown source can then be withdrawn, leaving the collector and the standard source in place. The sets of guard rings are attached to the ends of the chamber (fig. 4). The head amplifier is mounted directly on to a 7.5 cm diameter flanged port at the closed end of the tank and the output line is brought to it through a thick sheet of insulator which serves to seal the port opening. A screened box containing an electrical *RC* filter is mounted similarly on another port, through which the EHT line enters the chamber. This box is also used to provide the following facilities: (1) A means for checking the EHT supply connexions within the chamber, which are made by means of spring contacts, when the door of the chamber is closed, and (2) a test socket through which artificial pulses can be applied to the collector under normal operating conditions, as a means of testing the amplifier.

Before filling with gas the chamber can be evacuated to a pressure of 0.5 mm Hg, by means of a vacuum pump of 200 litres per minute nominal pumping speed.

In use, the chamber is filled to atmospheric pressure with a 98 : 2 argon-methane mixture, which has a somewhat lower saturation field strength than the 90 : 10 mixture normally used in pulse ionisation chambers. A continuous purification system is provided in order to ensure constant conditions of electron collection efficiency and electron collection time throughout the course of a measurement, and also to remove any radon which might accumulate in the chamber. The gas is first passed over a column of metallic calcium turnings maintained at a temperature between 300°C and 350°C. It then passes over a column of charcoal cooled to about — 78°C in a bath containing a mixture of solid CO_2 and acetone. In order to economise in solid CO_2 the gas connexions to the charcoal column are made through a heat exchanger. The total volume of the gas chamber is 500 litres and the gas can be circulated through the purification system, by means of a variable speed pump, at a rate of 4, 8 or 12 litres per minute.

It has been found in practice that the electron collection efficiency varies inversely with the temperature of the chamber gas, presumably due to the persence of electronegative vapours introduced with the source, the effective outgassing of which is considered to be impracticable. For this reason it has been necessary to maintain the temperature of the gas chamber constant within plus or minus one centigrade degree.

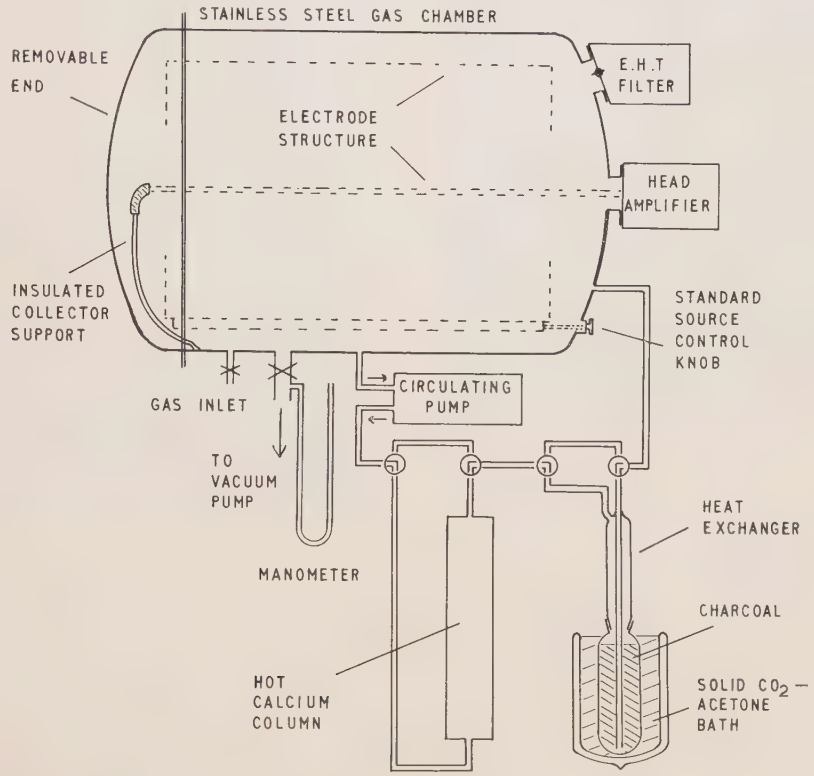

Fig. 3. Gas chamber and gas circulation system.

5. Electronic Equipment

The instrument is used in conjunction with a type 1049 B amplifier (using the improved version of the H.F. head amplifier, Ekco type N 568B) and the spectrum is analysed by means of a C.D.C. 100 channel pulse height analyser. With this equipment the measured contribution of amplifier noise to the

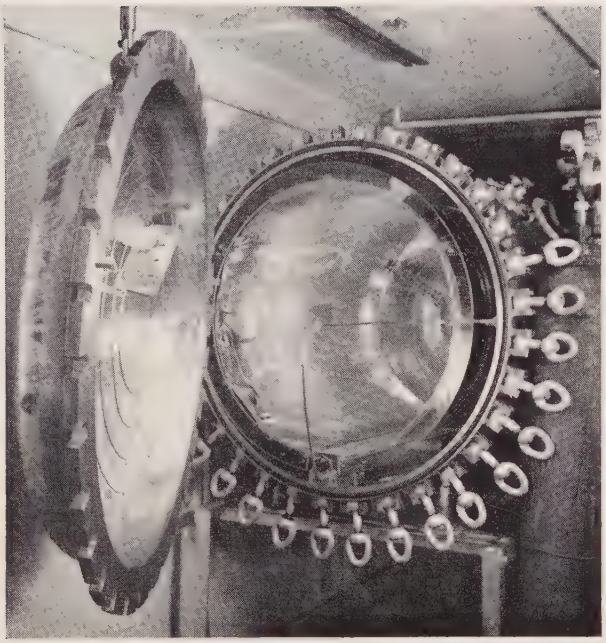

Fig. 4.
View of interior of chamber, showing electrode arrangement

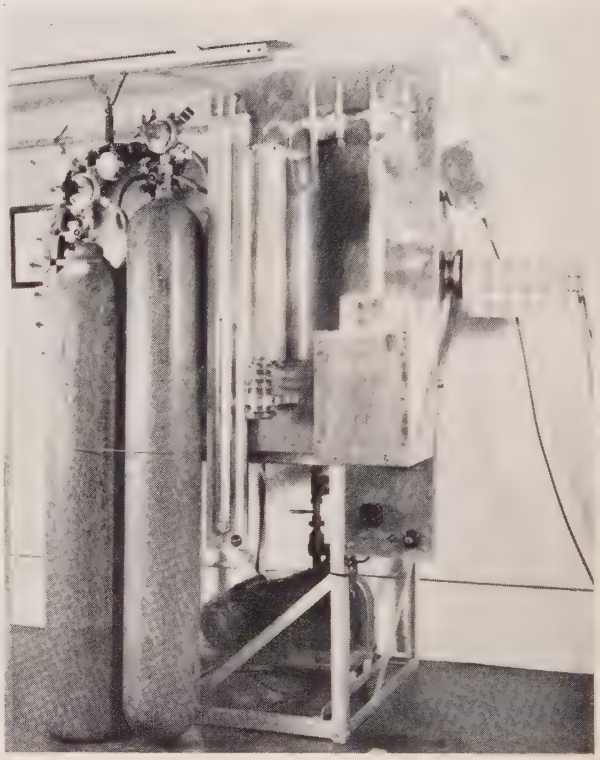

Fig. 5. General view of chamber.

half width of a spectral line at 5.5 MeV is 75 keV. This value was measured by observing the pulse height distribution produced in the 100 channel analyser when a series of 20 microsecond square pulses was applied to the head amplifier input at a level that simulated the pulse due to a 5.5 MeV alpha particle in the chamber. An electrode potential of 5 kV is normally employed but only a very slight deterioration in performance is observed when this value is decreased to 3 kV.

6. Source Preparation

In the preparation of sources the object is always to reduce the starting material to a form in which the maximum particle size is of the order of one micron, and then to apply the material to the surface of a cellulose acetate sheet in such a way as to spread it uniformly and avoid processes, such as the formation of large crystals or clusters of particles, which would lead to excessive self-absorption in the source. To achieve the required particle size with most of the materials encountered in practice, prolonged grinding is necessary. When adequate material is available the grinding can conveniently be carried out in a steel ball mill, but when, as is often the case, only about a gramme of material is available, loss of material by adhesion to the surfaces of the ball mill becomes too great and other means of grinding have to be used. For this purpose an agate hand pestle and mortar has been used. To save time and effort, a power operated drive has been constructed using an old 78 r.p.m. electric gramophone. The mortar is mounted on the turntable, slightly eccentrically, with the pestle, suitably weighted, resting on it and restricted to free movement along its own vertical axis. With this device wet grinding can be continued for several hours with only occasional attention and with negligible loss of material. Animal tissues containing protein can be handled without ashing by acetone drying and subsequent grinding in a ball mill. The ground tissue can then be digested with pepsin, resulting in most of the material going into solution.

The aqueous suspension or partial solution obtained by the methods described above is sprayed on to a cellulose acetate sheet. A simple spray, working on the familiar scent spray principle and connected to a compressed air supply, has been

found quite adequate for the purpose, provided that it is constructed and used in such a way as to avoid the formation of large droplets. Before commencing spraying, the cellulose acetate sheet is wetted by wiping with a paper tissue soaked in a wetting agent. A 5% solution of "Teepol" has been found suitable for this purpose. In order to obtain a uniform film by this technique it is necessary to spray on an amount of liquid that is sufficient to allow the sample material to spread evenly over short distances without showing any tendency to collect in puddles as a result of unevenness in the cellulose acetate sheet.

7. Performance of the Instrument

The optimum radius for the centre electrode was selected experimentally as 0.45 cm. Although, in principle, slightly better resolution should be obtainable with a smaller collecter radius, this improvement is difficult to achieve, due partly to the accompanying decrease in electron collection stability.

The resolution obtainable is indicated by fig. 6, which shows the spectrum of a sample of thorium nitrate. The line width measured for the thorium C′ peak (8.78 MeV) is 350 keV, in good agreement with

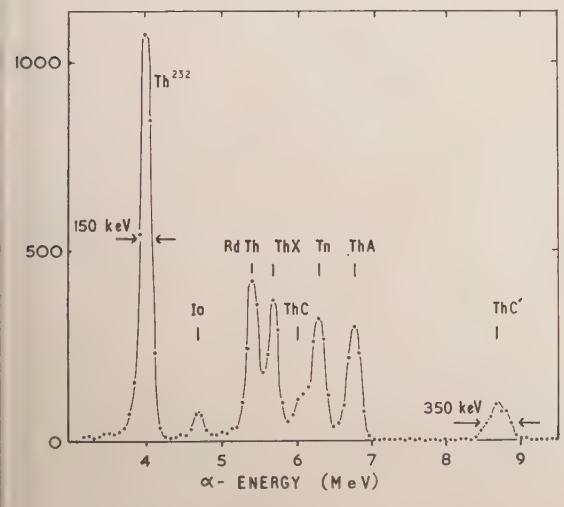

Fig. 6. Test spectrum obtained for a thorium salt.

the positive ion effect to be expected with the particular combination of electrode radii (fig. 1), and this effect therefore appears to provide the main limitation on line width at the high energy end of the spectrum. For the thorium-232 peak (3.98 MeV), however, the measured line width is 150 keV while the theoretical positive ion effect is only 40 keV. The discrepancy here is accounted for partly by the amplifier noise contribution of 75 keV and the remainder is probably due to the formation of crystals and consequent self absorption in the source. A line width of 110 keV has been obtained for an Am^{241} source (5.48 MeV) under normal operating conditions.

In the analysis of normal biological materials the resolution obtained in practice may be decreased as a result of several factors. It is usually necessary to count a sample for a period of 16 hours or more, during which period a certain amount of drift in amplifier gain and in the gas characteristics may occur. This is normally no greater than 50 keV and can be checked by means of the standard source. Self absorption in the source is another cause of loss of resolution, and, in the case of sources of very low activity, statistical fluctuations in the number of pulses recorded in each channel may also act significantly to reduce resolution.

The sensitivity of the instrument is illustrated by the background spectrum of fig. 7, which was obtained by exposing a plain sheet of aluminised cellulose acetate for a 48 hour counting period. It will be seen that the counting rate per channel varies from about 2.4 cph, in the alpha particle energy range 4 to 5 MeV, down to 0.35 cph in the range 8 to 9 MeV. The overall background counting rate in

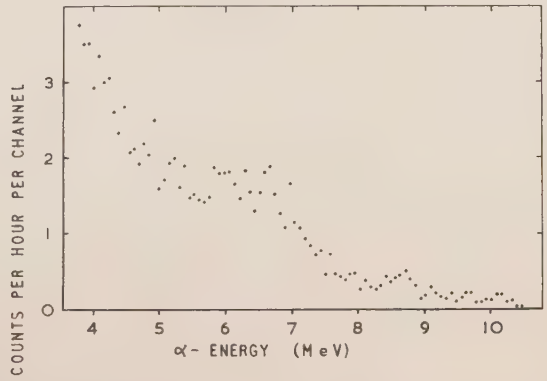

Fig. 7. 48 hour background.

the range 4 to 9 MeV is about 90 cph, which is little more than had been expected on the basis of the measured alpha emission of the cellulose acetate (between 2 and 4 cph per 1000 sq. cm, effective over a total area of 15000 sq. cm).

Between 4 and 6 MeV the mean background counting rate in the energy range covered by a single spectral line (equivalent to about 3 channels) is 6 cph or 0.1 cpm. Since the counting efficiency is 50%, it requires only about 0.1 pc of a mono-energetic nuclide in up to 1.5 g of source material (15000 cm² covered at a mean thickness of 0.1 mg/cm²) to double the background counting rate. Sensitivity of this order has been regularly achieved in practice and fig. 8 shows a spectrum obtained of a sample of normal human kidney ash whose total alpha activity was 1.0 pc in 1.07 g of ash (derived from about 200 g of wet tissue). From this it will be seen that the alpha activity of the tissue ash is due predominantly to polonium-210 (5.30 MeV) and that, in particular, uranium-238 (4.19 MeV) does not contribute more than about 5% of the total activity.

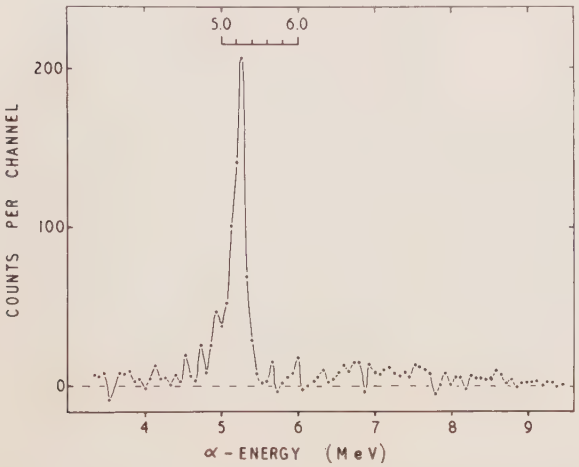

Fig. 8. Alpha spectrum of a sample of normal human kidney.

The separate identification of several nuclides occurring together in a material is illustrated by the spectrum obtained from the ashed leaves of a Malayan Brazil nut tree (fig. 9), which evidently contain both Ra^{226} and Th^{228} (Rd Th), together with their respective decay products.

8. Conclusion

The instrument described in this paper is at present being used in an investigation of the natural alpha radioactivity of human tissues. In such work it is capable of measuring, with an error of 100 keV or less, the alpha energy of nuclides occurring in a material at specific activities down to approximately one tenth of a picocurie per gramme. The technique is reasonably simple and is amenable to routine operation.

The effectiveness of such an instrument has been found in practice to be very greatly enhanced if it is used in conjunction with a sensitive total alpha counter of the type employed in this Department[9]).

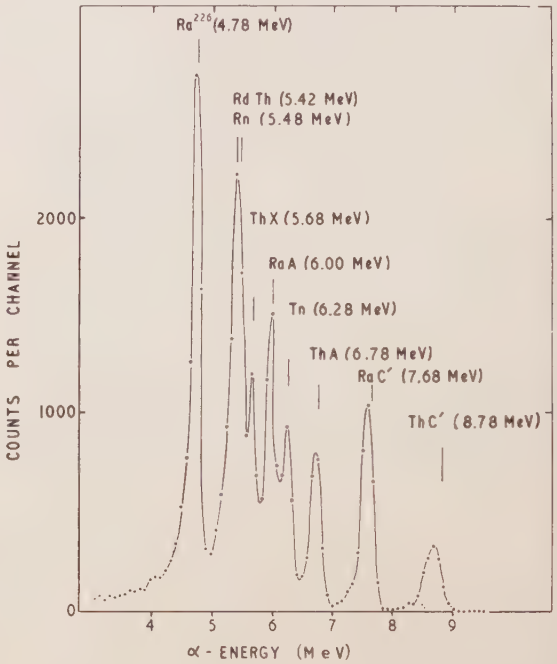

Fig. 9. Alpha spectrum of ashed Brazil nut tree leaves.

In this way not only is it practicable to survey a greatly increased number of specimens in a particular investigation, but independent data on identification can also conveniently be obtained from observation of the half-lives of a number of the nuclides commonly encountered.

I wish to record my sincere thanks due to the numerous members of this Department from whom I have received willing help and advice in the course of the above work, and particularly to Mr. H. Hodt and Mr. S. P. Newbery for their assistance with the mechanical construction and the electronics. I am greatly indebted to Prof. W. V. Mayenord for originally suggesting this work and for his subsequent support and encouragement.

9) R. C. Turner, J. M. Radley and W. V. Mayneord, Brit. J. Radiol. **31** (1958) 397.

NUCLEAR INSTRUMENTS AND METHODS 12 (1961) 307–315; NORTH-HOLLAND PUBLISHING CO.

SOME TRANSISTOR CIRCUITS FOR NUCLEAR PHYSICS RESEARCH†

R. GABRIEL and A. M. SEGAR††

The Enrico Fermi Institute for Nuclear Studies, The University of Chicago, Chicago, Illinois

Received 1 March 1961

Useful transistor circuit modules are described, including coincidence and anticoincidence circuits, gating circuits, amplifying and pulse-shaping circuits, and a trigger circuit, all operating with resolution times of about 10^{-8} sec.

As examples of the use of these modules, a circuit for counting neutrons from muon-capture reactions is given and a circuit for discriminating neutrons from gamma rays by analysis of pulse shape.

1. Introduction

The circuits described here are a development of those described by Miller[1,2]) and Gabriel, Garwin and York[3]). Most of the electronic logic systems needed for high energy counter experiments can be built up from the units (or "modules") described here, and two examples are given of complete electronics systems which have been used in such experiments.

The coincidence and trigger circuits described in the references[1,2,3]) are given again here, with several modifications which have proven necessary in using these circuits for many experiments. In addition, several new circuit modules are given, all of which have been used in experiments on the 460 MeV synchrocyclotron at the University of Chicago.

There are many such modules and several complete systems of electronics described in the literature[4–9]). Several of these designs place emphasis on extreme speed, in having both short resolving times and high counting rates, at the expense of simplicity and convenience. Others describe plug-in units suitable for large scale production in a large laboratory. Cable impedances used vary through the full range of commercially available types, 50 to 200 ohm. The choice of cable impedance is basic in circuit design, e.g. the grounded base configuration of the transistor is very suitable with 50 ohm circuits but not with higher impedances.

The circuits described here were designed with the following requirements in mind:

1. To be sufficiently simple and reliable to be built quickly in quantities suitable for the logic of complex experiments.

2. All fast circuits to use type 2N501 or 2N1500 transistors, these types presenting the best compromise between the conflicting requirements of speed and reasonable price.

3. Cable impedance 180 ohm (RG114-U). The change to 125 ohm is trivial in most cases and several circuits have been used with the lower impedance cable.

4. Coincidence circuit resolving times to be better than 4×10^{-8} sec. The most intense beams used were pion beams, intensity $\approx 10^5$ per sec., radio frequency modulation of 18 Mc/s, duty cycle 45, repetition rate 60 cps. Even in this extreme condition, the average number of particles per R.F. cycle is only 0.25, so little is to be gained by having

† Research supported by a joint program Office of Naval Research and the U.S. Atomic Energy Commission.

†† Now at Rutherford High Energy Laboratory, Harwell, Didcot, Berks., England.

[1]) R. H. Miller, Rev. Sci. Inst. **30** (1959) 395; and UCRL 8706.

[2]) R. H. Miller, Rev. Sci. Inst. **31** (1960) 1047.

[3]) R. Gabriel, E. L. Garwin and C. M. York, Nucl. Instr. **5** (1959) 247.

[4]) R. Sugarman and W. A. Higinbotham, BNL 4997.

[5]) R. M. Sugarman, BNL 4436-R.

[6]) A. Barna, J. H. Marshall and M. Sands, Nucl. Instr. **7** (1960) 124.

[7]) S. C. Baker, H. G. Jackson and D. A. Mack, UCRL 9000.

[8]) G. B. B. Chaplin and A. J. Cole, Nucl. Instr. **7** (1960) 45.

[9]) F. S. Goulding and R. A. McNaught, Nucl. Instr. **9** (1960) 282.

a resolving time much less than the R.F. period of 56 mμs.

5. Dead time of circuits involving coincidence pulses to be less than 0.1 μs. This requirements was suggested by the resolution of the 10 Mc/s scalers used. At the highest counting rates encountered, 10^5 with duty cycle 45, appreciable counting loss was occurring but was easily allowed for and was not important. Counting rates in muon experiments were always very low.

6. Counter singles rates to be less than 10^6 per second, most rates being much lower than this.

2. Pulse-Shaping Circuits (fig. 1)

These were designed initially for use with the time-sorting circuit of Culligan and Lipman[10]). This required pulses lengthened to times longer than the time range of the circuit, with as little deterioration of the pulse rise time as possible. This need for lengthened pulses arises in many other circuits, e.g. see fig. 9A.

Two circuits are shown, both accepting negative input pulses, the outputs being either positive or negative. The input pulse is first discriminated by the tunnel diode (1N653). Its characteristics bring

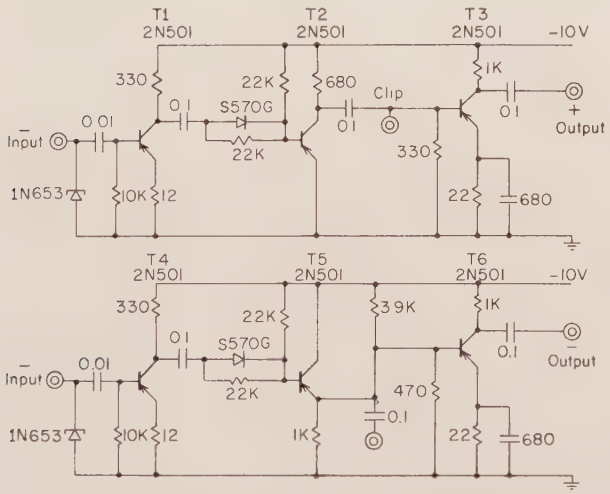

Fig. 1. Pulse shaping circuit for time to pulse height converter.

all but very small input pulses to a fairly uniform height or 1–3 volt. The indefinite input impedance of the circuit makes it essential to have a short input cable, terminated correctly at the far end, to avoid reflections.

The pulse is lengthened at the base of transistors T2 and T5, where the charge passed through the diode is stored in the base-emitter capacity of the transistors. At the collectors of T2 and T5, the pulse can be clipped to a defined length by a shorted length of cable, though normally this is not necessary.

The positive output is about 6 volt in 180 ohm, the negative output being limited by the T6 dissipation limits, to 3 volts in 180 ohm. Type 2N1500 transistors are preferred in positions like those of T6 and T2, for their higher dissipation rating of 50 mW.

Both T3 and T6 circuits are examples of simple amplifiers with feedback via the resistance in the emitter lead. The resistor is chosen to give the required degree of feedback, and it is by-passed with a condenser giving a time constant of about 10^{-8} sec. This gives the right degree of peaking of the frequency response to achieve fastest rise times. This series feedback method is preferred to the shunt feedback method because it is simpler. The shunt feedback circuit uses a resistor (of about 50 k), an inductance (of a few hundred μH) and an isolating condenser, compared with the two simple components of the series feedback circuit. The shunt circuit is capable of slightly greater peak output voltage, while the series circuit has a shorter recovery time after overload.

3. Limiter Amplifier

This circuit avoids the undesirable lengthening of the pulse which occurs when a transistor is saturated by a large pulse applied to the base. Since, with some scintillation counters, the range of pulse amplitudes may be 50 : 1, the saturation is very difficult to avoid unless the pulse is limited before being fed to any transistor. At the same time, the circuit presents an input impedance very close to the cable characteristic impedance for all input pulse amplitudes and, therefore, avoids undesirable reflections.

The input will normally be a counter pulse, the output a limited 1.7 volt pulse in 180 ohm, for all inputs greater than 0.3 volt. The output pulse is intended to be applied directly to the coincidence

[10]) C. Culligan and N. H. Lipman, Rev. Sci. Instr. **31** (1960) 1209.

circuits of fig. 4. The limiting is provided by the diode at the input, the negative input pulse switching the stending current of the diode into the base of T1. This same current pulse in T1 is obtained for al input pulses greater than 0.3 volt, larger inputs delivering only small additional current through the back resistance and the capacity of the diode. T1 and T2 are simple series feedback amplifiers. The limiting provided by the diode is not sharply

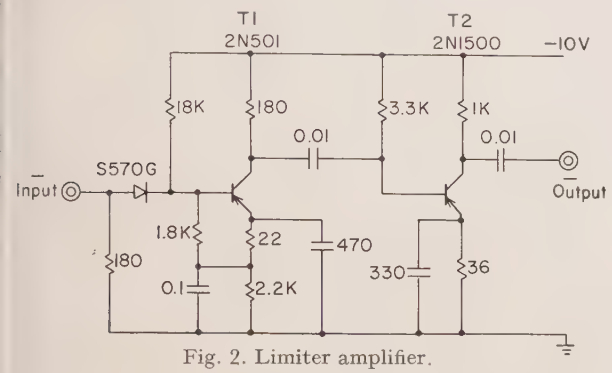

Fig. 2. Limiter amplifier.

defined, so the circuit provides that T2 also limits by being cut off, providing a clean flat-topped output pulse. The rise time of the output pulses is about 5 mμs, which allows resolving times of 10 mμs in the coincidence circuits following the amplifiers. Shorter resolving times than this can only be obtained by using larger and more costly amplifiers, such as the transistor distributed amplifiers of McMullen[11]). Our limiter amplifiers are so small and simple that 10 of them could be mounted on a single 4″ high rack panel.

Another method of obtaining limiting is to use a grounded base stage, which is cut off by the counter pulse. This configuration of the transistor is capable of fast rise times but is essentially just an impedance transformer with no current gain. The input impedance is low and rises abruptly to a high value once the transistor is cut off, so for correct matching to a cable, an emitter follower input stage is required. This input stage may show saturation effects. However, this type of circuit has been used successfully[4,6]).

4. Fast Linear Gate

The basic element of the gate is T5, which shorts any signal arriving at the gate via the 220 ohm resistor, unless a coincident pulse arrives from the limiter amplifier T4 to cut T5 off. The gate can be left "open" by applying a positive bias from the battery. Because of its simplicity, the gate is capable of very short resolving times, though it has not been used with times less than 30 mμs. The open time is determined by the length of the pulse applied to T4.

The associated amplifier has to be equally fast,

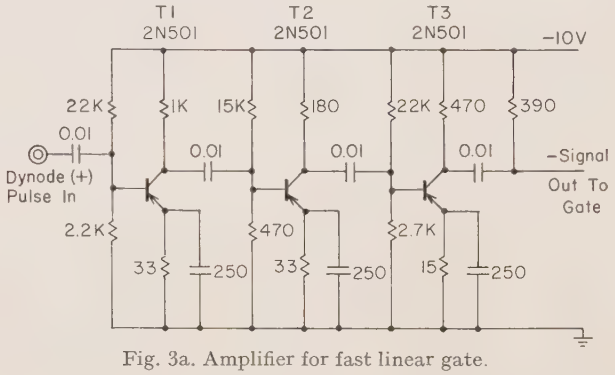

Fig. 3a. Amplifier for fast linear gate.

so preceding the gate we have an amplifier with three cascaded stages T1, T2, T3. The input to this circuit is normally a positive (dynode) pulse from a counter. Since the transistors are switching types, the resistor values have to be trimmed so that all three operate in linear portions of their characteristics. This procedure could be avoided by using more expensive amplifier-type transistors.

After gating, the counting rate is low, speed no longer necessary, so the pulse is integrated at the

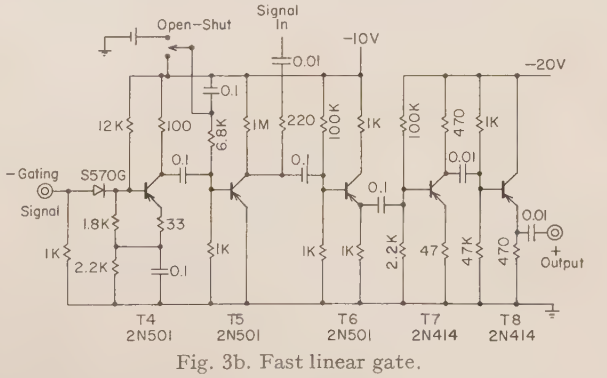

Fig. 3b. Fast linear gate.

base of T7, which produces a pulse of height proportional to the charge at its base, and rise time characteristic of the transistor, about 0.1 μs.

[11]) C. McMullen, Rev. Sci. Instr. **30** (1959) 1109.

Transistors T7, T8 provide output pulses linear to about 18 volt, the gate pedestal and feed through being about 0.5 volt at the output. The system is linear to within a few per cent in the range 0.5–18 volt output but does show non-linearity for very short pulses, due to the peaking of the amplifier. This performance was adequate, since the emphasis in the design was on speed, not linearity.

One may ask why the amplifiers do not have feedback applied over several stages, since this would certainly give better linearity and perhaps a better band width. The reason is that we are using the transistors with pulse rise times of the same order as the characteristic transistor rise time. The delay of a transistor amplifier stage is about the same as its ultimate rise time, so feedback applied over several stages takes effect too late. Thus the output of such an amplifier shows large spikes at the leading and trailing edges of the pulse, where the feedback is too slow to follow the pulse shape. One amplifier circuit that we have used, which applies feedback over two stages, is the cascade amplifier with series feedback. This consists of a grounded emitter stage, with feedback resistor, directly coupled to a grounded base stage.

5. Coincidence Circuits (fig. 4)

These have been described by Miller[1]). A modification to the original circuit is the inclusion of isolating emitter-follower stages on each input. These prevent unwanted "cross-talk" between inputs when the inputs are common to several circuits.

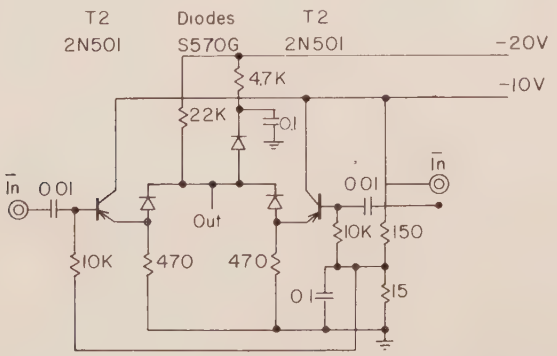

Fig. 4. Doubles coincidence circuit.

A double-coincidence circuit is shown, but these circuits can easily be adapted to multiple coincidences simply by connecting more coincidence diodes to the mixing point. To keep the current in each coincidence diode about the same, it is desirable to adjust the series resistor connected to the 20 volt supply, according to the number of coincidence diodes. For example, for quadruple coincidences we use 2.2k instead of the 4.7k shown, and for quintuple coincidences, 1.8k. The parallel 22k is omitted in these cases to improve the quadruples/triples and quintuples/quadruples discrimination.

6. Anticoincidence Circuit (fig. 5)

The transistor is used as a simple switch, having high collector to ground impedance in the normal condition and low impedance when an anticoincidence pulse is applied to the base.

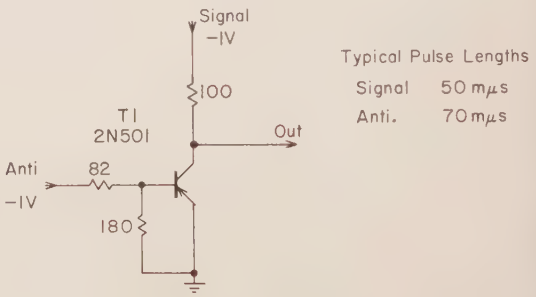

Fig. 5. Anticoincidence circuit.

The anticoincidence pulse should overlap the signal pulse on both the leading and trailing edges, for at least a time corresponding to the transistor rise time. Typically, the signal pulse with 50 mμs, the anticoincident pulse, 70 mμs. In cases where imperfect anticoincidence resulted from mistiming of the true and anti pulses, a simple solution was to integrate the output pulse with a small condenser, say 10 pF, thus increasing the discrimination against the short feed-through pulses resulting from anticoincidences. The effect of imperfect timing is shown in fig. 9B.

7. Discriminator of "One-Shot" Circuit

This is a sensitive discriminator circuit with dead time somewhat greater than 50 mμs, which can be triggered by 0.3 volt pulses as short as 5 mμs. It has an emitter follower isolated input (T1), and both fast negative (1 volt), and slow positive outputs.

Transistor T2 is a shunt trigger for the monostable circuit composed of T3 and T4. The bias on T2 is adjustable to provide a variable discrimination level. The length of the output pulse is also

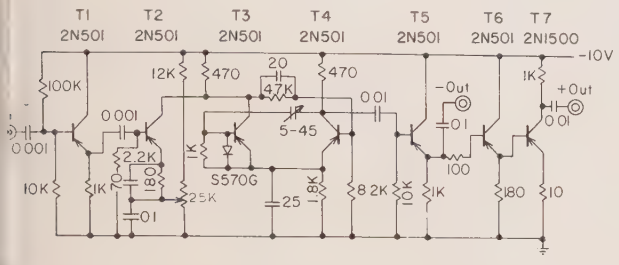

Fig. 6. "One Shot" trigger circuit.

adjustable, by varying the coupling capacitance between T3 and T4, but for reliable operation this length should not be shorter than 50 mμs. Transistor T5 is an emitter follower providing the negative output pulse, while the inverter T7 provides the positive output. Transistor T6 is necessary to isolate the negative output from the loading effect of T7. Transistor T7, the inverter, is turned on hard and the collector goes from — 10 volt to ground potential. This output is usually used to drive a scaler. For maximum counting rates, the input of the scaler should be terminated with $\approx$ 470 ohm. If not, the recovery time constant of the collector circuit is too long, and the collector potential cannot reach — 10 volt before another pulse arrives.

For large input pulses, the output pulse tends to shorten, the "one-shot" seeming to work as an amplifier recovering forcibly after the termination of the input pulse. This characteristic can be minimized by either using a disconnect diode between T2 and T3 or tapping the T2 collector connection up on the resistor common to T2 and T3. The disconnect diode does not appreciably reduce the circuit sensitivity, but the change of resistors does.

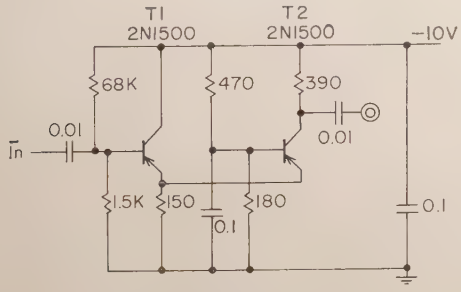

Fig. 7. Delay line driver.

8. Delay-Line Driver (fig. 7)

This circuit is useful in driving long lengths of delay cable with pulses derived from discriminator circuits.

It provides some gain, without inversion, and preserves rise times of 10 mμs. Transistor T1 is an emitter follower, T2 a grounded base amplifier. Transistor T1 is cut off by about 0.5 volt T2 collector carrying 15 mA. Maximum output is 2.0 volt in 180 Ω. The resistors in the base of T1, and at the base and collector of T2, are chosen to give a maximum negative output, without danger of exceeding the dissipation ratings of any 2N1500 transistor. A 2N501 transistor can be used in T2 position if the collector resistance is increased to 470 ohm.

9. Gate (fig. 8)

This is a gate similar in principle to that of fig. 3, but having a direct-coupled circuit capable of use at high counting rates. The pulse to be gated is normally attenuated by about $\frac{1}{200}$ by the 120 ohm resistors in series with the collector to ground impedances of T1 and T2. Transistors T1 and T2 are normally turned on hard by current supplied from T3 emitter. When a gating pulse is applied, T3 is

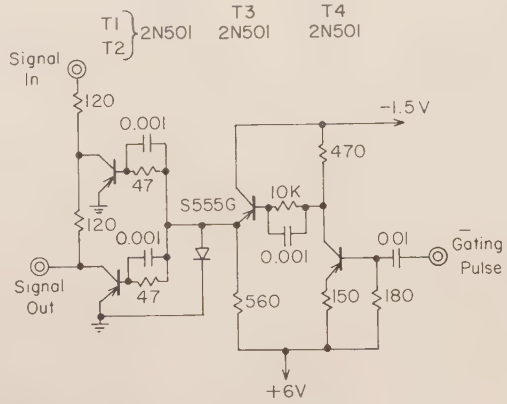

Fig. 8. Gate.

cut off, and current flowing from the + 6 volt supply through the S555G diode cuts off T1 and T2, allowing the signal pulse to pass with small at-

tenuation. The diode is essential in limiting the cut-off voltage applied to T1 and T2. Upon termination of the gating pulse, the circuit rapidly returns to its quiescent state, ready for another pulse.

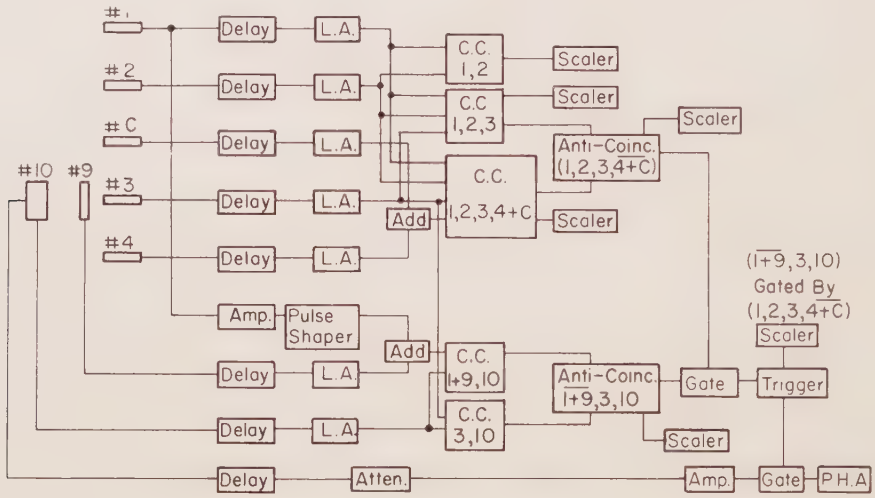

Fig. 9a. Block diagram for counting neutrons from muon capture.

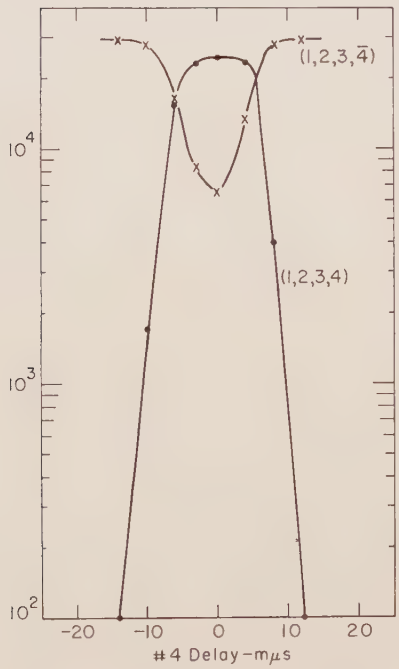

Fig. 9b. Coincidence circuit performance.

10. Electronics System for Counting Neutrons from Capture (fig. 9a, 9b)

The system shown was used for counting delayed neutrons arising from muons coming to rest in counter No. 3. Stopping particles pass through and produce counts in No. 1, No. 2 and No. 3, but not in No. C or in No. 4, so a logic $(1, 2, 3, \overline{4 + C})$ is constructed. The neutron is counted in No. 10, but not in No. 9, and there is a coincident recoil count in No. 3, so the logic $(\bar{9}, 3, 10)$ is followed. Since a background of neutrons produced promptly by pions in the beam is expected, No. 1 counter is added as an additional anticoincidence. No. 1 pulse is lengthened in the pulse shaper, so that even pion-produced neutrons which arrive late at counter 10, through following a long flight path, will still be rejected.

The delayed $(1, 2, 3, \overline{4 + C})$ pulse is used to gate the $(\overline{1 + 9}, 3, 10)$ pulses, so that only a fixed time interval of delayed neutron counts is accepted. The gated pulse is counted and is used to gate No. 10 dynode pulses for pulse-height analysis.

The abbreviation L.A. on the diagram refers to the limiter amplifiers and C.C. to doubles, triples and quadruples coincidence circuits.

Fig. 9B shows the performance of the quadruples circuit and of the anticoincidence circuit under conditions of an actual experiment, counting muons. The sharpness of the anticoincidence curve is due to the delay in the quadrupoles circuit, which brings the (1234) pulse to the anticoincidence transistor a little too late relative to the (123) pulse. Full anti-coincidence efficiency can still be obtained, but the

elay of the No. 4 pulse needs to be slightly less han that corresponding to the (1234) peak, and ne delay setting is critical, so the curve has a sharp inimum. This condition can be avoided by de- ying the (123) pulse with a short length of cable, nd this method was used in the more critical anti- oincidence circuits, such as that of $\overline{1+9}$.

1. Neutron Discriminator (fig. 10, 11, 12)

This is a second example of the use of modules in uilding up a complete electronics system. This ystem is an adaptation of the method of Owen[12]), ho with Brooks[13]), developed a system of dis- imination of neutrons and gamma rays in scintil- tion counters. The method depends on the obser- ation of Wright[14]) that, for heavy particles, the cintillation in certain organic crystals has a com- onent of much longer decay time than that for ghtly-ionizing electrons from gamma rays. The ntensity of this long-lived component is small. If ne looks at pulses from protons in liquid scintilla- or, using a fast oscilloscope, the effect appears as a gnificant but small increase in the noise level for ne first 200 mμs after the main pulse. A discrimi- ator circuit must be sensitive enough to record his small component of the pulse, whilst rejecting he normal noise associated with gamma pulses.

The circuit described here separates the fast and ow components of the pulse with a delayed gate nd an anticoincidence circuit, then mixes the two omponents in proportions such that gamma rays

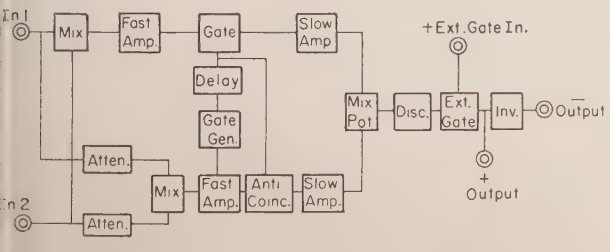

Fig. 10. Block diagram of neutron discriminator.

lways give positive pulses, neutrons negative ulses. A trigger circuit then selects only the latter ulses. Two inputs are provided for simultaneous iscrimination of two neutron counters. The inputs hould come direct from photomultiplier dynodes, nd it is most important that the pulses be free of any small reflections. Even one very small pulse following the main pulse will cause the circuit to register a neutron. There should be no cable mismatching or interference from anode pulses, and cables should be short. The inputs are limited and amplified in transistors T1 and T2, then mixed and further amplified in T3 and T4. An attenuated signal from both inputs is applied to T12, which amplifies it linearly. The pulse from T12, triggers a gate generator, which opens the gating transistor T6 and turns on the anticoincidence transistor T14. The gate delay is chosen such that the gate generator is not triggered till the main pulse and any small reflections have gone. The pulses from the gate and the anticoincidence circuit are amplified, then integrated and further amplified in T9 and T16. At the top end of the mixing potentiometer, we have a pulse of about 0.5 μs length, with height proportional to the slow component of the pulse, and at the bottom a pulse of about the same length, and proportional to the fast component of the pulse. These two are mixed in appropriate proportions and applied to the trigger circuit, whose output can be gated externally by transistors T10, T17 and T18. If internal gating is desired, the scaler pulse from the gate generator can be connected to the external gate input.

Usual settings were:

Gate generator threshold	0.1 MeV γ ehergy
Gate length	200 mμs
Gate delay	50 mμs
Mixing potentiometer	1 : 1.

The amplifier gains have been adjusted so that correct mixing occurs with the potentiometer in the center of its range. This degree of mixing was found to give the lowest neutron energy threshold without introducing gamma response.

The best way of testing the discriminator performance is to count (γ,n) and (γ,γ) coincidences from a polonium-beryllium neutron source, separating (γ,n) events by introducing a flight path for the neutron and time analyzing the coincidences with a time-to-pulse-height converter[10]) and a pulse-height analyzer. The discriminator is then made to

[12]) R. B. Owen, I.R.E. transact. on Nucl. Sci. NS-5, 3 (1958) 198.

[13]) F. D. Brooks, Nucl. Instr. and Meth. 4 (1959) 151.

[14]) G. T. Wright, Proc. Phys. Soc. B 49 (1956) 358.

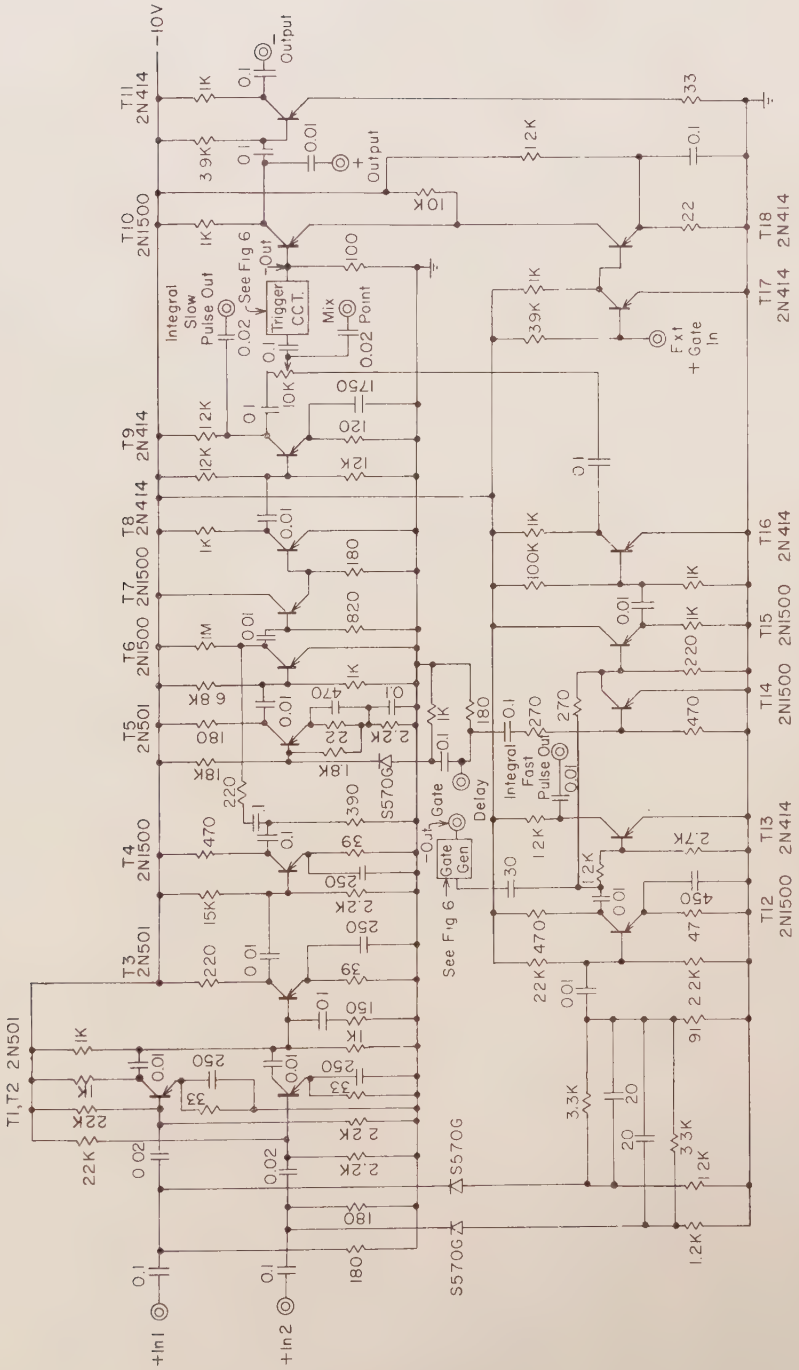

Fig. 11. Neutron discriminator circuit.

gate the pulse-height analyzer. Fig. 12 shows the result of such a test. The prompt peak corresponding to the detection of gammas, and the neutron peak corresponding to neutron detection are clearly separated in the ungated spectrum. When the discriminator is used as a gate, the prompt peak disappears, only random counts remaining in that part

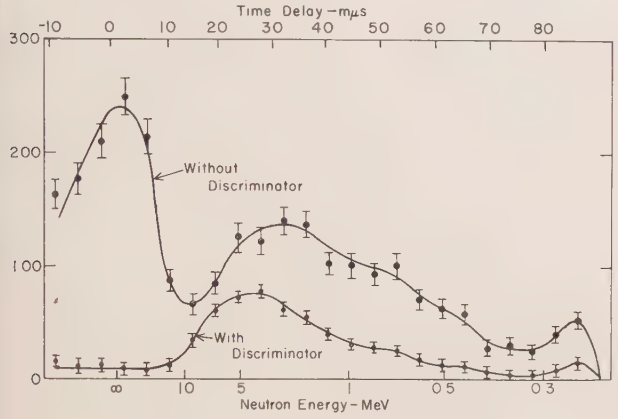

Fig. 12. Neutron discriminator test.

of the time spectrum. The neutron energy scale is also given in the figure and from this one can deduce the discriminator efficiency as a function of neutron energy. The threshold is seen to be at 0.4 MeV, and the efficiency, measured by the ratio of the gated count to the ungated count, with randoms subtracted, rises toward 100% at high neutron energies. Except at the lowest energies, the behavior of the efficiency is well accounted for by assuming that the discriminator has a sharp proton energy threshold, all proton recoils above this energy being counted. (The energy spectrum of proton recoils from monoenergetic low energy neutrons is rectangular.)

The threshold obtainable depends on the optical efficiency of the system and the photocathode efficiency. The case shown in fig. 12 was a favorable one, where a small scintillator was directly coupled to a 56AVP photomultiplier cathode. With large scintillators, coupled by light pipes to a photomultiplier, thresholds were ≈ 2 MeV. At low energies, the slow component of a pulse becomes comparable with noise, and the circuit becomes unable to distinguish noise fluctuations from genuine slow pulses from neutrons. The importance of the mixing is in balancing normal noise against the fast component of a pulse. There are suggestions that there *is* a slow component, but a smaller one, associated with gamma pulses, and if so the mixing might be important for canceling this, too.

Since the intensity of the slow component is small compared with that of the fast, the anticoincidence requirement has little effect on the fast pulse, but this is a refinement that is very easy to include so it was put in. There are accidental neutron counts where a second pulse happens to occur within the length of the 200 mμs gate. In experiments where the discriminator was used, these accidental events were never important and could be easily estimated and subtracted, but they could be a serious restirction in high rate experiments.

Lathrop has constructed a discriminator similar in logic to this but has not obtained low neutron energy thresholds. Hincks has constructed a system like that of Owen, with the pulses displayed on an oscilloscope in a two-dimensional plot. Neutrons and gammas appear as two distinct loci on the screen, and by masking one or other locus and viewing the screen with a photomultiplier, gating pulses can be obtained. This system works very well with very low energy thresholds.

Acknowledgement

Our thanks are due to Professor H. L. Anderson, Professor E. P. Hincks, Dr. C. S. Johnson, Mr. J. F. Lathrop and Mr. W. Stanula, who have all contributed substantially to this work.

NUCLEAR INSTRUMENTS AND METHODS 12 (1961) 316–322; NORTH-HOLLAND PUBLISHING CO.

AN IRON-FREE TOROIDAL β-SPECTROMETER WITH HIGH TRANSMISSION

N. A. BURGOV, A. V. DAVYDOV and G. R. KARTASHOV

Institute of Theoretical and Experimental Physics Academy of Sciences of USSR (Moscow)

Received 9 January 1961

An iron-free beta-spectrometer is described with transmission about 20 % from 4π. The main part of the spectrometer is a toroidal magnetic lense consisted of 810 turns. The maximum energy of the electrons to be focused reaches 3.3 MeV the current being about 130 amperes. The theory of the instrument is given in some details.

We have constructed an iron-free β-spectrometer intended, in the main, to work with gaseous sources. A toroidal magnetic field is used in the spectrometer. A spectrometer of this type was constructed for the first time by V. V. Vladimirsky and co-workers[1]). Subsequently a similar spectrometer was constructed by E. F. Tretyakov and co-workers[2]). We shall discuss the theory of this instrument.

1. Winding Shape of the Spectrometer

The essential part of the spectrometer is a cylindrical lens, constructed of separate turns through which an identical current passes (see fig. 1). The electrons from the source S, which is positioned on the instrument axis, move between the lens turns and are focused at the point F on the axis.

In order to obtain the electron focus the section of the winding must have a quite definite shape in the region where the electrons enter and leave the lens. To a good approximation, which will be specified later, the magnetic field outside the lens winding is equal to zero, and inside the winding it will only have the component H_φ perpendicular to the plane $\varphi = \text{const.}$ and equal to

$$H_\varphi = \frac{2nI}{cy} = \frac{\varkappa}{y}. \qquad (1)$$

Here, y is the distance to the spectrometer axis. For electrons emitted from a point on the axis, their path in such a field will be plane.

From a solution of the equation of the electron motion in such a field the parametrical representation of the electron trajectory can easily be obtained.

$$y(\theta) = y_0 \, e^{-\beta(1-\cos\theta)}$$

$$x(\theta) = y_0\beta \int_0^\theta e^{-\beta(1-\cos\theta_1)} \cos\theta_1 \, d\theta_1 . \qquad (2)$$

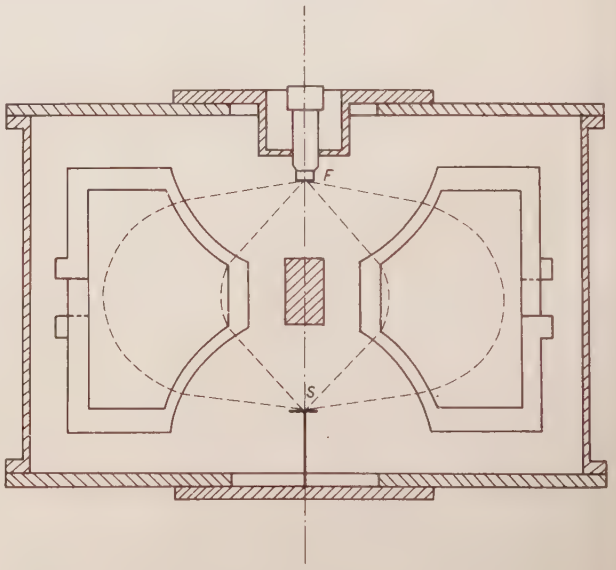

Fig. 1.

The origin of the coordinates was chosen so that if $y = y_0$ then $x = 0$ ($\cos\theta = 1$) (see fig. 2). The trajectory is symmetrical with respect to the straight line $x = 0$. We obtain the equation for the curve,

[1]) V. V. Vladimirsky, Eu. K. Tarasov, Yu. V. Trebukhovsky, PTE 1 (1956) 13.

[2]) Eu. F. Tretyakov, L. L. Goldin, G. I. Grishuk, PTE 6 (1957) 22.

which determines the winding shape for a given focal distance, f, by solving the equation of the trajectory and including the focusing condition:

$$y_1(\theta) = [f - x_1(\theta)] \tan\theta \qquad (3)$$

where x_1, y_1 are coordinates of the curve which determines the turn shape (see fig. 2). We obtain as a solution

$$\frac{y_1(\theta)}{f} = \frac{1}{\operatorname{ctan}\theta + F(\beta,\theta)}; \quad \frac{x_1}{f} = \frac{F(\beta,\theta)}{\operatorname{ctan}\theta + F(\beta,\theta)}. \qquad (4)$$

Here

$$F(\beta,\theta) = \beta\, e^{-\beta\cos\theta} \int_0^{\theta} e^{\beta\cos\theta_1}\cos\theta_1\, d\theta_1 \qquad (5)$$

$$F(\beta,\pi) = \beta\, e^{\beta} \int_0^{\pi} e^{\beta\cos\theta_1}\cos\theta_1\, d\theta_1 = \pi\beta\, e^{\beta} I_1(\beta) \qquad (6)$$

where $I_1(\beta)$ is a Bessel function of the first order from the absolutely imaginary argument. The expansion

$$F(\beta,\theta) = \beta\sin\theta + \beta^2\left(\tfrac{1}{2}\theta - \tfrac{1}{4}\sin 2\theta\right) + \beta^3\left(\tfrac{3}{8}\sin\theta - \tfrac{1}{2}\theta\cos\theta + \tfrac{1}{24}\sin 3\theta\right) + \beta^4\left(\tfrac{3}{16}\theta - \tfrac{14}{96}\sin 2\theta + \tfrac{1}{8}\theta\cos 2\theta - \tfrac{1}{192}\sin 4\theta\right) + \ldots \qquad (7)$$

is valid for $F(\beta,\theta)$.

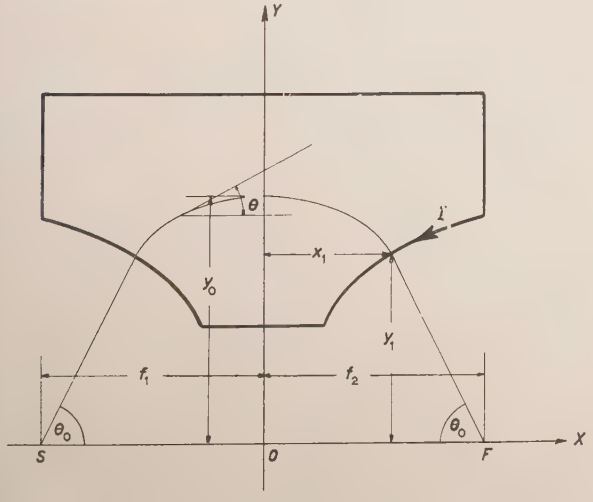

Fig. 2. θ is the angle between the tangent to the trajectory and the spectrometer axis (axis OX).
$\beta = cp/ex$ is a dimensionless parameter.
p is the electron momentum.
y_0 is the point of maximal distance of the trajectory from the axis OX.

Table 1

Values of the function $F(\beta,0)$

	0.1	0.2	0.3	0.4	0.5	0.615
40°	0.0649	0.1313	0.1995	0.2699	0.3484	0.4432
45°	0.0722	0.1473	0.2255	0.3068	0.3915	0.4880
50°	0.0785	0.1610	0.2478	0.3387	0.43424	0.5502
55°	0.0844	0.1740	0.2690	0.3698	0.4766	0.6070
60°	0.0897	0.1860	0.2892	0.3998	0.5183	0.6682
65°	0.0945	0.1970	0.3083	0.4288	0.5593	0.7221
70°	0.0986	0.2070	0.3259	0.4564	0.5993	0.7803
75°	0.1021	0.2158	0.3422	0.4825	0.6382	0.8370
80°	0.1048	0.2232	0.3567	0.5067	0.6447	0.8996
90°	0.1082	0.2342	0.3805	0.5495	0.7450	1.0059

The values $F(\beta,\theta)$ for 5° intervals in θ and for various values β are given in table 1.

It is most convenient to construct the spectrometer so that both the front and the back focal distances, f_1 and f_2 respectively, are equal. Then the turns will be symmetrical with respect to the straight line $x = 0$.

2. Influence of the Winding Turn Width on the Electron Trajectories

It is rather difficult to obtain analytically the value of the magnetic field between the winding turns for the given, rather complicated, shape. However, one may use the expression for the magnetic field between the n infinite wires of the given shape disposed symmetrically around the axis. In this case the problem of the magnetic field calculation is solved analytically.

If $z = x + iy = re^{i\varphi}$ and $H_z = H_y + iH_x$ then

$$H(z) = \frac{2j}{cz}\int_{R_1}^{R_2} R\, dR \int_{-\alpha}^{+\alpha} d\varepsilon \frac{z^n}{z^n + R^n e^{in\varepsilon}}. \qquad (8)$$

The axis OX is positioned on the bisector between two turns (fig. 3). The complete number of the turns is n, the angle between the turns is $2\pi/n$ and j is the current density. The magnetic field has two components: $H_\varphi = \mathrm{Re}\,[H(z)\,e^{i\varphi}]$ and $H_\rho = \mathrm{Im}\,[H(z)\,e^{i\varphi}]$. The analysis of the expression (8) permits one to conclude that in the region $R_1 < r < R_2$ the component H_φ has the constant term equal to

$$H_\varphi = \frac{2}{cr} I(r), \qquad (9)$$

where $I(r)$ is the current intensity in all the n turns at the distance r from the axis, and a variable term, the amplitude of which is proportional to $1/n^2$.

The component H_ρ has only the variable term with the amplitude being also proportional to $1/n^2$. Outside the turns the amplitudes of the variable

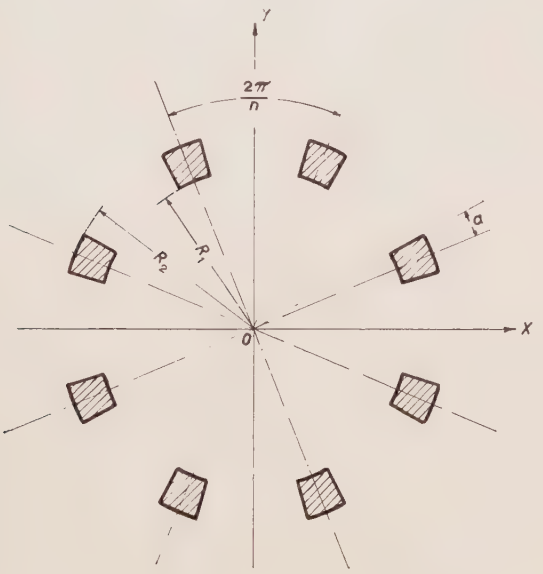

Fig. 3.

terms decrease as $(1/n)\ (r/R_1)^n$ when $r < R_1$ and as $(1/n)\ (R_2/r)^n$ when $r > R_2$. With n being large (in our instrument $n = 45$) the variable terms are negligible.

The examination of the magnetic field in the intervals between the infinite wires of the given shape, disposed on the generatrix of the cone gave similar results. This problem also permits an analytical solution.

One may compare the electron movement in the field (as determined by formula (9)) in the space between the turns and in the field, which is equal to zero outside the turn and which is determined by formulae (1) inside the turn. From this comparison of results the following conclusion is obtained. If the winding turn has a width a and the turn middle line is determined by the formulae (4), then there is a displacement g of the electron focus point, which depends on θ_0, the angle of the electron emission relative to the spectrometer axis.

This displacement is very small and is expressed by the formula

$$g = \frac{a^3 \cos\theta_0 \cdot f^2}{40\beta^2 y_1^2 \sin^2\theta_0} \tag{10}$$

Here y_1 is determined by the formulae (4), and a is the width of the winding turn.

The substitution of the various values of the angles when $a = 20$ mm, $f = 270$ mm, yields: $g(90^0) = 0$; $g(40^0) < 0.2$ mm.

Thus when the middle line of the turn is determined by the curve (4), the displacement of the focus point has practically no influence on the performance of the instrument.

3. Trajectories with Several Revolutions

It is obvious in the spectrometer of the type described that, apart from the "normally" focused electrons, the electron trajectories, which make one or more revolutions inside the spectrometer winding, may also emerge (fig. 4).

When the construction of the instrument is correct it is possible to arrange that the trajectories are not inside the turn, i.e. they would go out of the turn and not converge at the focal point F. It is obvious that the trajectories of the type described are possible when the electron energy is less than the energy of the electrons focused by the given current I.

It can be easily obtained from the equation connecting the momentum β_0 of the electrons which pass "normal" to the trajectory with an angle of incidence θ_0 in the spectrometer, and the momentum of the electrons β_k, entering with the same angle, but making k revolutions inside the turn. The equation is

$$\begin{aligned} F(\beta_0, \theta_0) &= F(\beta_k, \theta_0) + \tfrac{1}{2} k\, e^{\beta_k(1-\cos\theta_0)} F(\beta_k, 2\pi) \\ &= F(\beta_k, \theta_0) + k\, e^{-\beta_k(1+\cos\theta_0)} F(\beta_k, \pi) \\ &= F(\beta_k, \theta_0) + k\, e^{-\beta_k \cos\theta_0}\, \pi\beta_k I_1(\beta_k)\,. \end{aligned} \tag{11}$$

Solving this equation numerically it is possible to obtain the value β_k for different angles θ. The result of such a solution for $\beta_0 = 0.615$ is given in table 2.

Having calculated the values β_k it is possible to plot the electron trajectories. When plotting, it

appears that all the trajectories in the case of the given turn shape do not go within the turn, but go outside, either on the lower branch of the trajectory (for the trajectory with one revolution) or on the side branches of the trajectory (for the trajectory with two and more revolutions).

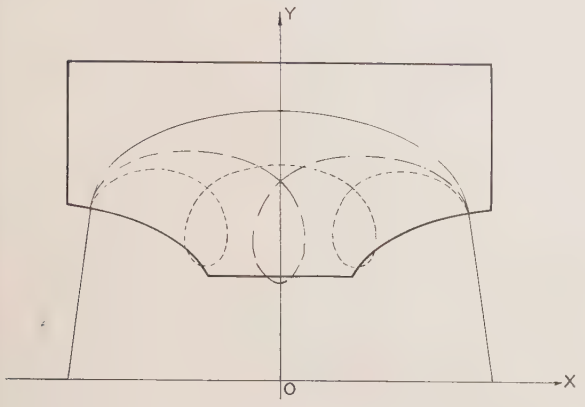

Fig. 4.

TABLE 2
Values of β_k for $\beta_0 = 0.615$ and for the various angles θ_0

θ_0	β_1	β_2	β_3
40°	0.389	0.307	0.261
50°	0.407	0.326	0.282
60°	0.426	0.347	0.303
70°	0.438	0.362	0.313
80°	0.452	0.378	0.330
90°	0.452	0.386	0.339

4. On Dispersion and Resolution of the Spectrometer

If the point source S had been placed in the front lens focus and electrons, the momentum of which differs from the focused electrons by the value $\Delta\beta$, are emitted from it, these electrons would cross the spectrometer axis not in the back focus F, but at a certain distance $b(\theta)$ $(\Delta\beta/\beta)$ from it. The calculations which are not given here, give the following expression for $b(\theta)$

$$b(\theta)\frac{\Delta\beta}{\beta} = \frac{2y_1^2(\theta)}{f\beta\sin^3\theta}\frac{\partial F(\beta,\theta)}{\partial\beta}\Delta\beta \qquad (12)$$

where

$$\frac{\partial F}{\partial\beta} = \frac{F(\beta,\theta)}{\beta}\left[1-\beta\cos\theta+\beta\frac{\int_0^\theta e^{\beta\cos\theta_1}\cos^2\theta_1\,d\theta_1}{\int_0^\theta e^{\beta\cos\theta_1}\cos\theta_1\,d\theta_1}\right]. \qquad (13)$$

Therefore it is possible to rewrite (12) in the form:

$$b(\theta)\frac{\Delta\beta}{\beta} = \frac{2x_1(\theta)y_1(\theta)}{f\beta\sin^3\theta}\times$$

$$\times\left[1-\beta\cos\theta+\beta\frac{\int_0^\theta e^{\beta\cos\theta_1}\cos^2\theta_1\,d\theta_1}{\int_0^\theta e^{\beta\cos\theta_1}\cos\theta_1\,d\theta_1}\right]\Delta\beta. \qquad (14)$$

If the electron detector is a cylinder with radius R and height H, placed so that its axis coincides with the spectrometer axis, and the back lens focus is on the detector's axis at an equal distance from its front and back plates, then the electrons which have

$$\left|\frac{\Delta\beta}{\beta}\right| \leqslant \frac{R}{b(\theta)}\left(\operatorname{ctan}\theta+\frac{H}{2R}\right) \qquad (15)$$

will be incident in the detector, (see fig. 5).

Having calculated $b(\theta)$ it is possible to plot the expected line shape for such a detector when the current is changed in the spectrometer, since

$$\left|\frac{\Delta\beta}{\beta}\right| = \left|\frac{\Delta I}{I}\right|.$$

The calculated line shape for a detector with diameter and height equal to 10 mm is given in fig. 6.

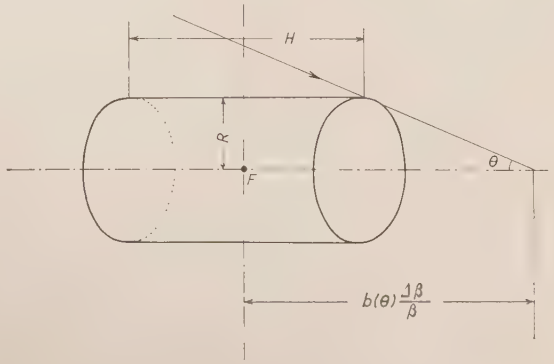

Fig. 5.

If the point source, which is on the spectrometer axis, is displaced from the front focus by the distance a, it may be shown that the electrons emitted from this source will cross the axis at the distance

$$a\left[1 + \frac{a^2}{f^2}\psi(\theta) + \ldots.\right] \qquad (16)$$

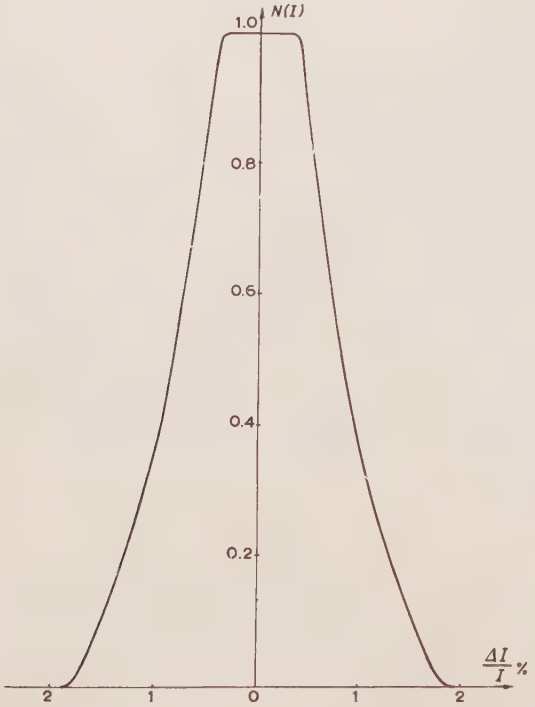

Fig. 6.

from the back focus, where $\psi(\theta)$ is a certain function of the emission angle θ. Consequently, the points near the front focus are images by the points near the back focus with an accuracy of the second order of the magnitude.

For the points displaced from the axis, in addition to the trajectories lying in the plane $\varphi =$ const., the trajectories not lying in this plane should also be examined.

5. Spectrometer Construction

The geometry of the constructed spectrometer is determined ay the parameters $\beta = 0.615$ and $f =$ 27 cm. The detector may register electrons emitted in the diapason of the angles 40°–90° with respect to the spectrometer axis. The toroidal magnetic lens consists of 810 turns connected in series, joined in the 45 packages with 18 pieces in each of them. The turns are patterned and cut from the sheet copper 0.5 mm thick. Each package is placed in a brass housing, the lateral walls of which are cooled by water following in opposite directions in two copper tubes brazed to them. The separate turns are isolated from each other with mica, 0.03 mm thick. The packages are isolated from the walls of the housing by a layer of ftorplast (teflon) 0.3 mm thick. The general view of one of the housings having the turns package is given in fig. 7.

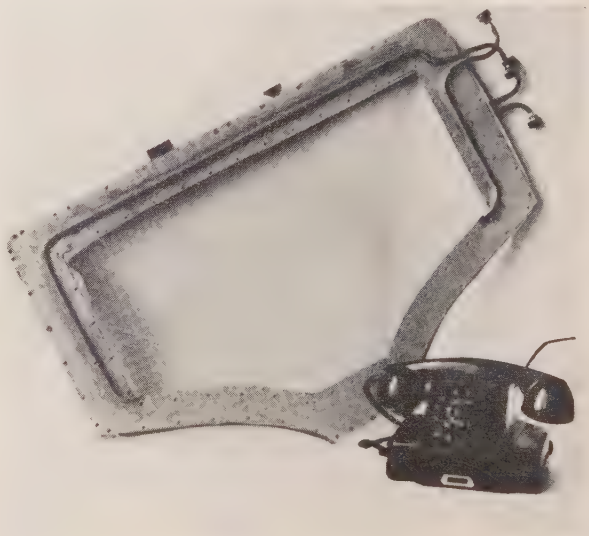

Fig. 7.

The sections of the curve-shaped turns are 20 mm width (the cross-section area is 10 mm²); the middle line of these sections follows (4). The sections of the rectilinear turns have a larger cross-section (width from 30 to 45 mm). The temperature of the inner package region, when the current was 120 A, reached 150–170°C.

The water for the cooling of the spectrometer has a pressure of 4.5 atm and is brought to the distributive circular tube that is connected with all the 90 cooling tubes by vacuum rubber joints. The second circular tube is used to let the water out of the spectrometer.

All the forty five packages and the cooling system are assembled as a united block inside the aluminium cylinder (see fig. 8). The packages are fixed

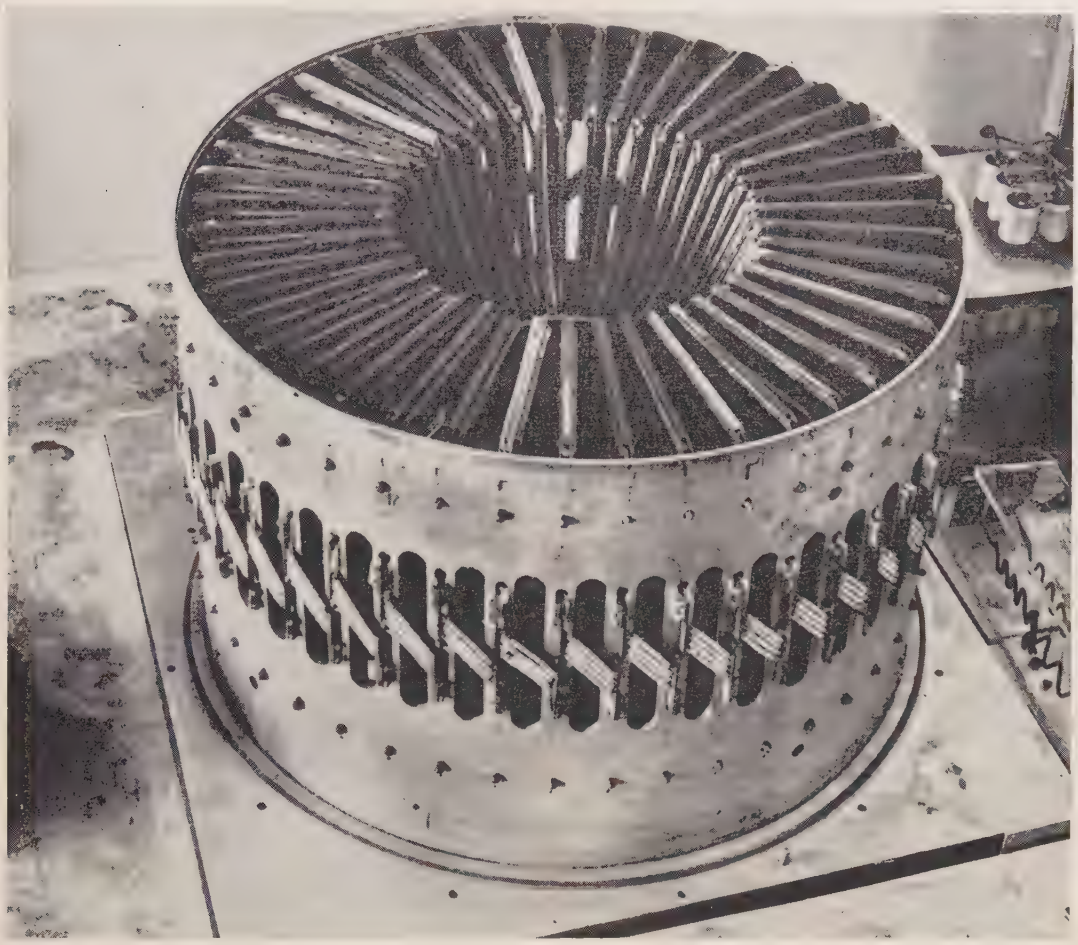

Fig. 8.

in a certain position relative to each other with the help of a cylindrical bushing to which they are connected by bolts.

The vacuum chamber of the β-spectrometer is the aluminium cylinder with a diameter 130 cm and 90 cm height placed on the duraluminium frame about one meter from the floor. The system is pumped out by the forevacuum and diffusion pumps. The pressure in the vacuum chamber is about 10^{-4} mm Hg after maximal warm-up of the turns of the spectrometer.

The scintillation counter consists of a small photomultiplier, FEU-35, and a scintillating plastic cylinder, which is used as an electron detector. The photomultiplier is positioned directly in the vacuum system on the rubber joint, which makes it possible to exclude a lightpipe.

The thickness of the packages with the turns is such that they overlap nearly 50% of the solid angle in which the electrons are emitted through the diaphragms of the system which is near the source. (The diaphragms are absent near the detector.) Thus, the geometric transmission of the device proves to be equal to about 20% of 4π for the diapason of angles of the electron emission mentioned above.

The electron sources intended to work with the gaseous β-emitters are made of two metal cylinders connected with thin cross-pieces. The space between the cylinders is the working volume of the source; it is separated from the vacuum system by a terylene film 1–2 mg^2/cm^2 thick stuck on the metal cylinders. The connecting joint of the film is on one of the cross-pieces. Thus, the working volume has a cylindrical shape.

The current for the magnetic lens of the spectro-

meter is taken from the constant current machine PN-205, of which the exciting winding is fed from the electromachine amplifier EMU-25.

The control windings of the latter, in their turn, are connected with the ordinary stabilization electronic system, which relates the current changes with respect to the potential difference on the thermostated constance resistance.

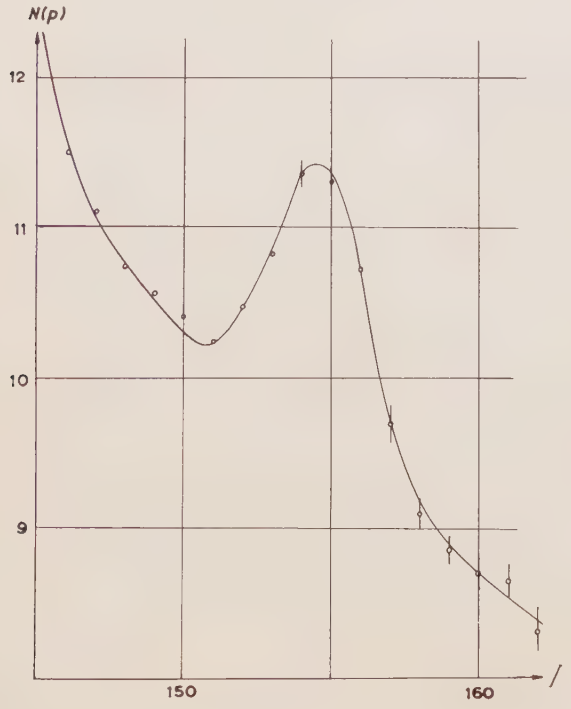

Fig. 9.

The current is measured by a similar second resistance and potentiometer PPTV of the 2–d class.

The current constancy during the measuring time of one spectrum point (several minutes) is maintained with an accuracy up to 0.05 A. The maximum current which our generator can give is 130A and thus it may focus electrons with the energy $\sim$ 3.3 MeV.

The general view of β-spectrometer winding is shown in fig. 8. The part of the β-spectrum of A^{41} with the conversion line, corresponding to the 1290 keV transition from the excited state of K^{41} to the ground state, is given in fig. 9. 99% of the A^{41} decays occurs from this level[3]). The relative width of the conversion line is $\sim$ 2.3%. The source had the diameter 10 mm, and height 12 mm. The gas in the source was under atmospheric pressure. The measurement was performed in the diapason of the angles 40–75° (transmission 13% from 4π).

The spectrum of P^{32} was measured in order to determine the number of the registered electrons scattered by the inner parts of the spectrometer. Such measurements show that the value of the electrons fixed by the detector in the region above the limit energy is about 0.2% from the counting rate in the β-spectrum maximum and decreases rapidly when the magnetic field increases.

The authors are indebted to the members of staff Alpatov V. G. and Nekrasov Yu. I., who took a great part in the assembling and setting in operation of the instrument, and express their gratitude to their collaborators Bisina G. Ye., Pavlov V. S., Zubkov A. I., Rostovtzev K. N., Khrudev Yu. V. for their help in adjustments. The authors are also indebted to Eu. F. Tretyakov for valuable advice.

[3]) B. S. Dzelopov, L. K. Peker. Decay schemes of Radioactive Nuclei (Publication of Academy of Sciences of the USSR, 1958) p. 84.

NUCLEAR INSTRUMENTS AND METHODS 12 (1961) 323–328; NORTH-HOLLAND PUBLISHING CO.

A 12 cm LIQUID DEUTERIUM BUBBLE CHAMBER

H. W. K. HOPKINS, M. DAVISON†, L. LYONS, J. M. BREARE, D. ROAF and D. F. SHAW

The Clarendon Laboratory, Oxford

Received 29 April 1961

A bellows expanded bubble chamber, 12 cm in diameter, 9 cm deep, has been designed for use with liquid deuterium. Good quality electron tracks have been observed over the temperature range 31.2° to 34.1°K, with a minimum volume expansion ratio of 1.6 per cent. It has been used with the Harwell synchrocyclotron to study the interaction of 80 MeV protons with deuterons. The results are being analysed with a modified rectangular coordinate plotter.

1. Introduction

A liquid deuterium bubble chamber, 12 cm in diameter, has been constructed at the Clarendon Laboratory, Oxford, for the investigation of nucleon-deuteron scattering over the energy range 30–100 MeV. This size is sufficient to achieve the well known advantages of bubble chambers: protons of energy > 2 MeV and deuterons of energy > 3 MeV may be detected, and their energies measured to 10 per cent at the lower energy, and to 2 per cent at 20 MeV; protons may generally be discriminated from recoil deuterons down to the lowest energies by kinematic analysis. A cross section of 1 mb may be determined to 3 per cent accuracy in 50 h operation.

This paper describes the design features and operational performance of the bubble chamber. Other chambers operating with liquid deuterium have been described by Gow[1]), Courant *et al.*[2]), and Kolganov *et al*[3]).

2. Construction

2.1. CRYOSTAT

Fig. 1 illustrates the main features of the cryostat. The chamber (A) is suspended by a stainless steel tube below a pressurised liquid hydrogen reservoir (B). It is surrounded by 2 copper radiation shields bolted to the liquid hydrogen and liquid nitrogen reservoirs (C) respectively. To give a low radiant heat input to the chamber, optical windows are clamped on to the shields over indium gaskets. The whole system is suspended by stainless steel tubes from the top plate of the vacuum tank. Flanged connections with indium O rings on the top of the nitrogen reservoir make it readily demountable to provide access to the piping systems lying between the reservoirs. The pressure in the vacuum tank could be kept below 0.01 microns, with the oil diffusion pumps closed off, by the pumping action of the liquid hydrogen reservoir.

2.2. CHAMBER

The chamber body was machined from a billet of O.F.H.C. copper, with a flange of α-β brass soldered into the wall to carry the expansion bellows (D). The orifice (E), 6.3 cm in diameter, is shaped to give a smooth liquid flow on expansion. The chamber wall is reduced from the normal thickness of 1.6 cm, to 3 mm over two 3.8 cm squares to form beam entry and exit ports. The windows are 2.5 cm thick commercial plate glass with MgF_2 anti-reflection coatings on both sides; five fiduciary marks, etched on the inside of each window, serve as reference points for the accurate spatial reconstruction of events. Gaskets onto the chamber are made with double indium O rings, with an intermediate monitor space between each pair. With an inner O ring of 1% silver-indium alloy, and the outer of

† Now at Imperial College, London.

[1]) J. D. Gow, U.C.R.L. Engineering Note 4312–03 M15 (1956).

[2]) H. Courant, J. E. Jensen, R.I. Louttit and J. R. Sandford, Rev. Sci. Instr. **30** (1959) 280.

[3]) V. Z. Kolganov, A. V. Lebedev, S. Ya. Nikitin, V. T. Smoliankin and A. P. Sokolov, Pribory i tehk. eksper **4** (1958) 30.

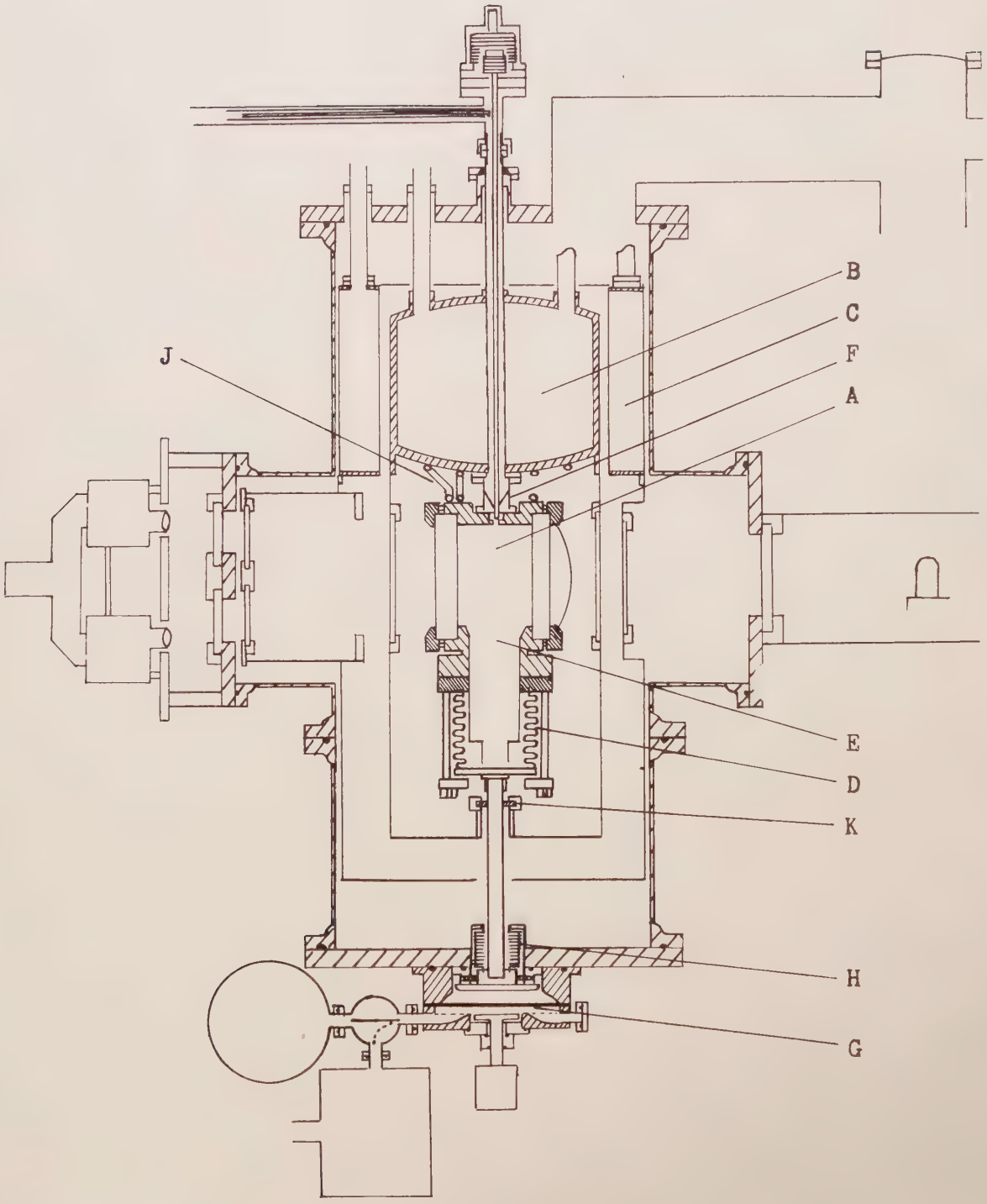

Fig. 1

pure indium, a satisfactory seal which can be cycled between liquid hydrogen and room temperature is obtained when the twenty-four 6 mm stainless steel bolts on the window clamping ring are tightened to 50 cm kg torque. Brass petrol couplings with indium coated nipples are used for pressure and vacuum connections onto the chamber, and have given no trouble when temperature cycling.

A fixed heat leak (F) connects the top of the chamber to the bottom of the liquid hydrogen reservoir, giving a temperature drop of about 4°K in the steady state. In parallel with this is a cooling spiral (J), consisting of a copper pipe soldered around the chamber and to the bottom of the hydrogen reservoir, providing a heat transfer mechanism variable by control of the amount of hydrogen within it.

High conductivity copper is used for the walls of the chamber to keep a low temperature difference from top to bottom. This allows slow convection currents to maintain temperature uniformity in the liquid.

2.3. EXPANSION MECHANISM

The chamber liquid is expanded by means of a single ply stainless steel bellows, 8.9 cm in diameter, with 10 convolutions over a length of 8.2 cm. The bellows† is made from sheet steel (FDP or 18/8/1), rolled and welded into a tube, and hydraulically formed; with a 5 mm compressional stroke, 10^5 cycles have been completed at liquid hydrogen temperature without failure. The bellows is controlled through a stainless steel push rod by compressed air acting on a neoprene diaphragm (G) outside the vacuum tank. The push rod is guided by a PTFE bearing (K) mounted on the liquid hydrogen shield. Release of the pressure below the diaphragm allows the chamber to expand naturally until the motion is arrested by the back stop, which can be moved to vary the expansion ratio. A single 18 mm Barksdale valve, operated by a pulsed power tetrode, is used to release the pressure; the expansion time of 12 msec is governed largely by the time taken for the compressed air to escape from beneath the diaphragm. A bellows (H) separates the diaphragm from the main vacuum, and the interspace is pumped and monitored so that any diaphragm failure is immediately detectable. Stops inside and outside the chamber bellows prevent movement beyond the elastic limits. The outer stop allows replacement of the diaphragm assembly while the chamber is under pressure; the inner stop allows the chamber to be vacuum tested.

3. Photography

The chamber is photographed with a pair of modified Shackman CF/100 30 metre cameras, mounted together with a common sprocket drive and fitted with matched Taylor-Taylor Hobson Cooke Speed Panchro 5 cm lenses at an aperture of F/22. Dark field illumination with a condensing lens mounted flat against the chamber back window focuses the light into the plane of the camera lenses, providing an illuminated volume of 82 per cent of the chamber. Slight flares in the centre of the photograph are produced by reflections within the condensing lens forming secondary images on the inside of the chamber windows, but do not obscure the tracks completely at any point. A reference number is placed on each frame by photographing the same register through the back of each camera. The demagnification of the system is 7:1, (in the centre of the chamber), giving a minimum bubble image size of 15μ with a $\frac{1}{2}$ stereo angle of $9\frac{1}{2}°$. The cameras are wound on automatically after the flash pulse is picked up by a photocell.

The tracks are continuously monitored with closed circuit television††, using a Vidicon camera to view the chamber. Individual tracks can clearly be seen, and track quality readily assessed. So far no attempt has been made to use the television circuit for electronic registration of track coordinates. The resolution of the present system is about 500 microns in space.

4. Safety

Considerable care has been taken to ensure the safety of personnel and apparatus. In particular, all glass components subject to stress are purchased in three times the quantity required, one third being pressure tested to destruction, one third life tested for 100 h at three times the maximum permitted

† Obtained from Teddington Aircraft Co.

†† Made available by courtesy of MARCONI LTb.

pressure, the remaining one third being used and retained as spares. The vacuum tank has been designed and tested to withstand an internal pressure of 100 psig. The liquid hydrogen reservoir was pressure tested to 300 psig, and the bubble chamber to 465 psig. The first two are provided with rupture discs designed to break at $\frac{1}{2}$ the test pressure, that from the vacuum tank leading back to the deuterium storage vessel (fig. 2). During operation, the chamber is closed off by a needle valve, which is opened automatically when the chamber pressure exceeds 150 psig. In parallel with this is an emergency blow off line, closed off at room temperature by a disc rupturing at one third of the test pressure. A spring loaded ball valve at the low temperature end prevents a jet of vapour from the line entering the chamber on expansion.

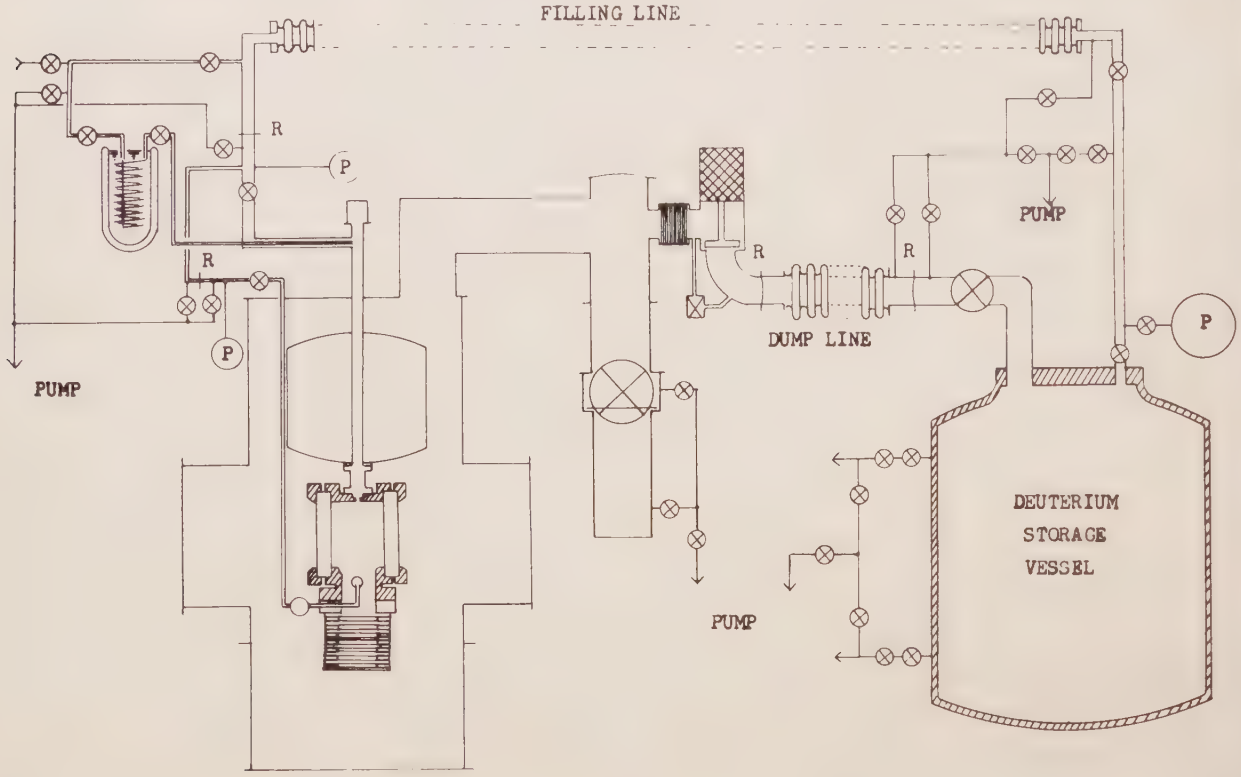

Fig. 2.

5. Deuterium

The deuterium was prepared by the reduction of 99.8 per cent heavy water (obtained from Norsk-Hydro) in a magnesium furnace at 550°C, and on subsequent analysis was found to contain about 1 per cent hydrogen. The deuterium gas is stored in a 720 litre stainless steel vessel at 40 psia. This was cleaned, outgassed and vacuum tested to a leak rate < 0.1 lu-sec before admitting the deuterium gas. The deuterium system was designed to minimise the danger of contamination of the gas. Special care is taken to prevent H-D exchange, and neoprene is excluded from the system as far as possible by the use of PTFE sealing taps and indium O rings. In the event of fracture of the bellows or a window when the chamber is full of liquid deuterium, the liquid would be deposited in the hydrogen shield surrounding the chamber. It would boil off from there until the pressure in the vacuum tank rises sufficiently to burst the rupture disc in the 5 cm diameter line leading back to the storage vessel. The deuterium left in the vacuum tank could then be removed by absorption into a liquid nitrogen cooled charcoal trap.

6. Operation

The chamber is allowed to cool to nitrogen temperature over a period of 16 h; it then takes a further 90 minutes to fill with hydrogen; or 150 min to fill with deuterium, (a greater time is necessary because the latter is stored at a low pressure). The hydrogen and liquid deuterium. Cycling rates up to one in 0.85 sec have been used, but the cameras could not wind on faster than 1 frame/1.6 sec. With liquid hydrogen as the working medium, tracks of recoil electrons produced in the liquid by a $Co^{60}\gamma$ source have been observed over the temperature

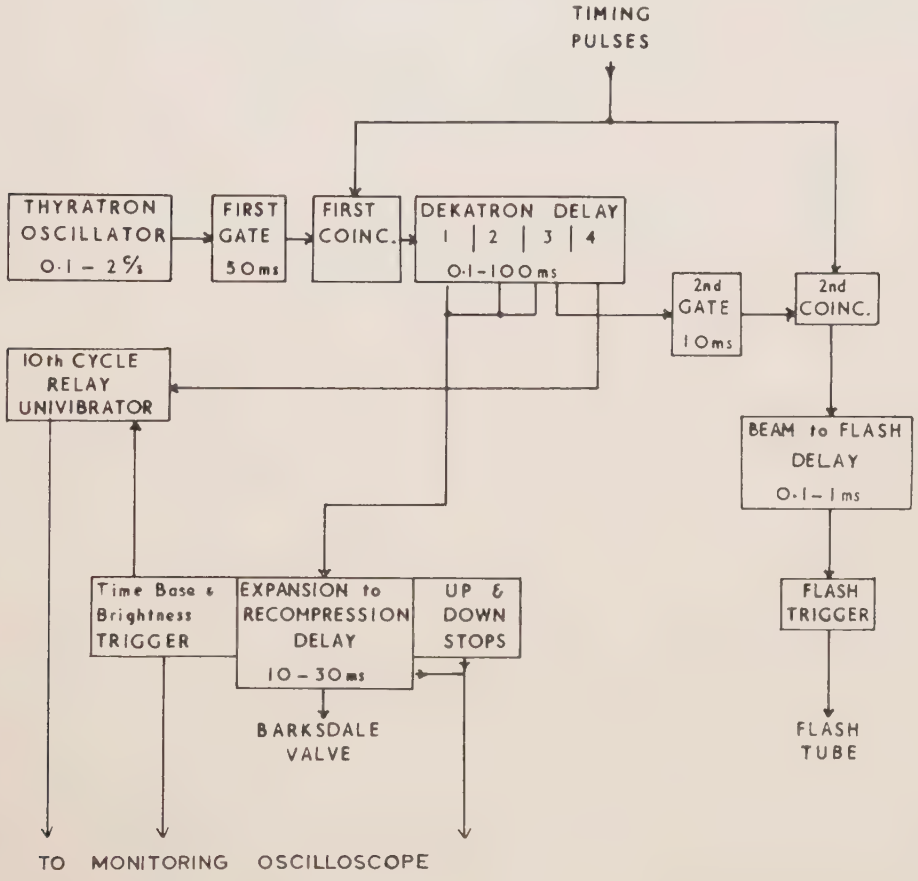

Fig. 3.

deuterium pressure falls to 10 psia as the chamber fills, making it necessary to cool the chamber below 22.4°K, the temperature corresponding to this vapour pressure. When cooling and filling the chamber the pressure in the cooling spiral is increased so that more liquid hydrogen circulates in it; at the beginning of cycling the pressure is reduced allowing the chamber to warm up to the operating temperature. The spiral pressure is adjusted to give a stable temperature for a given dynamic heat input.

The chamber has been operated with both liquid range 26.8°K–30.2°K with an overpressure of 10–20 psi. A minimum volume expansion ratio of 0.9 per cent was required at 27°K. Electron tracks have been obtained in liquid deuterium over the range 31.2°K–34.1°K, with a minimum volume expansion ratio of 1.6 per cent at 32.5°K.

The chamber pressure is monitored with a CAV† strain gauge transducer. The sensitive time is 7–8 msec, being limited by self repressurisation due to parasitic boiling in the bellows. Correct functioning of the expansion mechanism is checked by

† Made available by courtesy of CAV Ltd.

taking monitoring pulses from electrical contacts in the diaphragm chamber. The static heat load on the system is 6.2 W (0.7 litres of liquid hydrogen per hour), and the dynamic load for a delay of 8 msec in the expanded state and a repetition rate once in 2 sec is a further 6W. The liquid hydrogen reservoir is pressurised to 25 psig, corresponding to a temperature of 24.2° K, to boil off the deuterium which would otherwise collect in the filling line on top of the needle valve and act as a highly efficient heat transfer mechanism, cooling the chamber below operating conditions. The total heat load is equivalent to a liquid hydrogen consumption of 1.3 litres of liquid per hour at 20° K, increasing to 1.7 l/h at the operating temperature. Photographs of proton tracks in liquid deuterium indicate that bubbles reach a suitable size after a growth time of $\frac{1}{2}$ msec. Slight distortions in the tracks due to local turbulence become apparent after 1 msec and the bubble size becomes excessively large after about 5 msec. The bubbles are not finally squashed out until 22 msec after recompression.

Operation of the bubble chamber with a particle accelerator necessitates a closely controlled sequence to maintain track quality throughout an experimental run. The first gate, shown in the block diagram of fig. 3, controls the cycling rate of the bubble chamber and admits a timing pulse from the accelerator. This timing pulse initiates the expansion. There is a minimum delay of 21 msec inherent in the Barksdale valve and the chamber does not become sensitive until after a further 12 msec. The control of the second gate is preset on the Dekatron delay unit so that it opens when the chamber becomes sensitive. A beam pulse then triggers the flash tubes after a short delay. A variable delay, between the first timing pulse and the initiation of the expansion, allows the time at which the particle beam enters the chamber to be set at the optimum for track formation.

An investigation of the interaction of 80 MeV protons with deuterions has been undertaken and 10000 photographs were obtained using the cyclotron at A.E.R.E., Harwell. The beam was limited to 10–20 tracks per photograph giving about one useful event per frame. About 1500 events have now been measured once, and a second measurement of the same events is being undertaken to check the accuracy of the data.

Acknowledgements

It is a pleasure to thank Mr. B. Rose and the cyclotron group at A.E.R.E., Harwell for invaluable co-operation and advice. Dr. D. Colvin kindly made available to us his deuterium separating plant, and Mr. R. Johnson helped with the gas extraction.

The project was supported by research contract from A.E.R.E., Harwell. One of us (H.W.K.H.) wishes to acknowledge maintenance grants from the Co. Londonderry Education Authority, and from the Ministry of Education, Northern Ireland; L.L. and J.M.B. were maintained by grants from D.S.I.R.

We wish to express our thanks to Professor D. H. Wilkinson for his continued support and encouragement throughout the work.

NUCLEAR INSTRUMENTS AND METHODS 12 (1961) 329–334; NORTH-HOLLAND PUBLISHING CO.

STABILIZATION OF THE COUNTING RATE BY IRRADIATION OF THE LIQUID SCINTILLATION COUNTING SOLUTIONS WITH UV-LIGHT†

W. LOHMANN and W. H. PERKINS

Department of Medicine, University of Arkansas Medical Center and Radioisotope Service, Consolidated Veterans Administration Hospital, Little Rock, Arkansas

Received 24 March 1961

While counting certain compounds, labeled with tritium or S^{35}, by liquid scintillation counting, we observed that the counting rates decreased rapidly during the first 2–3 hours. Even after this time, the counting rates continued to decline, but at a slower rate. The influence of temperature, agitation of the vials, and addition of alcohol upon this phenomenon was investigated. In each case the counting rates decreased, except with additions of 2 ml or more of ethanol. All ethanol additions to the stock solutions produced a quenching of the counting rates. However, an irradiation of the stock solutions with UV-light of 2537 Å (Hg-line) stabilized the counting rates even without appearance of quenching. A possible theoretical explanation of these observations is given.

Exposure of glass vials, used in liquid scintillation counting, to sunlight or fluorescent light has been reported to cause counting errors due to fluorescence of the glass[1]). While counting solutions containing tritium as tritiated digoxin†† or S^{35} as SO_4, we observed a rapid decline in counting rates for 2 to 3 hours followed by a slower decline for several days. Counting, with a Packard Automatic Tri-Carb Liquid Scintillation Spectrometer, was started immediately after addition of the stock solutions††† to the vials.

The results obtained with tritiated digoxin solutions of different specific activities are shown in fig. 1. After about 150 minutes, the counting rates decreased 20 to 40%, with the reduction in rate appearing to be dependent upon the specific activity of the solution. This suggests that some effects other than the luminescence of the glass is responsible for the progressive decrease in counting rates.

First, the effect of ultraviolet light on the vials was considered. Several vials were irradiated from one to two hours at room temperature and at 2°C with UV-light of 2537 Å (Hg-line). These were counted immediately in the liquid scintillation spectrometer without addition of solution with the results as shown in fig. 2. The counting rate obtained from fluorescence of the glass fell to background level after 5 to 25 minutes. After addition of 15 ml of counting solution to these empty vials (see fig. 2A), there was resumption of counting which again dropped to background level after 8 minutes. With the addition of counting solution to vials immediately following UV-irradiation, a higher initial counting rate was obtained which fell to background levels within 10 minutes.

The addition of 15 ml of stock solution (counting rate 36×10^3 cpm) to the empty vials several minutes after irradiation (fig. 2B) resulted in the same initial counting rate and no change in the rate of decline of the counting rates. Therefore the decrease in counting rates observed over a period of several days cannot be explained by the effect of UV-light on the glass vials.

Next, we considered the influence of temperature, probably through its effect on solubility, on the counting rates. This was considered because our

† Dedicated to Professor Dr. E. Buchwald on the occasion of his 75th birthday.

†† Supplied as Lanoxin^R by Burroughs Wellcome, Ltd., Bloomfield, New York, through the courtesy of Dr. Stanley T. Bloomfield.

††† As "stock solution" we denote the mixture of digoxin dissolved in 95% ethanol (1mg/ml) with a counting solution (composition see explanation for fig. 1).

[1]) J. D. Davidson and P. Feigelson, Int. J. App. Rad. and Isotopes 2 (1957) 1.

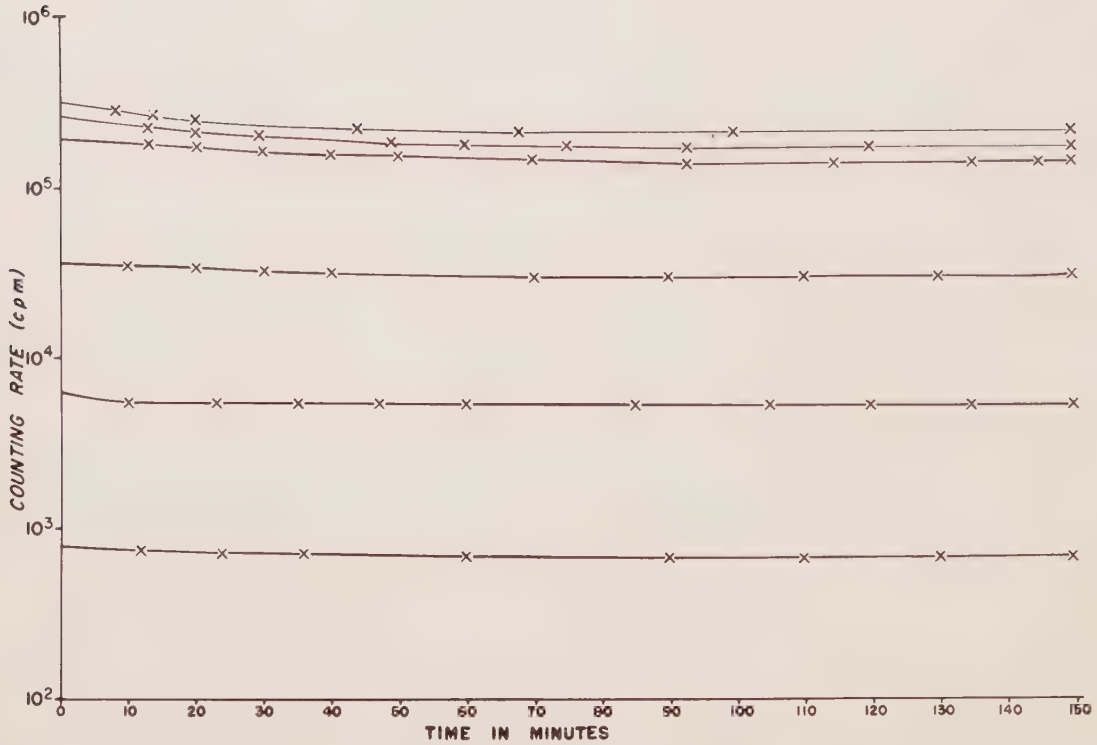

Fig. 1. The counting rate as a function of the counting time and of different specific activities of the H^3-digoxin solutions. The vials were filled with these solutions shortly before counting. The stock solutions consist of H^3-digoxin dissolved in ethanol (95 %) and a counting solution (4 gm. 2,5-diphenyloxazole (PPO) + 0.1 gm. p-bis-2(5-phenyloxazolyl)-benzene (POPOP) q.s. 1000 ml toluene).

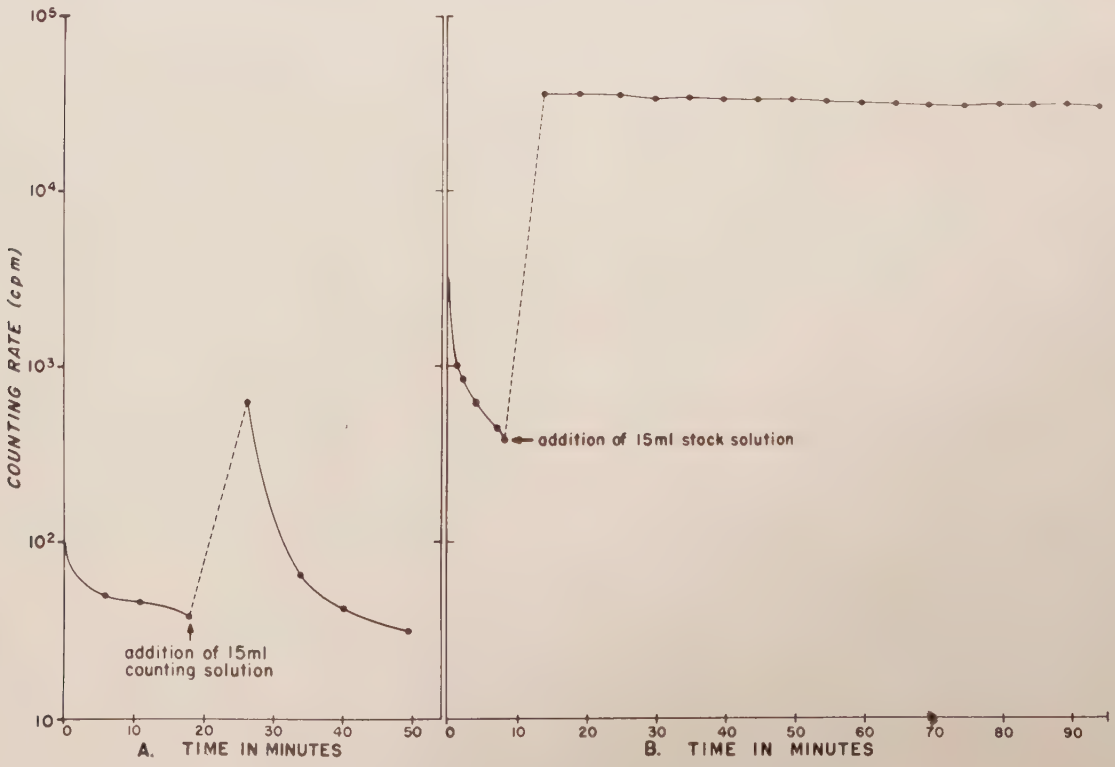
COUNTING RATE (cpm)
addition of 15ml counting solution
A. TIME IN MINUTES
addition of 15ml stock solution
B. TIME IN MINUTES

Fig. 2. Influence of ultraviolet-irradiation on the counting vials followed by the addition of solutions. (a) Addition of 15 ml counting solution; (b) Addition of 15 ml stock solution.

stock solutions were stored at room temperature, while the temperature in the freezer unit of the liquid scintillation spectrometer was about 11°C in the storage compartment and about 0°C at the level of the photo-multiplier tubes.

First, the vials containing stock solutions were placed in water at 50°C for several minutes prior to counting. The decrease in counting rates showed no change from samples kept at room temperature.

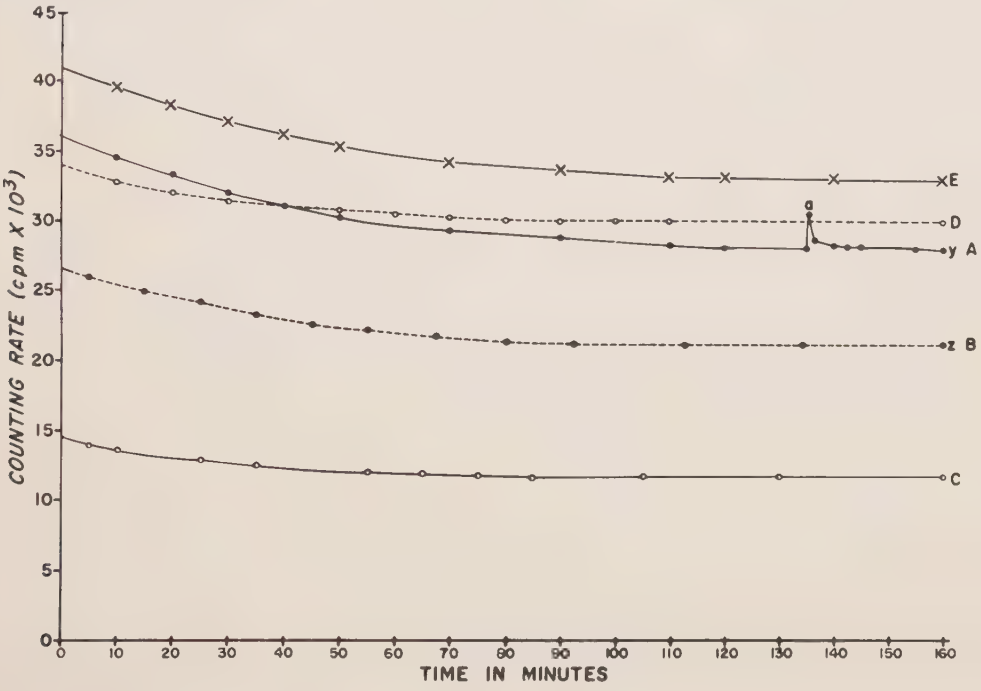

Fig. 3. Influence of different factors on the counting rate. (a) Normal solution (15 ml stock solution). At point "*a*" vial vigorously shaken; (b) Solution of sample A transferred to sample B at point *y*; (c) Solution of sample B transferred to sample C at point *z*; (d) Vial and stock solution held at 2°C for 24 hours; (e) Vial saturated with unlabelled digoxin solution.

Then the stock solution and empty vials were stored in the dark at 2°C for 24 hours. The progressive decrease in counting rates immediately following the addition of 15 ml of the cold stock solution to the cold vials was still present, but the decline was slower (fig. 3, curve D). This amounted to about 12% after 150 minutes. Thus, it seems, that temperature variations are responsible for part of the decline in counting rates.

This effect of temperature could be due to a change in the solubility of digoxin. Shaking of the vials after an appreciable decline in counting rates caused the counting rates to increase again (see curve A, point "*a*" in fig. 3). We believe this to be due to a suspension of precipitated particles. The subsequent increase in counting rates after shaking was observed only for about 10 minutes. After this time, the counting rates returned to that found immediately prior to shaking.

It is well known that a part of radioactive compounds may be lost from a solution because of adsorption on glass. In this instance, it could be due either to adsorption of the digoxin itself or of the tritium from the digoxin.

Several vials were filled with a saturated solution of unlabeled digoxin in toluene and left for several days. When they were used to count tritiated digoxin, a higher initial counting rate was obtained, but the rate of decline of the counting rates was the same as that obtained from bottles which had not been saturated with unlabeled digoxin (fig. 3, curve E).

After most of the decline in counting rates had occurred, we put the contents of sample A, at time *y* on curve A, into another vial, at room temperature,

now called sample B (fig. 3, curves A, B, and C). The counting rates obtained from sample B declined at the same rates observed when fresh stock solutions were used. At point z, curve B, we put the contents of sample B into another vial, also at room temperature, now called sample C. The same initial decline in counting rates was again observed.

The addition of 95% ethyl alcohol to the stock solution increases the solubility of digoxin. We found that the addition of less than 1.0 ml of 95% ethyl alcohol retarded the rate of decline of the counting rates. Two or more ml caused the counting rates to remain constant from the beginning (fig. 4), but all additions of ethyl alcohol caused quenching.

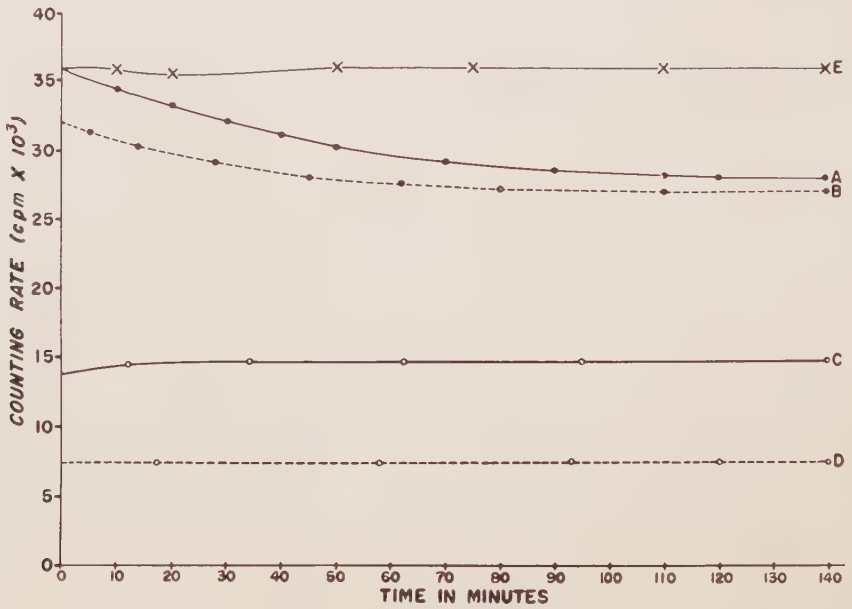

Fig. 4. Influence of ultraviolet-irradiation and of different amounts of alcohol on the counting rate. (a) Normal solution (15 ml stock solution); (b) 15 ml stock solution 0.5 ml ethanol (95%); (c) 10 ml stock solution; 3 ml counting solution; 2 ml ethanol (95%); (d) 8 ml stock solution; 3 ml counting solution; 4 ml ethanol (95%); (e) Normal solution (15 ml stock solution) ultraviolet-irradiation (2537 Å, 2 hours).

The progressive decline in counting rates seems to be a combination of the effects of temperature and adsorption of radioactivity on glass. Both effects may be due to a rupture of the weak interaction between tritiated digoxin and the solvent or between radicals produced by the influence of the β-radiation. For example, if we represent tritiated digoxin, the solute, as A, and toluene the solvent, as B, a constant counting rate will be obtained only if the reaction occurs in the following direction

$$A^* + B \rightarrow AB\,. \qquad (1)$$

Such a reaction is possible if either A or B is polyatomic and if either is in an excited state. For instance, the solute A may be in an electronic excited state A*. This kind of reactions, called exchange reactions, has been studied by Franck and co-workers[2]). They found that excitation of a molecule of either the solute or the solvent by absorption of photons causes mostly a deactivation without luminescence or dissociation. This is due to internal conversion in a polyatomic pseudo-molecule, consisting of the excited molecule and a portion of the surrounding molecules of the solvent or solute. Figure 5 shows in a simplified model such an internal conversion. As usual, the potential energy, V, is represented as a function of the mean interatomic distance. By absorption of energy, as from ultraviolet light, there is a transition of the electron from the ground state A to a vibrational level of some excited electronic state B.

[2]) J. Franck and R. Platzman, Radiation Biology I, Part 1 (McGraw-Hill Co., New York, 1954) Ch. 3.

From this higher level it can return to the energetic lower level A by emitting of (fluorescence) radiation or by radiationless transition on the intersection point of the potential curves of the states A, B, and/or C (not all ordinarily in the same plane) to state A or to another electronic state C.

If the initial and final energy levels should have a different spin coupling of the electrons, for instance, triplet and singlet states, the matrix element of the

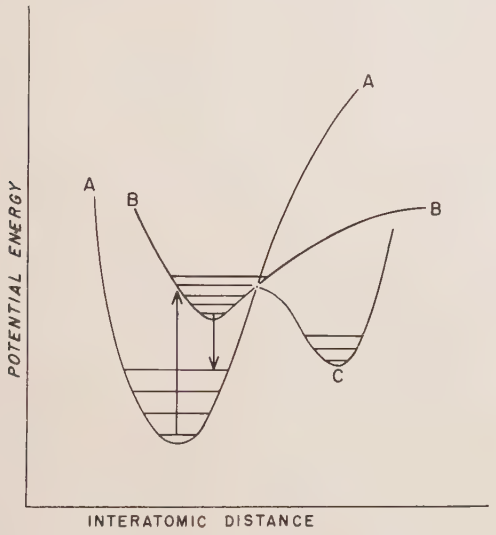

Fig. 5. Diagram to illustrate a radiationless transition.

electronic moment between the initial and final states—and therefore the transition probability—becomes exceedingly small. This means that these triplet-singlet transitions are forbidden. In that case there is no fluorescence radiation and the atom or molecule can lose its excitation energy only by internal conversion or by a collision of the second kind.

For internal conversion, the energy of the system has to remain constant during the radiationless transition. According to the Franck-Condon principle, the atomic configuration may not change during an electronic transition between quantum states. If the excitation energy of state C should be below the dissociation energy of that state, then the excitation energy will be converted into vibrational energy of that molecule and of other molecules on impact. When no fluorescence occurs, the internal conversion of the excitation energy must be very fast. If the final state is not the ground state but a metastable state, a molecule with that excitation energy has a great chance for a collision of the second kind. So the recombination energy present in process (1) is quickly dissipated to the many oscillational degrees of freedom of that system. The final chemical change is a newly formed molecule or a reinforcement of an interaction, for instance, between tritiated digoxin and the toluene solvent. It is impossible to dissociate that new molecule or to break the interaction with low energies. Several degrees of temperature variation should have no influence on this interaction.

Therefore, one can expect that irradiation of our stock solutions containing tritiated digoxin in toluene with ultraviolet light should prevent the progressive decline in counting rates. After removing the caps from the vials, we irradiated the stock solution for 1 to 2 hours with ultraviolet light of 2537 Å (Hg-line). This was done at room temperature and at 2°C. The vials were counted immediately after irradiation and the results are shown in fig. 4, curve E. The counting rates no longer declined with time, but remained constant and were the same as the initial rates for the unirradiated samples. Also, they remained constant for several days.

These experimental results confirm our theoretical explanation. Therefore, in the system studied, an internal conversion and a collision of the second kind should occur. One can calculate the rate of internal conversion if the concentration of the excited molecules N^* is known. The rate of formation of excited molecules depends upon the rate of excitation of normally reacting molecules k_1N; the rate of the fluorescence, k_2N^*; the rate of internal conversion, k_3N^*; and the rate of quenching caused by collisions of the second kind, $k_\gamma M_\gamma N^*$. This last expression refers to molecules M of the kind γ. Thus the rate of formation ot excited molecules N^* may be expressed by the following formula

$$\frac{dN^*}{dt} = k_1N - k_2N^* - k_3N^* - \sum_\gamma (k_\gamma M_\gamma)N^* . \quad (2)$$

Solving the formula for a steady state and assuming no fluorescence occurs ($k_2N^* = 0$), we obtain the following equation

$$N^* = \frac{k_1 N}{k_3 + \sum_\gamma k_\gamma M_\gamma} . \qquad (3)$$

The intensity of internal conversion equals the rate at which N^* molecules disappear with radiationless transition, with "a" as a proportional factor

$$I_{\text{i.c.}} = a k_3 N^* = a(k_1 N) \left\{ \frac{k_3}{k_3 + \sum_\gamma k_\gamma M_\gamma} \right\} . \qquad (4)$$

The factor

$$\frac{k_3}{k_3 + \sum_\gamma k_\gamma M_\gamma}$$

represents that portion of excited molecules which undergo internal conversion when fluorescence does not occur. The expression $\Sigma\, k_\gamma M_\gamma$ represents collisions of the second kind. According to Eyring *et al.*[3]) the probability of a transition from state A to state B, resulting in absorption of energy from an electromagnetic field is

$$k_1 = \rho(\nu_{AB}) \frac{2\pi}{3\hbar^2} \left| \int \psi_B^* \Sigma e_i r_i \psi_A \, d\tau \right|^2 \qquad (5)$$

where $\rho(\nu_{AB})$ is the density. The expression for the rate of internal conversion is

$$k_3 = \varkappa \frac{kT}{h} \exp(-\Delta F/RT) \qquad (6)$$

[3]) H. Eyring, J. Walter and G. E. Kimball, Quantum Chemistry (John Wiley & Sons, New York, 1957).

where $\varkappa$ is the transmission coefficient for the transition from state B to state A and ΔF is the so-called free energy of activation.

With an external applied force, such as a collision with a molecule of the same or another type, which has a component g along the reaction path, ΔF will be decreased by an amount $\frac{1}{2}gx$, if the force acts through a distance $\frac{1}{2}x$ from the normal to the activated state. The resulting specific rate of collision of the second kind will be

$$k_4 = k_3 + \sum_\gamma k_\gamma M_\gamma = \varkappa \frac{kT}{h} \exp\{ -(\Delta F - \tfrac{1}{2} n L g x)/RT \} \qquad (7)$$

where L is Loschmidt's number and n the number of molecules per ml. These formulae contain factors for temperature and concentration.

In addition to these types of reactions there may be an interaction between the glass of the vials and the solution. This may be due to an electron transfer resulting from the ultraviolet irradiation of the glass. The existence of such an interaction is indicated by the reduction in the rate of decline of the counting rates found when the stock solution, which had been exposed to UV-light, was counted in bottles which also had been exposed to UV-light.

We should like to express our thanks to Mrs. Rochelle McMahen for expert technical assistance.

NUCLEAR INSTRUMENTS AND METHODS 12 (1961) 335–340; NORTH-HOLLAND PUBLISHING CO.

PRODUCTION OF HIGH INTENSITY ION PULSES OF NANOSECOND DURATION†

L. CRANBERG

Los Alamos Scientific Laboratory, Los Alamos, New Mexico

and

R. A. FERNALD and F. S. HAHN

High Voltage Engineering Corporation, Burlington, Massachusetts

and

E. F. SHRADER

Case Institute of Technology, Cleveland, Ohio

Received 13 April 1961

A system for producing high intensity ion bursts of nanosecond duration is described. It consists of a Van de Graaff accelerator fitted with a deflection pulser in the terminal and a post-acceleration Mobley magnet with a bunching factor of about 12. Results are given on the overall performance at 3 MeV proton energy, observing the neutrons and gamma rays from the reaction $Mn^{55}(p, n)Fe^{55}$. The system performs in accordance with design expectations and delivers ion bursts of less than 1 ns duration at a peak current of several milliamperes.

1. Introduction

Ion pulses which are homogenous in energy, of nanosecond duration, and of the greatest possible peak current are essential for fast neutron spectroscopy by the pulsed-beam time-of-flight method, and are very useful for the study of short-lived nuclear states and for many other types of investigations particularly in the field of fast-neutron physics[1]). The present report describes a system for the production of such pulses in which an essential role is played by the Mobley time-compression or bunching magnet[2]), and gives an account of the first operational use of such a magnet. Peak currents have been obtained of several milliamperes in bursts of about 1 ns duration.

The system has been tested by observing neutrons and gamma rays from the reaction $Mn^{55}(p, n)Fe^{55}$. Choice of this reaction has been governed by considerations of convenience and suitability as a means of testing the system.

2. Apparatus

A diagram of the system is illustrated in fig. 1 (ref.[3])). In the high voltage terminal of a 3 MeV Van de Graaff an rf ion source delivers a steady current estimated at several hundred microamperes

† Work partially performed under the auspices of the U.S. Atomic Energy Commission.

[1]) For discussions of the technology and applications of nanosecond pulsed beams see articles by J. H. Neiler and W. Good in "Fast Neutron Physics" edited by J. B. Marion and J. L. Fowler (Interscience, New York), 1960; by L. Cranberg and L. Rosen in "Nuclear Spectroscopy" edited by F. Ajzenberg-Selove (Academic Press, New York, 1960); and "Fast Neutron Spectroscopy" by B. V. Rybakov and V. A. Sidorov, Supplement No. 6 of the Soviet Journal of Atomic Energy, 1958 (published in English translation by Consultants Bureau, Inc., New York 1960). For a preliminary account of the system described in this paper see R. J. Connor, Nucl. Instr. and Meth 11 (1961) 122.

[2]) R. C. Mobley, Phys. Rev. 88 (1952) 360; R. C. Mobley and B. R. Albritton, Phys. Rev. 98 (1955) 232. The basic idea of the time-compression magnet was conceived independently by R. J. Van de Graaff and presented as a post-deadline paper at the Denver meeting of the American Physical Society, June 30, 1952.

[3]) Fig. 1 illustrates the system as it will be installed at Case Institute of Technology. In the tests described in this report, which were carried out on the premises of the High Voltage Engineering Corporation, the accelerator was horizontal and the mass-energy analysing magnet was omitted, but neither of these features can be regarded as playing a significant role in the results to be expected.

of mass-1 protons. The ion beam is focused on a small aperture and is deflected across the aperture in an elliptical pattern by an electrostatic deflection pulser[4]) which produces a triangular pulse 10 ns wide at half maximum every thousand ns. The ions are accelerated and focused at the base of the accelerator, then refocused through a mass-energy analyzing magnet in the conventional way. The

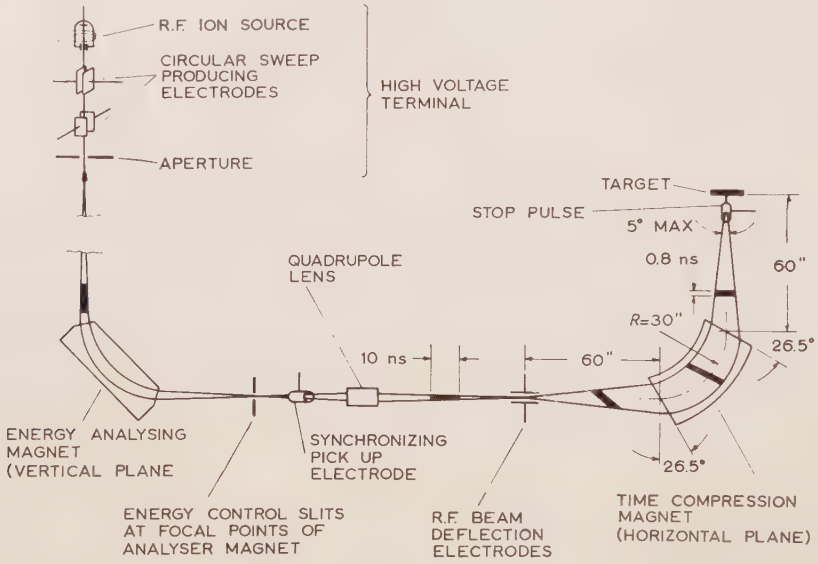

Fig. 1. Schematic diagram of pulsed-beam system.

image of the ion source is refocused by means of a magnetic quadrupole to a point between the electrostatic deflector plates of the Mobley magnet deflection system. Finally, the Mobley magnet delivers the time- and space-focused beam to the target.

The Mobley magnet incorporated in this system is essentially a conventional 90-degree, double-focusing, uniform-field magnet of 30-inch radius of curvature, rated nominally at a mass-energy product of 12 MeV-mass units. It's pole tips are tilted to 26.5° to give unity magnification. The uniform-field region of this magnet is wide enough to accommodate a beam 12 cm wide in the direction normal to the magnetic field. Sweeping the beam over this width at the proper linear rate causes a 24 cm length of beam to arrive at the conjugate point of the magnet focused in space and time. The compression factor to be expected depends on the ratio of the sweep length accepted by the magnet to the dimension of the unswept beam at the entrance to the magnet in the direction of sweeping. A conservative figure for the latter of 1 cm is arrived at by assuming a nominal beam divergence of $\pm 10^{-3}$ radians and a spot size at the deflection plates of 0.3 cm. On the basis of the relevant dimensions the bunching factor to be expected is then 12. For 3 MeV protons the dimensions given imply a 10 ns pulse will be condensed to not more than 0.8 ns.

To realize the minimum burst duration permitted by the geometry of the situation the writing speed of the deflection system at the magnet entrance must be $\frac{1}{2}v$ where v is the ion velocity. This sweep rate is approximated by using for the deflection voltage a 10 mc sinusoid which is adjustable in amplitude. The voltage is applied to a pair of deflector plates 19.2 cm long separated 1.1 cm. Under these conditions proper deflection of 3 MeV protons requires a peak-to-peak voltage of 45 kV, which is supplied by a power amplifier of 1 kW plate dissipation. To synchronize the deflecting action with the arrival of a pulse from the accelerator, a signal is obtained by electrostatic induction in a small cylindrical electrode designated "synchronizing signal pick up", which surrounds the beam. This signal, appropriately amplified, phase-shifted, and

[4]) The design is similar to that described in the article in "Fast Neutron Physics" referenced in footnote 1.

multiplied in frequency drives the power amplifier.

Adjustment of phase and amplitude of the deflecting voltage is accomplished by observation of the magnitude and duration of the ion current pulse. The phase is adjusted by maximizing the average current on target; the amplitude is adjusted on the basis of high-resolution time measurement. Two methods of time measurement have been used; observation of the current pulse with a sampling scope, and observation of neutrons and gamma rays from a nuclear reaction. At present the latter method is considered the more reliable and is the basis of the results reported here.

2.1. TESTS

To obtain a practical test of the overall system the reaction $Mn^{55}(p, n)Fe^{55}$ was used. A manganese target about 5 keV thick was prepared by evaporation on a tantalum backing.

The time measurement system is based on use of a time-to-pulse-height converter and is essentially that described previously[5]), but with modifications adapted to the requirements of this system. Thus, "stop" signals were obtained by amplifying the induction signal obtained from a pick-up electrode a few inches from the target as shown in fig. 1, a method essentially similar to that used to obtain synchronizing signals for operation of the deflector.

The detector consisted of a plastic scintillator $1\frac{3}{4}''$ in diameter by $\frac{1}{2}''$ thick coupled to an RCA 7264 photomultiplier. Following the photomultiplier was a delay-line clipper and preamplifier to minimize jitter due to pulse-height variation by utilizing the "zero crossing" time[6]) as the time to be measured.

The pulse-height spectrum was displayed on a 256-channel pulse-height analyzer whose gate was opened by pulses from a "slow" amplifier side-channel biased at an effective proton recoil energy of about 400 keV.

A sample spectrum obtained with the detector at a distance of 1 meter from the target for a running time of 2.7 minutes is shown in fig. 2. The proton energy was 3 MeV as determined by a generating voltmeter, and the direction of observation was zero degrees relative to the proton direction. With the rf deflector turned off all the lines in fig. 2 widened to about 10 ns full width at half maximum.

Calibration of the time scale for the spectrum illustrated in fig. 2 at 0.39 ns per channel was obtained from preliminary runs in which the displacement of the gamma-ray line was observed corresponding to a 2 meter displacement of the detector from the target. The neutron energies assigned in the figure were calculated from the levels in Fe^{55} as reported previously[7]) from the reaction Fe^{54} (d, p)Fe^{55}, assuming a proton energy of 3.1 MeV.

It may be noted parenthetically that the assignment of energies on the basis of the level data from Fe^{54}(d, p)Fe^{55} and an assumed proton energy of 3.1 MeV results in a time calibration which varies smoothly by $\pm$ 4% from one end of the time scale to the other. Such a variation is not consistent with previous checks of the flatness of the time-scale, and further investigation is required to resolve the discrepancy. For present purposes, however, this discrepancy is of no consequence.

The half-widths, $\frac{1}{2}\Delta E$, of the lines as given in the figure represent the energy spread reckoned from the maximum of each peak to the half-way down point on the high-energy side. In each case the corresponding time is closely 0.56 ns.

It is pertinent to note that the total time covered in the spectrum of fig. 2 is only about 0.1 μs or about one-tenth of the time between ion pulses at the target. Thus the flight-path, and hence the energy resolution of the system, could be substantially increased, particularly for the higher neutron energies, without producing overlap of successive cycles of data. However, to display the full time interval between pulses with appropriate resolution would require a pulse-height analyzer with about 2500 channels.

2.2. ANALYSIS OF RESULTS

To interpret the resolution results given in fig. 2 in terms of the contributions of the various elements of the system, table 1 has been prepared. The conditions considered correspond to those for the least and most energetic neutron groups in fig. 2.

[5]) W. Weber, C. W. Johnstone and L. Cranberg, Rev. Sci. Inst. **27** (1956) 166.

[6]) H. Lefevre and J. Russell, Rev. Sci. Inst. **30** (1959) 159.

[7]) A. Sperduto, MIT LNS Progress Report (Nov. 30, 1957) p. 51; (May 31, 1958) P. 127, quoted in Nuclear Data Sheets, C. J. McGinnis, ed.

It is particularly illuminating to consider the first four numbers in table 1 since they indicate the relative importance of the two adverse effects introduced by the bunching system. The two adverse effects are an increase in the energy spread of the beam due to the action of the deflection system and an increase of the convergence angle of the beam at the target.

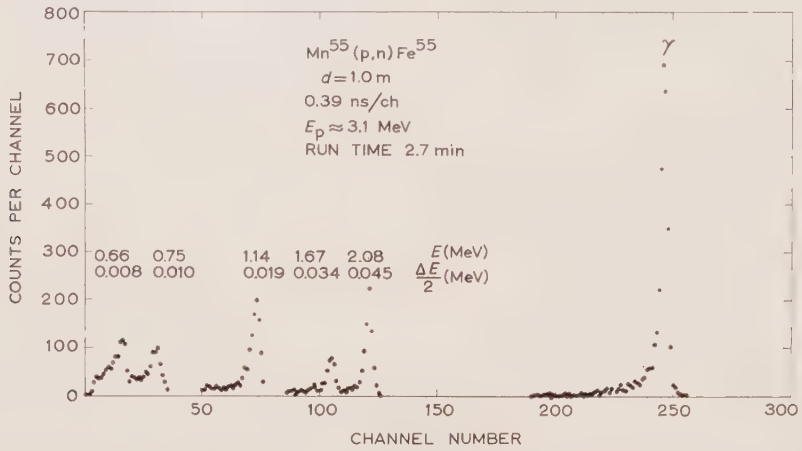

Fig. 2. Time spectrum for neutrons and gamma-rays from the reaction $Mn^{55}(p, n)Fe^{55}$ for zero-degree observation and the other conditions indicated on the figure.

Table 1

Time spreads (ns) for neutrons from $Mn^{55}(p, n)Fe^{55}$ at 1 meter at $E_p = 3$ MeV

	MeV	MeV
Neutron energy	0.66	2
Accelerator energy fluctuation (0.2 %)	0.44	0.07
Linear accelerator effect (0.38 %)	0.84	0.14
Beam divergence, unbunched (0.003)	< 0.01	< 0.01
Beam divergence, bunched (0.043)	< 0.05	< 0.02
Burst duration (1 cm beam at Mobley magnet)	0.84	0.84
Target thickness (6 keV)	0.44	0.07
Detector thickness (0.5 inch)	1.12	0.65
Δt (full width at half maximum)	1.29	0.70
Δt obs. [$Mn^{55}(p, n)Fe^{55}$]	1.75	1.1
Detector jitter, Δt, calc.	1.2	0.85

The energy spread due to a deflection system has been discussed recently in a general way by T. K. Fowler and W. M. Good[8]) and has been calculated in detail for the case under consideration by H. A. Enge[9]).

The energy spread due to the deflector is a consequence of the change in potential of the deflector plates during an ion's traversal of the deflector plates. The magnitude of the effect for the Mobley deflection system is given to first order by:

$$\frac{\Delta T}{T} = \frac{L^2}{48a^2} + \frac{Ld}{12a^2} - \frac{\Delta y}{a} - \frac{L}{2a}\left(\frac{dy}{dx}\right)_1, \qquad (1)$$

where

ΔT is the change in ion energy
T is the ion energy
L is the length of the deflector plates
a is twice the radius of curvature of the magnet
d is the length of beam accepted for compression
Δy is the width of the beam at the deflector plates parallel to the direction of deflection
$(dy/dx)_1$ is the natural divergence of the beam in the deflection plane.

The figure 0.38%, or 11.3 keV for 3 MeV protons as given in table 1 is obtained from eq. (1) using the parameters $L = 19.2$ cm, $a = 152$ cm, $d = \pm 12$ cm, $\Delta y = \pm 0.15$ cm, $(dy/dx)_1 = \pm 1 \times 10^{-3}$.

The figure of 0.2% or 6 keV for the accelerator energy fluctuation is generous. The energy spread ΔT due to the action of the deflector in the terminal of the accelerator may be calculated using the result of Fowler and Good:

[8]) T. K. Fowler and W. M. Good, Nucl. Instr. and Meth. 7 (1960) 245.

[9]) H. A. Enge, On Post-Acceleration Millimicrosecond Compression Equipment, (March 31, 1960), private communication.

$$\Delta T\, \Delta t = \Delta p_y\, \Delta y \qquad (2)$$

where

Δt is the pulse duration from the terminal deflector

Δp_y is the maximum transverse component of momentum of the beam at the terminal deflector plates

Δy is the diameter of the aperture across which the terminal deflector sweeps the beam.

Thus, assuming a terminal accelerating potential of 30 keV, $\Delta t = 10$ ns, $\Delta y = 0.2$ cm and maximum angular divergence of 0.1 rad, ΔT is only 0.5 keV.

It is clear, therefore, that the post-acceleration deflector of the present design introduces energy spread in the beam which is not negligible compared to the spread associated with the accelerator, but in the examples considered in table 1 the effect on the full width of the higher energy line is only 0.14 ns/m and on the lower energy line 0.84 ns/m.

The other adverse effect to be considered is associated with the increase in angular convergence of the beam on target from an assumed value of $\pm$ 0.001 radians due to the natural divergence of the beam from the accelerator to $\pm 2.5°$ or $\pm$ 0.043 radians. This increase in angle can be converted to an increase in the spread of energy and hence of flight time of the reaction products observed at a given angle. As can be seen from table 1 this effect of beam divergence is very small indeed, and the degradation of beam quality introduced by bunching may be regarded as entirely negligible from this point of view. The upper limits given in table 1 are the values calculated for the case of the reaction T(p, n)He^3 for which the effect of beam divergence is particularly large.

The effects of the various items have been combined to give effective widths at half maximum, Δt, for which the results are 1.29 and 0.70 ns for the low and highenergy groups respectively. Comparing these results with the observed values for the widths allows one to estimate the contributions of the items not considered thus far such as photon statistics, fluctuations in photomultiplier transit time, jitter in the time converter, finite channel width, etc., all of which are characterized together as "detector jitter". The values inferred for this quantity of 1.2 and 0.85 ns are of a magnitude which is consistent with the results of previous work.

It is interesting to note that in fig. 1 the gamma-ray line is, if anything, a bit broader than the 2 MeV neutron line, yet for the gamma-ray the detector thickness plays a negligible role. This discrepancy might be resolved by better statistics, but if it is real it implies there is a gamma-ray component of appreciable strength with a half-life in the neighborhood of 1 ns. There are no previous results on Fe^{55} which bear significantly on this point.

3. Comments and Conclusions

It is clear that to first order the design of Mobley magnet described above works in accordance with expectations and that it represents an extremely useful means of producing high intensity ion bursts in the nanosecond and sub-nanosecond range for particles with a velocity up to that of 3 MeV protons.

Some consideration has been given to extension of the range of usefulness of the Mobley magnet buncher to particles with velocities higher than those of 3 MeV protons. The chief problem is that of satisfying the requirement that the writing speed of the deflection system at the magnet entrance shall equal $\frac{1}{2}v$. Extension to 6 MeV should be possible with the present magnet if appropriate changes are made in the deflection system. Doubling of the frequency of the deflection drive is probably the single most important change required. Preliminary consideration suggests that with appropriate modifications of the design parameters of the system, including an increase in the dimensions of the magnet, useful compression could be achieved at energies in the region of 10–12 MeV, so that the Mobley magnet might be a useful accessory for a tandem accelerator.

Lower velocity particles may be readily accommodated by adjustment of the rf deflection amplitude and of magnetic field strength, and it was found to be a simple matter to adjust conditions for lower energy protons. No difficulty is anticipated in this respect with heavier particles, but it is clear that as particle velocity diminishes the minimum burst duration and compression time both increase proportionately. If the increase in burst duration

becomes objectionable it can be diminished at some sacrifice in average current by inserting an aperture at the quadrupole which restricts the extension of the beam in the deflection plane.

For low velocity particles the compression time corresponding to use of the full aperture of the magnet can become sufficiently great that effects of non-linearity of the deflection voltage become significant. This effect is not expected to be important for this system, however, for velocities above 0.7×10^9 cm/sec (1 MeV alpha particles) for 1 ns burst duration.

The range of usefulness of the system described above will be revealed only by extensive use, but it is interesting to construct some sort of figure-of-merit for the system envisaged as a source of neutrons for neutron spectroscopy, and compare it with the corresponding figure for a system such as that at Los Alamos which has already been applied to a wide range of problems.

There are several ways in which a figure of merit can be constructed. One way which is significant for many purposes is to estimate the signal-background ratio as influenced by the relevant characteristics of the neutron source for given energy resolution.

Clearly the signal is proportional to the average target current and inversely proportional to the square of the time resolution. Assuming for simplicity that the background is random in time, then the counting rate due to background in any given resolution interval must be proportional to the duty cycle. It is on this basis that the figure for signal-background ratio has been estimated. The relevant quantities are given in table 2 for the LASL system and for the system described above under the heading "Case (Present)". Under the heading "Case (Proposed)" are the corresponding figures for the system as it is hoped it will perform when the ion source is operating at projected levels. In table 2 the values of signal-background ratio have been normalized to unit for the LASL system.

In constructing table 2 no account has been taken of the fact that to achieve higher resolution some sacrifice must frequently be made in detector thickness and therefor in signal counting rate, but this is at least partially offset by the corresponding reduction in background. In any case the essential point remains that the combination of higher current ion-source and Mobley-magnet bunching gives improvement by two to three orders of magnitude over a system which itself has been of substantial usefulness.

TABLE 2
Comparison of various pulsed-beam systems

	LASL	Case (present)	Case (proposed)
$I(\mu A)$	0.8	2.5	10
Δt(ns)	4.4	1.1	1.0
Duty cycle (%)	1.7	0.11	0.10
Signal	1.0	770	4100
Background			

Should the system described above prove to be as useful as it is expected to be, a one-word description or name might be convenient for ready reference. "Pilac" (pulsed-ion linear accelerator) is the name which has been used thus far.

Acknowledgements

Special thanks are due to H. A. Enge for his contributions to the analysis and design of the compression system and to A. John Gale for his interest and support. Professors R. A. Zimmerman and R. F. Scharenberg were most helpful in the carrying out of the performance tests. Thanks are due to R. M. Ghen of Technical Measurement Corporation for loan of a 256-channel pulse-height analyzer and for his help during the running of a portion of the tests reported in this paper.

NUCLEAR INSTRUMENTS AND METHODS 12 (1961) 341–344; NORTH-HOLLAND PUBLISHING CO.

LOW JITTER PULSE DISCRIMINATOR AND SHAPER

M. AGENO

Istituto Superiore di Sanita, Rome

Received 11 March 1961

Conventional fast pulse discriminators and shapers give jitters of the order of 10 nanoseconds when the pulse amplitude just exceeds the threshold. In addition to this defect there are also variable delays, due to the discriminator level and pulse amplitude.

This paper describes a simple method whereby variable delays are practically removed by the introduction of a fixed delay.

Amplitude discriminators normally used for measuring the output pulses from a scintillation counter are made up of a biased diode, which determines the threshold, followed by a trigger circuit which must be sensitive to the smallest output obtained from the diode and which gives a standard output pulse.

In practice, these circuits have serious drawbacks which limit their use, and in order to avoid these it is generally necessary to use more complicated electronic systems to handle the data from scintillation counters.

The first and most notable defect is the introduction of a variable delay which is between zero and the total rise-time of the pulse depending on the discrimination threshold and on the pulse amplitude.

To overcome this drawback "zero-crosser"-type systems[1]) were introduced, one of which was constructed independently in our laboratory. However, even these systems are not quite satisfactory. In the first place they require a differentiation of the incoming pulses. If the pulses are not quite free from noise (which often occurs), the point where the differentiated signal passes through zero is not constant. Moreover, depending on the value of the anode resistence of the photomultiplier, such a point corresponds either to the maximum value of the anode current or to its decline. In both cases the triggering time is subject to jitter because of the discontinuous structure in time of the electric charge collected. This jitter is considerably greater than what would pertain should the triggering time coincide with the arrival of the first electrons at the anode.

Another serious defect of the ordinary discriminator is related to the characteristic features of the valve of the trigger circuit. The latter is always a positive feedback circuit with a low threshold, which is added to the threshold of the discriminating diode. The promptness of the triggering is obviously dependent on the valve amplification, and consequently on its transconductance. When the circuit is quiescent the transconductance of the valve is zero; it reaches a maximum in the triggering process. Since the increase in transconductance occurs gradually, if the grid signal is too small, it will not be sufficient in itself to bring the valve to its maximum transconductance. Triggering will thus occur only after the valve signal is sufficiently amplified, which will necessitate its return, sometimes more than once, through the feedback circuit. The delay caused in this way may be quite appreciable, especially if the signal just exceeds the threshold. In a Moody-type discriminator[2]) delays can approach 40 ns if the input signal does not exceed the threshold by 0.5 V.

Figure 1 illustrates this phenomenon, and was obtained in the following manner. The signal from a pulser not very stable in amplitude was sent through a Moody discriminator with the threshold adjusted so that about half the pulses were able to trigger the discriminator. This was observed on the grid of the EFP 60. The small triggering pulse is

[1]) W. Gruhle, Nucl. Instr. and Meth. **4** (1959) 112.
[2]) N. F. Moody, Electronic Engng. **24** (1952) 214.

clearly visible followed by the large pulse coming from the feedback circuit several times corresponding to the triggering (1 cm = 2 × 10^{-8} s).

In order to overcome these drawbacks, at least partially, we have constructed a new type of pulse discriminator and shaper which appears to offer some advantages over the conventional circuits.

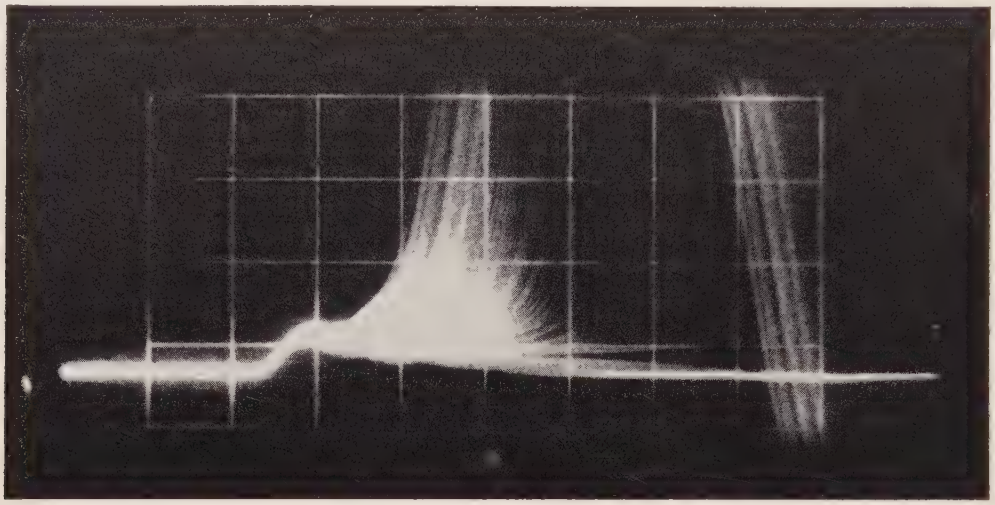

Fig. 1. Jitter of a Moody discriminator (1 cm = 2 × 10^{-8} s) seen at the control grid of the EFP 60.

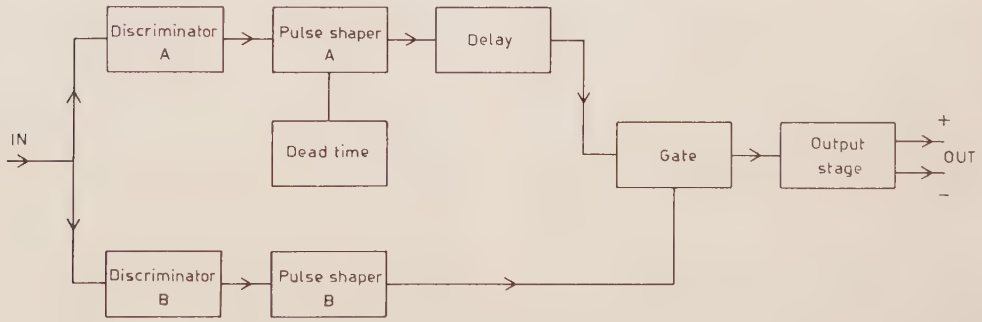

Fig. 2. Block diagram of the circuit.

The basic principle of our circuit, which is very simple, is shown in the block diagram of fig. 2. It consists in separating the two functions of "amplitude discrimination" and "standard pulse formation". Channel B provides the amplitude discrimination and Channel A the formation of the standard output pulse.

The input pulse is sent simultaneously through the two channels, each having a discriminator and an ordinary type pulse shaper. Channel B triggers only if the incoming pulse exceeds the selected threshold; and though delays often occur due to different causes as discussed above, they are, at the maximum, 5 × 10^{-8} s. Channel B is triggered only in order to open a gate for a period equal to this maximum delay.

The threshold of Channel A, on the contrary, is set as low as possible, at least 0.5 V lower than the minimum threshold of Channel B. The pulse shaped by Channel A has a fixed delay of 5 × 10^{-8} s and passes through the gate, opened by the pulse coming from the other channel, to the output stage.

In this manner the following results are obtained.

1. An output pulse is obtained only if the gate has been opened, i.e. only if the amplitude of the input pulse exceeds the selected threshold.

2. Whatever the delay in the triggering of Channel B, the output pulse is delayed with respect

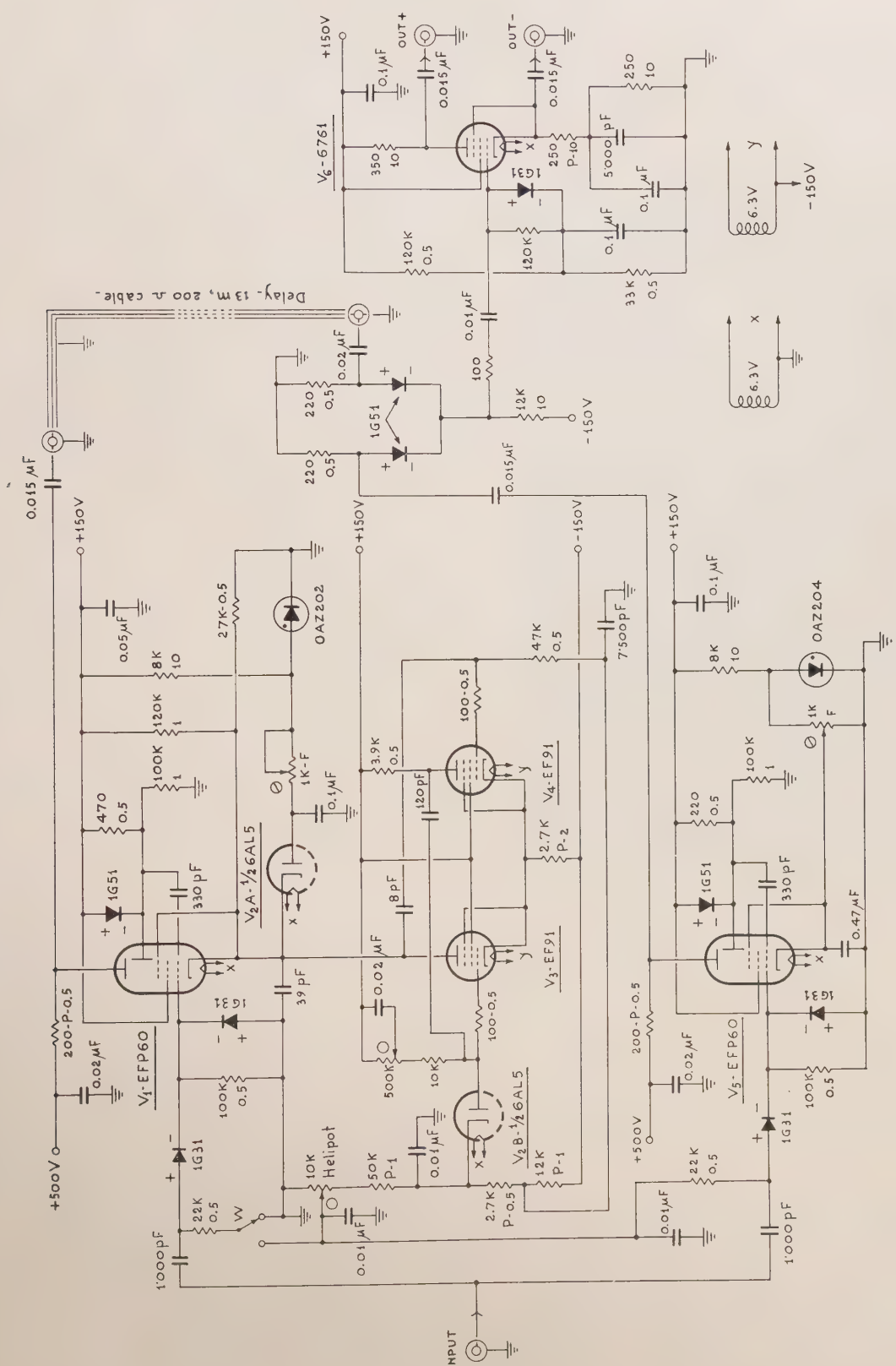

Fig. 3. Electric diagram of the circuit.

to the input by a fixed time interval equal to 5×10^{-8} s. In fact, in Channel A the input pulse always exceeds the threshold by at least 0.5 V, and therefore the triggering occurs without significant delay.

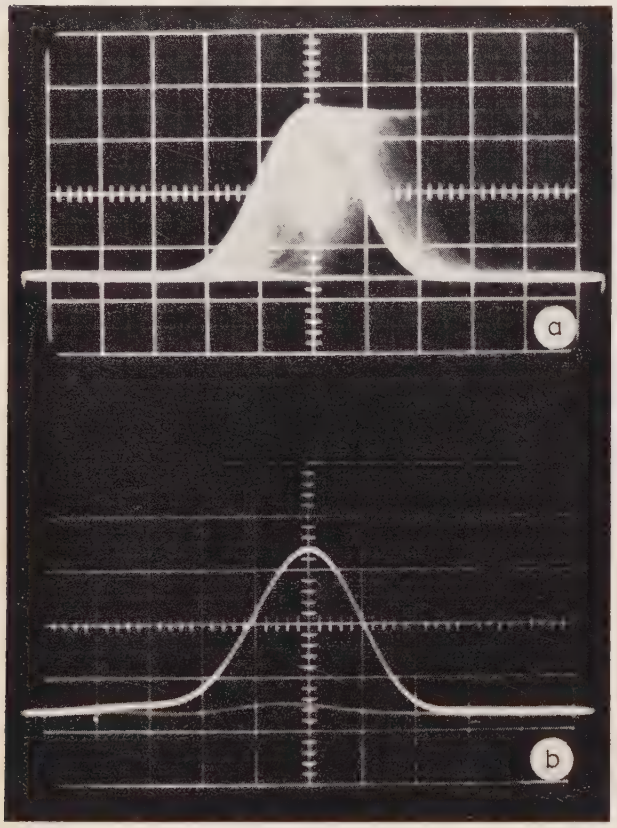

Fig. 4. Jitter of a Moody discriminator (a) and of our circuit (b) seen at the output, under the same conditions.

3. Since the threshold of Channel A is very low and is always fixed at the same level, variable delays due to the amplitude and the discriminator level are removed.

4. Since the circuit of Channel A triggers with the first electrons of the incoming pulse, jitter due to the time structure of the electric charge collected is minimized.

Figure 3 shows a schematic diagram of the circuit which comprises two Moody type discriminator-pulse shapers with secondary emission valves of the EFP 60 type. The dead-time introduced into Channel A prevents a second pulse following too closely after the first one as it passes to the output, in cases when the delay of B is appreciable and the gate is therefore open long after the pulse from Channel A has passed.

The gate is of the Garwin type[3]) and comprises a pair of 1G 51 diodes. The output stage simultaneously supplies positive and negative output pulses. The same circuit has also been constructed in a different way, using in each channel a type of pulse shaper without secondary emission valves. This type will be discussed elsewhere.

Figure 4 gives an idea of the performance of the circuit. Both photographs were obtained in the same way as that of fig. 1, except with the observation being made at the output. Photograph b refers to our discriminator and was obtained under the same conditions as photograph a. The jitter is clearly not appreciable; it is probably less than 1 ns.

The main drawbacks of our circuit are as follows:

1. The presence of a fixed delay of about 50 ns, which probably should not cause trouble or introduce complications in the subsequent circuits.

2. An increase in the minimum threshold to about 0.6 V, which results from the necessity of triggering circuit A promptly.

3. A limitation in the acceptable pulse frequency. In practice, one should never have two pulses in a time interval equal to the constant delay, which is also the dead-time of Channel A. If this 5×10^{-8} s the circuit can easily handle up to 10^5 pulses per second.

It is likely that the presence of delays due to the input pulse amplitude and the discrimination level may not be serious, whereas jitter resulting from the transconductance of the trigger circuit valve is always quite serious. On the basis of this premiss, it may be of advantage not to fix the threshold of Channel A, but to tie it to the threshold of Channel B, keeping it always 0.5 V below the threshold. In this way Channel A is less subject to input pulse pile-up and the circuit can handle a greater number of pulses per second. This would be of definite advantage for instance, if the spectrum of pulses being studied decreases rapidly with increasing amplitude.

[3]) R. L. Garwin, Rev. Sci. Instr. **30** (1959) 373.

NUCLEAR INSTRUMENTS AND METHODS 12 (1961) 345–348; NORTH-HOLLAND PUBLISHING CO.

MAGNETOHYDRODYNAMIC METHOD OF INJECTING CHARGED PARTICLES INTO A MAGNETIC FIELD

C. C. CHANG

University of Minnesota, U.S.A.†

Received 25 January 1961

A new scheme of injecting high-energy charged particles into a nuclear accelerator or thermonuclear device such as Astron is described. The injection can be carried out at small or even zero injection angle with a plane being perpendicular to the applied uniform magnetic field. The orbiting particles are estimated not to hit the injection systems which can be kept safely at reasonable radial clearance from the trajectory and orbit envelopes of the charged particles, for instance the location of the cylindrical E-layer.

The method can be applied to inject charged particles without much restriction to its energy level. The attachments to the regular injection system such as electron gun are simple, economical and easy to develop.

1. Introduction

In controlled thermonuclear fusion such as Astron, Pyratron, etc., it is necessary to inject into a uniform magnetic field high-energy charged particles as heating sources for plasma. It is difficult to design such an injection system which meets the requirement: the orbiting charge particles do not hit the system after injection into a magnetic field. In Oak Ridge National Laboratory, Luce[1]) discovered an ingenious scheme of dissociating or splitting the orbiting D_2^+ ions each into two D^+ ions as passing through an "energetic carbon arc", which must unfortunately be located in the regular orbit of the D^+ ions in a uniform applied magnetic field. It is rather inconvenient to place such a carbon arc inside any controlled nuclear device, unless further improvement on Luce's scheme can be worked out. Besides, it cannot be applied to inject electrons.

Christofilos[2]) proposed an interesting scheme for injection of relativistic electrons into Astron, which is claimed to be suitable only for very high energy electrons above 20 MeV and to be difficult to apply for electrons of energy below 5 MeV. During the Second International Conference on Peaceful Uses of Atomic Energy, Alfvén[3]) indicated a feasible method for producing a plasma ring which can stretch or drift the magnetic lines of force far out of the mechanical parts of the magnetic system. Recently he and his associates[8]) verified his idea with experiments. Some extension of his idea may be utilized to design a new injection system. This note will present some preliminary study of such a system.

Take the case of Astron as an example. The injected relativistic electrons, upon leaving the usual injection gun, are immediately subjected to the influence of the applied uniform axial magnetic field. The field then will interact with those electrons and accelerate them to move more in the circular orbit, which will hit the mouth of the gun unless it is extremely small. One method of avoiding this is to incline the gun direction at a reasonable angle with the plane being perpendicular to the axial field, so that the pitch of the helical trajectory of the injected electrons will miss the gun mouth. However, this is effective only for the forward moving helical trajectory. It will still be hit hot only by the electrons which are reflected from both

† Now with Aerospace Corporation, El Segundo, California, U.S.A.

[1]) J. S. Luce, Proceedings of Second United Nations International Conference on the Peaceful Uses of Atomic Energy **31** (1958) 305.

[2]) N. Christofilos, Astron Electron Injection, UCRL-5617-T (June 22, 1959) (unpublished).

[3]) H. Alfvén, Proceedings of Second United Nations, International Conference on the Peaceful Uses of Atomic Energy **31** (1958) 3.

ends of the mirror fields, but also by those electrons orbiting in the cylindrical E-layer which are injected early, because the gun mouth has to be very close to the cylindrical orbit surface of the E-layer. This dilemma is well known in the field of high energy particle accelerator and has not been solved.

2. Apparatus and its Operation

The present device consists of the novel electron gun with tubular barrel (1) made of mu-metal wall which is used to shield any existing magnetic field outside the gun as shown in fig. 1. The size of the barrel (1), the outlet opening (4) and the outer insulation (5) should be kept as small as possible.

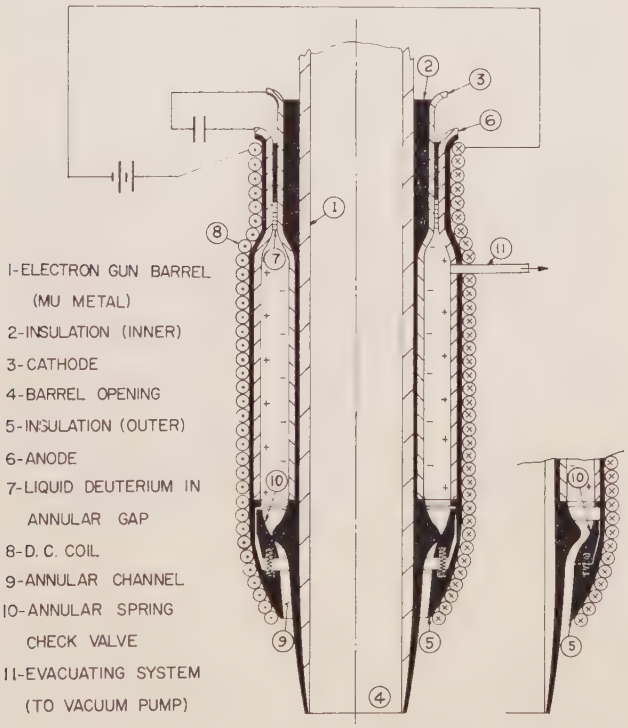

Fig. 1. Attachments to regular electron gun for magneto-hydrodynamic injections.

In addition, an insulating sleeve (2) fits the outside of the barrel (1). Just outside the sleeve (2), a cylindrical electrode or cathode (3) is located at a specified annular gap (7) from a cylindrical anode (6). Both of these electrodes are coaxial with the barrel (1), and the gap is much smaller than is shown here. The anode (6) is attached to the inside of a long insulating cylindrical shell (5) which is much higher in position than the barrel opening (4) so that the relativistic electrons on (5) can never hit insulator (5) before they hit the barrel (1). Above the gap (7) between (3) and (6) there is a feeding system of liquid deuterium which is a simple device and is not shown in this sketch. This feeding system can supply a droplet of liquid deuterium of definite quantity in a short time. The gap (7) is sealed at the top. The quantity of the injected deuterium to the gap can be controlled very accurately and is held in the gap as a liquid film by capillary action. Outside the insulator (5), a fine helical copper coil (8) is wired to cover the whole system far above the gap (7). A desirable steady magnetic field can be obtained by passing a steady electric current through the coil (8), so that uniform axial magnetic field extends over the whole annular channel (9). The functions of the annular spring check valve (10) and evacuating system (11) will be discussed later.

Some discussion of the magnetic field may be in order. In the long annular channel (9) between cathode (3) and anode (6), very little magnetic field strength of the helical coil (8) remains because the magnetic lines will pass easily through the sides of the barrel (1) which, being made of mu-metal, have very high magnetic permeability. However, this is not so at the lower end of the coil (8) where the magnetic lines will run practically radially across the annular gap, because of the high permeability of the barrel (1). Now, the wall thickness of (1) at the mouth is tapered so thin that magnetic saturation may be reached, and consequently a part of the lines of force run across the gap and the rest may extend for down to crowd the outside of the opening (4).

Next, we may discuss how to generate a plasma ring of deuterium. Suppose that a proper amount of deuterium is first stored in gap (7). As soon as a condenser bank which connects between the electrodes (3) and (6) is discharged through the liquid deuterium, the heat of the discharge evaporates the liquid deuterium into plasma to reach high temperature and pressure as the plasma expands downward through the upper part of the annular channel (9) next to the long electrodes. The high pressure drives the annular plasma sheet downward with enough velocity (see stage 1 of fig. 2) across the

radial magnetic field to generate an electric current in circumferential direction according to dynamo rule. The current in the plasma is strong enough so that it pinches the plasma together to form a plasma ring as shown in stage 2 of fig. 2. Furthermore, the generated Lorentz force will slow down the motion of the plasma ring slightly. The plasma ring, which passes through the lower end of the channel (9), will carry magnetic field with it as predicted by Alfvén[3]) as shown in stage 3 of fig. 2. Thus, a local

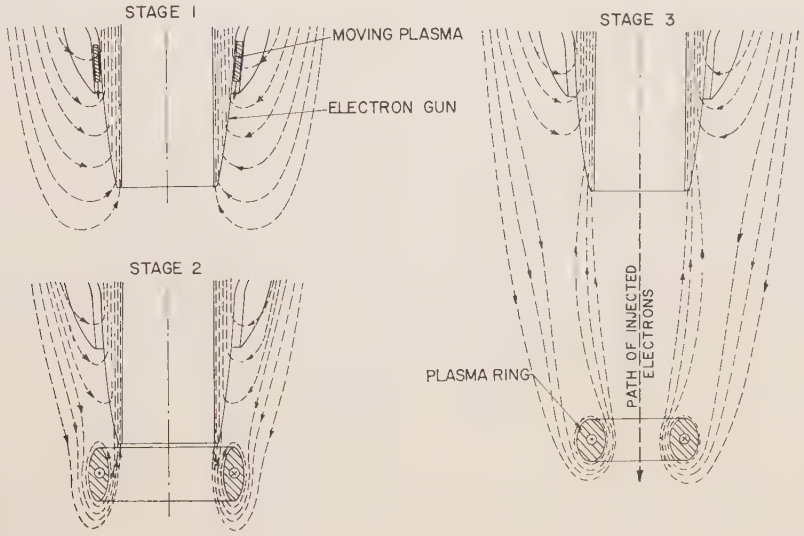

Fig. 2. Time sequence of generating plasma ring and injecting relativistic electrons from electron gun.

axial magnetic field is produced transiently for a length of a few diameters just outside the mouth of the electron gun. The combined magnetic field in the axial direction will guide the axial motion of the shooting relativistic electrons as if the electron gun had become longer by a few gun diameters than its true length. The velocity of the plasma ring can be adjusted to a desirable value and can also be controlled by the gap size of the lower opening of the channel (9). Now, as the electrons are shooting from the electron gun through the opening (4) and, if the magnetic field is stretched to the lowest position (say stage 3 of fig. 2) right at that moment, the newly ejected electrons will begin to interact with the applied uniform filed and move in curved trajectory. The correct timing is very important. As the bundle of shooting relativistic electrons passes through the shielding magnetic field of the plasma ring, they are acted upon by the applied uniform magnetic field which will accelerate the electrons into orbit of E-layer. The trajectory of the bundle will be as indicated by the dotted line of fig. 3 and the bundle will be merged with the cylindrical E-layer as indicated. The speed of the plasma ring should be kept as low as possible, and the shooting velocity of relativistic electrons is practically equal to the speed of light. Accurate electronic devices for timing and program control are required to carry out such a delicate operation. At present, very little data on plasma rings is available except a few papers[4,5,6,7]). Their experiments are entirely different in nature.

Analytic calculation and estimation of the dynamic performance of the plasma rings across a magnetic field will be reported in a later paper.

For the electron injection system of the Astron,

[4]) W. H. Bostick, Proceedings of Second United Nations International Conference on the Peaceful Uses of Atomic Energy **31** (1958) 427;
Also, Plasmoids and Pinch Effect, Scientific American (Oct. 1957).

[5]) S. M. Osovetz, Y. F. Nasedin, E. I. Pavlov, Y. F. Petrov and N. I. Schedrin, Proceedings of Second Uuited Nations International Conference on Peaceful Uses of Atomic Energy **32** (1958) 311.

[6]) I. S. Bogdankevich, Zh. eksp. teor. fiz. **36** (1959) 835;
Also, Soviet Phys. JETP **36** (9) (1959) 589.

[7]) Yu. V. Vandakurov *et al.*, Zh. eskp. Lear. fiz. **29** (1959) 1312.

the injection time of the plasma gun can be kept as short as $\frac{1}{4}$ μ-second. If the plasma ring can be kept at a speed of the order of 10 cm/μ-sec, then during the time interval the corresponding displacement of plasma rings is of the order of $2\frac{1}{2}$ cm. In other words, the orbits of the first and last electrons on one pulse of injection can be kept within $2\frac{1}{2}$ cm. Of course, we can control the timing of the plasma ring so that the final orbit of the electrons in a pulse of injection can be kept at a safe distance from the mouth if the gun.

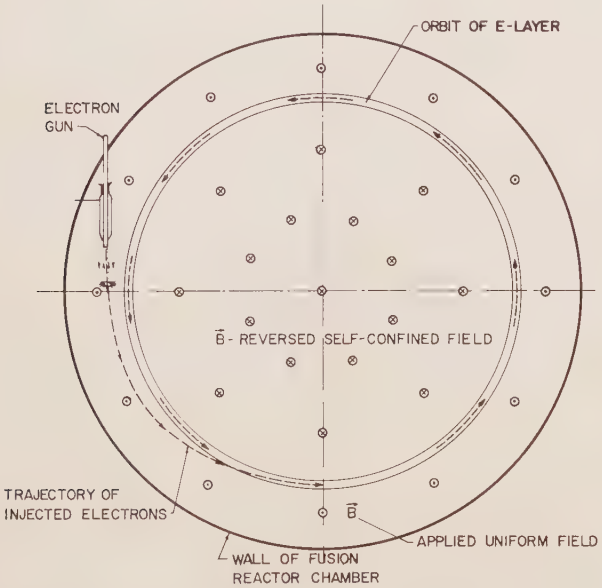

Fig. 3. Trajectory of newly injected electrons as merged with cylindrical E-layer.

So far the operating mechanism of a single magnetohydrodynamic injection is discussed. For the next pulse injection, the above sequence of operation can be repeated if the droplet of deuterium can be fed at the proper time. Furthermore, all the plasma remaining in the upper part of the annular chamber (9) will have to be withdrawn by means of the evacuating system (11) before a new plasma ring is produced. It is estimated that for an electron gun of 10^6 volts and 100 amperes with pulse duration of $\frac{1}{4}$ μ-second, the maximum rate of injection of electrons may reach the order of 100 pulses per second. The pressure inside reactor chamber is of the order of 10^{-5} cm Hg.

Someone may ask about the effects of local stretched field and plasma ring on the stability of the E-layer. It is rather difficult to answer the question definitely. However, if the E-layer is stable, the local disturbance of magnetic field due to such a small moving plasma ring cannot seriously damage the survival of the E-layer, because magnetic disturbances from other possible sources in the process of nuclear fusion are expected to be at least one order of magnitude higher. Another advantage of the present method is that when the shooting relativistic electrons are just shot out of the gun mouth, the transient magnetic field of the plasma ring serves also to readjust and focus them axially. As the plasma ring travels further downward from the position shown in fig. 3, its magnetic field will separate from that of the coil (8). It will decay in time and break up eventually as it strikes the chamber wall.

The experiments of Alfvén and his associates[8]) on plasma ring and the magnetic field of the plasma ring seemed to confirm the prediction (his fig. 14). The lifetime of the plasma ring was of the order of 8 μ-sec, which is much longer than $\frac{1}{4}$ μ-sec for the electron pulse mentioned before. The velocity of plasma ring was 6 cm per μ-sec and is within the desired range.

In view of the need for an injection scheme, some exploratory experimental studies of the above attachments seem worthwhile.

This work was prepared under the auspices of the U.S. Atomic Energy Commission.

This paper is a partially revised one, from the author's technical notes while at the Lawrence Radiation Laboratory at Livermore, California, August 1959. The author is presently employed by Aerospace Corporation, El Segundo, California. I wish to express sincere thanks to Dr. E. Teller, Director of the Laboratory, for the opportunity of working during the summer of 1959 on this problem, and to Dr. Chester M. Van Atta and Mr. N. Christofilos for their constant encouragement and support of this work and their stimulating discussions and suggestions during the course of investigation.

[8]) H. Alfvén, L. Lindberg and P. Mitlid, Nuclear Energy Part C: Plasma Physics **1** (1960) 116.

NUCLEAR INSTRUMENTS AND METHODS (1961) **12** 349–352; NORTH-HOLLAND PUBLISHING CO.

MAGNETIC FIELD OF ALTERNATELY CHARGED SYMMETRIC MULTIPOLE MAGNET

MASATERU SONODA, AKIRA KATASE, MASAO SEKI and TSUNEKAZU AKIYOSHI

Department of Nuclear Engineering, Kyūshū University, Fukuoka, Japan

Received 28 March 1961

The magnetic field of an alternately charged symmetric $2N$-pole magnet is calculated, using the conformal transformations. The formulae are given for the equipotential line, the line of force, the field strength, the magnetomotive force and the total magnetic flux passing through the surface of a pole piece.

1. Introduction

The magnetic field strength of an alternately charged symmetric $2N$-pole magnet (e.g., $N = 2$ for a quadrupole magnet and $N = 3$ for a sextupole one) is proportional to r^{N-1}, where r is the distance from the symmetry axis of the magnetic field, and has been frequently used for the hyperfine separation of atomic or molecular beam and the focusing of accelerated ion beam. However, the profile of the pole piece must be a part of a curve of n-th order, in order to make the r^{N-1} proportionality rigorously valid up to the pole piece surface, and the fabrication is very difficult.

To simplify the fabrication, a trapezoidal pole profile as shown in fig. 1 has been frequently adopted[1,2]). It is very important to calculate the field strength in such a case, in order to estimate to what extent r^{N-1} proportionality would hold. The calculation is also required to design a permanent magnet necessary to produce a desired field. However, such calculations are very difficult and have hardly been carried out. R. L. Christensen and D. R. Hamilton[2]) have recently made the approximation that the end surfaces of pole pieces locate symmetrically on the cylinder of radius r_0 as shown as the broken lines in fig. 1 and calculated the magnetic field, assuming the boundary condition that the magnetic potential on the cylinder is $\pm V_0$ on the end surfaces (alternating sign from one pole to the next) and zero elsewhere. It is obvious that their boundary condition is not accurate. The present paper dealts with the rigorous calculation by the successive conformal transformations for the same geometric condition as that of Christensen and Hamilton, adopting only the assumption that the magnetic potential on the pole piece surface is alternately positive and negative.

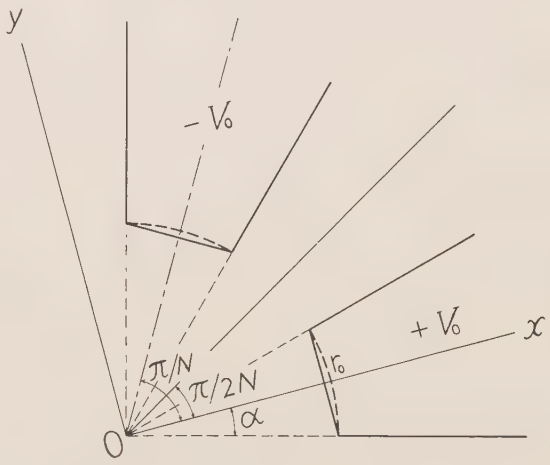

Fig. 1. Profile of pole piece of $2N$-pole magnet.

2. Method of Calculation

At first, we make the following transformation

$$z = r_0\, e^{w}\,, \qquad z = x + iy\,, \qquad w = u + iv\,. \tag{1}$$

Eq. (1) leads to the equations

$$x^2 + y^2 = r_0^2\, e^{2u}\,, \qquad y/x = \tan v. \tag{2}$$

Therefore, the pole profiles and the lines of symmetry $\theta = \pm \pi/2N, \pm 3\pi/2N, \ldots\ldots$ in the z-plane

[1]) A. Lemonick, F. M. Pipkin and D. R. Hamilton, Rev. Sci. Instr. **26** (1955) 1112.

[2]) R. L. Christensen and D. R. Hamilton, Rev. Sci. Instr. **30** (1959) 356.

are transformed to the semi-infinite rectangles and the straight lines $v = \pm \pi/2N, \pm 3\pi/2N, \ldots\ldots$ in the w-plane respectively as shown in fig. 2.

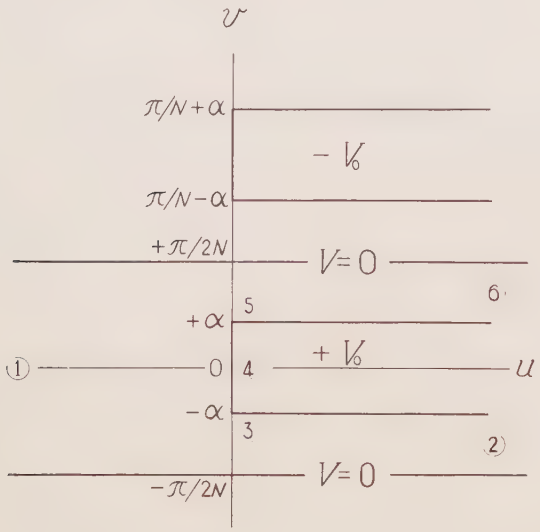

Fig. 2. Figures obtained by the conformal transformation $z = r_0 e^w$ from those of fig. 1.

Next, we consider the straight lines $v = \pm \pi/2N$ and the central semi-infinite rectangle in the w-plane to form a polygon and apply the following Schwartz transformation

$$\frac{dw}{dt} = C \prod_i (t - t_i)^{-\gamma_i/\pi} ,$$
$$t = \xi + i\eta . \tag{3}$$

The sides of the polygon in the w-plane are, then, transformed to the ξ-axis (real axis) in the t-plane. t_i in eq. (3) is the value of ξ-coordinate corresponding to the i-th point in fig. 2 and γ_i is the i-th exterior angle of the polygon. The values of t_i and γ_i are shown in table 1. Using these values, eq. (3) becomes

$$\frac{dw}{dt} = C(t^2 - 1)^{-1} (t^2 - a^2)^{\frac{1}{2}} . \tag{4}$$

Table 1

i	t_i	γ_i	$-\gamma_i/\pi$
1	$\pm \infty$	π	-1
2	-1	π	-1
3	$-a$	$-\frac{1}{2}\pi$	$\frac{1}{2}$
4	0	0	0
5	$+a$	$-\frac{1}{2}\pi$	$\frac{1}{2}$
6	$+1$	π	-1

By integrating and applying the boundary condition that w is equal to zero and $-i\alpha$ for the t-values of zero and $-a$ respectively, we get

$$w = \log \left(\frac{ia}{t + \sqrt{t^2 - a^2}} \right)^{1/N} \times$$
$$\times \left(\frac{\sqrt{t^2 - a^2} + t\sqrt{1 - a^2}}{\sqrt{t^2 - a^2} - t\sqrt{1 - a^2}} \right)^{\sqrt{1-a^2}/2N} . \tag{5}$$

Taking into account the change of v when t increases and gets over the point $t = 1$, the following relation between a and α is obtained:

$$\frac{\pi}{2N} = \frac{\alpha}{1 - \sqrt{1 - a^2}} . \tag{6}$$

By the transformation (5), the straight lines $v = \pm \pi/2N$ in fig. 2, on which the potential is zero, are transformed to the parts of the real axis in which ξ is greater or smaller than 1, and the semi-infinite rectangle, on which the potential is $+V_0$, is transformed to the one in which ξ is between -1 and $+1$. From eqs. (1) and (5), we obtain

$$z = r_0 \left(\frac{ia}{t + \sqrt{t^2 - a^2}} \right)^{1/N} \times$$
$$\times \left(\frac{\sqrt{t^2 - a^2} + t\sqrt{1 - a^2}}{\sqrt{t^2 - a^2} - t\sqrt{1 - a^2}} \right)^{\sqrt{1-a^2}/2N} . \tag{7}$$

Finally, consider the transformation

$$W = \frac{2V_0}{\pi} \coth^{-1} t ,$$
$$W = U + iV , \tag{8}$$

which will lead to the relations

$$\xi = \frac{\sinh \frac{\pi}{V_0} U}{\cosh \frac{\pi}{V_0} U - \cos \frac{\pi}{V_0} V} , \quad \eta = \frac{\sin \frac{\pi}{V_0} V}{\cosh \frac{\pi}{V_0} U - \cos \frac{\pi}{V_0} V} . \tag{9}$$

By this transformation, the part of the ξ-axis in which $|\xi| < 1$ (the potential is $+V_0$) and those in which $|\xi| > 1$ (the potential is zero) are transformed to the straight lines $V = +V_0$ and $V = 0$ in the W-plane respectively. The obtained figure in the W-plane corresponds to the case of infinite parallel plane magnets, the magnetic field of which is self-evident.

3. Results

The principal results obtained by the above-mentioned transformations are described below.

3.1. EQUIPOTENTIAL LINES

V takes a constant value on an equipotential line. Eliminating U in eq. (9), we obtain

$$\xi^2 \sin^2 \frac{\pi}{V_0} V = -\left(\eta \sin^2 \frac{\pi}{V_0} V - \cos \frac{\pi}{V_0} V\right)^3 + 1 . \qquad (10)$$

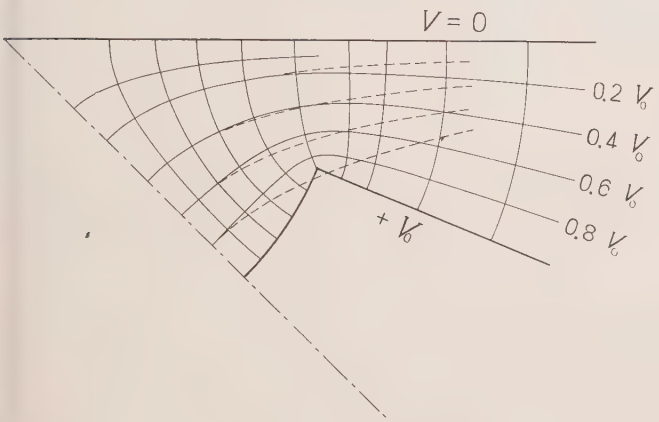

Fig. 3. Equipotential lines and lines of force for the quadrupole magnet, the α-value of which is taken as 22.5°.

Finding the values of $t = \xi + i\eta$ satisfying eq. (10) for a given value of V/V_0 and substituting them into eq. (7), the z-values on an equipotential line for the V/V_0 value are obtained.

The results for the quadrupole and sextupole magnets are shown in figs. 3 and 4 respectively for the case of

$$\alpha \Big/ \frac{\pi}{2N} = \tfrac{1}{2} .$$

The broken curves in the figures which are drawn for comparison show the ideal cases in which the r^{N-1} proportionality holds rigorously up to the pole piece surfaces.

3.2. LINES OF FORCE

The value of U is constant on the line of force. Eliminating V in eq. (9), we obtain

$$\eta^2 \sinh^2 \frac{\pi}{V_0} U = -\left(\xi \sinh \frac{\pi}{V_0} U - \cosh \frac{\pi}{V_0} U\right)^2 + 1 . \qquad (11)$$

Finding the values of $t = \xi + i\eta$ satisfying eq. (11) for a given value of U/V_0 and substituting them into eq. (7), the z-values on a line of force for the U/V_0 value are obtained. The results for the quadrupole and sextupole magnets are also shown in figs. 3 and 4 respectively for

$$\alpha \Big/ \frac{\pi}{2N} = \tfrac{1}{2} .$$

3.3. FIELD STRENGTH

As $W = U + iV$ is the complex potential, we get

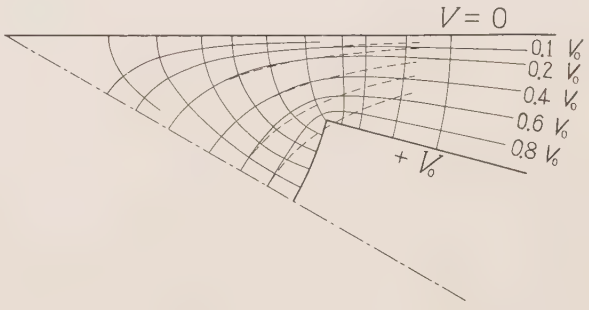

Fig. 4. Equipotential lines and lines of force for the sextupole magnet, the α-value of which is taken as 15°.

$$-\frac{dW}{dz} = H_y + i H_x . \qquad (12)$$

Substituting eqs. (8) and (7) into W and z respectively, the following relation is obtained:

$$H_y + iH_x = -\frac{H_0 a}{(z/r_0)\,(t^2 - a^2)^{\frac{1}{2}}} , \qquad (13)$$

or

$$H^2 = \frac{H_0^2 a^2}{(r/r_0)^2\,[(t^2 - a^2)\,(t^{*2} - a^2)]^{\frac{1}{2}}} . \qquad (13')$$

where t^* is the complex conjugate of t and H_0 is the value of H at $r = r_0$, namely

$$H_0 = 2NV_0/\pi r_0 a . \qquad (14)$$

As the examples, the values of H along the straight lines $\theta = 0$, $\theta = \alpha$ and $\theta = \pi/2N$ in the z-plane are plotted in figs. 5 and 6 for the cases of the quadrupole and sextupole magnets of $\alpha/\frac{\pi}{2N} = \frac{1}{2}$ respectively. It is seen from the figures that the deviations from the r^{N-1} proportionality are negligible for $r < 0.6\, r_0$ in both cases.

3.4. MAGNETIC FLUX PASSING THROUGH THE SURFACE OF POLE PIECE

The magnetic flux ϕ passing through the surface of pole piece is given as

$$\phi = \int [\boldsymbol{H}\cdot \mathrm{d}\boldsymbol{s}] = \int (H_x \,\mathrm{d}y - H_y \,\mathrm{d}x) .$$

Since

$$H_x = -\frac{\partial V}{\partial x} = +\frac{\partial U}{\partial y}, \qquad H_y = -\frac{\partial V}{\partial y} = -\frac{\partial U}{\partial x},$$

ϕ becomes

$$\phi = \int \mathrm{d}U . \tag{15}$$

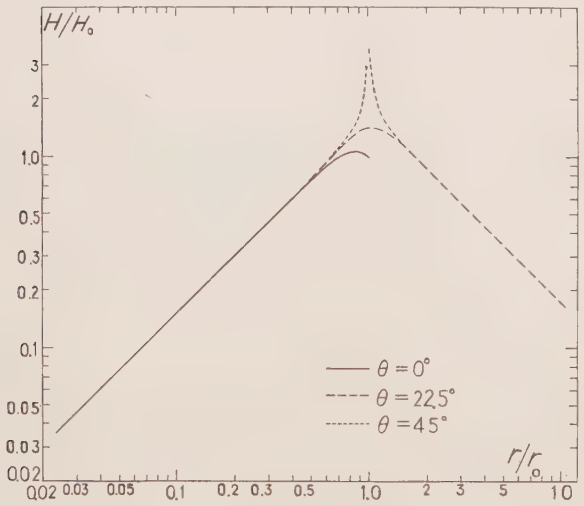

Fig. 5. Field strengths for the quadrupole magnet of fig. 3 along the straight lines $\theta = 0°$, 22.5° and 45°.

Substituting eq. (8), we obtain

$$\phi = \frac{4V_0}{\pi} \tanh^{-1} \xi_B = \frac{2H_0 r_0 a}{N} \tanh^{-1} \xi_B , \tag{16}$$

taking into account the fact that t is real on the surface of pole piece. ξ_B is the value of ξ at the point separating the pole piece and the permanent magnet. The total magnetic flux passing through the front face of the permanent magnet can be calculated by eq. (16). From this value and the residual flux density at the operating point on the demagnetization curve, we can obtain the width of permanent magnet and the length of pole piece required to produce the desired field.

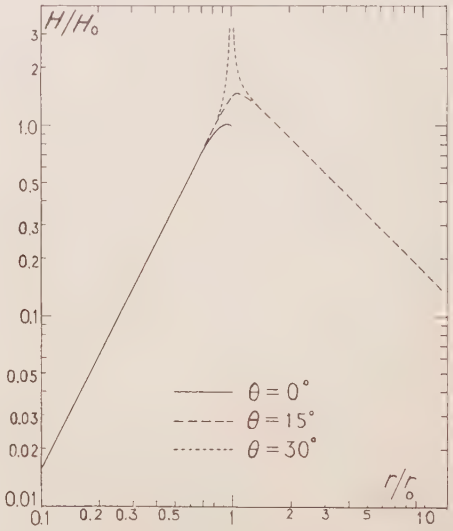

Fig. 6. Field strengths for the sextupole magnet of fig. 4 along the straight lines $\theta = 0°$, 15° and 30°.

3.5. MAGNETOMOTIVE FORCE

The necessary magnetomotive force is given from eq. (14) as

$$2V_0 = \pi H_0 r_0 a / N . \tag{17}$$

NUCLEAR INSTRUMENTS AND METHODS 12 (1961) 353–354; NORTH-HOLLAND PUBLISHING CO.

FINITE GEOMETRY CORRECTIONS FOR ANGULAR CORRELATION MEASUREMENTS

D. J. ROWE, G. L. SALMON and A. B. CLEGG

Clarendon Laboratory, Oxford

Received 13 April 1961

A method is presented for calculating the smearing effect of counters of finite angular resolution, on angular correlation functions with azimuthal angle dependence.

1. Introduction

In angular correlation measurements it is often necessary to work in poor geometry, with large counters, to obtain a sufficiently high counting rate; the result being that the measured angular correlation is a smeared-out version of the actual correlation.

For angular correlations of the form

$$W(\theta) = \sum_l a_l P_l(\cos\theta) \qquad (1)$$

various methods have been developed for making these corrections. In particular Rose[1]) has shown how the integrals involved may be evaluated analytically for counters of circular symmetry. In this note we extend the work of Rose to deal with more general angular correlations of the form

$$W(\theta, \phi) = \sum_{l,m} a_{lm} Y_{lm}(\theta, \phi) \,. \qquad (2)$$

Such angular correlations arise between gamma-ray and proton in the inelastic scattering of protons of 100–200 MeV, due to the complicated spin dependence of the nucleon-nucleon interaction[2]). In our studies of such angular correlations we have developed methods corresponding to those of Rose and publish them as they may also be of use in other similar cases, where polarization is involved.

It should be noted that the angles in eq. (2) are the angular coordinates of the gamma-ray with respect to the direction of the vector $K_i - K_f$, and the azimuthal angle ϕ is zero in the direction of the vector $K_i \wedge K_f$. In this way we follow Satchler and Clegg[2]) and use the notation of Kerman *et al.*[3]). This polar axis is identified with the recoil axis of the nucleus in the inelastic scattering of the proton and is determined by two body kinematics.

2. Calculation

For each point OP′ of a finite size proton counter there is a corresponding recoil direction OR′ with respect to which the gamma-ray angular distribution is given by $W(\theta', \phi')$. We now have to integrate over the finite solid angles subtended by both the proton counter and by the gamma-ray counter.

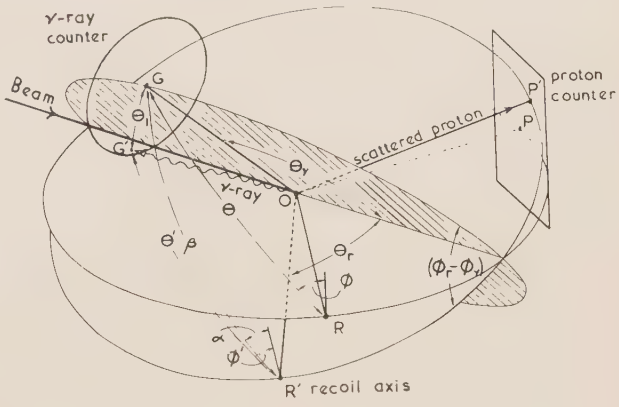

Fig. 1. Geometry for (p,p′γ) scattering.

If the centre of the gamma-ray counter has coordinates (θ, ϕ) with respect to the recoil direction OR, corresponding to protons going through the

[1]) M. E. Rose, Phys. Rev. **91** (1953) 610.
[2]) G. R. Satchler and A. B. Clegg, To be published (1961).
[3]) A. K. Kerman, H. McManus and R. M. Thaler, Annals of Physics **8** (1959) 551.

centre of the proton counter OP, the measured angular distribution for gamma rays will be

$$\overline{W}(\theta, \phi) = \frac{\int_{\Omega_1} \int_{\Omega_2} W(\theta', \phi') C_1 \, d\Omega_1 C_2 \sigma_2 \, d\Omega_2}{\int_{\Omega_1} C_1 \, d\Omega_1 \int_{\Omega_2} C_2 \sigma_2 \, d\Omega_2} \quad (3)$$

the integration being over the angles subtended at the target. $C_1 \, d\Omega_1$ is the interaction probability for a gamma-ray entering the element of solid angle $d\Omega_1$ of the gamma counter. $C_2 \, d\Omega_2$ is similarly defined for the proton counter and σ_2 is the differential cross section for the inelastic scattering.

We consider first the integration over the gamma-ray counter:

$$\int_{\Omega_1} W(\theta', \phi') C_1 \, d\Omega_1 = \sum_{l,m} a_{lm} \int_{\Omega_1} Y_{lm}(\theta', \phi') C_1 \, d\Omega_1 . \quad (4)$$

We now express $Y_{lm}(\theta', \phi')$ as a sum of spherical harmonics about the central axis of the gamma-ray counter OG using the rotation matrix[4]).

$$Y_{lm}(\theta' \phi') = \sum_{n=-l}^{+l} D^l_{nm}(\alpha, \beta, \gamma) Y_{ln}(\theta_1, \phi_1) \quad (5)$$

where (θ_1, ϕ_1) are the coordinates with respect to the gamma-ray counter axis of a direction (θ', ϕ'), i.e. OG', and (α, β, γ) are the Euler angles of the rotation which rotates the recoil axis OR' into the gamma-ray counter axis OG. So

$$\int_{\Omega_1} W(\theta' \phi') C_1 \, d\Omega_1 = \sum_{l,m,n} a_{lm} D^l_{nm}(\alpha \beta \gamma) \int_{\Omega_1} Y_{ln}(\theta_1 \phi_1) C_1 \, d\Omega_1 . \quad (6)$$

As the gamma-ray counter has cylindrical symmetry about its central axis, terms involving $n \neq 0$ vanish on integrating and

$$\int_{\Omega_1} W(\theta' \phi') C_1 \, d\Omega_1 = \sum_{l,m} a_{lm} D^l_{0m}(\alpha \ \beta \ \gamma) \int_{\Omega_1} Y_{l0}(\theta_1 \phi_1) C_1 \, d\Omega_1 = \sum_{l,m} a_{lm} Y_{lm}(\beta, \alpha) \int_{\Omega_1} P_l(\cos\theta_1) C_1 \, d\Omega_1 . \quad (7)$$

Then if we write:

$$J_l = \int_{\Omega_1} P_l(\cos\theta_1) \, C_1 \, d\Omega_1 \quad (8)$$

we have

$$\overline{W}(\theta, \phi) = \sum_{l,m} a_{l,m} \frac{J_l}{J_0} \frac{\int_{\Omega_2} Y_{lm}(\beta, \alpha) C_2 \sigma_2 \, d\Omega_2}{\int C_2 \sigma_2 \, d\Omega_2} . \quad (9)$$

In general it will be difficult to evaluate this integral analytically due to absence of circular symmetry, and a numerical method must be employed[5]).

It remains to give formulae for the Euler angles α and β, γ refers to a rotation about the axis of symmetry of the gamma-ray counter and so disappears on integrating. If the central axis of the gamma-ray counter, OG, lies along the direction $(\theta_\gamma, \phi_\gamma)$, where we now measure all angles with respect to the incident proton beam, then corresponding to a recoil direction OR', given by (θ_r, ϕ_r), we have

$$\cos\beta = \sin\theta_\gamma \sin\theta_r \cos(\phi_r - \phi_\gamma) + \cos\theta_\gamma \cos\theta_r \quad (10)$$

$$\sin\alpha = \frac{1}{\sin\beta} [\sin\theta_\gamma \cos\theta_r \cos(\phi_r - \phi_\gamma) - \cos\theta_\gamma \sin\theta_r] . \quad (11)$$

[4]) M. E. Rose, Elementary Theory of Angular Momentum (J. Wiley and Sons, New York) Ch. IV.

[5]) In our experiment the integral in eq. (9) was performed numerically using the Ferranti Mercury computer of the Oxford Computer Laboratory.

Acknowledgements

We wish to thank D. M. Brink for helpful discussion.

NUCLEAR INSTRUMENTS AND METHODS 12 (1961) 355–361; NORTH-HOLLAND PUBLISHING CO.

A NEUTRON TIME-OF-FLIGHT SPECTROMETER WITH A SEMI-MONOCHROMATIZING CHOPPER

S. HOLMRYD, K. E. LARSSON and K. OTNES

AB Atomenergi, Reactor Development Division, Stockholm

Received 8 April 1961

A new type of slow chopper intended for use in neutron inelastic scattering measurements has been constructed, which has a transmission curve much narrower than what is usual for slow choppers. This chopper is operated in conjunction with a beryllium filter to give a transmitted neutron spectrum of a half value width of ≈ 0.3 Å at 4 Å which is a considerable improvement over the usual width of the cold neutron spectrum of more than 1 Å. The time resolution of the new instrument corresponds to 12 μsec/meter. A full description is given of the construction and operation of the instrument.

1. Introduction

During the past five years a considerable effort has been devoted to the problem of producing a monochromatic neutron beam from the mixed reactor neutron spectrum. Neutron spectroscopists have tried to construct instruments able to work with good resolution in the thermal region, the main reason for this new-born interest in the thermal neutron flux being the newly discovered possibilities to use slow neutrons in the investigation of the detailed nuclear motions in many-body systems like solids and liquids. Unfortunately these systems are both expensive and requiring a high flux (10^{14} neutrons/cm^2 sec). In investigations of this kind, where the inelastic scattering process is the useful one, the experimental problem concerned with the neutron spectrometer is two-fold: a. to produce a monochromatic neutron beam b. to analyze the energy of the scattered neutrons as a function of scattering angle. The most general solutions of these problems involves the construction of a monochromator able to cut out a narrow wave length band from the Maxwellian spectrum at any arbitrary position in a wave length range from about 0.5 Å. Rather elaborate systems of several phased rotors or large crystal spectrometer arrangements will meet these requirements.

In this paper we will deal with a system intended to work in the very low energy neutron region only ($\lambda > 4$ Å) and which may be used with a somewhat lower flux (the equivalent of 10^{13} n/cm^2 sec will be satisfactory). The system simply consists of a new type of slow chopper which may preferably be operated in conjunction with a filter like a beryllium, berylliumoxide filter etc. This apparatus will be described and examples of its operational data given.

2. Principle of the New Spectrometer

A whole class of neutron spectrometers work on the principle to produce short bursts of more or less monochromatized neutrons which after being scattered at the sample are energy analyzed by the time-of-flight technique. Another class uses a device like a slow chopper merely to produce a pulsed beam of the neutrons already scattered at the sample. In this latter case the neutrons might have been monochromatized by crystal diffraction technique, by filter technique etc. This second class of instruments have been described in great detail in an earlier article[1]). While that second class of instruments is supposed to consist of *two* parts, the monochromator and the beam pulsing device, the first group just mentioned combines the actions of monochromatization and pulsing in *one* device.

The principle of the instrument is very simple as illustrated in fig. 1. A filter is used in a reactor beam hole to scatter out all neutrons except those which fall below a certain Bragg cutoff, like the well-known at 3.95 Å in beryllium. The transmitted cold

[1]) K. E. Larsson, U. Dahlborg, S. Holmryd, K. Otnes and R. Stedman, Ark. Fys. **16** (1959) 199.

neutron spectrum is in general rather broad which is of great disadvantage in cases where *small* energy transfers are to be investigated in inelastic scattering processes. However, as was shown theoretically as well as experimentally in the earlier work (*loc. cit.*), the transmission curve, $T(\omega\lambda)$, of a chopper is a

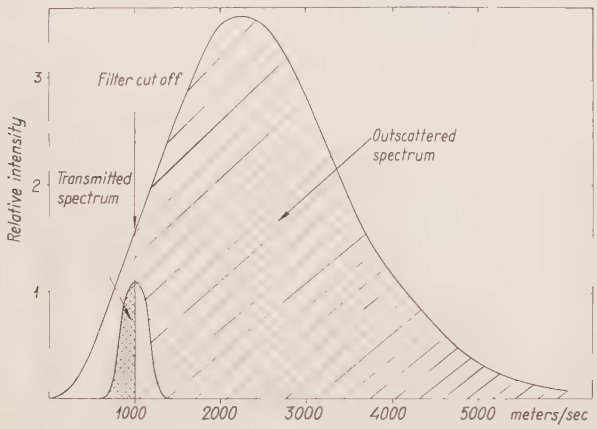

Fig. 1. Principle of the combined action of filter and chopper.

gaussian-like curve. If a chopper could be constructed, which had both a reasonably high transmission and narrow width of its transmission curve, it would be possible to operate the chopper at such a speed that exactly half of its transmission curve fell in the region where the filter had scattered all neutrons out of the beam (fig. 1). The width of the spectrum transmitted by the chopper would then be exactly half of the full width of the transmission curve, $T(\omega\lambda)$. There is a great gain in intensity by doing this compromise instead of making a chopper with a smaller value of its full width, because if the width of the transmission curve is decreased to very small values, the maximum transmission drops quickly to impractible values.

The constructional arguments for a chopper meeting the requirements outlined above follows from the formulas and discussion given in the reference. As was shown in that work, the transmission curve for a chopper with curved slits is

$$T(R) = \begin{cases} \dfrac{d}{2\pi r}\left(1 - \dfrac{1}{6}\dfrac{r^4}{d^2R^2}\right) & \text{if } \infty \geqslant R \geqslant \dfrac{r^2}{d} \\ \dfrac{d}{2\pi r}\left(\dfrac{8}{3}\dfrac{r}{\sqrt{Rd}} - 2\dfrac{r^2}{Rd} + \dfrac{1}{6}\dfrac{r^4}{d^2R^2}\right) & \text{if } \dfrac{r^2}{d} \geqslant R \geqslant \dfrac{r^2}{4d}. \end{cases} \tag{1}$$

In this equation $2d$ = slit width of the chopper
r = radius of the slit

$$R = \frac{h}{2m\omega\,|\,\lambda - \lambda_0\,|} \tag{2}$$

where

h, m = Planck's constant and the mass of the neutron;

ω = angular velocity of the chopper;

λ_0 = neutron wave length, which is fully transmitted with a transmission of $d/2\pi r$, if the chopper speed is defined by ω (top of transmission curve).

λ = arbitrary neutron wave length.

The maximum value of the transmission is given by

$$T_{\max} = \frac{d}{2\pi r}. \tag{3}$$

It is easy to see that the half-value of $T(R)$ occurs in the region of the second of the equations (1). Putting this expression equal to $\frac{1}{2}T_{\max}$ gives for R a value of $0.542\, r^2/d$ which according to (2) determines a value for the half value width

$$\Delta\lambda_A = \frac{h}{2m}\frac{d}{0.542r^2}\frac{1}{\omega} = 3.65 \times 10^5 \frac{d}{r^2\omega}. \tag{4}$$

From the reference it is also clear that the radius of curvature, R_0, of a central slit is

$$R_0 = \frac{v_0}{2\omega} = \frac{h}{2m\lambda_0\omega} \tag{5}$$

where v_0 = neutron velocity corresponding to λ_0. Combining (4) and (5) gives for the wavelength resolution

$$\frac{\Delta\lambda}{\lambda_0} = \frac{R_0 d}{0.542r^2}. \tag{6}$$

It is to be noticed that $\omega\lambda_0$ is a constant for a chopper (eq. (5)). Also it is observed from (6) that the wave length resolution, $\Delta\lambda/\lambda$, of the chopper seen as a *monochromator* is independent of the chopper speed. This is to be compared with the time resolution, $\delta t/t$, which is equivalent to a wave length resolution $\delta\lambda/\lambda$, for the chopper used as a neutron energy *analyzer* with a flight path of length l, which is (compare the reference)

$$\frac{\delta\lambda}{\lambda} = \frac{\delta t}{t} = c\frac{dv}{r\omega l} \tag{7}$$

with $c \approx 2$ for optimum working conditions. In this case the resolution is dependent on the chopper speed, which is easily understood from the fact that the chopper burst length is $d/r\omega$ for an infinitely well collimated neutron beam, where d/r is the chopper opening angle.

The chopper we are going to consider will have to work both as a neutron monochromator and as an energy analyzer by virtue of its pulsing action. Equation (6) describes its merits as a monochromator and eq. (7) its properties as analyzer. According to the eqs. (6) and (7) it is highly desirable that d/r is a small number as $\Delta\lambda/\lambda$ and $\delta t/t$ are to be small for a high resolution instrument. However, to make the instrument useful in practice it has to have a high transmission defined by (3). This implies that d/r should be as large as possible. A relatively large value of d/r could be accepted, if the rotational speed ω were large, because the $\delta t/t$ may still be kept small according to (7). Also considering a constant wave length λ_0 it is obvious that the radius of curvature R_0 may be made smaller, if ω were large leading to a smaller value of $\Delta\lambda/\lambda_0$ according to (6). This just stresses the standard condition for good rotors: their speed should be as high as possible. If, however, serious mechanical difficulties are to be avoided the peripheral speed must be kept within reasonable limits. Speeds, ωr, below 200 m/s are allowable for many materials. Also the rotational speed must not be too high, if neutrons transmitted in two successive bursts should not overlap. These questions were discussed in chapter V of the reference. On the whole the new chopper-time-of-flight spectrometer should be operated similarly to the chopper described in chapter VI of the reference, the only exception being that the chopper should be placed between the filter and the sample instead of after the sample.

3. Construction and Operation of the Chopper

The main conditions describing the desirable properties of the rotor are given by eqs. (3), (5), (6) and (7). With the knowledge that a chopper already in operation at the Swedish heavy water reactor, R1, flux 10^{12} n/cm^2 sec, with a value of d/r of 0.04 and using the full cold neutron spectrum as the "monochromatic" beam may be successfully used in cold neutron spectroscopy, it was decided that a decrease in d/r by a factor of 4 is allowable. Thus $2d$ was chosen as 0.350 cm and $r = 15$ cm, i.e. $d/r = 0.0117$. The relatively large radius dictated ω to be about 1000 radians/sec as a maximum, i.e. the peripheral speed is limited to 150 m/s. As the chopper was intended to work in conjunction with a beryllium filter ($\lambda_0 = 3.952$ Å), it was decided that $\omega\lambda_0$ should have the value of 4000 i.e. $\omega = 1000$ rad/sec at $\lambda_0 = 4$ Å. With these values of λ_0 and ω one obtains for the radius of curvature of the slits a value of 50 cm, which is also reasonable with respect to the chopper radius. The wave length resolution of this chopper seen as a monochromator is only $\Delta\lambda/\lambda_0 = 0.3/4 = 7.5\%$, this value being, however, a considerable improvement over the complete cold spectrum, for which $\Delta\lambda/\lambda \approx 30\%$. The resolution, $\delta t/t$, of the chopper as the heart of the neutron time-of-flight analyzer is as good as 0.5% at 4 Å, when the flight path is chosen to be 450 cm and when the time-of-flight analyzer is supposed to work under optimum conditions according to eq. (7) with $c = 2$. The chopper burst time alone, i.e. for an infinitely well collimated beam is 12 μsec for $\omega = 1000$. To increase the transmitted intensity of the chopper the area of the slits have to be as large possible. Each slit was chosen 8 cm high and 0.350 cm wide. The number of slits is eight. The calculated full transmission curve of the chopper is given in fig. 2.

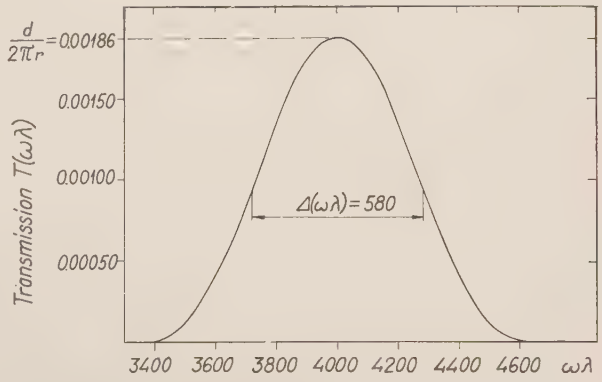

Fig. 2. Predicted full transmission curve for the chopper described in the text.

The actual construction of the chopper is shown in fig. 3. The central part (H) is made of steel as well as a surrounding shell (L) with large portions

cut away to decrease the centrifugal forces. The slits are defined by 2 mm steel plates coated with 0.05 mm cadmium on both sides. Both sides (J) of the central part, the slit system, are filled with boron carbide mixed into araldite wax to form a strong neutron absorber making the chopper black for thermal neutrons in any direction except through the slits. Around the periphery an aluminium ring (K) closes the system to make its air resistance small. The rotor is carried by a heavy axle carried by ball bearings, such that the chopper may be operated with its axis horizontal or vertical. The whole system is surrounded by a steel shield (G) also serving as a fore-vacuum housing. The gaskets consist of O-rings (D) or of a graphite ring (C). The rotor is driven by a simple d.c. 1 kW motor (A). The rotor and motor are connected with a simple rubber coupling (B). With this equipment the rotor is easily rotated at ≈ 10000 rpm or $\omega = 1000$ rad/sec. No speed control is associated with the driving motor. It is found that at $\omega = 1000$ the speed of the rotor stays constant within 0.5%

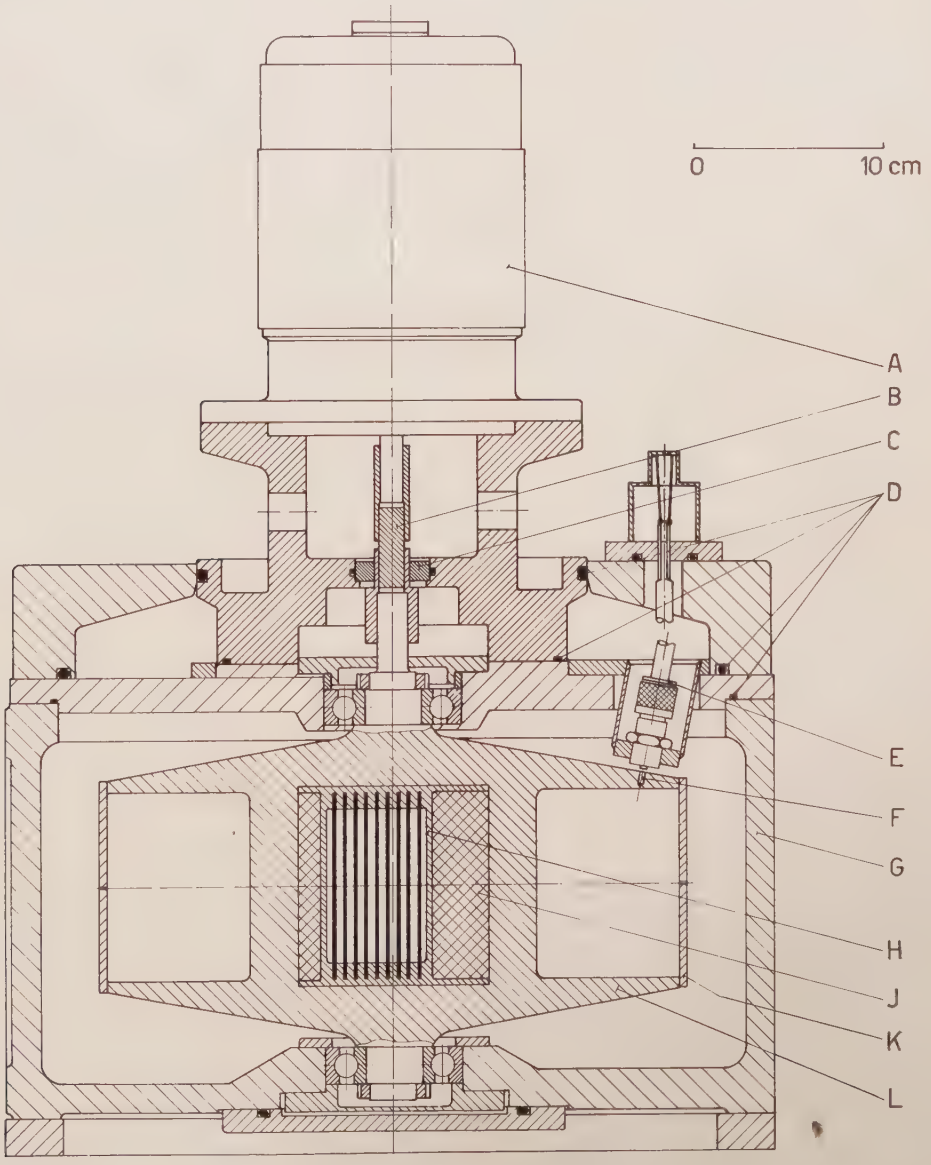

Fig. 3. Chopper construction.

which means that $\Delta\lambda$ is increased by no more than 7% because of variation in chopper speed. This follows from the displacement, $\delta\lambda_0$, at λ_0 of 0.5%, which at 4 Å is 0.02 Å, and when $\Delta\lambda = 0.3$ Å the percentage increase or decrease of $\Delta\lambda$ is $0.02/0.3 = 6.7\%$. For critical work an automatic speed control has to be used. Finally it should be mentioned that an electromagnetic pickup (E) is used to give the start signal to the multi-channel time analyzer. This pick-up is fixed to the chopper housing, but is adjustable in position and is looking at the chopper periphery where a brass plug (F) is screwed into the steel frame of the rotor.

4. Experimental Test of the New Spectrometer

To perform a test of the two chopper actions, monochromatization and energy analysis, the chopper was mounted with its axis vertical in front of one of the experimental channels of the reactor R1. In the channel a 30 cm thick beryllium filter cooled to liquid nitrogen temperature was producing the well-known sharp edge spectrum. A battery of 41 $B^{10}F_3$ counters coupled in parallel making a compounded detector with an area of 20×20 cm^2 and with a thickness of about 4 cm was used at a distance, l, of 450 cm from the chopper axis to detect the transmitted neutron bursts. The efficiency of the detector was 60% at 4 Å. The smallest angular opening of the arrangement was the reactor channel collimator with an effective opening of about 0.03 radians or 1.7^0. We remember that the chopper opening angle is $d/r = 0.0117$ radians or 0.67^0, which means that the angular part of the time resolution of the system chopper-collimator is completely determined by the collimator.

Using a 100 channel time analyzer with a channel width of 20 μsec the transmitted spectra were recorded as a function of chopper speed. Fig. 4 gives an example of the results obtained when the chopper was operated at a speed corresponding to $\lambda_0 \approx 3.95$ Å and another speed corresponding to $\lambda_0 = 5.6$ Å. To make the comparison of these two results more meaningful the cold neutron spectrum reaching the chopper is also shown. The sharp edges at $\lambda = 4.04$ Å and 4.67 Å correspond to the neutrons being scattered out of the beam by aluminium, 2.5 cm thick, and iron, 1.5 mm thick, making part of the reactor, the channel and the experimental plug containing the filter. First concentrating on the monochromatizing action, a width, $\Delta\lambda$, of 0.31 Å was observed compared to the calculated value of 0.29 Å at $\lambda_0 = 4$ Å. The full width, $2\Delta\lambda$, observed at $\lambda_0 = 5.6$ Å is 0.88 Å while the calculated width is 0.81 Å. The small discrepancies of about 8% between the calculated and observed values very probably depend on a small transmission of neutrons at the edge of the slits. This would decrease r which will increase $\Delta\lambda$. The average radius i.e. the length of the slits is also somewhat smaller than 15 cm because of the curvature of the chopper periphery. Also any variation of the chopper speed will increase the width. The main effect is, however, obtained, the transmitted spectrum being considerably narrower than the full cold neutron spectrum.

To demonstrate the quality of the second function of the spectrometer the details of a run at $\lambda_0 = 3.95$ Å is shown in fig. 5. As discussed elsewhere the observed width of the beryllium cutoff at 3.952 Å directly gives the resolution $\delta t/t$ (eq. (7)). As will be seen from the figure the observed resolution width, δt, is 53 μsec at a total neutron flight time of 4490 μsec (3.952 Å), which gives $\delta t/t = \delta\lambda/\lambda = 1.2\%$ or 12 μs/m. Theoreticly the resolution is calculated from a knowledge of the three factors: The first factor δt_ω, which in this case is the collimation angle, 0.03 radians divided by $\omega = 1000$ radians/sec which gives $\delta t_\omega = 30$ μsec. This is the chopper sweep time over the collimator opening. The second factor, δt_d, which is the time uncertainty caused by the maximum neutron flight time through the detector, which with a detector thickness of 4 cm and a neutron velocity of 1000 m/s gives $\delta t_d = 40$ μsec. The third factor is the electronic channel width $\delta t_e = 20$ μsec. It is to be noted, that the chopper's burst time which in this case is 12 μsec does not contribute because the collimator angular opening is larger than the chopper angular opening (compare eq. (15) of the reference). The calculated resolution is $\delta t = \sqrt{(\delta t_\omega^2 + \delta t_e^2 + \delta t_d^2)} = 54$ μsec in very good agreement with the observed value of 53 μsec.

The discussion of the resolution clearly shows the

dominant role played by the detector. The collimation angle is easily decreased to the optimal value of d/r or 0.67^0 to give the ideal value of $12\sqrt{2}$ instead of 30 μsec for δt_ω. The electronic channel width might be chosen to be very near the ideal where the beam chopping device is placed before the sample.

The third factor of practical importance is the experimentally found transmission. In fig. 4 the experimentally found transmission curves at $\lambda_0 = 4$

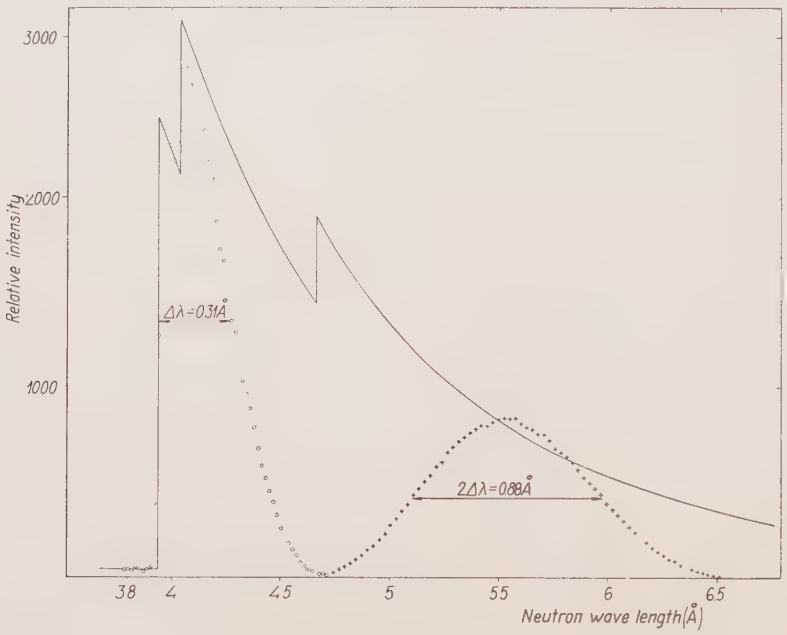

Fig. 4. Transmitted spectra at $\lambda_0 = 4$ Å and 5.6 Å. The cold neutron spectrum is arbitrarily normalized to the 4 Å run.

12 μsec. The neutron flight time through the detector should then also be 12 μsec which would mean in this particular case a detector thickness not exceeding 1.2 cm. Such a detector would not be efficient enough.

In the final use with a sample placed about 50 cm from the chopper centre and a spectrometer arm carrying the detector being rotated round the sample position, there will be an additional time-of-flight uncertainty as the chopper burst widens with time. The flight time for 4 Å neutrons ($v = 10^5$ cm/sec) over a distance of 50 cm is 500 μsec. The corresponding time for 4.3 Å neutrons is 538 μsec ($v = 0.93 \times 10^5$ cm/sec). There is thus a new term of 38 μsec to be added to the resolution width of 53 μsec (giving $\delta t = 65$ μsec). Also there might be additional uncertainties added, if the sample is not of very small dimensions. No general rule can be given, but care has to be exercised in analyzing data using a pulsed neutron spectrometer of the class, and 5.6 Å are given with their observed relative intensities. The cold neutron spectrum given is arbitrarily normalized to the 4 Å run. As expected the

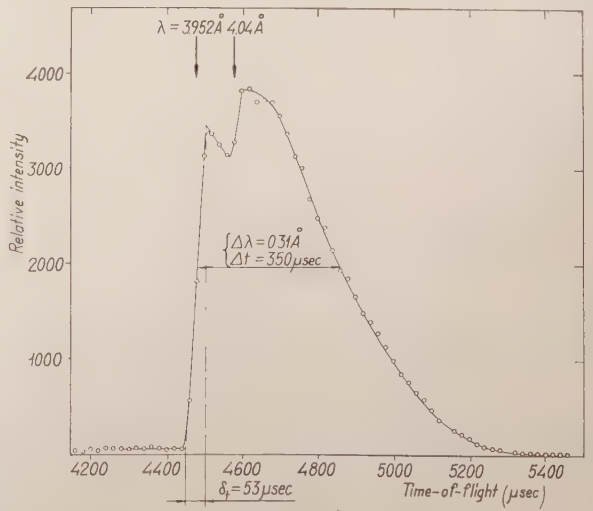

Fig. 5. Transmitted spectrum at $\lambda_0 = 3.95$ Å showing the time resolution and spectrum width.

relative transmitted intensities are determined by the intensity in the cold neutron spectrum, which disregarding the disturbing Bragg cutoff at 4.04 and 4.67 Å very nearly is given by $f(\lambda)\,\mathrm{d}\lambda \approx \mathrm{d}\lambda/\lambda^5$. Assuming the spectrum form without the breaks at 4.04 and 4.67 Å it is easy to calculate the chopper's

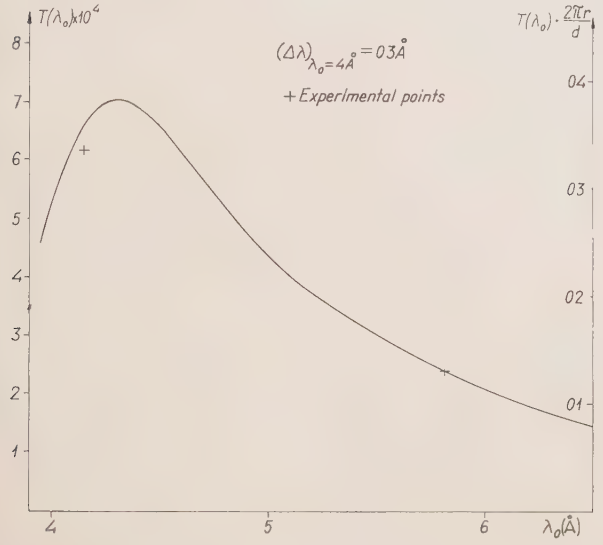

Fig. 6. Calculated chopper transmission as a function of λ_0. Given are also experimental values at $\lambda_0 = 4.15$ and 5.8 Å.

relative transmission round the wave length λ_0 from

$$T(\lambda_0) = \int_4^\infty f(\lambda) T(|\lambda - \lambda_0|)\,\mathrm{d}\lambda = \int_4^\infty \left(\frac{4}{\lambda}\right)^5 T(|\lambda - \lambda_0|)\,\mathrm{d}\lambda \tag{8}$$

where $\int_4^\infty f(\lambda)\,\mathrm{d}\lambda$ is normalized to 1.

This expression gives the percentage of cold neutrons transmitted. Over the most interesting wave length region from 4 to 6 Å this transmitted percentage is very small—about 0.055% of the total cold neutron intensity being transmitted. A more interesting figure is another one, which facilitates comparison with other choppers used in similar spectrometer arrangements. As the chopper burst time is a fraction of $d/2\pi r$ of the time for a full revolution, the fraction of cold neutrons transmitted *per burst* is $T(\lambda_0).2\pi r/d$. Multiplying $T(\lambda_0) \simeq 0.55 \times 10^{-3}$ with the number $2\pi r/d = 540$ gives for the fraction of the cold neutron spectrum transmitted per burst the figure 30%. Fig. 6 gives $T(\lambda_0)$ (ordinate to the left) as well as $T(\lambda_0)2\pi r/d$ (ordinate to the right). Experimental points at 4.15 and 5.8 Å (corrected for Bragg reflections) are also given. The neutron intensity transmitted by this chopper may now be compared with that for the chopper described in the reference for which $d/r = 0.042$. If it is assumed that the angular collimation is good and the same in both cases—much better than the smaller d/r — value — the ratio of the intensities transmitted by the new and the old instruments is about $0.3 \cdot 0.0117/0.042 \approx 8\%$. The prize that has been paid for the gain in the time resolution, $\delta t/t$, of a factor of 3 to 4 and a gain in wave length resolution, $\Delta\lambda/\lambda$, as defined above, of a factor of 3 to 4 is a loss of intensity of at least a factor of 12. These figures have been verified experimentally.

In conclusion one might say that in combination with a reactor delivering a flux about 5×10^{12} n/cm^2 sec at the reactor tank wall—equivalent to the bottom of the experimental channel—the new chopper is a cheap and simple monochromator and analyzer able to solve several problems connected with the research on slow neutron inelastic scattering. In conjunction with cold moderator facilities like liquid hydrogen, which will increase the cold neutron flux by a factor of ten, it will be of practical usefulness even with fluxes as moderate as 10^{12} or somewhat less.

NUCLEAR INSTRUMENTS AND METHODS **12** (1961) 362; NORTH-HOLLAND PUBLISHING CO.

LETTERS TO EDITOR

TOTAL CONVERSION COEFFICIENTS WITH A SUM-COINCIDENCE NaI SPECTROMETER†

J. C. VANDERLEEDEN and M. K. RAMASWAMY

Dept. of Physics, Ohio State University, Columbus, Ohio

Received 24 March 1961

The use of the summing technique for gamma-rays detected in a single NaI spectrometer has proved to be valuable in determining coincidence relationships. In cases where electron-capture occurs, it has been possible to determine the decay energy with reasonable accuracy[1]).

It is the purpose of this note to point out that in certain cases one can determine total conversion coefficients (α) of gamma-rays using the sum-coincidence technique. Consider the decay scheme in which γ_1 is followed by γ_2. Let us assume that all the decay occurs to the second level. Then if we measure the gamma-ray spectrum in a NaI counter employing close geometry, we will observe in addition to γ_1 and γ_2, the sum-coincidence peak at $\gamma_1 + \gamma_2$. If N_0 denotes the number of transitions proceeding to the second level, ε the gamma-ray detection efficiency and S the solid angle subtended by the crystal we can write

$$N_{\gamma 1} = N_0 \, \varepsilon_{\gamma 1} \, S \left(\frac{1}{1 + \alpha_1}\right) \tag{1}$$

$$N_{\gamma 2} = N_0 \, \varepsilon_{\gamma 2} \, S \left(\frac{1}{1 + \alpha_2}\right) \tag{2}$$

and

$$N_{\gamma 1+\gamma 2} = N_0 \, \varepsilon_{\gamma 1} \varepsilon_{\gamma 2} S^2 \left(\frac{1}{1 + \alpha_1}\right)\left(\frac{1}{1 + \alpha_2}\right) \int_S W(\theta) \, \mathrm{d}\theta \, . \tag{3}$$

† Supported by the U.S. Atomic Energy Commission.

Dividing (3) by (1) we obtain,

$$\frac{N_{\gamma 1+\gamma 2}}{N_{\gamma 1}} = \frac{\varepsilon_{\gamma 2} S}{(1 + \alpha_2)} \int_S W(\theta) \, \mathrm{d}\theta \quad \text{or}$$

$$\alpha_2 = \frac{N_{\gamma 1}}{N_{\gamma 1+\gamma 2}} \varepsilon_{\gamma 2} S \int_S W(\theta) \, \mathrm{d}\theta - 1 \, ;$$

a similar relation exists for α_1. Thus, if the efficiency and the solid angle of the counter, and $W(\theta)$ are known, we can compute the total conversion coefficient of either gamma-ray. Further, since the summing effect persists for relatively small solid angles, S can be computed rather accurately.

The method is applicable only when the lifetime of the intermediate level is shorter than the decay time of the scintillator employed, and is of advantage when the X-rays are obscured in Compton scattering.

We have computed α for the 79 keV transition in coincidence with the 358 keV gamma-ray in the decay of Ba^{133}, using the data of Ramaswamy, Skeel and Jastram[1,2]). The computed value of 1.9 is in reasonable agreement with the observed value for a predominantly M1 transition, and is also consistent with the value of 1.8 found by Bergström[3]) who used a magnetic spectrometer.

[1]) See for instance: M. K. Ramaswamy, W. L. Skeel and P. S. Jastram, Nucl. Phys. **19** (1960) 299.

[2]) M. K. Ramaswamy, W. L. Skeel and P. S. Jastram, Nucl. Phys. **16** (1960) 619.

[3]) I. Bergström, Arkiv Fysik **5** (1952) 191.

NUCLEAR INSTRUMENTS AND METHODS **12** (1961) 363–364; NORTH-HOLLAND PUBLISHING CO.

EXTRACTION OF A BEAM AND ENERGY REGULATION IN THE CYCLOTRON WITH AZIMUTHALLY VARYING MAGNETIC FIELD

A. A. ARZUMANOV, R. A. METSHCHEROV, E. S. MIRONOV,
L. M. NEMENOV, S. N. RIBIN and J. A. KHOLMOVSKIJ

Kurchatov's Atomic Energy Institute, The Academy of Sciences, Moscow, U.S.S.R.

Received 13 April 1961

The investigation was carried out at the 1.5 meter cyclotron at the Kurchatov's Atomic Energy Institute, the Academy of Sciences, USSR. Azimuthal variation of the magnetic field with a depth near $\pm 15\%$ was provided by three sectors with an angle of about 60° (refs.[1,2,3])). On the inner side of each cover of the accelerating chamber water-cooled circular windings were installed. Power-supply to the windings was provided by motor-generators. This system of windings permits one to correct the mean value of the magnetic field along the radius thus providing acceleration and extraction of ions in the wide range of the magnetic field values. Current carrying windings were

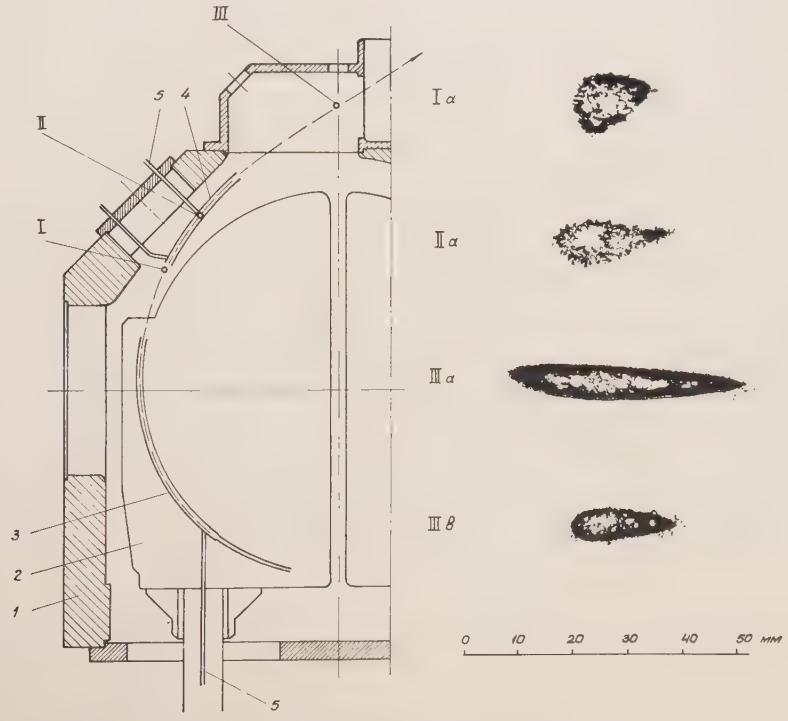

Fig. 1. 1. Accelerating chamber; 2. Dee; 3. Inner part of the deflecting system; 4. Outer part of the deflecting system; 5. High voltage leads.

I, II, III – Points where the plexiglass plates are installed; Ia, IIa, IIIa – Trace of the beam obtained with the inner part only; IIIb – Trace of the beam obtained by simultaneous action of the inner and the outer parts of the system. The scale refers to the photos of the beam traces.

also used to correct the "median plane" of the magnetic field and to regulate the first harmonic of the azimuthal inhomogenity.

The experiments were made at five values of the magnetic field — 5; 10; 13.6; 14.7 and 17 kGauss. Protons were accelerated to the energy of 5 MeV and H_2^+ ions to the energies of 10; 21; 24 and 31.5 MeV. The frequency of the resonant circuit was changed by shifting the shortening bars of the resonance lines. The ion source was of the "slit" type[4]). Extraction of the ion beam from the accelerating chamber was accomplished by means of a deflecting system with inhomogeneous electric field[5]). The coefficient of extraction at the different modes of acceleration was changed in the range from 25 to 60%, the ion current in the extracted beam being 50–400 μA. The experiments were carried out in a pulsed mode of operation with a duty-ratio range from 10 to 1000.

The deflecting system consists of two parts, one inside the dee, the other outside. The inner part of the deflecting system includes the plane electrode section and hyperbolic cross-section electrodes with angular dimensions of 25° and 65° respectively. The outer part has an angular dimension of 35° and its electrodes cross-sections form hyperbolas. Power-supply to the deflecting system is provided by two high voltage rectifiers.

The extraction of the beam was studied when both inner and outer parts of the system were functioning simultaneously as well as when the outer part was removed. The coefficient of extraction was practically unchanged in both cases. The traces of the beam on the plexiglass plates installed at the different points along the beam-path are shown in fig. 1. The deflecting system as a whole was studied at the magnetic field strength values of 5 and 10 kGauss. The voltage at the inner part leads was 23 kV, at the outer part leads 30 kV at a magnetic field of 10 kGauss. Such a system allows one to extract the beam from the accelerating chamber with a small angular divergence which in turn permits one to use the small aperture quadrupole lenses producing no loss in the ion beam intensity. Moreover, the small cross-sectional area of the beam at the boundaries of a fringing field of the cyclotron magnet permits the installation of the entrance slit of the magnetic analyzer at this point. The corresponding paper will be published.

In conclusion the authors express their gratitude to L. F. Kondrashev and S. I. Prokofiev for their efficient help in the preparation of the experiments.

[1]) J. A. Zavenyagin, R. A. Metschcherov, E. S. Mironov, L. M. Nemenov and J. A. Kholmovsky, Proceedings of the Intern. Conf. on High Energy Accelerators and Instrumentation – CERN (1959) p. 225.

[2]) R. A. Metshcherov, E. S. Mironov, L. M. Nemenov, S. N. Ribin and J. A. Kholmovsky, Atomnaja Energija **8** (1960) 201 (in Russian).

[3]) R. A. Metshcherov and E. S. Mironov, Atomnaja Energija **10** (1961) 127 (in Russian).

[4]) J. I. Afanasiev, L. F. Kondrashov, L. N. Mikhailov and A. I. Nastukha, Pribory i tekh. Exper. No. 6 (1959) 25 (in Russian).

[5]) A. A. Arzumanov and E. S. Mironov, Atomnaja Energija **6** (1959) 202 (in Russian).

NUCLEAR INSTRUMENTS AND METHODS 12 (1961) 365–366; NORTH-HOLLAND PUBLISHING CO.

THE SCATTERING SURFACE METHOD OF MEASURING DISPERSION RELATIONS WITH A PHASED CHOPPER VELOCITY SELECTOR†

R. E. SCHMUNK and R. M. BRUGGER

Phillips Petroleum Company, Atomic Energy Division, Idaho Falls, Idaho

Received 12 June 1961

The MTR phased-chopper velocity selector[1]) is being used to study single crystal coherent inelastic neutron scattering from beryllium. The experiment is directed toward obtaining the dispersion relations for the principal crystalline directions in beryllium, and the methods for determining these relations form a basis for comparing the data accumulating potential of the velocity selector with that of triple axis crystal spectrometers using the constant Q method[2]).

Two methods using the velocity selector and based on scattering surface interpolation are being used. Both methods take advantage of simultaneous data recording from multiple scattering angles. In the experimental arrangement, a total to twelve BF_3 detectors with a diameter of one inch and an active length of four inches were placed side by side with their center wires perpendicular to and at a distance of approximately two meters from the beryllium crystal. The detector pulses were stored in separate sections of the 4096 channel time-of-flight analyzer for individual detectors or for sets of two detectors in parallel, thus defining from six to twelve closely spaced scattering angles.

One of the methods being used is similar to the method of "successive approximations"[3]) used with triple axis spectrometers. An estimate of the dispersion curve in a symmetry direction is made and the experimental parameters are adjusted for the center scattering angle to confirm a point on the dispersion curve. Quite often the estimate is wrong; the point does not fall in the desired symmetry direction and in the method of "successive approximations" a new estimate is made based on the knowledge obtained from the preceding determination. However, when using a phased chopper velocity selector with multiple angles, an inelastic scattering peak with a given energy change which is observed in one detector is often observed with nearly the same energy change in the other detectors. These data when plotted in reciprocal space define scattering surfaces[4,5]). Where a scattering surface intersects a symmetry direction one can generate a phonon by calculation for the point of intersection by applying the conditions $\hbar\omega = E_0 - E'$ and $\mathbf{k}_0 - \mathbf{k}' = \mathbf{Q} = 2\pi\boldsymbol{\tau} - \mathbf{q}$. Here E_0 and E' are the energies for the incident and scattered neutrons respectively, and $\mathbf{k}_0$ and $\mathbf{k}'$ are their wave vectors. The phonon frequency and wave vector are ω and $\mathbf{q}$, and $\boldsymbol{\tau}$ is a translation vector of the reciprocal lattice. Hence, while one does not always realize the aim of observing neutron interactions with phonons which are traveling in some particular crystallographic direction, the desired data are often obtained by interpolation from scattering surfaces. Several examples of this scattering surface method are given in fig. 1.

A similar technique[2]), is illustrated in fig. 2. The energy of the incident neutrons is selected to satisfy the condition $k_0 \sin\theta = 2\pi \mid \boldsymbol{\tau} \mid$ where θ relates the crystal orientation to the direction of the incident

† Work done under the auspices of the U.S. Atomic Energy Commission.

[1]) R. M. Brugger and J. E. Evans, Nucl. Instr. and Meth. **12** (1961) 75.

[2]) B. N. Brockhouse, "Methods of Neutron Spectrometry", paper IS/18 IAEA Symposium on "Inleastic Scattering of Neutrons in Solids and Liquids", Vienna, October 1960.

[3]) B. N. Brockhouse and P. K. Iynegar, Phys. Rev. **111** (1958) 747.

[4]) G. Placzek and L. Van Hove, Phys. Rev. **93** (1954) 1207.

[5]) Carter, Palevsky and Hughes, Phys. Rev. **106** (1957) 1168.

neutron beam. Thus, the terminus of the wave vector, k_0, lies on a line between two reciprocal lattice points. By setting the array of BF_3 detectors at the proper scattering angles, neutron-phonon interactions are observed for phonons which are traveling nearly along the symmetry direction of interest. By this latter technique as many as 40 phonons and 5 scattering surfaces have been observed in a single data run. Again the scattering surface technique can be readily employed when the interactions are not exactly in a symmetry direction as evidenced by the data shown in fig. 2.

By using the scattering surface methods outlined above, at least one and often several transitions in the desired directions are observed in a single data run even though no actual data point falls in this direction. Since the times and counting rates required for a data run are similar to those obtained with a triple axis spectrometer using the constant Q method, the phased chopper velocity selectors have great potential when studying single crystal properties.

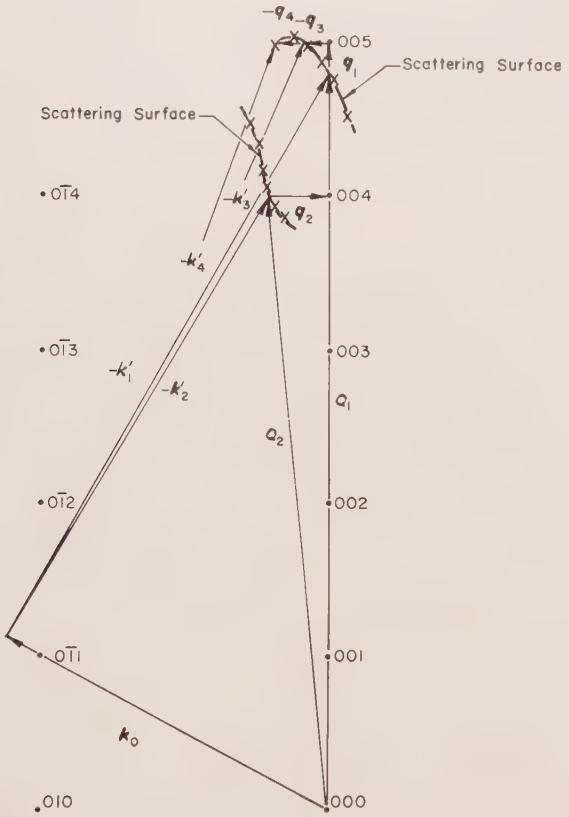

Fig. 1. Reciprocal lattice plot, in the plane $h = 0$, of beryllium dispersion curve data (16 hr. run) showing scattering surfaces and vector diagrams for generated phonons for points where the scattering surfaces intercept symmetry directions. Data points are indicated by x's.

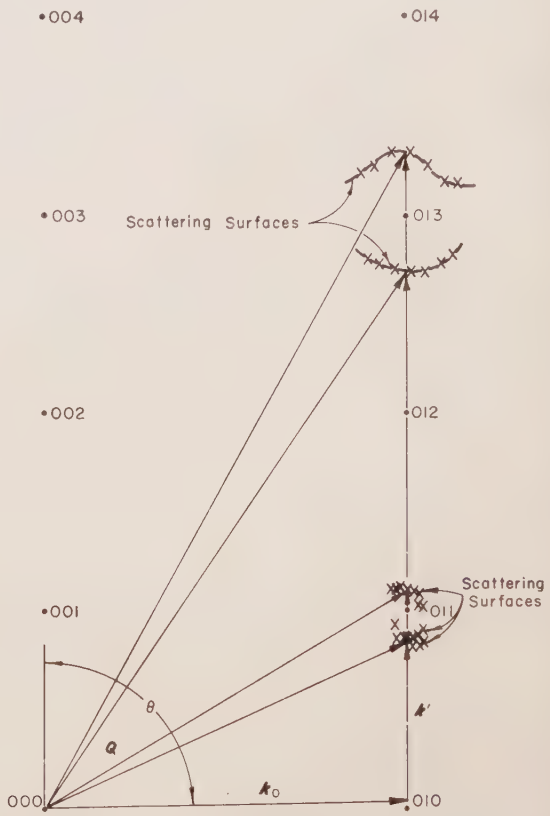

Fig. 2. Dispersion data and scattering surfaces for a data run (40 hr.) where the incident neutron energy satisfied the relation $k_0 \sin 0 = 2\pi|\vec{\tau}_{010}|$. The experiment is confined to the plane $h = 0$ of reciprocal space. Data points are indicated by x's.

BOOK REVIEWS

CODES FOR REACTOR COMPUTATIONS. (Proceedings of a Seminar, Vienna, April 25–29, 1960). Published 1961 by International Atomic Energy Agency, Vienna I.A.E.A. – Publications, Proceedings Series, STI/PUB/24 Pp. 540. U.S. $ 8.00.

In april 1960 a "Seminar on Codes for Reactor Computations" was held at Vienna. About 100 specialists –mathematicians, physicists and engineers– from 20 countries participated in this seminar, which was sponsored by the International Atomic Energy Agency.

In this volume I.A.E.A. publishes the complete proceedings of the Seminar. The information presented gives a very nice survey of the actual stage of nuclear reactor computations, thus making the book indispensable for everybody working in this field. However, because of the general character of many problems discussed during the Vienna Seminar, "Codes for Reactor Computations" will also be very useful for people dealing with any part of the computation field. The five main parts of the book are entitled as follows:

A. Facilities for reactor computations
B. Utilization of computers for reactor problems
C. Code libraries, existing and planned
D. Universal languages
E. Numerical and statistical methods.

WERNER SCHNEIDER

MODERN PHYSICS FOR THE ENGINEER (second series), edited by Louis N. Ridenour and William A. Nierenberg, (McGraw-Hill, 1961), p. 383. 74s.

The first series covered by the above book-title appeared in 1954. It represents an effort to abridge the gap between "pure" scientists and engineers, a gap becoming smaller and smaller as physical sciences develop. On one side this is clearly observed by the scientist in the physical laboratory who has to work with more and more advanced equipment and on the other side by the modern engineer who is faced with the problem of quickly trying to understand the consequences and possible applications of an increasing number of new physical discoveries. In many cases the time elapsed between a fundamental discovery in physics and a selling product may be surprisingly short and it is therefore of increasing importance to present the achievements of modern physics for the engineer.

The new volume constitutes a very ambitious and successful attempt in this respect. It contains three main parts with the general titles: 1. "The Laws of Nature", 2. "Man's Physical Environments", 3. "Technology". The first part is dominated by the great progress in nuclear physics and solid state and low temperature physics during recent years. Emilio Segrè and Luis Alvarez describe in two subsequent chapters the present status of elementary particles and Maria Goeppert-Mayer revues the basic concepts of the nuclear shell theory. Robert Hofstadter reports on his remarkable new techniques to obtain detailed information on nuclear structure by means of high energy electron scattering. The quick development is demonstrated by the note added in proof giving new results of great interest. W. Houston has given a condensed and clear survey of some of the foundations of solid state physics, entitled "Electrons and nuclei in ideal crystals". Low temperature physics has become a field of research where many ordinary-sized laboratories can take part thanks to the nowadays commercially available helium and hydrogen liquefiers. The properties of liquid helium which have occupied the interest of low-temperature-physicists for several decades are reviewed by John Pellam. Superconductivity has for a long time been a mysterious phenomenon which has found no satisfactory theoretical explanation until Bardeen, Cooper and Schrieffer put forward their famous theory (BCS theory) in 1957. M. Tinkham gives an interesting account of this subject. Alfredo Banos treats magnetohydrodynamic waves in another chapter. Other topics in the book are "The origin of nuclear species by means of nuclear reactions in stars" (William Fowler), "Radio astronomy" (Ronald Bracewell), "Origin of the earth's magnetic field" (Walter Elsasser), "Controlled thermonuclear fusion" (S. Colgate, H. York), "Nuclear Reactors – A novel technology" (Mark Miles), "Particle accelerators" (Robert Wilson) and "Frontiers of aerodynamic research" (Ronald Smelt).

KAI SIEGBAHN

ERRATUM

R. Benaroya and W. J. Ramler, Deflection coil for an external accelerator beam. Nuclear Instruments and Methods **10** (1961) 120.

Vol. **10** (1961) p. 120: Last line in the first column "proportional to the charge (Q^{+1}) and inversely" has been misplaced. It should follow the sixth line in the second column as shown below: "Since the deflection of this unit is directly proportional to the charge (Q^{+1}) and inversely proportional to both the nucleon number (N^{-1}) . . .".

AUTHOR INDEX

Ageno, M., Low jitter pulse discriminator and shaper 341
Akiyoshi, Tsunekazu, *see* Sonoda
Anderson, Herbert L., Alpha particle thickness gauge using a solid state detector 111
Arzumanov, A. A., R. A. Metshcherov, E. S. Mironov, L. M. Nemenov, S. N. Ribin and J. A. Kholmovskij, Extraction of a beam and energy regulation in the cyclotron with azimuthally varying magnetic field (Letter to the Editor) 363

Baker, Stanley C., Quentin A. Kerns, Frederick A. Kirsten, Dick A. Mack and Thomas A. Nunamaker, Test routines and monitoring for a large counter experiment 1
Baker, Stanley C., Frederick A. Kirsten, Dick A. Mack and Clyde Wiegand, An electronic data-acquisition system for use with a complex nuclear physics experiment 11
Baker, Stanley C., A transistor coincidence-discriminator circuit for 10^{-8}-second pulses 20
Barna, Arpad, J. Howard Marshall and Matthew Sands, A multifold coincidence-veto circuit using transistors 43
Bashandy, Ekbal, Methods for the measurement of sub-nanosecond lifetimes of low-energy nuclear levels . 227
Bell, R. E., Higher order events in coincidence counting (Letter to the Editor) 199
Benveniste, J., R. Booth and A. C. Mitchell, Observations on the response of two p–n junction diodes to protons 67
Bjerke, Arthur E., Quentin A. Kerns and Thomas A. Nunamaker, A solid-state chronotron for digitizing time delays 25
Bologna, G., G. Diambrini, R. Toschi, A. S. Figuera, U. Pellegrini, B. Rispoli and A. Serra, A pair spectrometer for energies up to 2 GeV 263
Booth, R., *see* Benveniste
Breare, J. M., *see* Hopkins
Brooks Shera, E., Further comments on accidental coincidences in fast-slow coincidence systems (Letter to the Editor) 198
Brugger, R. M., and J. E. Evans, MTR phased chopper velocity selector 75
Brugger, R. M., *see* Schmunk
Burgov, N. A., A. V. Davydov and G. R. Kartashov, An iron-free toroidal β-spectrometer with high transmission 316

Chang, C. C., Magnetohydrodynamic method of injecting charged particles into a magnetic field 345
Clegg, A. B., *see* Rowe
Cox, Gerald C., *see* Kerns
Cranberg, L., R. A. Fernald, F. S. Hahn and E. F. Shrader, Production of high intensity ion pulses of nanosecond duration 335

Davison, M., *see* Hopkins
Davydov, A. V., *see* Burgov
Dearnaley, G., and A. B. Whitehead, The semi-conductor surface barrier for nuclear particle detection 205
De Villiers, J. A. M., *see* Meyer
Diambrini, G., *see* Bologna
Dumitrescu, R., *see* Ţintă

Ehrman, J. R., *see* Margulies
Elliott, Jack H., Thick junction radiation detectors made by ion drift 60
Evangelisti, R., and G. Sacerdoti, Proposal for a storage ring for relativistic charged particles (Letter to the Editor) 201
Evans, Frank, and Frederick A. Kirsten, An 1800-bit buffer store and readout system 39
Evans, J. E., *see* Brugger

Falk, K., *see* Tove
Fernald, R. A., *see* Cranberg
Figuera, A. S., *see* Bologna

Gabriel, R., and A. M. Segar, Some transistor circuits for nuclear physics research 307
Goulding, Fred S., and William L. Hansen, Leakage current in semiconductor junction radiation detectors and its influence on energy-resolution characteristics 249

Hahn, F. S., *see* Cranberg
Hansen, William L., *see* Goulding
Hill, C. R., A method of alpha particle spectroscopy for materials of very low specific activity 299
Holland, R. E., The design of bunching magnets . . . 103
Holmryd, S., K. E. Larsson and K. Otnes, A neutron time-of-flight spectrometer with a semi-monochromatizing chopper 355
Hopkins, H. W. K., M. Davison, L. Lyons, J. M. Breare, D. Roaf and D. F. Shaw, A 12 cm liquid deuterium bubble chamber 323
Howe, F. A., *see* Muggleton

Katase, Akira, *see* Sonoda
Kartashov, G. R., *see* Burgov
Kerns, Quentin A., and Gerald C. Cox, A triggered nanosecond light source 32
Kerns, Quentin A., *see* Baker
Kerns, Quentin A., *see* Bjerke
Kholmovskij, J. A., *see* Arzumanov
Kirsten, Frederick A., *see* Baker
Kirsten, Frederick A., *see* Evans

Larsson, K. E., *see* Holmryd
Legge, G. J. F., A stable 0.1 % beam current integrator for the range 0.1 to 20 μA 195

Liu, F. F., and F. J. Loeffler, Transistorized linear gate for photomultiplier pulses 124
Loeffler, F. J., *see* Liu
Lohmann, W., and W. H. Perkins, Stabilization of the counting rate by irradiation of the liquid scintillation counting solutions with UV-light 329
Lyons, L., *see* Hopkins

Mack, Dick A., *see* Baker
Magda, T., *see* Ţintă
Margulies, S., and J. R. Ehrman, Transmission and line broadening of resonance radiation incident on a resonance absorber 131
Marshall, J. Howard, *see* Barna
Martalogu, N., *see* Ţintă
Metshcherov, R. A., *see* Arzumanov
Meyer, A., *see* Zerby
Meyer, M. A., J. A. M. de Villiers and A. J. van der Walt, Hodoscope system for experiments on the scattering of cosmic ray mu-mesons, Part III – Theory of the hodoscope 180
Mironov, E. S., *see* Arzumanov
Mitchell, A. C., *see* Benveniste
Muggleton, A. H. F., and F. A. Howe, The preparation of thin ^{18}O targets 192
Murray, R. B., *see* Zerby

Nemenov, L. M., *see* Arzumanov
Nordhagen, Rolf, Simple scheme for using the selective storage of a multichannel pulse height analyser in coincidence counting 151
Nordhagen, Rolf, Proton resonances suitable to shape calibrate a scintillation γ-ray spectrometer 291
Nunamaker, Thomas A., *see* Baker
Nunamaker, Thomas A., *see* Bjerke

Otnes, K., *see* Holmryd

Paulin, A., Betriebszustände des Mikrotrons mit geteiltem Magnet (racetrack microtron) 155
Pellegrini, U., *see* Bologna
Perkins, W. H., *see* Lohmann

Rabson, Thomas A., Utilization of tunnel diodes in fast trigger circuits 127
Ramaswamy, M. K., *see* Vanderleeden
Rautenbach, W. L., Experimental verification of the space charge law ($I = k(e/m)^{\frac{1}{2}}V^{\frac{3}{2}}$) for ion beams from a plasma ion source 169
Ribin, S. N., *see* Arzumanov
Rispoli, B., *see* Bologna
Roaf, D., *see* Hopkins
Rowe, D. J., G. L. Salmon and A. B. Clegg, Finite geometry corrections for angular correlation measurements 353

Sacerdoti, G., *see* Evangelisti
Salmon, G. L., *see* Rowe
Sands, Matthew, *see* Barna
Schmunk, R. E., and R. M. Brugger, The scattering surface method of measuring dispersion relations with a phased chopper velocity selector (Letter to the Editor) 365
Segar, A. M., *see* Gabriel
Seki, Masao, *see* Sonoda
Serra, A., *see* Bologna
Shaw, D. F., *see* Hopkins
Shrader, E. F., *see* Cranberg
Sonoda, Masateru, Akira Katase, Masao Seki and Tsunekazu Akiyoshi, Magnetic field of alternately charged symmetric multipole magnet 349
Sujkowski, Ziemowid, Adaptation of a $\pi\sqrt{2}$ beta-ray spectrometer for coincidence experiments 187

Ţintă, F., N. Martalogu, R. Dumitrescu and T. Magda, On the natural pulsing of cyclotron external beams in the nanosecond range 138
Toschi, R., *see* Bologna
Tove, P. A., and K. Falk, Transit time of charge carriers in the semiconductor ionization chamber 278

Vanderleeden, J. C., and M. K. Ramaswamy, Total conversion coefficients with a sum-coincidence NaI spectrometer (Letter to the Editor) 362
Van der Walt, A. J., *see* Meyer

Whitehead, A. B., *see* Dearnaley
Wiegand, Clyde, *see* Baker

Zerby, C. D., A. Meyer and R. B. Murray, Intrinsic line broadening in NaI(Tl) gamma-ray spectrometers . . 115

BOOK REVIEWS

E. Glueckauf, Editor, Atomic Energy Waste. Its Nature Use and Disposal (Torsten Lindqvist) 203
Advances in Electronics and Electron Physics, Volume XII, 1960: Photo-Electronic Image Devices (P. A. Tove) 203
Thomson, A. S. *et al.*, Editors, Nuclear Reactor Containment Buildings and Pressure Vessels, (Proceedings of International Symposium at the Royal College of Science and Technology, Glasgow) (Stig O. W. Bergström) 204
Directory of Nuclear Reactors, Vol. III; Research, Test and Experimental Reactors (Supplement to Vol. II) (International Atomic Energy Agency, IAEA, Vienna 1960) (Matts Strååt) 204
Codes for Reactor Computations. (Proceedings of a Seminar, Vienna, April 25–29, 1960) (Werner Schneider) 367
Ridenour, Louis N., and William A. Nierenberg, Editors, Modern Physics for the Engineer (second series, 1961) (Kai Siegbahn) 367

SUBJECT INDEX

Accelerators and Reactors

The design of bunching magnets, R. E. Holland . . . 103
On the natural pulsing of cyclotron external beams in the nanosecond range, F. Ţintă, N. Martalogu, R. Dumitrescu and T. Magda . . . 138
Betriebszustände des Mikrotrons mit geteiltem Magnet (racetrack microtron) A. Paulin . . . 155
Experimental verification of the space charge law ($I \sim k(e/m)^{\frac{1}{2}}V^{\frac{3}{2}}$) for ion beams from a plasma ion source, W. L. Rautenbach 169
Magentic field of alternately charged symmetric multipole magnet, Masateru Sonoda, Akira Katase, Masao Seki and Tsunekazu Akiyoshi . . . 349
Production of high intensity ion pulses of nanosecond duration, L. Cranberg, R. A. Fernald, F. S. Hahn and E. F. Shrader 335

Detectors

Thick junction radiation detectors made by ion drift, Jack H. Elliott . . . 60
Observations on the response of two p–n junction diodes to protons, J. Benveniste, R. Booth and A. C. Mitchell . . . 67
The semiconductor surface barrier for nuclear particle detection, G. Dearnaley and A. B. Whitehead . . . 205
Leakage current in semiconductor junction radiation detectors and its influence on energy-resolution characteristics, Fred S. Goulding and William L. Hansen . . . 249
Transit time of charge carriers in the semiconductor ionization chamber, P. A. Tove and K. Falk . . . 278
A 12 cm liquid deuterium bubble chamber, H. W. K. Hopkins, M. Davison, L. Lyons, J. M. Breare, D. Roaf and D. F. Shaw . . . 323

Erratum

R. Benarova and W. J. Ramler, Deflection coil for an external accelerator beam (Nuclear Instruments and Methods **10** (1961) p. 120) . . . 367

Instruments and Methods for Nuclear Spectroscopy

MTR phased chopper velocity selector, R. M. Brugger and J. E. Evans . . . 75
Alpha particle thickness gauge using a sólid state detector, Herbert L. Anderson . . . 111
Intrinsic line broadening in NaI (Tl) gamma-ray spectrometers, C. D. Zerby, A. Meyer and R. B. Murray . . . 115
Transmission and line broadening of resonance radiation incident on a resonance absorber, S. Margulies and J. R. Ehrman 131
Adaptation of a $\pi\sqrt{2}$ beta-ray spectrometer for coincidence experiments, Ziemowid Sujkowski . . . 187
The preparation of thin ^{18}O targets, A. H. F. Muggleton and F. A. Howe . . . 192
Methods for the measurement of sub-nanosecond lifetimes of low-energy nuclear levels, Ekbal Bashandy . . . 227
A pair spectrometer for energies up to 2 GeV, G. Bologna, G. Diambrini, R. Toschi, A. S. Figuera, U. Pellegrini, B. Rispoli and A. Serra . . . 263
Proton resonances suitable to shape calibrate a scintillation γ-ray spectrometer, Rolf Nordhagen . . . 291
A method of alpha particle spectroscopy for materials of very low specific activity, C. R. Hill . . . 299
An iron-free toroidal spectrometer with high transmission, N. A. Burgov, A. V. Davydov and G. R. Kartashov . . . 316
Stabilization of the counting rate by irradiation of the liquid scintillation counting solutions with UV-light, W. Lohmann and W. H. Perkins . . . 329
A neutron time-of-flight spectrometer with a semi-monochromatizing chopper, S. Holmryd, K. E. Larsson and K. Otnes 355

Instruments and Methods for High Energy Physics

Test routines and monitoring for a large counter experinent, Stanley C. Baker, Quentin A. Kerns, Frederick A. Kirsten, Dick A. Mack and Thomas A. Nunamaker 1
Hodoscope system for experiments on the scattering of cosmic ray mu-mesons. Part III – Theory of the hodoscope, M. A. Meyer, J. A. M. de Villiers and A. J. van der Walt 180
Finite geometry corrections for angular correlation measurements, D. J. Rowe, G. L. Salmon and A. B. Clegg 353

Letters to the Editor

Further comments on accidental coincidences in fast-slow coincidence systems, E. Brooks Shera 198
Higher order events in coincidence counting, R. E. Bell 199
Proposal for a storage ring for relativistic charged particles, R. Evangelisti and G. Sacerdoti 201
Total conversion coefficients with a sum-coincidence NaI spectrometer, J. C. Vanderleeden and M. K. Ramaswamy . . 362
Extraction of a beam and energy regulation in the cyclotron with azimuthally varying magnetic field, A. A. Arzumanov, R. A. Metshcherov, E. S. Mironov, L. M. Nemenov, S. N. Ribin, J. A. Kholmovskij 363
The scattering surface method of measuring dispersion relations with a phased chopper velocity selector, R. E. Schmunk and R. M. Brugger 365

Nuclear Electronics

An electronic data-acquisition system for use with a complex nuclear physics experiment, Stanley C. Baker, Frederick A. Kirsten, Dick A. Mack and Clyde Wiegand 11
A transistor coincidence-discriminator circuit for 10^{-8}-second pulses, Stanley C. Baker 20
A solid-state chronotron for digitizing time delays, Arthur E. Bjerke, Quentin A. Kerns and Thomas A. Nunamaker 25
A triggered nanosecond light source, Quentin A. Kerns and Gerald C. Cox 32
An 1800-bit buffer store and readout system, Frank Evans and Frederick A. Kirsten 39
A multifold coincidence-veto circuit using transistors, Arpad Barna, J. Howard Marshall and Matthew Sands . . . 43
Transistorized linear gate for photomultiplier pulses, F. F. Liu and F. J. Loeffler 124
Utilization of tunnel diodes in fast trigger circuits, Thomas A. Rabson 127
Simple scheme for using the selective storage of a multichannel pulse height analyser in coincidence counting, Rolf Nordhagen 151
A stable 0.1 % beam current integrator for the range 0.1 to 20 μA, G. J. F. Legge 195
Some transistor circuits for nuclear physics research, R. Gabriel and A. M. Segar 307
Low jitter pulse discriminator and shaper, M. Ageno 341

Plasma Physics

Magnetohydrodynamic method of injecting charged particles into a magnetic field, C. C. Chang 345